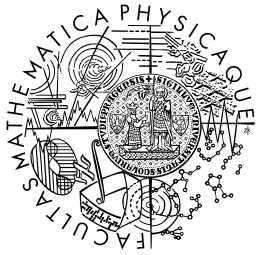

FACULTY
OF MATHEMATICS
AND PHYSICS
Charles University

DOCTORAL THESIS

Jana Alexandra Nemravová

Determination of accurate fundamental stellar properties of stars via analyses of suitable binary and multiple systems

Astronomical Institute of the Charles University

Supervisor of the doctoral thesis:	prof. RNDr. Petr Harmanec, DrSc.
Study programme:	Physics
Study branch:	4F1

Prague 2016

I declare that I carried out this doctoral thesis independently, and only with the cited sources, literature and other professional sources.

I understand that my work relates to the rights and obligations under the Act No. 121/2000 Sb., the Copyright Act, as amended, in particular the fact that the Charles University has the right to conclude a license agreement on the use of this work as a school work pursuant to Section 60 subsection 1 of the Copyright Act.

In ..... date ..... signature of the author

Title: Determination of accurate fundamental stellar properties of stars via analyses of suitable binary and multiple systems

Author: Jana Alexandra Nemravová

Institute: Astronomical Institute of the Charles University

Supervisor: prof. RNDr. Petr Harmanec, DrSc., Astronomical Institute of the Charles University

Abstract:
Context: Binaries and multiple systems are very frequent and form large fraction of all stellar systems. In contrast to their single counterparts, studying binaries provides the possibility to accurately determine fundamental properties of their components that are needed for testing models of stellar structure and evolution. On top of that, binaries can be used for accurate distance determinations. The mass exchange in close binaries remains the only mechanism, which completely alters their evolution.
Aims: The primary goal of my doctoral study was to determine orbital elements of selected systems and properties of their components — masses, radii, and effective temperatures. — In case of more complicated objects (e.g. interacting multiple systems, mass-transferring binaries, ...) the secondary goal was to confront our results with predictions of theoretical models.
Methods: Studies that I co-authored were based on three different types of observations, each sensitive to partly different properties of studied systems — photometry, spectroscopy, and spectro-interferometry. The analysis was carried out through several "observation-specific" models, whose outcome was critically compared to each other and to previous studies of the object in question.
Results: Throughout my study I contributed to: (i) Determination of sizes and orientations of all orbits of quadruple system ξ Tau and properties of its components. (ii) confirmation of duplicity of two Be stars BU Tau, and γ Cas, (iii) determination of orbital elements and fundamental properties of binary undergoing mass-transfer BR CMi, close triple system HD 152246, binary containing a pair of massive stars Y Cyg, binary with apsidal motion V346 Cen, a member of the putative cluster δ Lyr — BD+36 3317, and (iv) resolving the distance ambiguity of the eclipsing binary containing large dusty disk ϵ Aur.

Keywords: stars, multiple systems, spectroscopy, photometry, interferometry

I thank to my supervisor Petr Harmanec for guidance through the universe of binaries, to my consultants Denis Mourard and Olivier Chesneau for the introduction into optical spectro-interferometry and help in the investigation of ξ Tauri and β Lyrae systems, to Mirek Brož, whose help gave me the much needed impulse to finish ξ Tauri study, to Petr Pokorný whose sparkling character made the first two years of my doctoral study real fun. The biggest thanks belong to my wife Adélka, because I would never finish my doctoral study without her love and support. Finally I thank to my daughter Šášulka for bringing so much joy into my life.

Contents

1. Introduction

"Tell me how you behave and I tell you who you are.", could be a motto of binary research, because through the mutual (almost exclusively gravitational) interaction of two binary components, their properties, evolutionary status and structure can be inferred.

Here I provide introduction into the field. First the orbital motion is introduced, which is what makes two nearby stars a binary. It is followed by an overview of principal motivations for the binary research. Then I proceed to introduce more complicated objects — hierarchical multiple systems, and systems undergoing the mass transfer. Finally I briefly introduce Be stars, as their behaviour might be partially determined by binary interaction.

1.1 Binaries

A binary is a system of two gravitationally bound stars revolving around a common barycentre. In order to separate binary components and study their properties, their orbits have to be determined first. This is often not a simple task, because the orbital motion can be masked by various processes, but to introduce the subject I start with the simplest binary possible — a pair of gravitationally bound point masses.

1.1.1 Orbital elements

The trajectory of a binary resulting from the Newton's two body problem is an ellipse. The trajectory of secondary (less massive) component with respect to the primary (more massive) component is given by six parameters called orbital elements. The relative position of j-th component with respect to the barycentre of the binary is given by the Kepler's first law

$$|\vec{r}_j|\,(t) = \frac{a_j\left(1-e^2\right)}{1+e\cos v(t)}, \tag{1.1}$$

where $|\vec{r}|$ is the distance between j-th component and the barycentre, a the semimajor axis, e the eccentricity, and v the true anomaly. Index $j \in \{1,2\}$, where 1 denotes primary, 2 secondary. True anomaly is given by the following equation:

$$\tan\frac{v}{2} = \sqrt{\frac{1-e}{1+e}}\tan\frac{E}{2}, \tag{1.2}$$

where E is the eccentric anomaly given by the Kepler's equation

$$E = M + e\sin E, \tag{1.3}$$

M denoting the mean anomaly given by $M = 2\pi\left(t - T_\mathrm{p}\right)/P$. Transformation from the reference frame tied to the binary orbit, where the z-axis is perpendicular to the orbital plane, and x-axis goes through the periastron, to an arbitrary reference frame is carried out by the following transformation:

$$\vec{r}_{\mathrm{A},j} = R_z\left(-\Omega\right)R_x\left(-i\right)R_z\left(-\omega_j\right)\vec{r}_j, \tag{1.4}$$

where $\vec{r_\mathrm{A}}$ are barycentric Cartesian coordinates in an arbitrary reference frame, R_z (R_x) denotes the rotation matrix, around the z-axis (x-axis), Ω is the longitude of ascending node, i the inclination, ω the argument of periastron, and $\vec{r}$ are Cartesian barycentric coordinates in the reference frame tied to the binary. The arguments of periastron of individual binary components are not independent but related through $\omega_2 = \omega_1 + \pi$ (in radians).

In order to determine positions of both components with respect to the barycentre the following eight orbital elements have to be determined: a_1, a_2, e, i, ω, Ω, T_p, and P. They also determine the masses of both components through the third Kepler's law (Eq. 1.5), and definition of the barycentre (Eq. 1.6).

$$\frac{\left(a_1+a_2\right)^3}{P^2} = G\frac{\left(m_1+m_2\right)}{4\pi^2}, \tag{1.5}$$

$$m_1 a_2 = m_2 a_1, \tag{1.6}$$

where m denotes the masses, and G Newton's gravitational constant.

This is not the only possible set of orbital elements, because any combination of orbital elements is also an orbital element, e.g. for the description of radial-velocity curve it is beneficial to introduce semiamplitude of the RV-curve $K_j = f(a_j, e, P)$.

Orbital elements of this simplified model are constant, but realistic systems are not point masses, therefore in reality the orbits are not closed ellipses. For the majority of systems, the difference between the model and realistic stars is very small and does not produce an effect that would be observable on a human timescale. A list of common departures from the two-point-mass model is the following:

(i) **Stars cannot be reduced to point masses:** Tidal interaction between components is non-negligible and higher moments of the multi-pole expansion have to be included. This effect is typical for very close binaries and manifests itself as an apsidal advance.

(ii) **The system consists of more components:** Already three-body problem does not have an analytic solution, and orbital elements of systems consisting of three or more stars are not constant. Multiple systems are introduced in greater detail in Sect. 1.2.

(iii) **Component masses are not constant:** Mass of a star can significantly change due to mass-transfer in semi-detached and over-contact binaries, or due to strong stellar wind in O-type stars and Wolf-Rayet stars or late-type giant stars. Mass transfer is discussed in greater detail in Sect. 1.3.

(iv) **Newton's gravitational law is invalid:** In binary stars (excluding neutron stars and white dwarfs), the departures are usually very small and they demonstrate themselves by an advance of the argument of periastron. Another consequence of general relativity theory — the invariable speed of light — demonstrates itself by the light time travel effect.

1.1.2 How do we categorise binaries?

It is in the human nature to sort and label the surrounding universe as the first step to its (sometimes only apparent) understanding. Binaries are not an exception to this rule and various binaries were assigned different labels. There are two most common ways of their classification.

The first division is based on the observational method, through which the binary nature of a studied system is detectable.

1. **Spectroscopic binaries:** A Doppler shift of spectral lines of at least one component due to orbital motion is observed. Amplitude of this effect is proportional to orbital period $\sim P^{-1/3}$, hence the number of spectroscopic binaries drops significantly for orbital periods $\gtrsim 10^3$ d.

2. **Eclipsing binaries:** The favourable orbital inclination causes that the components eclipse each other at certain orbital phase. These binaries are most common among very close systems with period $P \lesssim 10^1 - 10^2$ d.

3. **Visual/Astrometric binaries:** Orbit of at least one component is resolved. Binaries with orbital periods $P \gtrsim 10^4$ d typically belong to this group, but this estimate depends on the distance of the system from us and on the spatial resolution of the instrument used.

The former two groups are much more numerous, because their observations are limited by magnitude only, while the latter is also limited by the spatial resolution. Note that the numbers given in the previous list serve only for orientation, because there are freaks, that fall outside any box. Also one binary can easily fit into all of these boxes thanks to high resolution observation techniques.

The second division was introduced by Kuiper (1941) and more systematically by Kopal (1955) and is based on the shape of the equipotential that the components are filling.

1. **Detached systems:** Both components are smaller then the last equipotential (the Roche limit) able to separate mass of individual stars.

2. **Semi-detached systems:** One component fills the Roche limit, while the other is below it. Mass from the Roche-lobe filling component may escape through Lagrange point L_1, and be attracted by the second component.

3. **(Over)contact systems:** Both components overfill their Roche limits and share a common envelope.

The latter two types are common only among close binaries, i.e. those whose separation is comparable to their radii.

1.1.3 Why are binaries important?

The principal motivation for the binary research is summarised here. The list is certainly incomplete as binaries provide much more insights into astrophysical processes starting with individual stars and ending with galaxies.

The binary frequency

Binary and multiple systems are very common – they are even more common than single stars, at least for some spectral types. Abt (1983) concluded that among normal stars the multiplicity fractions are 49:39:9:4% for B-type stars, and 45:46:8:1% for F-type to G-type stars, where the numbers denote percentage of single, binary, triple and quadruple systems. Later his findings for low mass stars were challenged by several authors (see, e.g. Duquennoy and Mayor, 1991). The currently accepted binary frequency among low-mass stars is 54:33:8:5 by Tokovinin (2014).

The frequency of multiplicity among massive stars was revised as well. Mason et al. (2009) studied a sample of $\simeq 300$ O-type/early B-type stars through speckle-interferometry and spectroscopy and found that the multiplicity frequency in his sample is reaching up to 75% in open clusters and OB associations. Chini et al. (2012) studied a sample of 250 O-type stars, and 540 B-type stars spectroscopically. Their findings for O-type stars agree very well with those of Mason et al. (2009), but they found that the binary fraction drops significantly for less-massive down to $\simeq 20\%$ among B9 V stars. Sana et al. (2014) conducted an interferometric survey of O-type stars and reported de-biased multiplicity fraction 91% among all O-type stars, and 100% among main-sequence O-type stars. They also found high companion fraction ($\simeq 2.2$) for these objects, suggesting that the majority of massive stars forms in multiple systems. Finally Aldoretta et al. (2015) studied 224 O-type and B-type stars with the Hubble Space Telescope, they arrived at results consistent with previous studies (Mason et al., 2009; Chini et al., 2012).

Hence the possible role of multiplicity has to be evaluated in the majority astrophysical processes in that stars are involved, especially if those are massive stars.

Stellar masses and other fundamental parameters

Binaries provide the best source of accurate stellar masses that are free of any calibration. Unfortunately this statement is not valid for every binary. Until quite recently the only binaries providing the masses were eclipsing spectroscopic binaries (showing spectral lines of both components), which restricted the useful systems only to those having high orbital inclination or very low orbital period, with a handful of oddities such as ϵ Aur.

Visual binaries can provide an estimate of the component masses if distance to the system is known (e.g. from the parallax) but those measurements often lack precision. Speckle-interferometric measurements can be used for the determination of the total mass only, because they provide only separation of two binary components, but not their exact barycentric positions needed for the determination of their mass ratio.

The advent of high-angular resolution techniques such as the optical and infrared spectro-interferometry removed the requirement of the high inclination for sufficiently bright spectroscopic binaries. The number of these systems grows steadily as the technique reaches to fainter objects and uses longer baselines.

The "other" fundamental parameters are the radius, effective temperature, and metallicity.

There are only two sources of accurate stellar radii. The first one are spectroscopic eclipsing binaries. The second source are high resolution techniques, mainly the optical and infrared spectro-interferometry, which has to be coupled with distance estimate or the studied system has to be a spectroscopic binary.

The effective temperature of both components can be estimated through multi-passband photometry for eclipsing binaries. A single-passband photometry constrains only the ratio between the effective temperature of the primary and secondary. A more effective approach is to study stellar spectra, but in case of binaries a special attention must be given to the line blending. Probably the safest approach is to find an appropriate synthetic spectrum for each binary component. However this approach may be also a source of an error, as for close or rapidly rotating binaries the output flux varies from the equator to the pole and the effective temperature estimated this way will depend on the aspect angle.

The situation is very much similar for the metallicity. A common approach is to estimate abundance of individual elements from the equivalent widths of prominent spectral lines. This approach can be falsified by the line blending of binary components. The problem can be again solved by finding a suitable synthetic spectrum for each component.

Why did I chose to discuss these particular properties? Because they together are comparable to the outcome of models of stellar structure and evolution.

Tests of stellar evolution

Binary components are born in the same molecular cloud and have the same age, and initial chemical composition. Binary formation due to N-body interaction is extremely unlikely (maybe with the exception of globular clusters).

Evolution of a single star depends mainly on its initial mass and chemical composition. Further it is also affected by rotation, magnetic activity, mass-loss due to stellar wind, and turbulent mixing, but the impact of these effects on the evolution is minor compared to that of the mass and chemical composition, although their cumulative effect over the lifespan of a star can be significant. Detached binaries unaffected by the mass transfer provide a test of the stellar evolutionary models through a comparison of the measured and predicted position of the binary in the Hertzsprung-Russel diagram or radius-effective temperature diagram.

Such tests using high precision binary data spanning from O-type to M-type stars (ΔR, $\Delta m \leq 3\%$) were carried out by Andersen (1991) and later using a larger set of binaries by Torres et al. (2010). Both authors emphasise the need for such accuracy if any deficiencies of evolutionary models are to be discovered. *This is the primary motivation to re-visit already investigated binaries every time the observational and analytic methods improve enough to yield more accurate fundamental properties.* High quality binary data can be used to refine models of stellar structure, e.g. to estimate the helium abundance, to asses role of the convective overshooting, etc.. Andersen (1991) demonstrates that the full set of parameters (mass m, radius R, metallicity Z, and effective temperature $T_{\rm eff}$) is needed to test the models of stellar structure and evolution. All of them cannot be obtained through one type of observation, *hence it is necessary to observe binaries through several observational methods.*

Determination of reliable properties of all components was one of the goals of all studies that I participated in.

Binaries as probes

Not every member of a binary is a dull detached main-sequence star. On the contrary, pulsating stars, Be stars, spotted stars, giants, super-giants, young stars, white dwarfs and others can be (and often are) members of a binary, which offers opportunity to get fundamental properties of these "rascals" and better estimate their evolutionary status and help in understanding of processes that shape them.

Close eccentric binaries probe the internal structure of stars, because the classical apsidal motion is a function of radial density profile of a star. Nonetheless the effect scales as $\sim r^5$, where r is the ratio between stellar radius and the semimajor axis. Hence the effect is observable on a human timescale only for very close systems. Such test was carried out, for instance by Claret and Gimenez (1993).

Distance determination

Binaries offer two methods for distance determination. The first method is very simple: If one is able to resolve orbit of a spectroscopic binary, the distance to it is given by the ratio of the

angular and physical size of the semimajor axis. Unfortunately these two requirements reduce greatly the number of so far available binaries.

The second is based on the estimation of the distance modulus. This approach is not free of calibration, because each star has to be dereddened, i.e. corrected for the interstellar extinction. This effect has only minor impact on near objects, but can be a source of significant uncertainty for very distant objects, because the interstellar extinction is not homogeneous and isotropic (Fitzpatrick, 2004).

Binaries can also be used to measure distances indirectly. For example the spectroscopic parallax, which is a calibration between the gravitational acceleration and effective temperature (in other words spectral type), and the absolute magnitude $M = f(T_{\rm eff}, \log g)$. Another example is the calibration between the distance and the strength of certain interstellar lines derived by Guinan et al. (2012) to estimate distance of ϵ Aur.

1.2 Multiple systems

The vast majority of multiple stellar systems is organised hierarchically, because this configuration is stable on a long timescale. The hierarchical structure implies that the influence of outer orbit on the inner (and vice versa) has the form of a small perturbation.

This "small perturbation" may play role in the formation of close binaries. Tokovinin et al. (2006) reported that the majority (96 %) of close binaries with periods $P \lesssim 3$ d have a third companion. Close binaries could not form only few solar radii from each other, because the stellar radius decreases significantly (by factor from 10 to 100) as the star moves from the Hayashi line to the zero-age main sequence. The fact that every such binary has a third companion suggests that its presence plays a role in their formation.

Dynamical interaction between inner and outer orbit in a triple system will cause precession of both orbital planes around the total angular momentum vector and rotation of the outer orbit if it has a non-zero eccentricity (Soderhjelm, 1975; Breiter and Vokrouhlický, 2015). Periods of these effects are proportional to the mutual inclination angle, and the ratio P_2^2/P_1, where P_2 (P_1) is the orbital period of the outer (inner) orbit. These effects occur on a human timescale only for close triple systems. They are unable to change semimajor axes of the two orbits.

The situation changes completely if the mutual orbital inclination is $j \gtrsim 40$ deg. In this case the three-body interaction excites oscillation of the eccentricity of the inner orbit and the mutual inclination of both orbits known as Kozai cycles (Kozai, 1962) *The amplitude is independent of the strength of the perturbation*, but depends only on the initial eccentricity of the inner body and the initial mutual inclination. For very high initial inclinations, the amplitude of the oscillation of eccentricity is reaching up to one, bringing the members of the inner binary very close to each other. If the periastron separation is only a few stellar radii, tides can partially dissipate the orbital energy and decrease the semimajor axis of the inner system. This mechanism is called Kozai cycle with tides (Harrington, 1968; Eggleton and Kiseleva-Eggleton, 2001). Fabrycky and Tremaine (2007) found through a synthetic population of triple systems, that the final distribution of inner orbital periods has a peak at $P \simeq 3$ d and the distribution of the mutual inclination has peaks at $j \in \{39.2, 140.8\}$ deg, which are limiting angles. Kozai cycles occur only in between these limits. This prediction was observationally confirmed by Rappaport et al. (2013) whose sample consisted of 39 triple systems, and by Borkovits et al. (2015) who analysed 26 triple systems.

Close binaries represent the richest source of fundamental stellar parameters. Understanding their formation is very important and theoretical works such as Fabrycky and Tremaine (2007) present strong motivation to re-investigate close binaries to observationally asses the true importance of Kozai cycle with tides. For a complete comparison one needs to determine the mutual inclination of the inner and outer orbit j. It can be determined either if both orbits are resolved, or from the perturbation of the inner orbit by the third body. Resolution of close binaries requires a very high spatial resolution and is a task for modern long baseline interferometry.

In my doctoral study I investigated a hierarchical quadruple system ξ Tau. The inner triple subsystem is close (the ratio of semimajor axes is $\simeq 10$), but its orbits are aligned ($j \simeq 0$ deg). Such configuration probably results from the dynamical interaction of the triple with the primordial nebula (see Fabrycky and Tremaine, 2007; Tokovinin, 2008).

Finally, a complete statistics of the frequency of more bodies in binaries is desirable since it can be used to constrain various possible models of the binary formation. A catalogue of multiple stars founded by Tokovinin (1997) had been growing steadily. Tokovinin (2008) offers a comparative statistics of the catalogue. One of his findings is that the distribution of periods of the inner orbit is bi-modal. The scarcity of binaries with inner orbit periods $P \simeq 10^3 - 10^4$ is a selection effect due to observational bias. Radial-velocity variations of these binaries are low and difficult to detect, but the angular separation of these binaries is low for standard imaging techniques. This should be overcome with high angular observation techniques, such as interferometry, hence the scarcity is called "the interferometric gap".

The outer bodies are discovered either directly, if they are bright enough, or through observed perturbations of the inner pair. An isolated eclipsing binary is a very accurate clock ticking twice each orbital period. If the clock is not strictly periodical, presence of a third body might be the cause for the irregularity. If it is so, a part of the eclipse timing variations results from the light time travel effect, which is a purely geometrical effect, or from the dynamical interaction of its components if the triple system is close enough (Borkovits et al., 2003; Breiter and Vokrouhlický, 2015). The latter approach is powerful since it requires only a good series of photometric observations, which can be carried out even for very distant and faint objects. This was observationally demonstrated by Rappaport et al. (2013), who investigated eclipse timings of 2157 binaries observed by the Kepler satellite (Koch et al., 2010).

1.3 Mass transfer

The mass transfer remains the only physical process in a binary, which completely alters the evolution of its components, as it interchanges the initial binary mass ratio. The reversal occurs shortly after the beginning of the process and this fact explains the long-standing Algol paradox, i.e. why the mass-losing component is the less massive component Crawford (1955) in the majority of semi-detached binaries. The existence of the large-scale mass exchange was first numerically modelled by Kippenhahn and Weigert (1967) and the results of early evolutionary model calculations were summarised by Plavec (1970); Paczyński (1971) and compared to the observed binaries undergoing the mass transfer.

In a typical semi-detached binary the mass ratio has been already reversed. The mass transfer rate is low $\dot{m} \simeq 10^{-8}\,\mathrm{M}_\odot\,\mathrm{yr}^{-1}$, and it is conservative, i.e. all mass leaving the mass-losing component (donor) is accreted by the mass-gaining component (gainer). The donor is over-luminous — resembling an earlier-type star then it should according to its mass, because inner layers were exposed by the mass transfer. The gainer is partially or fully embedded within an accretion disk, which is partially opaque (forming a pseudo-photosphere) and partially transparent. The mass of the accretion disk is negligible in comparison to the mass of the gainer (see Hubený and Plavec, 1991; Linnell et al., 1998, for the β Lyr system). Spectral lines of the gainer usually have an emission component, which makes the determination of the RV of the gainer difficult. In favourable cases the RV can be measured by comparison of direct and mirrored profiles of the steep wings of the emission lines (Božić et al., 1995, see application of the method to ϕ Per).

The phase of the rapid mass transfer is significantly shorter than the rest of the process but the mass transfer rates are much higher $\dot{m} \simeq 10^{-5}\,\mathrm{M}_\odot\,\mathrm{yr}^{-1}$. This phase of the mass transfer is probably non-conservative (i.e. a part of the mass and angular momentum leaves the system). At the site of interaction of the mass stream with the accretion disk and/or the stream with itself, when it encircles the gainer, the material is heated forming a hot spot and partially expelled from the system either due to radiative shielding of the hotspot as proposed by Deschamps et al. (2013), and/or due to hydro-dynamical interaction of the mass stream with itself as proposed by Bisikalo et al. (1998).

Mass transfer is the inevitable fate of many close binaries. A post mass transfer binary components are not comparable to models of stellar evolution of single stars. A definitive model of the process of mass transfer has not been found yet, and especially the total mass lost from the system during the process remains very uncertain. Hence description of binaries at various stages of the mass transfer, preferably its rapid phase is much needed to understand the process. During my doctoral studies I studied two stars undergoing the mass transfer: BR CMi probably undergoing already rather slow later phase of the mass transfer, and β Lyr, which is still in the rapid phase, although already after the initial mass ratio reversal.

1.4 Be stars

The most conservative definition of a Be star is that it is a B-type star whose Balmer lines have exhibited an emission component at least once during its recorded spectroscopic history. There is a general agreement that the emission arises from an optically thin circumstellar envelope around the object (a single star or a binary). Nonetheless, the stars having an emission component in their Balmer lines can also be found from M-type to O-type stars.

This conservative definition is too general, because in many cases we are aware of the process responsible for the presence of circumstellar mass. Those processes are: (i) the mass transfer between binary components, when one component overflows its Roche-lobe, (ii) stellar wind, (iii) remnants of primordial nebula in young Herbig stars, (iv) stars at the end of their life — asymptotic giant branch stars, or super giant stars.

I shall adopt the definition of a "Classical Be star": a rapidly rotating ($80 - 90\%$ of the break-up velocity) B-type star that forms a Keplerian gaseous disk and does not belong into any of the above-mentioned categories. They vary on timescale starting from few seconds to tens of years.

The Be phenomenon was not the primary subject of my thesis[1], hence only basics are provided here. A more detailed overview of the subject is in Harmanec (2000); Porter and Rivinius (2003); Rivinius et al. (2013).

Be stars vary on timescales starting from few seconds up to the whole observational time span. A basic overview of their observational properties is the following:

(i) The emission lines of Be stars are double-peaked. In some Be stars, cyclic variations of their ratio were observed. Emission lines of some Be stars have a shell line – a deep and narrow absorption core. For example BU Tauri cyclically varies between a pure emission-line phase and a shell-line phase (see Fig. 1 in Nemravová et al., 2010). Balmer lines are not the only emission lines in their spectra. A number of metallic lines also have emission components. The ultra violet spectra do not differ from standard B-type stars, and some Be stars have an excess of radiation in the far infrared.

(ii) The objects also show photometric variability, not necessarily cyclic. (Harmanec, 1983) recognised three time scales of variability and for the long-term ones explained the positive and negative correlation between the colour and magnitude during onset of an emission phase as an effect of different aspect angle.

(iii) Continuum visible radiation of Be stars is significantly polarised (e.g. Wood et al., 1997).

(iv) Spectro-interferometric studies (e.g. Meilland et al., 2012) proved that Be stars are surrounded by a disk-like structure, whose opaque parts span several stellar diameters in the infrared. The disks are all Keplerian and the central star rotates at high velocity, but probably below the break-up velocity ($\approx 15\%$ according to Meilland et al., 2012).

(v) X-ray radiation was detected for some Be stars (e.g. γ Cas, Smith et al., 2012).

Several formation mechanisms were proposed. They are the following: (i) Compression of the stellar wind to the equatorial plane. (ii) Ejection of material from the equatorial plane of the rapidly rotation star. The former mechanism was originally proposed by Bjorkman and Cassinelli (1993) and has already been ruled out as it was not able to produce accretion disks with the observed properties. The properties of the latter agree better with the observations and it is currently widely accepted formation model.

This finding raised a question, what kind of process leads to ejection of material? The original idea by Struve (1931) was that the star rotates at the break-up velocity is not supported by observations. The following explanations were proposed: (i) binary interaction, (ii) magnetism, (iii) non-radial pulsations.

The last mechanism proposed by Baade (1988) is widely accepted and seen as the most probable explanation of the Be phenomenon. The latest photometric ground-based and space-borne surveys detect multi-periodicity of the objects. For example Semaan et al. (2013) analysed CoRoT observation of 13 Be stars and concluded that all of them are pulsators.

[1] I participated in studies of two Classical Be stars BU Tauri (Nemravová et al., 2010), and γ Cas (Nemravová et al., 2012b), but those studies were both submitted before the beginning of my doctoral study.

A mass transfer (or episodic mass transfer during a periastron passage) has been proposed as the mechanism for the formation of accretion disks in Be stars by Kriz and Harmanec (1975). This hypothesis has been ruled out by infrared observations. A Roche-lobe filling donor was not found in Classical Be stars. Also the binary frequency among Be stars does not deviate much from that estimated for (regular) B-type stars ($\simeq 40\%$).

Later the binary hypothesis was re-visited by Harmanec et al. (2002). The authors proposed that the mass is ejected from a rapidly rotating component due to tidal interaction during the periastron passage (i.e. non-zero eccentricity is required). Nonetheless the authors found that the mechanism requires equatorial rotational velocity very close to the break up velocity, which is not supported by the observations (Frémat et al., 2005; Meilland et al., 2012). However, there are still authors (e.g. Townsend et al., 2004) who point at possible bias of the measured rotational velocities of Be stars, and at possibility that these objects are actually closer to the break-up velocity. Also at the high rotational velocity required by their hypothesis other instabilities may also lead to the ejection of the matter.

Detection of duplicity was the primary goal of our studies about BU Tauri (Nemravová et al., 2010) and γ Cas (Nemravová et al., 2012b). We were able to prove duplicity of these objects, but a direct link between an onset of emission phase and the duplicity was not found in both systems. In γ Cas it is also ruled out by the zero eccentricity of its orbit. Although duplicity probably plays only minor role in the formation of the accretion disk, it may partially cause its variations. Hence duplicity should should be evaluated in any Be star.

During my doctoral study I have participated in the investigation of ϵ Aur, β Lyr, and BR CMi. Balmer lines of all these stars have an emission component, but the latter two are binaries undergoing mass transfer and the former contains large dusty disk, hence none belongs to the group of Classical Be stars.

1.5 Outline of the thesis

The structure of the thesis is the following:

1. The acquisition, and reduction of spectroscopic, photometric and spectro-interferometric observations are summarised Chap. 2. The key benefits for binary research of different observational techniques are also discussed. A special attention is given to introduction of the CHARA/VEGA spectro-interferometer, and to reduction of its observations, because the observations from this instrument play a key role in the investigation of ξ Tau and β Lyr. An overview of contemporary techniques for radial-velocity measurement is provided, along with their critical comparison. I refer back to my studies about BU Tauri (Nemravová et al., 2010), and γ Cas (Nemravová et al., 2012b), because our research was aimed at confirming the duplicity of these objects through radial-velocity measurements. Both studies are attached to the thesis.

2. Semi-analytic models that I used in the study of various binary and multiple systems are described in Chap. 3. All the presented models are tailored to one observation type. There is a model for interpretation of radial velocities of multiple systems, light curves of binary systems, complex visibility and closure phase of interferometric fringes of multiple systems and binaries showing traces of circumstellar matter, and normalised spectra of multiple systems. The majority of models described in this chapter were forged into a program, which is described in Chap. 6. Special attention is given to the comparison of the observed and synthetic spectra. I applied this method in studies of several binaries and developed a robust program for the task *Pyterpol*. Application, and limits of each model are discussed.

3. An overview of my research on the quadruple hierarchical eclipsing binary ξ Tau is presented in Chap. 4. The study is based on series of spectroscopic, photometric, and spectro-interferometric observations, which were analysed using "observation-specific" models described in Chap. 3 and a N-body model by Brož (2016, submitted to ApJL). The results of the investigation are confronted with predictions of the perturbation theory, and were published in a preliminary study by Nemravová et al. (2013) and a complex final study by (Nemravová et al., 2016). Both articles are attached to the thesis.

4. Progress in the study of a binary undergoing rapid mass-transfer phase β Lyr is presented in Chap. 5. The study is based on large number of visible and infrared spectro-interferometric observations. I carried out a preliminary analysis of the continuum and arrived at conclusion, that the observations are inconsistent with an accretion disk represented by an uniform cylinder. To progress further with the analysis I need to develop a more physically sound model. Preliminary results were published at the conference Physics Of Evolved stars in Nice (Nemravová et al., 2015).

5. A user's manual for three programs, that I developed during my doctoral study is provided in Chap 6. (i) The program *ERV* for the measurement of radial-velocities through comparison of observed and template spectra. (ii) The program *FRV* for the interpretation of radial-velocities of multiple hierarchical systems. (iii) The program *FV* for the interpretation of squared visibility and closure phase of binary and triple systems. All these programs are also available at the enclosed DVD.

2. Observations and reductions

In the first part of this chapter acquisition, reduction and benefits for the binary research of the spectroscopy, photometry and the spectro-interferometry, is summarised. A special attention is given to the spectro-interferometry, because it is still "a rather young technique", and the instrument CHARA/VEGA, because I studied primarily observations from it.

In the second part an overview and critical comparison of methods of radial-velocity measurement is given.

2.1 Overview of standard observational methods

Basics regarding the acquisition, reduction and benefits for binary research of the spectroscopy, photometry, and spectro-interferometry are provided in this section.

2.1.1 The photometry

The photometry is the most common observational method, due to its simplicity, since it studies the integral flux F coming from the observed system. The photometric observations are currently acquired in a wide range of wavelengths from the gamma radiation to radio waves. Here I deal with observations acquired in visible and near infrared wavelengths only.

Instead of absolute linear flux scale, relative logarithmic scale is generally preferred

$$m_2 - m_1 = -2.5 \log \left(\frac{F_2}{F_1} \right), \tag{2.1}$$

where m denotes magnitude of an object. The photometry can be used to study binaries, if the flux (or light) variations are caused by the binary interaction. The two most common cases are eclipses (one star is passing in front of the other from observer's point of view), and ellipsoidal variations caused by changes of the projected flux from a binary component that is deformed by the gravitational force of the secondary.

Acquisition and reduction of optical and near-IR observations

The photometry became popular with the use of photoelectric detectors along with photomultipliers due to their high sensitivity and broad dynamical range (compared to photographic plates). Nowadays these detectors are slowly being replaced by charged coupled devices (CCDs), which offer higher sensitivity in near-IR region and allow simultaneous observations of a large number of scientific and calibration stars, although they still suffer from discrepancies, which are generally more important, for bright objects (small FOV, non-zero shutter closing time, readout time). A detailed summary of the history of photometry is in Hearnshaw (1996).

The photometric observations are affected by the atmospheric and the instrumental extinction. The first one is varies significantly with the air mass X, and cannot be considered constant over time larger than a few minutes. This problem can be overcome if an non-variable star having similar colour properties and position on the sky (called comparison star), is observed along with the variable star. Some observers are satisfied with such measurements and use them for estimation of epochs of minima, but the measurements could not be compared to any absolute-calibrated model, because they are still affected by the instrumental and atmospheric extinction, meaning also that comparison to measurements from any other instrument is impossible.

To overcome this and also to sample the spectral energy distribution function of stars, standard photometric systems were devised. A standard photometric system consists of a set of magnitudes measured for a large sample of stars spread over the whole sky at specific well defined spectral filters with known transmission curves. Two very popular systems are the Johnson's broad-band UBVRIJKL (Johnson et al., 1966) and the Strömgren's narrow-band ubvy (Strömgren, 1966). More details on the photometric systems were reviewed by Bessell (2005).

A brief summary of steps necessary to transform instrumental magnitudes m to a standard system follows. CCD plates have to be corrected for the bias, the dark current, and divided by flat-field first, similarly as it is described in section 2.1.2.

- **Atmospheric extinction:** It is caused by the absorption and scattering of the incoming flux in the atmosphere of the Earth. The extinction is decreasing with the wavelength in visible (due to Rayleigh scattering). The degree of the extinction is strongly influenced by the air mass X between the object and the observer. The instrumental magnitude (outside the atmosphere of the Earth) m_0 is given by

$$m = m_0 + k(t, \lambda)X, \tag{2.2}$$

  where k the atmospheric extinction coefficient, t the time and λ wavelength. In their reduction package HEC22[1] Harmanec et al. (1994); Harmanec and Horn (1998) use polynomials up to the fifth order to model nightly variations of the atmospheric extinction.

- **Drift of the zero-point of the magnitude scale:** It may be caused by temperature variations of the instrument or changes of the voltage of the photo-multiplier. In HEC22 it is modelled with polynomials up to second order. The Eq. (2.2) has to be modified to

$$m = m_0 + k(t, \lambda)X + c(t), \tag{2.3}$$

  where the term c represents time dependent zero-point drift. The zero-point drift behave the same in all photometric filters, which makes it distinguishable from the extinction variations, which behaves differently in each filter.

- **The seasonal transformations:** The true magnitude $m(\lambda)$ (for an ideal instrument with flat transmission $R(\lambda) = 1$) as a function of wavelength λ can be expanded to the Taylor series:

$$m_0(\lambda) = m(\lambda) + \sum_{i=1}^{N} \frac{\mathrm{d}^{(\mathrm{i})}m}{\mathrm{d}\lambda^i}(\lambda - \lambda_0), \tag{2.4}$$

  where the derivative $d^{(i)}m$ is usually approximated with a colour index or their (non-)linear combination, and m_0 is the instrumental magnitude. Finding a transformation between an instrumental and a standard one means to find transformation formulæ between two such series. Hardie (1966) suggested a transformation including only linear coefficient of the Eq. (2.4), which was later challenged by several authors (e.g. Young, 1992), who have shown that higher order terms (up to fourth order) in the expansion are still relevant and their negligence leads to systematic errors in the transformation. It depends on the colour of stars and cannot be derived until a representative sample of both cool and hot stars was measured. Therefore it is carried out after longer period of time (i.e. season). In case of the most widespread Johnson UBVR system the transformations are given by Eqs. (7) and (8) in Harmanec et al. (1994).

The necessity to remove atmospheric extinction is not valid for space telescopes, but the transformation to a standard system is often complicated, either because of limited FOV of the telescope (e.g. Kepler mission Koch et al., 2010), meaning that the FOV does not contain enough standards to successfully transform the observations, or because the mission was focused at stars, which lie outside the standard systems (e.g. Spitzer mission Werner et al., 2004) or due to absence of the zero-point correction (e.g. MOST mission Walker et al., 2003).

Successful transformation formulæ of the Hipparcos photometric observations to Johnson's UBV system were carried out by Harmanec (1998). Harmanec and Božić (2001) argued that similar transformations can be carried out for arbitrary instrument, if there are stars, among those observed with the instrument, for which well-established colour indices in the desired standard system exist.

On the other hand, the transmission of these instruments is usually well known and if the observations are corrected for it, the observations are directly comparable to absolutely calibrated models of stars and binary systems.

At wavelengths shorter than near-UV and longer than far-IR, there are not any standard widespread photometric systems.

[1]The program is available at: `http://astro.troja.mff.cuni.cz/ftp/hec/PHOT/`

Benefits of the photometry

Photometry provides insight into many astrophysical phenomena. These are pulsations, eruptions, rotation, binaries, tides, multi-body dynamic interactions, relativistic effects, and distance estimates.

Eclipsing binaries are the most important for binary research, their photometric observations (or light curves) yield following parameters:

- **Ratio of effective temperatures $T_{\rm eff\,1}/T_{\rm eff\,2}$:** Prša and Zwitter (2006) argued that it is not possible to correctly disentangle temperatures of two stars unless colour-constraining (described therein) is employed. The authors show that neglecting this may lead to an error in the temperature up to few hundreds of Kelvins and is more pronounced for eclipsing binaries with similar components. The common practice how to circumvent this problem is to estimate one effective temperature with another method and fix it.

- **Relative radii $r_{1,2} = R_{1,2}/a$:** They are strongly constrained if the eclipses are total. There is a degeneracy in relative radii $r_{1,2}$ and the inclination i, which is more pronounced if the eclipses are partial only.

- **The orbital inclination i:** The inclination is strongly constrained by the eclipses. The interval of the inclination is given by the size of the semimajor-axis and component radii.

- **The orbital eccentricity e and the periastron argument ω:** These two parameters are constrained by the relative position of the primary and secondary eclipse.

Apart from these, an eclipsing binary is an excellent stopwatch. Uneven time difference between two pairs of consequent minima may point to tidal variations between components (Cowling, 1938; Eggleton et al., 1998), the mass transfer (e.g. β Lyr, Kuiper, 1941), the relativistic apsidal motion (Levi-Civita 1937), the dynamic interaction (i.e. eclipse-timing variations) between the binary and additional components of the system (e.g. Harrington, 1968).

Total flux variations do not have to be necessarily connected with duplicity. They can be caused by pulsations changing temperature and/or total projected surface on the sky (e.g. Cepheids Goodricke and Englefield, 1785; Cox, 1974), spots (e.g. some chemically peculiar stars Preston, 1974), and circumstellar matter (e.g. some Be stars Secchi, 1866; Rivinius et al., 2013).

Photometric observations used in this thesis

The easier-to-acquire ground-based observations, studied within this thesis, were taken in some standard photometric system (usually Johnson's UBVR). All ground-based observations were given to me fully reduced and I did not partake in their reduction, but I partook in the acquisition of photometric observations at the Hvar Observatory in Croatia.

Space-borne observations studied within these thesis are: 1) Observations of ξ Tau acquired with satellite MOST (Walker et al., 2003), and 2) archival observations from satellite Hipparcos (Perryman et al., 1997; van Leeuwen, 2007). The observations from MOST were almost fully reduced, I had to filter the signal caused by stray light from the atmosphere of the Earth. Hipparcos archive data were fully reduced.

2.1.2 The spectroscopy

The spectroscopy is an observational method, which can be used to probe kinematics of a binary and its components, their radiative properties, and their chemical composition. The information contained in a spectrum is so complex that even the classification of stars is based on the incidence and shape of various spectral lines. Currently available spectra of stars cover the gamma, X-ray, UV, visible, IR and radio regions. In my doctoral study, I worked only with spectra from visible and near IR regions. Therefore following sections deal with the spectra from these regions only, although some information may be universally valid.

Acquisition and reduction of optical and near-infrared spectroscopic observations

A spectroscopic observation is obtained by inserting a dispersion element (usually a grating) before the detector. The resulting flux as a function of the wavelength $F(\lambda)$ is affected by the instrumental and the atmospheric transmittance. The most important characteristics of a spectrograph is its spectral resolution R given by

$$R = \lambda/\Delta\lambda, \tag{2.5}$$

where λ is the wavelength, and $\Delta\lambda$ the difference between two pixels of the detector. The resolution limits the precision with which we are able to measure properties such as radial velocities, line shapes, equivalent widths, etc.. Another key parameter determining possibility and accuracy of measurements is the signal-to-noise ratio (SNR).

Spectrographs come in many flavours based on their purpose. The simplest ones are those producing slit spectra such as the one at the Ondřejov observatory[2], which record only one spectral order. More advanced are echelle spectrographs, such as FEROS (Kaufer et al., 1999) which disperse the orders with an additional grating and record them simultaneously, or multi-object spectrographs, such as FLAMES (Pasquini et al., 2002), which benefit from aperture masks and optical fibres, and are able to record spectra of several objects simultaneously.

Spectrum recorded on a CCD is affected by the transmittance of the instrument and the atmosphere (unless the observation was carried from outside the Earth's atmosphere). Reduction of a spectrum is a series of steps during which these effects are (partially) removed. The basic procedure is following:

- **Bias subtraction:** Each pixel of a CCD is connected to some basic voltage, which generates a small signal. This signal is estimated either by taking image with zero exposure time or from part of a chip (called the over-scan region) where no light is recorded during exposure. This image has to be subtracted from the science and remaining calibration images.

- **Dark subtraction:** Unless the CCD chip is cooled, it is necessary to obtain one image with closed shutter and with the same exposure as the science target, because the detector emits thermal electrons. This image has to be subtracted from every science and calibration image.

- **Flat-fielding:** Each instrument suffers from inhomogeneities in the optical path of the beam and in the sensitivity of the CCD chip pixels. Flat field is an image of equally lit surface (e.g. dome-flat), sky at the dawn or a lamp with a flat field, by which the spectrum of a science target is divided.

- **Wavelength calibration:** The spectrum of science target has to be transformed from the pixel scale to the wavelength scale. For this task a calibration spectrum is recorded using a source with known and well defined sets of spectral lines (e.g. ThAr lamp, iodine cell). The spectral dispersion is estimated over the calibration image and transferred to the scientific one. If present, measurements of RV on telluric lines can be used to correct the zero-point of the RV scale.

- **Continuum normalisation:** If colour dependent transmittance of the instrument and the atmosphere cannot be removed, the continua of the spectrum are fitted by a low-order polynomials, and then divided by it, so the continuum flux $F_c = 1$.

The true reduction procedure depends on the properties of each individual instrument. Nowadays the reduction of cutting edge instruments became very difficult, hence it is often carried out by the staff operating the instrument and the astronomer is given reduced data. A more detailed description of acquisition and reduction of spectroscopic observations is given in Eversberg and Vollmann (2015).

[2] see `http://stelweb.asu.cas.cz/web/index.php?pg=2m_telescope&subpg=2m_telescope_coude_spectrograph`

Benefits of spectroscopy

The stellar spectra come packed with a large amount of information. Many binary researchers are satisfied with the radial velocities (RVs), which are then used to estimate the orbital elements of a binary. A description of RV measurements is given in Sect. 2.3.

Additional properties can be estimated with the help of synthetic spectra, which were computed from a stellar atmosphere model. Although these models are computed under several approximation (limited lists of species and transitions, one-dimensional models, simplified opacity treatment), they provide a good representation of the observations, especially for the main-sequence stars. During my doctoral study, I worked only with pre-computed grids of synthetic spectra based on 1D atmosphere models, which are described by a subset of following parameters:

- **The effective temperature $T_{\rm eff}$:** The population of atomic levels is given by the Boltzmann equation and the degree of ionisation by the Saha equation, which are both functions of temperature. Hence the effective temperature is strongly constrained by the strength of spectral lines.
- **The gravitational acceleration $\log g_{\rm [cgs]}$:** It is strongly constrained by the shape of lines which are broadened by Stark effect, these are usually hydrogen and some helium lines (see Kallrath and Milone, 2009, p.56).
- **The metallicity Z:** It is given by incidence and depth of spectral lines. The influence of the metallicity on the line depth is a second-order effect compared to the influence of $T_{\rm eff}$ in a sense, that a small variation of the temperature leads to larger difference in the resulting spectrum, than the same relative change of the metallicity.
- **The α-element abundance Z_α :** It is the ratio between the iron abundance and the abundance of α-elements [α/Fe] The α-elements are light elements (proton number $Z < 22$), whose most abundant isotopes are multiples of α-particle: C, O, Ne, Mg, Si, S, Ar, Ca, and Ti. This ratio is an age indicator, since α-elements are produced especially in SNII explosions, but less (compared to iron) in SNIa explosions, therefore the ratio is maximal for metal-poor stars and is decreasing with the metallicity (see Gratton et al., 2004, p.395-396).
- **The micro-turbulence $v_{\rm MIC}$:** It acts similarly to the thermal broadening, but the cause is not the motion of individual particles, but the motion of photospheric cells, which are smaller than the mean free path of a photon. The micro-turbulent broadening is small $v_{\rm MIC} = 1 - 2\,{\rm km.s^{-1}}$. (see Gray, 2005, p.430).

The synthetic spectra given by preceding parameters do not match the observed ones well, because the synthetic spectra account only for the collisional broadening, the Stark broadening, the micro-turbulent broadening, and the thermal broadening. Real spectra are broadened by additional effects. The most common ones are following:

- **The macro-turbulence $v_{\rm MAC}$:** It is caused by the relative motion of turbulent cells, in which a photon is created and those from which it escapes the photosphere. Each cell provides a Doppler-shifted stellar spectrum, which is broadened by the micro-turbulence. A radial-tangential model of the macro-turbulence assumes, that the turbulent cells move in both radial and tangential direction relative to the stellar surface with Gaussian velocity distribution. The model is described in Gray (1975). Some authors (Lucy, 1976; Aerts et al., 2009) suggest that the physical phenomenon standing behind are high-order pulsations.
- **The rotation $v \sin i$:** All stars rotate, e.g. early-type stars, which are the main concern of this thesis, often rotate with velocities exceeding several hundreds of ${\rm km.s^{-1}}$. The rotation may be very complicated and due to limited resolution of observed spectra and time span of the observations rigid body rotation is often assumed. In that case the spectrum of a rotating star can be obtained by a simple convolution of normalised spectra with the flux-weighted rotational profile (see Eq. 18.12 Gray, 2005, p.464). Note that this model does not take the gravity brightening into account and may lead to underestimation of the rotational velocity for rapidly rotating stars (see Townsend et al., 2004).

- **The instrumental broadening:** It is a degradation introduced by the instrument due to finite width of the entrance slit, CCD pixel size and optical aberrations. Therefore the recorded spectrum is a convolution of an "unspoiled" image and the instrumental profile. The instrumental profile is accounted for either by deconvolution of the two, or by broadening of the synthetic spectra with an instrumental profile. The instrumental broadening kernel is often simplified to a Gaussian, although its can be more complicated.

Estimation of stellar properties through comparison of the synthetic and observed spectra was one of the main goals of my doctoral work and is presented in Sect. 3.1.4.

Line-profile profile variations indicate inhomogeneities in the flux or velocity distributions over the stellar surface. The velocity variations (usually caused by pulsations and rotation) can be described either by direct line-profile modelling or by studying variations of their moments (see Aerts et al., 1992, for a detailed description of the method). The properties of pulsations (modes, frequencies, amplitudes) are studied by asteroseismology, who uses these measurements to infer properties of stellar interior (see Aerts et al., 2010, for a complete description of the field and its achievements). Inhomogeneities of the flux (or spots) can be mapped by the Doppler imaging (see Rice, 1996). The idea behind the method is that any spot on the stellar surface introduces a bump into the studied spectral line. The indeterminacy in the "mapping of the bump back on the stellar surface" is removed by studying several observations with different phase, although in case of a unfavourable inclination of the rotational axis ($i = \{0, \pm 90\}$) the indeterminacy cannot be overcome.

Spectrophotometry

Spectrophotometric observations are additionally corrected for the atmospheric and the instrumental extinction. This allows recovery of the spectra energy distribution (or SED), which provides an additional constraint on the effective temperature of binary components. The correction for atmospheric extinction is difficult, because there is a lack of comparison stars, hence the observations are usually carried out by space telescopes.

Studied spectroscopic observations

In this thesis I worked mainly with medium resolution slit spectra ($R \approx 12000$) acquired at the Ondřejov observatory and with high resolution echelle spectra acquired with instruments FEROS, HERMES (Raskin et al., 2011), ELODIE (Moultaka et al., 2004), and BESO (Steiner et al., 2008) and with slit spectra from other observatories. I had to fully reduce only slit spectra of ξ Tauacquired at the David Dunlap Observatory and took part in preparation of a full reduction procedure for echelle spectra acquired at the Ondřejov observatory. Both reductions were carried out in IRAF (Tody, 1986, 1993). The remaining spectra, that I used in my work required only the continuum normalisation, which I carried out using Hermite polynomials through suitably chosen normal points.

2.1.3 The optical interferometry

The main advantage of the (optical) interferometry is that it achieves very high spatial resolution, which allows to resolve various objects. A common telescope has its resolution governed by the following equation:

$$\Theta_{\mathrm{T}} = \frac{\lambda}{D}, \tag{2.6}$$

where Θ_{T} is the limiting resolution of a telescope with an aperture with diameter D operating at the wavelength λ. Any ground-based optical telescope would, however have an effective resolution of an instrument with aperture size $D = 0.2\,\mathrm{m}$ due to atmospheric turbulence, unless some kind of adaptive optics or speckle imaging is employed. The resolution of an interferometer is given by the following formula:

$$\Theta_{\mathrm{I}} = \frac{\lambda}{B}, \tag{2.7}$$

where B is the separation of the two telescopes (also called baseline). The resolution achieved by contemporary optical interferometers is $\Theta \approx 0.1\,\mathrm{mas}$.

Such spatial resolution allows the investigation of various objects and phenomena, but for the binary research the most important is the ability to resolve the orbit of close binaries (with short semimajor axes) and binaries distant from the observer.

Brief historical overview of the optical interferometry

Hippolyte Fizeau came up with the idea behind interferometry (i.e. interferometric fringes are smeared by the size of the studied object, hence its angular size can be estimated from the degree of smearing called the visibility), and is followed by the most of the contemporary interferometer designs.

The first optical interferometer (called Michelson stellar interferometer) was constructed by A. A. Michelson, who first measured diameters of Galilean moons (Michelson, 1891) and later α Ori (Michelson and Pease, 1921). In following years researchers used Michelson's technical design of an interferometer, which limited the baselines to several meters and was useful for measurements of close stars only. A new impulse came in the field, when (Hanbury Brown, 1956) developed the intensity interferometer. The instrument was used to measure diameters of bright stars (Hanbury Brown et al., 1974), which provided empirical estimates of the effective temperature of these stars (Code et al., 1976).

The Fizeau's amplitude interferometry was revived by Antoine Labeyrie, who devised the method of speckle-interferometry. It uses the randomness of atmospheric turbulence to obtain diffraction-limited images (Labeyrie, 1970). Later (Labeyrie, 1975) coherently combined the light from two telescopes separated by 13.8 m. The majority of contemporary optical and infrared interferometers follows his construction design. A more detailed history of optical interferometry is in Labeyrie et al. (2006, p.1-7).

The optical interferometer

An optical interferometer consists of two (or more) apertures (telescopes). The monochromatic wavefronts from each telescope (denoted 1 and 2) propagate to the beam combiner, where they interfere with each other. The wavefronts are given by the following equations:

$$\begin{aligned} E_1 &= E_0 e^{-i(\omega t - \vec{k}\cdot\vec{r})}, \\ E_2 &= E_0 e^{-i(\omega t - \vec{k}\cdot(\vec{r}+\vec{B}))}, \end{aligned} \tag{2.8}$$

where, E_0 is the amplitude of the electric intensity, ω the angular frequency, $\vec{k}$ the wave vector, $\vec{r}$ the position of the first telescope and $\vec{r}+\vec{B}$ the position of the second telescope. The baseline vector is then $\vec{B}$ and path difference between two telescopes $D = \vec{s}\cdot\vec{B}$, where $\vec{s}$ is direction to the observed star. The superposition of the two wavefronts, assuming $\vec{k}$ and $\vec{r}$ are parallel, is the following:

$$E = E_1 + E_2 = E_0 e^{-i\omega t}\left(e^{ikr} + e^{ikr+\vec{s}\cdot\vec{B}}\right), \tag{2.9}$$

and the intensity I is

$$I = E_1 E_2^* = 2E_0\left[1 + cos(k\vec{s}\cdot\vec{B})\right], \tag{2.10}$$

where the asterisk denotes the complex conjugation. The intensity given by Eq. (2.10) varies with the spatial frequency and is producing interference stripes called *fringes*. The optical path differences (OPD) introduced by the different distances of telescopes from the source is compensated with delay lines. These compensations are necessary, because each instrument works with a polychromatic light of a finite bandwidth $\Delta\lambda$ an the total intensity integrated over the bandwidth is the following:

$$I(\lambda_0, \Delta\lambda) = \int_{\lambda_0-\Delta\lambda/2}^{\lambda_0-\Delta\lambda/2} 2E_0(1 + \cos(2\pi k D))\mathrm{d}\lambda. \tag{2.11}$$

The integration of Eq. (2.11) yields

$$I(\lambda_0, \Delta\lambda) = 2E_0\Delta\lambda\left[1 + \frac{\sin(\pi\Delta\lambda D/\lambda_0^2)}{\pi\Delta\lambda D/\lambda_0^2}\cos(2\pi D/\lambda_0)\right], \tag{2.12}$$

where

$$M\left(\lambda_0, \Delta\lambda\right) = \frac{\sin(\pi\Delta\lambda D/\lambda_0^2)}{\pi\Delta\lambda D/\lambda_0^2}, \tag{2.13}$$

is the attenuation term, and characteristic attenuation scale $\Lambda = \lambda_0^2/\Delta\lambda$ is called the coherence length.

The van Cittert-Zernike theorem

Each source projected on the sky is characterised by a certain intensity distribution $I = I(\vec{s})$, where vector pointing to the direction to an object can be written as follows $\vec{s} = \vec{s_0} + \vec{\Delta s}$, where $\vec{s_0}$ points to the centre of the studied object and $\vec{\Delta s}$ is a displacement of each point of the source relative to its centre.

Assuming that the delay lines have compensated the optical path delay introduced by $k\vec{s_0}\cdot\vec{B}$, the total measured power P is given by integration of Eq. (2.12) over the whole projected surface of the source Ω:

$$\begin{aligned} P(\lambda_0, \Delta\lambda) &= \int_{\mathbb{R}^2} I(\lambda_0, \Delta\lambda, \Omega)\mathrm{d}\Omega \\ &= \int_{\mathbb{R}^2} I_0(\Omega)\left[1 + M(\lambda_0, \Delta\lambda)\cos(k\vec{\Delta s}\cdot\vec{B})\right]\mathrm{d}\Omega, \end{aligned} \tag{2.14}$$

where $I_0 = 2E_0\Delta\lambda$ and $M(\lambda_0, \Delta\lambda)$ is the attenuation term from Eq. (2.13). Assuming that decoherence introduced by the use of polychromatic light is negligible, one can rewrite the last equation as follows:

$$P(\lambda_0, \Delta\lambda) = P_0 + Re\{\int_{\mathbb{R}^2} I_0(\Omega)e^{-ik\vec{s}\cdot\vec{B}}\mathrm{d}\Omega\}. \tag{2.15}$$

The total power from an extended source will be modulated by the second term. If one assumes that the source is very small and that the displacement $\vec{\Delta s}$ is perpendicular to $\vec{s_0}$, then $\Delta s = (\alpha, \beta, 0)$, and one can write the second term:

$$P_1(u, v) = \int_{\mathbb{R}^2} I_0(\alpha, \beta)e^{-i2\pi(u\alpha + v\beta)}\mathrm{d}\alpha\mathrm{d}\beta, \tag{2.16}$$

where $(u, v) = (B_\mathrm{x}/\lambda, B_\mathrm{y}/\lambda)$ are spatial frequencies, and (α, β) are Cartesian coordinates on the sky measured along the east-west (α), and north-south (β) direction. The van Cittert-Zernike theorem is obtained by normalisation of Eq. (2.16):

$$V(u, v) = \frac{\int_{\mathbb{R}^2} I_0(\alpha, \beta)e^{-i2\pi(u\alpha + v\beta)}\mathrm{d}\alpha\mathrm{d}\beta}{\int_{\mathbb{R}^2} I_0(\alpha, \beta)\mathrm{d}\alpha\mathrm{d}\beta}, \tag{2.17}$$

where V is called the complex visibility of interference fringes. This relation links the projected source intensity $I_0(\alpha, \beta)$ with the visibility modulus (i.e. the fringe contrast) and its phase. The main obstacles of the imaging (i.e. the inversion of Eq. 2.17) are the following:

- **Filling the Fourier plane:** One has to sample $V(u, v)$ densely enough to make the inversion non-degenerate. There is no definitive number, because it depends highly on the complexity of the studied object and the desired accuracy of the resulting image. To increase the number of $V(u, v)$ measurements one has either to increase the number of telescopes in an array or to observe in more spectral filters (the simplest option), or observer at more configurations of the system instrument-object. The last option is not valid if the object varies on timescale shorter than the typical observation time needed to sample the Fourier plane.

- **The visibility phase:** The atmospheric turbulence introduces phase shifts, which vary on timescale $\tau = r_0/v$, where r_0 is the Fried parameter (Fried, 1966), and v the typical wind velocity. The Fried parameter scales as $\lambda^{6/5}$ and is $\approx 0.2\,\mathrm{m}$ in the Johnson V band. The turbulence: (i) prevents completely direct measurements of the intrinsic (i.e. source)

visibility phase, (ii) limits the exposure times T_e to $T_e < \tau$. The former can be overcome with the closure phase ϕ_c, which is the argument of the complex triple product T_3:

$$T_3 = V_1 V_2 V_3^* = |V_1|\,|V_2|\,|V_3|\,e^{i(\phi_1+\phi_2-\phi_3)}, \tag{2.18}$$

where V_i ($i \in \{1,2,3\}$) is the complex visibility for each baseline within a closing triangle and the closure phase is $\phi_c = \phi_1+\phi_2-\phi_3$. The closure phase is independent of atmospheric phase. For an array of N telescopes there are $N(N-1)/2$ independent phases and $(N-1)(N-2)/2$ independent closure phases, meaning that the phase can be recovered only partially, but the recoverable fraction of the phase information grows with the number of co-phased telescopes.

In most situations the Fourier plane is not filled enough to permit direct inversion of Eq. (2.16) and more sophisticated methods, like CLEAN (Högbom, 1974) or MEM (Cornwell and Evans, 1985) have to be used.

It is quite common (especially in the optical interferometry) that one is unable to measure the closure phase and/or sample sufficiently the Fourier plane, hence the usage of the imaging yields no result. In those cases one often adopts "an opposite approach": (i) creates a model of the studied object and transforms it into the Fourier space, and (ii) one compares it directly to the observed visibility. I used this approach in case of ξ Tau and β Lyr, whose spectro-interferometric observations sampled the Fourier space sparsely and/or lacked closure phase measurements.

Benefits of the optical interferometry

Optical interferometry can be beneficial to any study, where images of the object are needed and the object (or the effect) is resolvable with the instrument. The main achievements in the field were: (i) Measurements of stellar diameters along with limb darkening are used to test models of the stellar evolution and of stellar atmospheres (e.g. Wittkowski et al., 2001), (ii) measurements of radii of pulsating stars such as Cepheids (e.g. Kervella et al., 2004) or Miras , (iii) resolving the circumstellar environment of young stellar objects, Be stars, evolved stars, and planetary nebulae. One of the key objects of this thesis — β Lyr— belongs to this group, (iv) resolving of binary orbits, which — if complemented with a distance estimate or with an orbital solution — can be used to estimate masses of the binary components, and the distance of the system. Another key object of this thesis — ξ Tau— belongs to this group, and (v) astrometry in a sense of relative measurements of the star position and their proper motion with precision reaching to one mas, which can be used to measure parallax of an object or to detect binary companions from the motion of the primary.

Caveats of the optical interferometry

The main problem of the method is its restriction to bright objects. There are mainly two reasons for that:

- **Complexity of the instrument:** In each interferometer the flux is diluted due to a large number of reflections and/or refractions.
- **The atmospheric turbulence:** The rapid variability of the atmosphere at optical wavelengths introduce a need for short exposure times ≈ 10 ms.

Both problems are limiting the contemporary instruments to magnitudes lower than ≈ 8 mag. This situation should improve greatly with the installation of adaptive optics, which will allow to use longer exposure times.

The optical interferometers are not widespread especially due to high demands on the precision and stability of the instrument. The OPD between two arms of an interferometer has to be equal with the precision of few microns and the delay lines have to able to compensate for phase shifts introduced by the atmosphere.

Decoherence is also introduced if the flux and the polarisation properties are not equal between the two arms. This requires precise alignment of individual parts of the instrument and homogeneity of the two arms.

The last caveat is innate to any imaging technique — any image is in the angular scale, hence the observations have to be complemented with a distance estimate to convert the image into the physical scale.

2.2 The spectro-interferometer VEGA/CHARA

The Visible spEctroGraph and polArimeter (Mourard et al., 2009) is attached to the interferometer at the Center for High Angular Resolution Astronomy (ten Brummelaar et al., 2005) at the Mount Wilson, the USA. The instrument works in the optical region and is able to reach spatial resolution up to 0.03 mas, which is not matched by any other contemporary instrument. It is given a special attention in this work, because observations acquired with VEGA/CHARA were used in the study of the multiple system ξ Tau (Nemravová et al., 2016) and in the study of the binary system β Lyr.

2.2.1 Characterisation of the instrument

A brief description of the interferometric array CHARA and the spectrograph VEGA is given here.

The interferometric array CHARA

The array consisting of six telescopes is located on the Mount Wilson, CA, USA. A sketch of the array is shown in Figure 2.1. The telescopes are built in an Y-shaped non-redundant configuration. The non-redundancy ensures that each baseline draws an almost unique curve in the Fourier space (with minimal number of intersections) as the telescopes follow an object on the sky. The baseline lengths are ranging from 34 m to 331 m.

Each telescope has a 1 m primary mirror. The mount of telescopes is very stiff and massive and the positions of their foci are stable. The secondary mirror is equipped with an adaptive tip-tilt control, which is the first-order adaptive optics[3]. The movable secondary mirror compensates for the motion of the distant target image in the focal plane introduced by the atmospheric turbulence. The light from the telescope goes through its pedestal to evacuated beam-lines, which bring it into a beam combiner. Seven mirrors are necessary to transfer the light and one or two additional to preserve its original polarisation.

The beam combiner contains delay lines, which maintain zero optical path difference (or OPD) between the beams. They consist of a fixed and movable part. The fixed part, which removes the bulk of the OPD called 'Pipes of Pan' or 'PoPs', is a set of parallel tubes with different length. The movable part is a mirror on a rail, which is able to compensate the OPD in real time up to 92 m with the precision of 20 nm. The beam combiner is able to use light from all six telescopes. VEGA is able to combine light from up to four telescopes[4].

The spectrograph VEGA

The instrument is a successor to the previous spectrograph that was installed at the GI2T (Mourard et al., 1994). After decommissioning of the GI2T it was adapted for use with the CHARA interferometer.

VEGA operates in the visible region (from 4500 Å to 8500Å) and offers three different spectral resolutions $R \in \{1700, 5000, 30000\}$. The signal is recorded with two photon-counting cameras that can operate simultaneously in medium and high spectral resolution regimes. The spectral range covered by each camera is only a few tens (a few nm) of nm in medium (high) spectral region. A polarimeter following the design from Rousselet-Perraut et al. (2006) can be placed before the grating.

Individual frames are recorded with a frequency of 100 Hz comparable to timescale of atmospheric turbulence. The frames are grouped into blocks of 1000 frames. Each observation consists of several tens of blocks.

2.2.2 Reduction of the CHARA/VEGA observations

Observations from CHARA/VEGA can be exploited for three types of observables: (i) the squared visibility V^2, (ii) the differential visibility δV and phase $\delta\phi$, and (iii) the closure phase

[3] An adaptive optics including a wavefront monitor and a deformable mirror is being installed (see Che et al., 2013).

[4] The successor of VEGA, FRIEND, will be able to combine light from all six telescopes in the visible region (Berio et al., 2014).

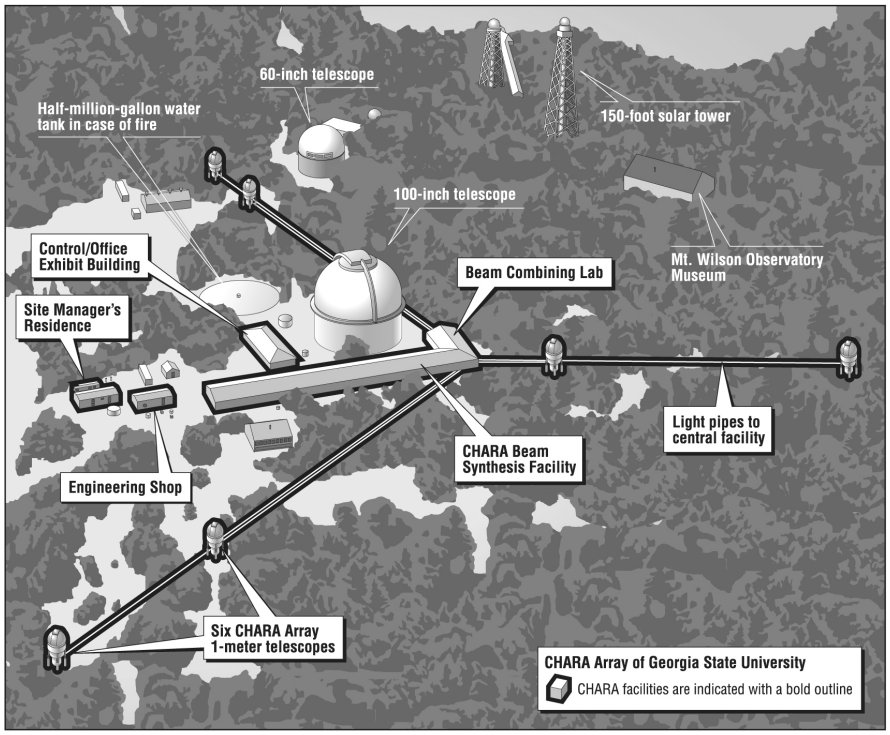

Figure 2.1: A sketch of the CHARA interferometric array.

ϕ_c. The third item can be estimated only if an observation was carried out with at least three telescopes. The reduction of the VEGA/CHARA observations is almost fully automatised, a user is allowed to choose a spectral region and reference stars (or calibrators). The procedure is complex and has to deal with several GBs of data acquired during each observation. The reduction procedure is described here.

Estimation of the squared visibility

To estimate V^2 one has to select a part of the acquired spectrum. Its width is usually ~ 10 Å. While a longer segment of the spectrum contains more photons and makes the estimation V^2 easier, it also introduces decoherence due to curvature of the spectrum on the plate and intrinsic properties of the studied object. Hence one always has to compromise between these two.

The fringes recorded on individual frames are slightly shifted with respect to each other due to atmospheric turbulence. This is not the case for their Fourier transforms. Therefore the averaging of all frames acquired within a block is carried out in Fourier space.

Let us assume that there is only one speckle in the image, then the interferometric image in the focal plane $I(x, y)$ is given by following formula:

$$I(x, y) = I_0(x, y) \left[1 + V \cos\left(2\pi(ux + vy) - \phi\right)\right], \tag{2.19}$$

where the x, y are angular coordinates on the sky with reference centre at the position of the source, I_0 is the telescope PSF (an Airy disk for one speckle), u, v the spatial frequency $(u_0, v_0) = (B_x, B_y)/\lambda$, V the fringe visibility modulus and ϕ the fringe phase including atmospheric phase and B projection of the baseline on the sky. As a next step, we compute Fourier transform of the previous equation:

$$\tilde{I}(u, v) = \tilde{I}_0(u, v) + \frac{V}{2}\tilde{I}_0(u - u_0, v - v_0) - \frac{V}{2}\tilde{I}_0(u + u_0, v + v_0), \tag{2.20}$$

In cases, when the separation of the two telescopes is larger than their apertures, one can express the Fourier transform of the interferometric image as a product of Fourier transform of the source object $\tilde{O}$ and the modulation transfer function T, which is Eq. (2.20) for a point

(i.e. unresolved) source

$$\tilde{I}(u,v) = \tilde{O}(u,v)T(u,v). \tag{2.21}$$

Assuming that the source is unresolved with a single aperture, and that the source function is real, hence $\tilde{O}(-u,-v) = \tilde{O}(u,v)$, the Eq. (2.20) can be rewritten to

$$\begin{aligned} \tilde{I}(u,v) &= \tilde{O}(0,0)T(u,v) + \tilde{O}(u_0,v_0)T(u-u_0,v-v_0) - \\ &- \tilde{O}(u_0,v_0)T(u+u_0,v+v_0). \end{aligned} \tag{2.22}$$

Comparison of Eqs. (2.20), and (2.22) reveals an equation for the visibility modulus $|V|$:

$$|V| = \left| \frac{\tilde{O}(u_0,v_0)}{\tilde{O}(0,0)} \right|. \tag{2.23}$$

Eq. (2.23) shows that the energy ratio of the low-frequency (W_L) and high-frequency part (W_H) of the power spectrum can be used to estimate the visibility modulus. The individual parts are following:

$$W_\mathrm{L}(u,v) = \left|\tilde{O}(0,0)\right|^2 T^2(u,v), \tag{2.24}$$

$$W_\mathrm{H}(u,v) = \frac{1}{4}\left|\tilde{O}(u_0,v_0)\right|^2 \left[|T(u-u_0,v-v_0)|^2 + |T(u+u_0,v+v_0)|^2\right]. \tag{2.25}$$

The final estimator for the squared visibility $V^2 = |V|^2$ is

$$\frac{V^2}{2}(u_0,v_0) = \frac{\iint W_\mathrm{H}\mathrm{d}u\mathrm{d}v}{\iint W_\mathrm{L}\mathrm{d}u\mathrm{d}v}. \tag{2.26}$$

The Eq. (2.26) is applicable only if one speckle is recorded. CHARA telescopes have 1 m apertures and therefore detect large number of speckles[5]. Each speckle is modulated by an interference pattern, so Eq. (2.26) has to be generalised. The derivation is carried out in Roddier and Lena (1984). Estimator, which is used to extract V^2 from the images acquired with CHARA/VEGA is given by Eqs. (14), and (19) therein. The Eqs. (2.24), and (2.25) are valid for quasi-monochromatic light. In case of polychromatic light the two equations have to be also integrated over the studied bandwidth.

The estimated visibility is usually lower than the real one due to instrumental effects (especially uneven light loss during transfer of light from telescopes to the beam combiner). Therefore it is necessary to calibrate the observations. The ratio between the instrumental and the real visibility is called transfer function (TF). Calibrators are observed to estimate TF of the interferometer. A calibrator is a single star of a known diameter, which is not more than few degrees far from the science target. TF is estimated as ratio between visibility given by calibrator model (usually a uniform disk) V^2_M and the observed V^2_O of the calibrator. The calibrated visibility V^2_CAL of the science target is a product of the transfer function and the instrumental (or raw) visibility V^2_RAW of the science target.

$$V^2_\mathrm{CAL} = \frac{V^2_\mathrm{M}}{V^2_\mathrm{O}} V^2_\mathrm{RAW} \tag{2.27}$$

The transfer function depends on the altitude of the target and the seeing conditions. Hence it is not stable during a night and a calibrator has to be observed before and after each observation of a science target.

Estimation of the differential visibility and phase

The differential visibility δV and phase $\delta\phi$ are usually studied in spectral lines, where a significant variation of visibility is expected, but the line is too narrow to sample it with a channel several nm wide using the method described in previous section.

[5] $N_\mathrm{speckle} = S_\mathrm{pm}/(\pi r_0^2)$, where N_speckle is the number of speckles, S_pm surface of the primary mirror and r_0 the Fried parameter.

Therefore one has to choose one wide channel, outside the spectral line, over which the visibility is approximately constant and a narrow scientific channel (shorter than the width of the studied spectral line). A wide reference channel is chosen, since the signal to noise ratio of the resulting differential visibility and phase is proportional to $\sqrt{S_\mathrm{r} S_\mathrm{s}}$, where S_s (S_r) is the signal within the scientific (reference) channel. Then the spectral line is scanned by moving the scientific channel over the spectral line. The differential visibility and phase are computed for each step using the following method.

The estimator is very similar to Eq. (2.26), but instead of computing a power spectrum given by Eqs. (2.24), and (2.25) a cross power spectrum between the two channels is computed. Assuming that the modulation transfer function T does not vary between the effective wavelengths of both channels (λ_1, λ_2) the low frequency (W_L) and the high frequency (W_H) part of the cross spectrum are

$$W_\mathrm{L}(u,v) = \left|\tilde{O}_{\lambda_1}\tilde{O}^*_{\lambda_2}(0,0)\right| T^2(u,v), \tag{2.28}$$

$$W_\mathrm{H}(u,v) = \frac{1}{4}\left|\tilde{O}_{\lambda_1}\tilde{O}^*_{\lambda_2}(u_0,v_0)\right| \times \times \left[|T(u-u_0,v-v_0)|^2 + |T(u+u_0,v+v_0)|^2\right]. \tag{2.29}$$

The differential visibility $|\delta V|^2 = \delta V^2$ and phase $\delta\phi$ are given by

$$\frac{\delta V^2}{2}\exp(i\delta\phi)(u_0,v_0) = \frac{\iint W_\mathrm{H}\mathrm{d}u\mathrm{d}v}{\iint W_\mathrm{L}\mathrm{d}u\mathrm{d}v}. \tag{2.30}$$

Eqs. (2.28), (2.29), and (2.30) are again simplified and apply to quasi-monochromatic light. An estimator, which is used in the VEGA reduction pipeline is given by Eq. (17) in Berio et al. (1999).

The resulting differential visibility and phase as a function of wavelength are usually warped due to residual atmospheric piston (or residual phase difference between two telescope introduced by the atmospheric turbulence, see Labeyrie et al., 2006, p.110) and have to be corrected by fitting a model represented by Eq. (3) in Mourard et al. (2009).

Unless we are only interested in the relative change of the visibility between the reference and scientific channels, it is necessary to calibrate the differential visibility by estimating the squared visibility for the reference channel.

Closure phase

The number of co-phased telescopes usually does not exceed three for VEGA observations, hence there is only one independent closing triangle. The closure phase ϕ_c is estimated from a complex bi-spectrum B given by

$$B(u_1,u_2,v_1,v_2) = \tilde{I}(u_1,v_1)\tilde{I}(u_2,v_2)\tilde{I}^*(u_1+v_1,u_2+v_2), \tag{2.31}$$

where $u_{1,2}, v_{1,2}$ are spatial frequencies for the two projected baselines and $\tilde{I}$ is Fourier transform of the mean interferogram I, where the mean is computed from all frames for a given block. The closure phase is the argument of the bi-spectrum given by

$$\phi_\mathrm{c} = \arg\{B(u_1,u_2,v_1,v_2)\}. \tag{2.32}$$

Justification for this approach is given in the studies Cornwell (1987) and Woan and Duffett-Smith (1988).

2.3 Techniques for the radial-velocity determination

The radial velocity (RV), i.e. the projection of the velocity vector of a star into the line of sight of an observer provide a valuable insight into the orbital motion of a star. It is measured from the Doppler shift of spectral lines, which is in a non-relativistic case given by the following formula:

$$RV = (\lambda - \lambda_0)\frac{c}{\lambda_0}, \tag{2.33}$$

where λ is the measured wavelength of a spectral line, λ_0 its laboratory wavelength, and c is the speed of light in vacuum.

There is a number of methods for the estimation of the RV from the shift of a spectral line, but essentially they are all based either on the comparison of observed spectra and a suitable template, or on the measurement of line properties. An overview of some methods and their applications is given in Sect. 2.3.1. A special attention is given to a direct comparison of synthetic and/or disentangled spectra in Sect. 2.3.2, because it is potentially a source of a systematic error if the disentangling is coupled with an orbital solution.

2.3.1 An overview of methods for the radial-velocity estimation

Here I provide a list of techniques of RV measurements, used in the studies that I participated in (i.e. this not a complete list of all available methods) along with several remarks and an example of their application. The techniques are the following: (i) the comparison of spectral lines with analytic functions, (ii) the comparison of direct and mirrored line profile, (iii) the cross-correlation, and (iv) the comparison of observed and synthetic spectra.

The last technique is given a closer look, because I developed a program based on this technique.

The comparison of spectral lines with analytic functions

The spectral lines of stars are broadened by two mechanisms (excluding the rotation and the macro-turbulence): (i) pressure and Stark broadening, which lead approximately to the Lorentz profile (Gray, 2005, p.238-243), and (ii) thermal broadening, which leads to the Gaussian profile (Gray, 2005, p.253-254). A convolution of these two mechanisms forms the Voigt profile. Only hydrogen and helium spectral lines (in early-type stars) have pronounced Lorentzian wings, which means that the majority of spectral lines can be approximated satisfactorily with a Gaussian function.

This technique is useful for the RV determination of unblended spectral lines. Each additional spectral line, regardless of whether it comes from the same or another member of the system, requires an additional Gaussian function (each being described by three parameters — the central wavelength, width, and depth), which renders this method useless for long spectra or spectra with strongly blended lines. Hence the method is used especially in case of early-type stars such as SZ Cam (Mayer et al., 2010).

I applied this method to the measure properties of Hα — RV, FWHM and height of the central emission I_p — of the Be star γ Cas (Nemravová et al., 2012b). In this application we were primarily interested in the latter two characteristics and their variations, because we modelled the line only with one Gaussian function, although the Hα blends with a number of telluric lines, and suffers from additional departures from the Gaussian shape (Lorentzian wings of the spectral lines, emission emanating from an accretion disk surrounding the central star). Given these discrepancies it is not surprising that the method does not perform well vs. the comparison of direct and mirrored profiles. That does not necessarily mean that the method is not convenient for this application, but it has to be adapted (e.g. by fitting the emission wings of Hα only, and excluding prominent telluric lines). A comparison of the RVs measured by the fitting of a Gaussian function to the Hα profile and those obtained through the comparison of direct and mirrored profiles is shown in Fig. 2.2.

The comparison of direct and mirrored of a spectral line

A single stellar spectral line is symmetrical around the axis going through its centre, unless there is a mechanism causing departures from this symmetry (e.g. pulsations, spots, stellar wind, ...). Therefore it is possible to measure RV of a spectral line by sliding its direct and mirrored profiles along each other until the best match is achieved. This technique was at first applied to the RV measurement on photographic plates with the Grant machine (Rickard et al., 1975).

This method is superior to the fitting of the Gaussian function, because we are using "the same spectral line" as a template. The main discrepancy of this method is its inability to deal with line blends. If the line blends with other lines, than the mirrored profile is no longer a correct model and its validity depends on the measure of the blending. In binary stars this

limitation often means that we are able to measure RVs of its components around quadrature, when the lines of the two components are separated, but we loose precision or are unable to measure RVs at all, if the stars are near conjunctions.

I applied this method to measure RVs of two Be stars BU Tauri (Nemravová et al., 2010) and γ Cas (Nemravová et al., 2012b). In case of these two studies we measured RV on steep wings of emission lines (Hα and He I 6678 Å) in order to detect duplicity of these two objects. In both systems only lines of the primary (brighter and more massive) component are seen in the visible, but the measured lines partially come from the central star and partially from its circumstellar envelope. Hα blends with a number of telluric lines. Although it may seem that the properties of the measured spectral lines would prevent me from the usage of the comparison of direct and mirrored profile, the opposite is true.

First the steep wings of these lines are symmetric, because they likely originate from inner parts of the circumstellar disk, because the disk is very likely Keplerian, as it was proved in case of γ Cas (see Stee et al., 2012) and other Be stars (see Meilland et al., 2012) using the spectro-interferometry, meaning that the rotational velocity scales with the radius as r^{-1}. Second the emission in the Hα is so strong (rising up to five times above the continuum flux for both stars), that the telluric lines cannot significantly alter the position of the steep wings. The approach to measure RVs of Be stars on steep wings of emission lines was first used by Božić et al. (1995) and a detailed justification of the approach can be found in Ruždjak et al. (2009).

I carried out the measurements in program SPEFO (Horn et al., 1996; Škoda, 1996), in which this method is implemented manually only. The biggest advantage of the manual approach is, that the user can account for blends, but at the cost that he or she introduces a certain degree of subjectivity and is unable to estimate the uncertainty from a single line. Therefore in case of both studies PH and JN measured the RVs independently and on several spectral lines to give more credibility to the results. Also in case of γ Cas A. Miroshnichenko succeeded in the automatising of the method. Both ways manual and automatic gave similar RVs and the consequent orbital solution similar scatter of the residuals (see Nemravová et al., 2012b, Table 8). A comparison of automatically and manually measured RVs is also shown in Fig. 2.2.

An example of RV measurements of γ Cas and BU Tauri using the comparison of direct and mirrored line profiles is shown in Figure 2.3. Note that RV changes are a superposition of the orbital motion and long-term variations, we had to remove the latter first to study the former.

The cross-correlation

Strictly speaking the subtitle can refer only to the maximisation of the cross-correlation of an observed spectrum I and a template spectrum T given by the following equation:

$$I \star T\,(RV) = \int_{\mathbb{R}} I\,(\lambda)\, T\,[\lambda\,(1 + RV/c)]\,\mathrm{d}\lambda, \tag{2.34}$$

where RV denotes the radial velocity, c the speed of light, and λ the wavelength. It is advantageous to use the following property of the cross-correlation:

$$\mathcal{F}\{I \star T\} = \mathcal{F}\{I\}^{*}\mathcal{F}\{T\}, \tag{2.35}$$

where $\mathcal{F}$ denotes the Fourier transform, and the asterisk the complex conjugation, which allows the user to exploit the Fast Fourier Transform (FFT).

This technique was first used to measure RVs of stellar spectra by Simkin (1974). The Eq. (2.34) represents only the simplest form — an observed spectrum is cross-correlated with one template only (i.e. RV of one component is estimated). A generalisation of the technique for spectra containing two sets of spectral lines was derived by Zucker and Mazeh (1994), implemented within program TODCOR. In their application the cross-correlation is computed with a composite template $T = T_1 + \alpha T_2$, where T_1 is the template for the primary, T_2 the template for the secondary, and α the flux ratio of these two components. The last parameter also restricts the user to cross-correlation of spectra segments, over which α does not vary significantly. Following a similar approach Zucker et al. (1995) generalised the technique for systems with three sets of spectral lines, and (Torres et al., 2007) for systems with four sets of spectral lines. Zucker and Mazeh (1994) showed that the cross-correlation gives incorrect RV estimates if one cross-correlates less templates than number of detected component spectra.

Usually synthetic spectra, or observed spectra of a similar spectral type serve as templates. The main advantage of this technique is its ability to deal with intrinsic line blends (excluding interstellar and atmospheric line blends).

We used this technique to measure RVs of semi-detached binary undergoing the last phase of the mass transfer BR CMi (Harmanec et al., 2015). Authors of the study used modification of the TODCOR written by Y. Frémat (called asTODCOR). In this particular study we used disentangled spectra as templates. This approach turned out to be quite dangerous, since the use of disentangled spectra acquired with program KOREL (Hadrava, 1995, 1997, 2009) introduces a systematic error, which is very subtle and it is difficult to account for it. An illustration of this is in Sect. 2.3.3.

2.3.2 Radial-velocity estimation based on the comparison of observed and synthetic spectra

The cross-correlation is a standard technique, which is widely used to determine displacement between two matrices, but it has no statistical meaning, and in the stellar application the width of the cross-correlation peak is related to the rotational broadening of a spectral line rather than to statistical uncertainty of the measured velocity.

Hence I decided to carry out the RV estimation, by minimisation of χ^2 defined by the following equation:

$$\chi^2_{\mathrm{RV}} = \sum_{i=1}^{N_{\mathrm{P}}} \left[\frac{I_i - \sum_{j=1}^{N_{\mathrm{C}}} T_{i,j}\left(RV_j\right)}{\sigma_i} \right]^2 , \tag{2.36}$$

where I_i denotes i-th pixel of an observed spectrum, $T_{i,j}$ i-th pixel of a template spectrum representing the j-th component of the studied binary, N_{P} the number of pixels of the observed spectrum, N_{C} the number of components visible in the spectrum, and RV_j the radial-velocity of the j-th component.

The advantages of this approach are: i) Simple numerical computation of the χ^2 compared to cross-correlation, where computation of the N_{C}-dimensional Fourier transform is necessary to estimate RV. Also observed spectra have to be over-sampled, and apodized at each end to increase the resolution. ii) One is allowed to fit unevenly sampled spectra. FFT of unevenly sampled spectra is not possible, meaning that one is not allowed to remove parts of spectra affected by e.g. interstellar lines, or one has to sacrifice FFT for discrete Fourier transform (DFT), which is significantly slower. iii) χ^2_{RV} has direct statistical meaning and can be used to evaluate goodness-of-fit, and estimate uncertainty of the RV.

The last point on the list holds only if the templates fit the observed spectra well, which is a strong requirement on their choice. I tried to deal with that by choosing an optimal spectrum from a grid of synthetic spectra. The technique is described in Sect. 3.1.4

I have written a simple Python script (named *ERV*), which implements this technique (represented by Eq. 2.36). The program fits N_{C} component to the observed spectra. The user has to supply the templates, so they do not necessarily have to be synthetic spectra. A brief description of the program along with a simple tutorial are given in Sect. 6.1.

2.3.3 Perils of the radial velocity estimation based on the comparison of observed and disentangled spectra

This section demonstrates that the use of disentangled spectra as templates for any technique discussed in previous sections can be a source of a systematic error. Unfortunately we were not aware of this in our study of the BR CMi binary (Harmanec et al., 2015), and it led to the underestimation of the mass ratio, and to incorrect estimates of component masses, radii, and the orbital inclination, and their uncertainties.

BR CMi is a binary undergoing a slow mass-transfer phase. The primary is a A0 type star, partially obscured by a circumstellar envelope made from gas drained from the Roche-lobe filling K type secondary. In the spectrum of BR CMi we can see large number of sharp lines coming from the cool secondary and broad lines of the fast-rotating primary. Balmer lines have an emission component coming from the circumstellar gas. It is most prominent in Hα, but almost missing in Hγ and Hδ.

To obtain RV curve we used the following approach: (i) We measured RV variations of the secondary by the comparison of the direct and mirrored line profiles. The precision was very high, because secondary lines are very sharp and easy to measure. (ii) We fitted the RV measurements with an orbital model and obtained precise estimates of the eccentricity, the period, the periastron epoch, the semiamplitude of the RV curve, and the periastron argument. (iii) The same technique was not applicable to the lines of primary, which are broad, blend with lines of secondary and the strongest primary lines — the Balmer lines — have an emission component, which obscures the true motion of primary. Therefore we disentangled the spectra (using program KOREL) in the spectral region $\Delta\lambda = [4397; 4608]$ Å, in which the spectral lines are likely unaffected by the emission from the accretion disk. (iv) We used disentangled spectra as templates for RV measurement using the cross-correlation. This technique produced a very fine curve for both components, which we fitted with an orbital model and obtained a mass ratio q, which was used in the consequent light-curve analysis.

Unfortunately we introduced a systematic error into our analysis by using the disentangled spectra. First we incorrectly assumed, that the dependence of the shape of disentangled line profiles on the corresponding orbital solution is weak. There is no strong ground for this assumption, because the sum of squares of minimised by KOREL (Eq. 4 in Hadrava, 1997) clearly depends on the shape of the disentangled profiles. Typically the number of free parameters is $10^3 - 10^5$, and the degeneracy of the solution is high, i.e. one wrongly estimated parameter can be compensated by another one. We also did not carefully analyse the uncertainty of individual parameters — especially the mass ratio q, which is really the only poorly constrained parameter, because the remaining ones are well determined from the RV curve of the secondary.

I carried out a mapping of the Eq. (4) in Hadrava (1997), in the mass ratio $q = M1/M2$ (valid only in this Sect.) and the semiamplitude of the RV curve K and scaled it to represent the χ^2. I estimated 68%, 95%, and 99.7% confidence intervals, which represent one, two, and three standard deviations. The map is shown in Fig. 2.4. After I found the minimum I re-ran KOREL starting from the minimal point to optimise it. The final mass ratio was $q = 10.57^{+4.4}_{-3.0}$; the error bars represent one σ. The value $q \approx 16.7$ reported by Harmanec et al. (2015) is not completely incorrect, it lies within two-σ region (see Fig. 2.4, yellow line), but the error estimate of K_1 (the primary semiamplitude) is completely wrong, because *the shape of the disentangled spectra depends on the orbital elements for which they were obtained.* If the disentangled spectra are used for RV measurement, they will give a RV curve with orbital elements very much similar to those for which they were disentangled.

To demonstrate this I disentangled the spectra for mass ratios $q \in \{7.5; 10.57; 14.8\}$ (all within one σ), used these spectra to measure RVs on the studied spectra with program *ERV* described in Sect. 6.1, and fitted them with an orbital model with the program *FRV* (see Sect. 6.2). In all three cases the program produced a fine curve for both components. The secondary RV curve was practically the same for all three cases, but each primary RV curve has a clearly different amplitude. The best-fitting orbital model gave following estimates of the mass ratios (errors were estimated locally) $q \in \{8.11 \pm 0.14; 10.79 \pm 0.26; 13.07 \pm 0.36\}$. The measured RV curves and their fits are shown in Fig. 2.5. Because an incorrect value of the mass ratio was used, the model of the light curve presented in Table 6 of our study Harmanec et al. (2015), including mass and radius estimates, should be revised. This also demonstrates that disentangled spectra are not appropriate templates for RV measurement, unless a careful error analysis of the corresponding orbital solution was done.

A resolution of this situation would be to measure RVs of the primary with an alternative method, which does not bind the individual RVs with an orbital model.

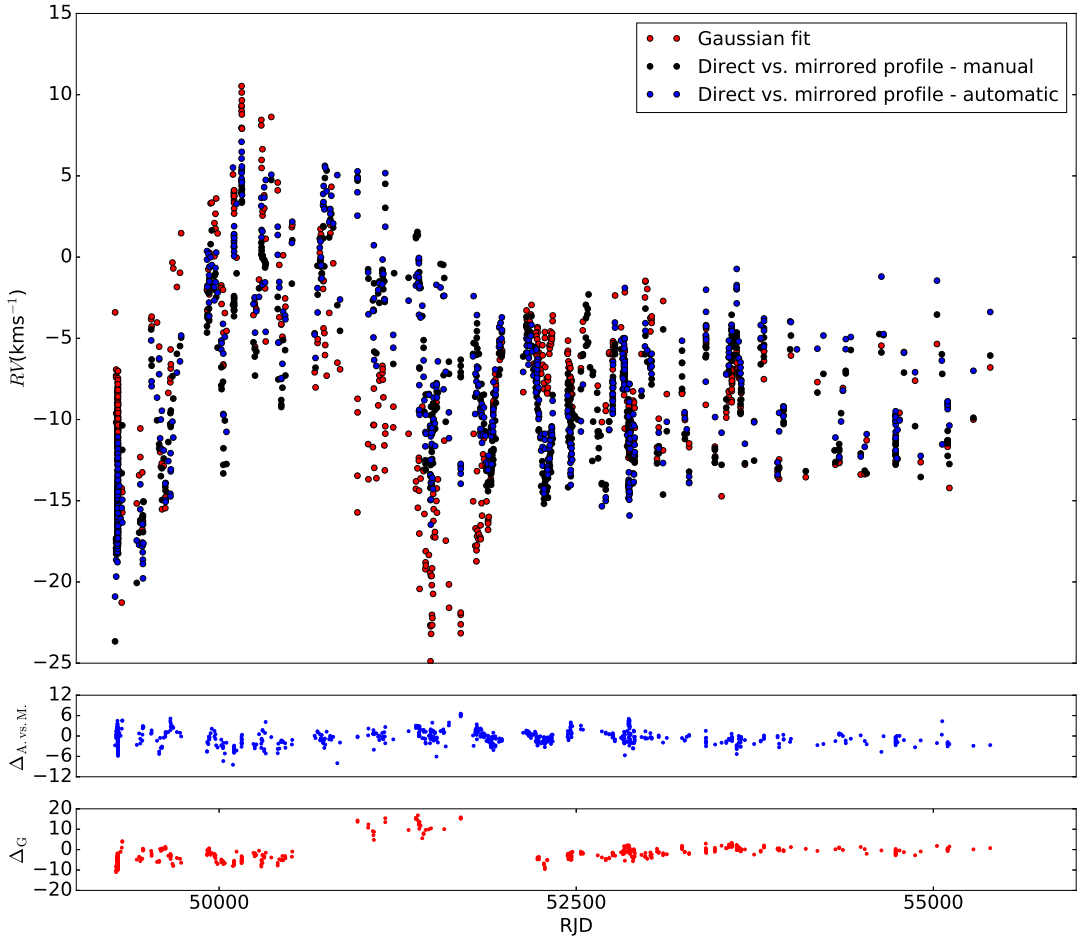

Figure 2.2: A comparison of RVs measured on the Hα of γ Cas. *Top panel:* RVs measured by the comparison of direct and mirrored profiles of Hα manually in SPEFO are denoted by black points; typical uncertainty of these points is $\approx 1.8\,\mathrm{km.s^{-1}}$, RVs measured by the comparison of direct and mirrored profiles of Hα automatically by means of χ^2 minimisation with a program developed by Dr. Miroshnichenko are denoted by blue points; typical uncertainty of these points is $\approx 2.0\,\mathrm{km.s^{-1}}$, RVs measured by the fitting of Gaussian function to the Hα profile are denoted with by red points; the uncertainty was not evaluated, but is very likely higher than those in the two preceding cases, although still less than $5\,\mathrm{km.s^{-1}}$. The uncertainty estimates are based on the assumption, that the spectroscopic observations are strictly homogeneous, and that the orbital model fitted to them (see Nemravová et al., 2012b) is correct. *Middle panel:* $\Delta_{\mathrm{A.vs.M}}$ denotes residuals (in $\mathrm{km.s^{-1}}$) of the manually measured RVs and automatically measured RVs using the comparison of direct and mirrored profiles. *Bottom panel:* Δ_{G} denotes residuals (in $\mathrm{km.s^{-1}}$) of the manually measured RVs and automatically measured RVs using the comparison of direct and mirrored profiles. Note that these RV measurements are still affected by the circumstellar envelope of γ Cas and we had to remove the long-term variations first before studying the multiplicity of the system.

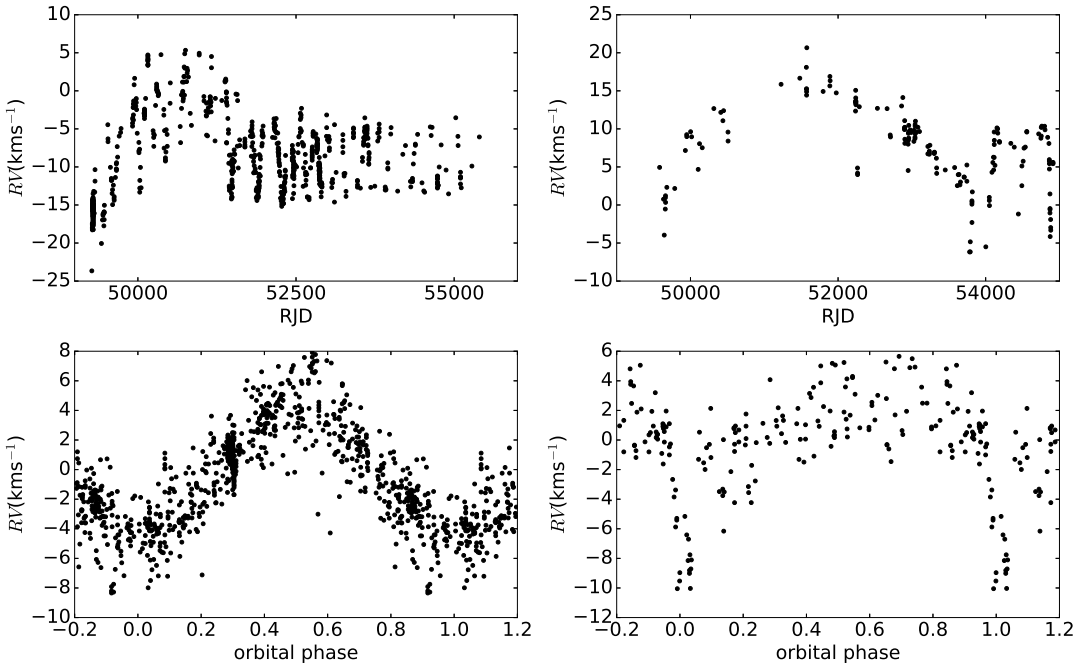

Figure 2.3: Radial-velocity measurements obtained by comparison of direct and mirrored Hα profile. *Top left:* γ Cas including the long-term variations. *Bottom left:* γ Cas after removal of the long-term RV variations which were estimated with a Hermite polynomial fit to local values of the systemic (γ) velocity (see Nemravová et al., 2012b, p.6-7; for details on the approach). *Top right:* BU Tauri including the long-term variations. *Bottom right:* BU Tauri after removal of the long-term RV variations which were estimated with a Hermite polynomial fit to local values of the systemic (γ) velocity (see Nemravová et al., 2010, p.4-6; for details on the approach).

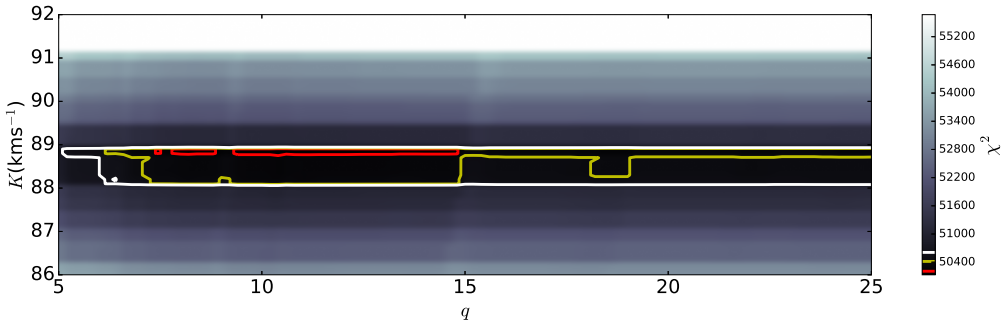

Figure 2.4: A map of the χ^2 given by the Eq. 4 in Hadrava (1997) for the BR CMi system around the global minimum of Eq. (4) (see Sect. 2.3.3 for details). The number of data points is 167935, the minimal $\chi^2 = 50131$, meaning that we have overestimated the uncertainty of studied spectra. That is not surprising, because the uncertainty was estimated from the flux noise in the continuum, which is difficult to find given the large number of lines of the cool secondary. The mapped parameters are the mass ratio $q = M_1/M_2$, and the semiamplitude of the RV curve of secondary K. Remaining parameters were kept fixed at values from Table 3 in Harmanec et al. (2015).

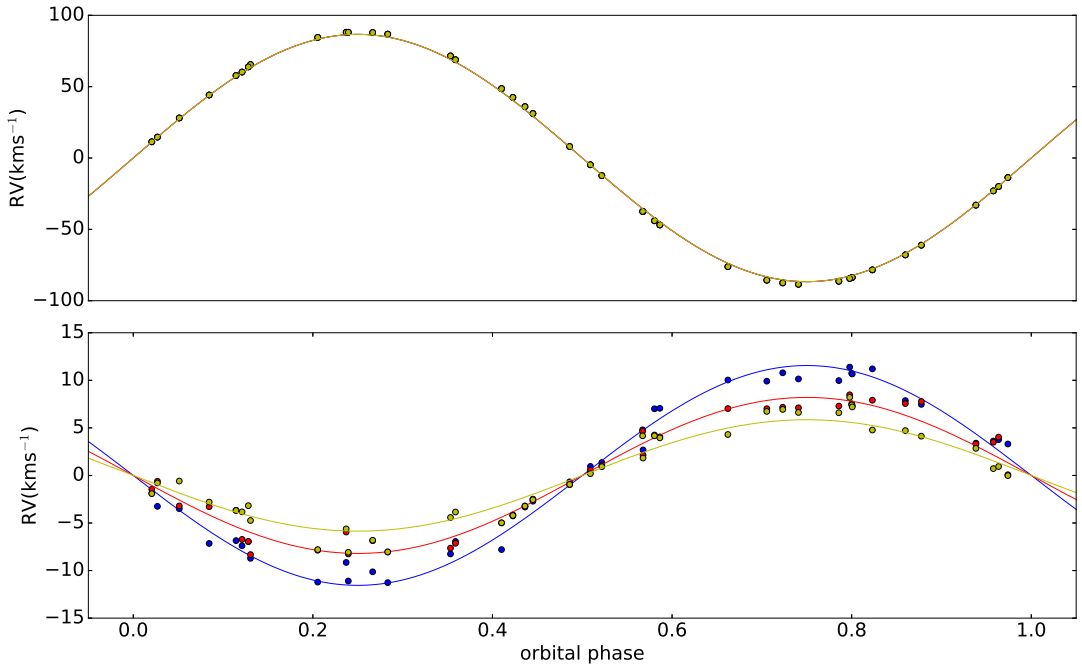

Figure 2.5: RVs of BR CMi components measured using comparison of observed and disentangled spectra, which were obtained for different values of the mass ratio q (see Sect. 2.3.3 for explanation). *Upper panel:* Measurements of the secondary RV using disentangled spectra for: (i) $q = 7.50$ (blue dots), (ii) $q = 10.57$ (red dots), and (iii) $q = 14.80$ (yellow dots). The line denotes the best-fitting synthetic Keplerian RV curve to the RV measurements of corresponding colour. The measurements and models are practically the same and overlap each other. *Lower panel:* Measurements of the secondary RV using disentangled spectra for: (i) $q = 7.50$ (blue dots), (ii) $q = 10.57$ (red dots), and (iii) $q = 14.80$ (yellow dots). The line denotes the best-fitting synthetic Keplerian RV curve to the RV measurements of corresponding colour. The mass ratio given by the fit two these RV curves are $q_{\mathrm{RV-CURVE}} \in \{8.11 \pm 0.14; 10.79 \pm 0.26; 13.07 \pm 0.36\}$. This demonstrates that disentangled spectra are not independent of the orbital solution for which they were obtained.

3. Modelling of multiple systems

Each binary (or multiple system) is a very complex object, whose behaviour is determined by many physical phenomena. In general, a researcher is unable to probe the systems and can only study their observable behaviour using various methods and infer the physical phenomena standing behind it. Each observation is limited by its (i) time distribution, (ii) resolution, and (iii) signal-to-noise ratio (SNR). Generally it is not possible to study effects that occur on a timescale that is significantly longer than the time spanned by the available data. Many astrophysical processes take millions of years (e.g. the stellar evolution) and cannot be observed directly. An astronomer is then forced to study different objects at different phase of the process. The resolution along with the SNR limits number of details, that can measured on an observation. The noise in astronomical observations is usually Poissonian, meaning that it scales with the square root of a signal. Also there is no ultimate observational method that extracts the whole observable behaviour. Instead each method captures its part only.

By "modelling of a multiple system" I mean an effort to create a model of the studied system, *which agrees with the observations*. The last sentence says, that our model has to be complex only to that degree, so it re-produces the observations. Unfortunately there are processes, which are very hard to model (e.g. dynamics of the circumstellar environment). In these situations either purely mathematical "ad hoc" models are used to describe such phenomena and somehow to separate them from processes that can be described with a physical model, or one just surrenders and uses an incorrect model with all dangers corresponding to this approach.

In this chapter I discuss models that I used throughout studies that I co-authored.

3.1 Models tailored for one observational method

Each observational method provides only limited insight in the properties of a binary. Why would anyone used models, which are comparable only to one observation type?

The main reason is their simplicity — these models rely on a smaller number of parameters, meaning that finding the best-fitting parameters is easier. Also when one has only one kind of observable at her or his disposal, using a complicated model may feel like "Swatting flies with a sledgehammer".

Usage of several models based on different types of observations independently also serves as a self-check. It may help to identify systematic errors affecting one or more observation sets.

Nonetheless data from one observational method are generally insufficient to constrain the size, and position of a binary orbit and properties of its components. Hence one is obliged either to use one model for more kinds of observations, or to apply iteratively models for one observation type.

In the following sections I go through "traditional models" which are tailored to spectroscopic, photometric and spectro-interferometric observations. These models were applied in various studies, especially in the ξ Tau study (Nemravová et al., 2016).

3.1.1 The radial velocity curve

RV variations are a valuable source of information about binary orbital elements, because they can be accurately measured from the shift of component spectral lines (Eq. 2.33). Although RV curve alone does not constrain the size and geometric orientation of a Keplerian ellipse completely, it constrains the majority of Keplerian orbital elements.

In the following paragraphs I construct a simple model to interpret RVs of members of a multiple system. Usually these equations turned out to be sufficient representation of observed RV curves of binaries, that I studied.

A list of methods for the RV measurements, which I used in studies, that I participated in, along with comments and their application is in Sect. 2.3.

The simplest case - a binary

A direct consequence of Kepler's first law (Eqs. 1.1, and 1.4) is the following formula:

$$RV_i\,(t) = K_i\left[\cos\left(\omega_i + v\,(t, P, e, T_\mathrm{p})\right) + e\cos\omega_i\right] + \gamma, \tag{3.1}$$

where K is the semi-amplitude of the RV curve, ω the periastron argument, v the true anomaly, P the period, e, the eccentricity, T_p the epoch of the periastron passage, and γ the relative velocity of the barycentre of Solar system, and the barycentre of the studied binary. The index i denotes a component of the binary (1 = primary, 2 = secondary). Parameters without the index i in Eq. (3.1) are the same for both components. The semi-amplitude of the RV curve depends on the period, eccentricity, semimajor axis a, and inclination i by the relation:

$$K_i = \frac{2\pi a_i \sin i}{P\left(1-e^2\right)^{\frac{1}{2}}}. \tag{3.2}$$

Eqs. (3.1), and (3.2) imply that only RV curve model cannot be used to determine the semi-major axis, and orbital inclination, but merely their product $a\sin i$, meaning that one of these parameters (usually the inclination) has to be obtained elsewhere – either from the light curve if the studied binary is eclipsing or ellipsoidal at least, or from the astrometry. The semiamplitude of RV curve has to be determined for each component. In my programs I do not use pair of binary semi-amplitudes K_1 and K_2, but I use the first one and their ratio q, because clearly from Eq. (3.2), and the definition of centre of mass, the ratio corresponds to the mass ratio of primary and secondary

$$\frac{K_1}{K_2} = \frac{M_2}{M_1} = q. \tag{3.3}$$

A RV curve also does not constrain the longitude of the ascending node Ω.

This model is often sufficient, when the perturbations causing a shift of a whole component (e.g. tides), or somehow obscure, or change the RV distribution over the surface of a component (e.g. circumstellar matter, Rossitter-McLaughlin effect, ...) are negligible or their typical time-scale is much longer than the time span of the observations.

I used this model to estimate properties of two Be stars BU Tauri and γ Cas. The model was implemented in program SPEL (Horn et al., 1994, 1996). In these two applications the program was used to (i) estimate local systemic velocity, which turned out to give the best description of the long term radial-velocity variation (see also Nemravová et al., 2012a), and (ii) and to fit the RVs from which the long-term trend was removed (Nemravová et al., 2010, 2012b). The model also turned out to be sufficient representation of RV variations of an eclipsing binary BD+36 3317 (Kıran et al., 2016), whose RV curves are only slightly deformed by the Rossitter-McLaughlin effect (RME).

A multiple system

The analytic RV curve is generalised for a hierarchical multiple system by summing RVs from N_O orbits relevant for the motion of the i-th component.

$$RV_i\,(t) = \sum_{j=1}^{N_\mathrm{O}} K_j\left[\cos\left(\omega_j + v_j\,(t, P_j, e_j, T_{\mathrm{p},j})\right) + e_j\cos\omega_j\right] + \gamma. \tag{3.4}$$

The presence of more orbits also introduces significant time delay caused by the finite speed of light called Light Time Travel Effect (LTTE) given by the following formula:

$$\Delta t_{\mathrm{LTTE,i}}\,(t) = \sum_{j=1}^{N_\mathrm{O}} \frac{P_j K_j\left(1-e_j^2\right)^{\frac{3}{2}}}{2\pi c}\frac{\sin\left[\omega_j(t) + v_j(t)\right]}{1 + e_j\cos v_j(t)}, \tag{3.5}$$

where Δt_LTTE denotes the delay of i-th component produced by N_O orbits relevant for its motion. This delay has to be subtracted from t, hence the Eq. (3.4) should be computed for time $\tilde{t} = t - \Delta t_\mathrm{LTTE}$.

This model is sufficient in extended multiple systems, where the dynamical interaction between its orbits can be neglected. The Eqs. (3.4), and (3.5) also hold for co-planar, compact

hierarchical multiple systems, which are still distant enough for the tides to be negligible. They only have to be complemented by a third formula:

$$\omega_i\left(\tilde{t}\right) = \omega_i(T_{0,i}) + \dot{\omega}_i\left(\tilde{t} - T_{0,i}\right), \tag{3.6}$$

which represents the apsidal motion, which results from the dynamical interaction between two adjacent orbits in a hierarchical system (see Sect. 1.2). Here $\dot{\omega}_i$ is constant, meaning that the apsidal advance is linear.

The model represented by Eqs. (3.4), (3.5), and (3.6) was sufficient for the study of ξ Tau (Nemravová et al., 2016). I wrote a program *FRV*, which fits the model represented by these equations to RVs of hierarchical systems containing maximum of three levels in the hierarchy. The optimisation is carried out by minimisation of the following χ^2:

$$\chi^2 = \sum_{i=1}^{N_\mathrm{C}} \sum_{j=1}^{N} \left[\frac{RV_{\mathrm{O},i,j} - RV_{i,j}}{\sigma_{i,j}}\right]^2, \tag{3.7}$$

where RV_O denotes the observed RV, σ its uncertainty, RV synthetic radial velocity given by Eq. (3.4), corrected for the LTTE and the apsidal motion. The summation goes over N_C components for which N observations are available. Description of the program *FRV* is in Sect. 6.2.

Nonetheless generally for a compact binary this model is insufficient, because the dynamical interaction can produce plenty of effects, which are far beyond scope of this simple model. In those cases one has to use an N-body model such as that one developed by Brož et al. (2010), and Brož (2016, submitted to APJL) and successfully applied to the investigation of ξ Tau system.

3.1.2 The light curve

A light curve can be used to determine orbital elements of a binary and properties of its component, if the modulation is caused by the orbital motion. The most common causes are the eclipses and ellipsoidal variations. Less usual are the beaming (Shakura and Postnov, 1987), and tidally induced oscillations (Welsh et al., 2011).

The light curve itself does not constrain all orbital elements, but if it is complemented with the physical size of the semimajor axis, or the RV curve solution, all orbital elements can be determined except for the longitude of the ascending node Ω. On the other hand the light curve provides more information about binary components — especially if it is calibrated and obtained in several passbands — radii, effective temperatures, surface gravitational accelerations, and absolute magnitudes.

I have not developed any light curve models, but I used the program PHOEBE (Prša and Zwitter, 2005, 2006), which is an enhanced wrapper around the widespread Wilson-Devinney code (WD) (Wilson and Devinney, 1971; van Hamme and Wilson, 2003). Dr. Wilson and others have been actively improving the program. One of quite recent additions to the program is the ability to fit minima timings (see Wilson and Van Hamme, 2014).

The orbital model

In this section I briefly describe the model implemented in WD (release 2007), which is implemented in PHOEBE. Only final relations are presented here and one should inspect either Kallrath and Milone (2009) or PHOEBE scientific reference[1] (PSR).

In this model binary components gravitationally interact as point masses surrounded by mass-less atmospheres. The shape of gravitational potential in this configuration was first described by (Roche, 1859). The shapes of components are then identical to the shape of equipotential they fill, i.e. this model binds the orbital properties and shapes of stars together. Kopal (1959) came with a representation of the gravitational potential in dimensionless form, which is implemented WD in a slightly modified form:

$$\Omega_\mathrm{K} = \frac{1}{\rho} + q\left(\frac{1}{\sqrt{\delta^2 + \rho^2 - 2\rho\lambda\delta}} - \frac{\rho\lambda}{\delta^2}\right) + \frac{1}{2}F^2\left(1+q\right)\rho^2\left(1-\nu^2\right), \tag{3.8}$$

[1]The reference was written by Dr. A. Prša and is publicly available at `http://phoebe-project.org/1.0/docs/phoebe_science.pdf`.

where $\Omega_{\rm K}$ is the Kopal potential, $\rho = r/a$ the radius relative to the semimajor axis a, q the mass ratio, $\delta = D/a$ the absolute separation of binary components at time t given by the first Kepler law (Eq. 1.1), $F = \omega_{\rm R}/\omega_{\rm O}$ is the synchronicity ratio between the rotational $\omega_{\rm R}$, and orbitals periods $\omega_{\rm O}$. The beginning of the coordinate system is in the centre of primary. Spherical coordinates are employed ($x = r\sin\theta\cos\phi = r\lambda$, $y = r\sin\theta\sin\phi = r\mu$, $y = r\cos\theta = r\nu$) with the orbital plane lying in xy plane. Given the choice of the coordinates and the normalisation of the Kopal potential the following transformation gives the size of the secondary potential $\Omega'_{\rm K}$:

$$\Omega'_{\rm K} = \frac{\Omega_{\rm K}}{q} + \frac{q-1}{2q} \tag{3.9}$$

(see Kallrath and Milone, 2009, p.95-102) for the derivation of Eqs. (3.8), and (3.9).

The Eq. (3.8) does not constrain absolute size of radii, or semimajor axis, only their relative values. Also the mass ratio is constrained poorly, because departures from spherical symmetry appear only for very compact systems showing significant ellipsoidal variations.

Eclipses and ellipsoidal variations are purely geometrical effects given by the projection of the binary components on the sky. The on-sky distance Δ of phase centres of binary components is given by the following formula:

$$\Delta^2 = D^2\left(\cos^2 i + \sin^2 i \sin^2\theta\right), \tag{3.10}$$

where i is the orbital inclination, and θ the geometric phase give as follows:

$$\theta = \omega + v - \frac{\pi}{2}, \tag{3.11}$$

where v is the true anomaly, and ω the periastron argument. A detailed derivation of Eq. (3.10) is in Kallrath and Milone (2009, p.77-81). This relation is particularly important, because it shows that the orbital inclination is constrained by the light curve.

The PHOEBE model also includes a linear apsidal motion $\dot{\omega}$ (similar to Eq. 3.6) and linear change of the orbital period $\dot{P}$ (see PSR; p.41-42).

The radiative model

The first Kepler law (Eq. 1.1) established the binary orbit, Eq. (3.8) the shape of its components, and Eq. (3.10) their projection on the sky, but to create a model of a light curve one also has to set radiative properties of both components. First it is necessary to create a set of triples $\{\lambda_i, \mu_i, \nu_i\}_{i=1..N}$ and compute $\{\rho_i\}_{=1..N}$ for a given surface potential Ω_K and sample surfaces of primary and secondary, and then set the radiative properties of each surface element. In PHOEBE the following effects are taken into account: (i) the atmospheric radiation, (ii) the limb-darkening, (iii) the gravity darkening, and (iv) the reflection.

- **The atmospheric radiation:** An atmospheric model provides the monochromatic intensity for a given wavelength, effective temperature $T_{\rm eff}$, gravitational acceleration g, metallicity z, and aspect angle γ. The function is then integrated over a passband, multiplied by its transmission function to get the passband emergent intensity. PHOEBE uses the Kurucz's stellar atmosphere models (Castelli and Kurucz, 2004), but WD allows the user to switch to the black-body radiation. A common practice is not to compute the intensity for a given aspect angle, but to use pre-computed spectra for $I(\gamma) = I(0)$ and dampen the intensity using a limb-darkening law and coefficients from a pre-calculated grid, when computing the flux from the whole surface of a binary component.

- **The limb-darkening:** The limb-darkening is the attenuation of the intensity towards the edge of a star, because we see systematically higher photospheric layers, which are cooler and hence less bright. Instead of computing $I(\gamma)$ directly from an atmospheric model one uses a limb-darkening law, which is an analytic mathematical function approximating the real intensity centre-to-limb variations:

$$I(\gamma) = I_0 \sum_{i=1}^{N_{\rm C}} x_i f^i(\gamma), \tag{3.12}$$

where I_0 is the intensity for $\gamma = 0\,\mathrm{deg}$, x_i are coefficients of the limb-darkening, f^i mathematical functions defining the law, N_C is the number of terms in the sum. In the past several limb-darkening laws were proposed, each more suited to a different range of effective temperatures. These were superseded with the four-parameter law proposed by Claret (2000):

$$I = I_0 \sum_{i=1}^{4} x_i \left(1 - \cos^{\frac{i}{2}} \gamma\right) \tag{3.13}$$

which is applicable to effective temperatures ranging from 2000 K to 50000 K. In PHOEBE the coefficients of the adopted limb-darkening law are obtained via interpolation in pre-computed grids covering a wide range of effective temperatures, surface gravitational accelerations, metallicities, and wavelengths prepared by van Hamme (1993), and Prša (2012; unpublished).

- **The gravity brightening:** The local surface temperature is proportional to the local gravitational acceleration. The scaling of the local flux F_l over the stellar surface is the following:

$$F_l = F_p \left(\frac{g_l}{g_p}\right)^{\alpha}, \tag{3.14}$$

where F_p the polar flux, g_l the local effective gravitational acceleration, g_p the polar effective gravitational acceleration, and α is an exponent depending on the state of the surface layers. For atmospheres in radiative equilibrium $\alpha = 1.0$ (von Zeipel, 1924), and in convective equilibrium $\alpha = 0.32$ (Lucy, 1967). Tables of $\alpha\,(T_\mathrm{eff})$ covering the two states and providing a smooth transition between them were computed by Claret (1998).

- **The reflection effect:** The incoming flux from one binary component to the other one is partially reflected and partially absorbed (heating the other star). The ratio between reflected and absorbed energy is usually modelled with a single parameter called bolometric albedo A. The local temperature T' on an irradiated star is then modified by the following equation:

$$T' = T \sqrt[4]{1 + A\frac{F_s}{F_t}}, \tag{3.15}$$

where T is the temperature before inclusion of the reflection, F_s the bolometric flux coming from the irradiating star, and F_t the bolometric flux on a star without reflection. Tables showing dependence of the bolometric albedo on the effective temperature $A\,(T_\mathrm{eff})$ were published by Claret (2001). Stars whose atmospheres are in radiative equilibrium have $A = 1$ (Eddington, 1926). The reflection is computed iteratively in PHOEBE/WD; several reflections have to be computed, until the T' converges.

The last property that does not fit in the previous list, but is included in PHOEBE/WD model, is the third light L_3, which can come either from one or more components physically bound to the studied system, or from an unrelated star lying too close to the studied star on the sky, so it cannot be safely separated.

PHOEBE/WD is also able to model spotted stars, but I have not tested this functionality yet, because I have never studied spotted stars. ξ Tau exhibits rapid light variations, which we attributed to either spots or pulsations of the tertiary (Nemravová et al., 2016). Unfortunately we were unable to model this system with PHOEBE, since the tertiary is treated as the main contributor of the third light.

Applications of the model

We have seen that the PHOEBE/WD model is quite complex, the parameters defining the model are, $\Omega_{\mathrm{K},1}$, $\Omega_{\mathrm{K},2}$, i, q, a, P, $\dot{P}$, T_0, e, i, ω, $\dot{\omega}$, z, $T_{\mathrm{eff},1}$, $T_{\mathrm{eff},2}$, F_1, F_2, A_1, A_2, $\sum_{i=1}^{N} x_i f^i\,(\cos\gamma)$, α_1, α_2, and L_3. Generally it is impossible to infer all these properties even if one samples the flux $F(\lambda)$ with a large number of pass-bands, and in the most favourable geometrical configuration

— the system is eclipsing and the eclipses are total — because the inverse problem would be too degenerate. Hence the limb-darkening coefficients, bolometric albedos, and gravity brightening coefficients are taken from Tables (van Hamme, 1993; Claret, 1998, 2001). Parameters a, q, $\Omega_{\rm K}$ are completely correlated (see Eq. 3.8), which means that a change in one parameter is compensated by the remaining two with no difference in the outcome. This indeterminacy can only be broken by fixing one of those parameters (or by fitting RVs as well, but then we get outside observation-specific models). Prša and Zwitter (2006) argues that effective temperatures are completely correlated and (again) cannot be determined along each other unless colour-constraining technique described by the authors is applied or one temperature fixed. The mass ratio q is also poorly constrained unless the components are highly deformed by the mutual gravitational interaction. Another set of highly correlated parameters is Ω_1, Ω_2, i and L_3.

These correlations always forced us to fix some parameters by using another method. This was the case for BR CMi (Harmanec et al., 2015), where the secondary effective temperature was obtained from the spectroscopy, and the mass ratio and $a \sin i$ from the RV fit (although the error bars were underestimated significantly, see Sect. 2.3.3). Similar approach was adopted in the study of ξ Tau, and the semi-detached binary TW Dra (Božić et al., 2013) that I co-authored.

The degeneracy of the inverse problem is illustrated in Fig. 3.1. Here we can see a genetic algorithm on its way towards the global minimum, and the sample with the best χ^2 in a generation oscillates wildly showing that the fitted set of parameters: $\Omega_{\rm K,1}$, $\Omega_{\rm K,2}$, T_0, i, $L_3^{\rm MO}$, $T_{\rm eff,2}$, can clearly compensate each other, even though the very accurate observations of ξ Tau acquired with the satellite MOST are fitted.

3.1.3 The complex visibility of interferometric fringes

The complex visibility yields information on the intensity distribution over the sky of the studied object and for binaries it should employ a model similar to the one implemented within WD/PHOEBE or better. Unfortunately spectro-interferometric observations are often incomplete (they lack phase, or have poor uv-plane coverage), and they can be well explained with variety of models.

The range of possible applications of interferometry is wide, but for binary research the following four application are of a particular interest: (i) resolving of the orbit, (ii) resolving of the component radii, (iii) resolving the limb-darkening, and (iv) resolving the circumstellar matter.

During my doctoral study I created a simple analytic model to do (i), and (ii) for a hierarchical binary ξ Tau and (i), (ii), and (iv) for a binary undergoing mass transfer β Lyr. Here I describe the models for these two objects.

A model for a hierarchical triple system

The key contribution of the interferometry is its ability to resolve the binary orbit and provide the orbital inclination for arbitrarily inclined orbits (the eclipses are usually restricted to a limited range of angles surrounding 90 deg). It is also able to provide the longitude of ascending node Ω. Unfortunately the astrometry provides the orbit in angular scale only, meaning that a distance estimate, or a RV curve are needed to obtain the orbit in the physical scale.

In Nemravová et al. (2016) I created a simple analytic model of the inner triple subsystem of ξ Tau. The stars move in standard Keplerian ellipses given by the first Kepler law (Eq. 1.1), their on-sky positions are the following:

$$\begin{pmatrix} x \\ y \end{pmatrix} = \begin{pmatrix} A & C \\ B & D \end{pmatrix} \begin{pmatrix} x_{\rm E} \\ y_{\rm E} \end{pmatrix}, \tag{3.16}$$

where x is the on-sky position in the east-west direction, y the on-sky position in the north-south direction, $(x_{\rm E}, y_{\rm E})$ the position in the orbital plane given by the following equations:

$$\begin{pmatrix} x_{\rm E} \\ y_{\rm E} \end{pmatrix} = \tilde{a} \begin{pmatrix} \cos E - e \\ \sqrt{1-e^2} \sin E \end{pmatrix}, \tag{3.17}$$

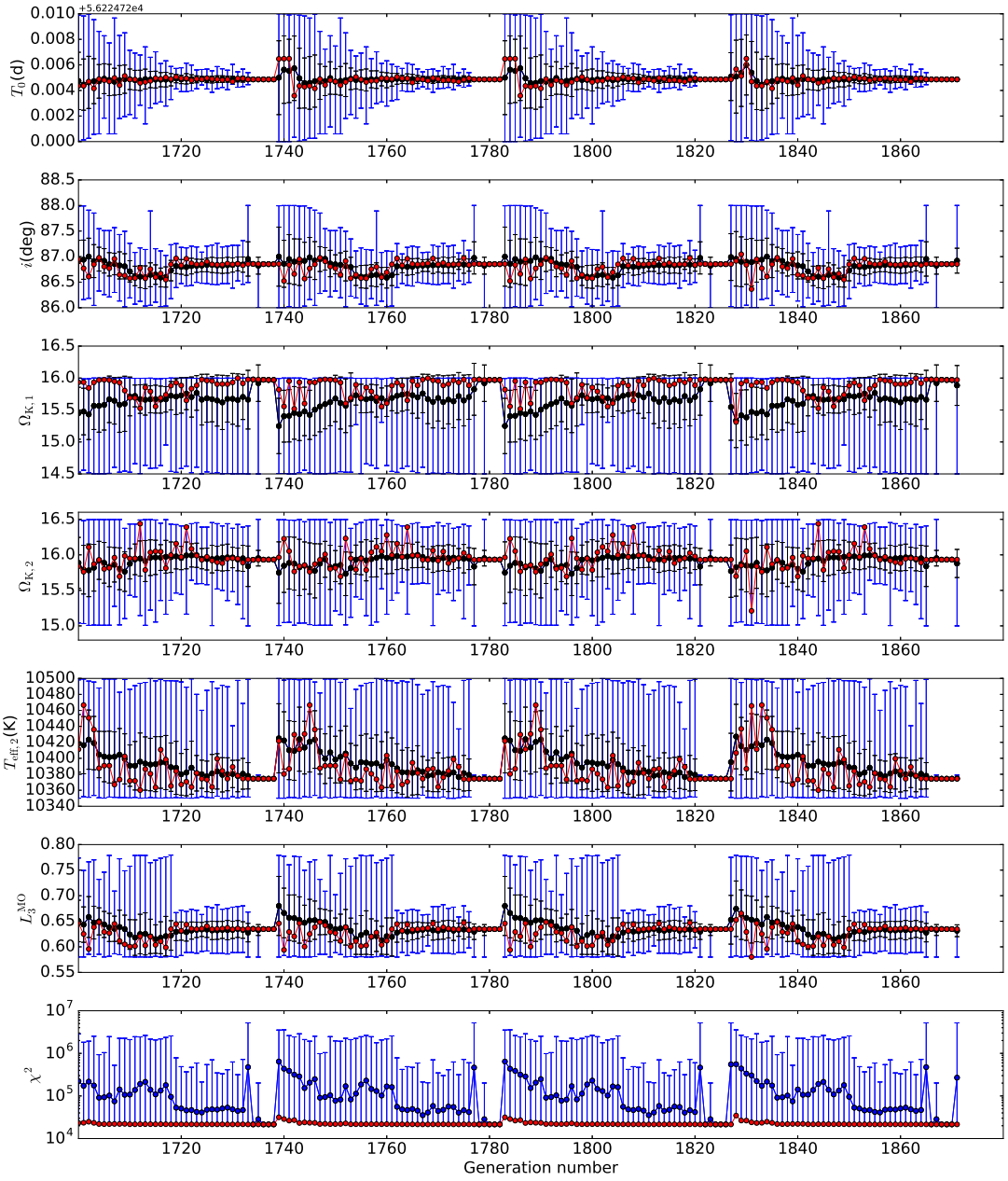

Figure 3.1: Convergence of a genetic algorithm towards a minimum. Light curve of ξ Tau acquired by the satellite MOST was fitted. Each panel represents the evolution of one parameter. Black points represent the mean value in a generation, blue error bars the parameter interval span by the samples in a generation, and red points value for the sample having the least χ^2. The bottom panel shows behaviour of the χ^2. The slow convergence is caused by unrealistically low convergence criterion, and the large fraction of mutations, which prevented the whole generation from degenerating, and also the degeneracy of the task; the mutations were not producing samples "wrong enough" to be immediately removed.

where E is the eccentric anomaly given by the Kepler equation (Eq. 1.3), e the eccentricity, and $\tilde{a}$ the angular semimajor axis. The elements of the transformation matrix are the following:

$$\begin{pmatrix} A \\ B \\ C \\ D \end{pmatrix} = \begin{pmatrix} \cos\omega \sin\Omega + \sin\omega \cos\Omega \cos i \\ \cos\omega \cos\Omega - \sin\omega \sin\Omega \cos i \\ -\sin\omega \sin\Omega + \cos\omega \cos\Omega \cos i \\ -\sin\omega \cos\Omega - \cos\omega \sin\Omega \cos i \end{pmatrix}, \tag{3.18}$$

where ω is the periastron argument, Ω the longitude of the ascending node, and i the inclination. In my model the third component moving in the outer orbit along with the inner binary is placed at the beginning of the reference frame, because the Fourier transform is invariant to the position of the system as whole. Due to significant apsidal motion of the outer orbit in ξ Tau the model contains apsidal motion of both orbits given by Eq. (3.6).

The next step is to represent the components of the hierarchical triple. For ξ Tau uniform disks turned out to be a sufficient representation of its components, because we had insufficient resolution, and all components remained only partially resolved. The complex visibility V for this model is given by the following formula:

$$V(u,v) = \frac{\sum_{j=1}^{3} L_j \frac{2J_1(\pi\theta_j B/\lambda)}{\pi\theta_j B/\lambda} e^{-2\pi i(ux+vy)}}{\sum_{j=1}^{3} L_j}, \tag{3.19}$$

where $(u,v) = (B_x, B_y)/\lambda$ are spatial frequencies, $B = \sqrt{B_x^2 + B_y^2}$ the length of the projected baseline, L the relative luminosity, J_1 the first-order Bessel function, θ the uniform disk radius, and λ the wavelength. This model is implemented within the program *FV*, that I wrote (see Sect. 6.3).

The radiative model is very simple and contains two very strong simplifications: (i) Stellar disks are uniform. — The error introduced by *not* using the limb-darkened disks is $\approx 5\%$ for a A-type/B-type main-sequence star (see Eq. 13 in Davis et al., 2000). (ii) L and θ are constant. — In reality they are both functions of the wavelength λ. Variations of the former will be higher if the two binary components have significantly different effective temperatures. The latter dependence is weak and the difference between V and K diameters is $\approx 5\%$ for a main-sequence star.

In program *FV* the latter assumption is partly circumvented. The user can split the data into subsets and derive separate relative luminosities L for each subset. This approach is efficient only for a small number of such subsets, because each subset introduces $N_\mathrm{C} - 1$ new parameters, where N_C is the number of components. If the observations span long spectral ranges, one should use a more physical radiative model.

The former assumption can be accounted for by introducing the limb-darkening. The complex visibility of a circular limb-darkened disk, resulting from the van Cittert-Zernike theorem (see Eq. 2.17), is the following:

$$V = \frac{\int_0^1 I(\mu)\, J_0\left(x\sqrt{1-\mu^2}\right) \mu \mathrm{d}\mu}{\int_0^1 I(\mu)\, \mu \mathrm{d}\mu}, \tag{3.20}$$

where I is the intensity, μ the cosine of the aspect angle γ, J_0 the zero-order Bessel function, and x is defined as follows:

$$x = \frac{\pi B \theta_\mathrm{LD}}{\lambda}, \tag{3.21}$$

where $B = \sqrt{B_x^2 + B_y^2}$ is the length of the projected baseline, θ_LD the limb-darkened disk diameter, and λ the wavelength.

A model for binaries surrounded with circumstellar matter

The spectro-interferometry can be used to study the distribution of the circumstellar matter in various objects. This task is more difficult than building a hierarchical triple, because the shape and radiative properties of circumstellar matter can be very complicated — even more

in binaries, where the distribution is shaped by the binary potential and/or the dynamical interaction between the mass stream and an accretion disk in semi-detached and over-contact binaries.

The circumstellar matter *can* contribute to both continuum and line flux. The stars themselves *contribute* to the line and continuum flux.

If the observations are numerous enough one can do the imaging and then properties of the studied system can be carried out by the comparison of the resulting image and a model image. The observations of β Lyr are not numerous enough and lack phase measurements, hence the imaging is not possible. Therefore we have to create a model, compute synthetic visibilities for it and compare them to the squared visibility $|V|^2$, differential visibility δV, and differential phase $\delta\phi$. The latter two yield interesting results only for spectral lines. A similar approach was adopted by A. Meilland, who developed a program for modelling of a star surrounded with a disk, which he applied in several studies of Be stars (Meilland et al., 2007, 2011; Stee et al., 2012).

I would like to expand his model to make it applicable to eclipsing binaries surrounded by circumstellar matter (e.g. Algol-type binaries, β Lyr, ...). This is not a simple task, because it has to be constructed in three dimensions (3D) to account for the eclipses and the Roche geometry. The main intensity altering effects — the limb-darkening, and the gravity brightening — have to be included, and the dependence of radiation intensity in spectral lines on RV has to be accounted for.

The program (called *DV*) is being developed mainly for the interpretation of interferometric observables of β Lyr system, but I am trying to make it modular and easily extendable for additional applications in the future.

A preliminary version of the program was presented by Nemravová et al. (2015), but I have not been developing it since then. I will not provide a description of the program in Sect. 6, because the program is still far from being finished, and anything written down will likely be changed. Hence I only outline the program and discuss some possible extensions.

- **The geometric layout:** The playground is a 3D array. The resolution of an object is given by the number of cells at each side and their angular difference. The coordinate system is Cartesian. The line of sight of an observer is parallel to the z-axis. The xy plane is identical to the plane of sky under the assumption of a small field of view (FOV), meaning that $\sin\delta \simeq \delta$ for an angle spanning over the whole FOV. The x-axis is oriented in the east-west direction, and y-axis in the north-south direction.

- **The object:** Each object is represented by the position of its centre x_0, y_0, z_0, Euler angles α, β, γ, and a volume it fills, given its shape. To all cells lying in this volume intensity, opacity, and RV is assigned. Then the object is translated given its centre position, and rotated.

- **The opacity:** The cell opacity is given by the attenuation factor $\gamma \in [0, 1]$, which defines the fraction of the flux coming from neighbouring cell along the line of sight that will be absorbed. For opaque objects $\gamma = 1$, meaning that light can escape only the surface cells. All invisible cells are excluded from a further computation.

- **The intensity:** Currently only a relative intensity can be assigned to an object. This means that flux of a single visible cell l_i will be:

$$l_i = \frac{L}{N}, \tag{3.22}$$

  where L is the relative luminosity, and N the number of visible cells of an object.

- **The velocity:** Each visible cell is assigned a velocity vector $\mathbf{v} = (v_x, v_y, v_z)$ given by the adopted law. Currently two models of the velocity distribution are implemented: (i) the power law, and (ii) the expanding shell. The former is given by the following formulae:

$$|v| = v_0 \left(\frac{r}{r_0}\right)^{\beta}, \tag{3.23}$$

$$\mathbf{v} = |v| \left(-\frac{y}{r}, \frac{x}{r}, 0\right), \tag{3.24}$$

where v_0 is the absolute rotational velocity at the radius r_0, $r = \sqrt{x^2 + y^2}$ the radius, and β the exponent of the power law. Clearly for $\beta = 1$ one has the rigid-body rotation and for $\beta = -1$ the Keplerian rotation. The expanding shell is given by the following formulae:

$$|v| = v_t \frac{r}{r_0}, \tag{3.25}$$

$$\mathbf{v} = |v| \left(-\frac{x}{r}, \frac{y}{r}, \frac{z}{r}\right); r < r_0, \tag{3.26}$$

$$\mathbf{v} = v_t \left(-\frac{x}{r}, \frac{y}{r}, \frac{z}{r}\right); r \geq r_0, \tag{3.27}$$

where v_t is the terminal velocity, which is reached at radius r_0, and $r = \sqrt{x^2 + y^2 + z^2}$. The velocity is rising linearly with the radius until a terminal velocity is reached and then for $r > r_0$ it remains constant.

- **The image:** Each object is build separately. It is first rotated and then placed within the intensity cube, that is common for all objects. The same transformation undergoes the velocity vector $\mathbf{v}$ which is then projected into the direction of the observer $\mathbf{p} = (0, 0, 1)$. Optionally a velocity channel ΔRV can be selected, meaning that all cells whose projected velocity does not lie within ΔRV are excluded from further computation. The 3D cube is then flattened along the direction to the observer, starting with the cells most distant from the observer. The opacity is evaluated along each column. Final product is a 2D image of the system. The scale of the final image is angular. The units is radians.

- **The observables:** A power spectrum of the image is computed using the 2D Fast Fourier Transform (FFT; see James W. Cooley, 1965; Press et al., 2002). The image is zero-padded to increase the sampling of the power spectrum (this does not increase the true resolution - i.e. the ability to resolve two neighbouring frequencies of course). Then the bi-cubic interpolation (see Press et al., 2002, p.136-138) is used to obtain the complex visibility V for a certain spatial frequency $f = (u, v)$ from the power spectrum. The squared visibility modulus $|V|^2$, differential visibility δV, and differential phase $\delta\phi$ can be computed from the complex visibility quite straightforwardly.

A demonstration of the program is given Fig. 3.2. A simple model consisting of an opaque uniform sphere, and a transparent disk is shown for three velocity channels $\Delta RV = [-140; -90]$, $[-24; 24]$, $[90; 140]\,\mathrm{km.s^{-1}}$. The luminosities were assigned by assigning an absorption profile for the sphere and an emission profile for the disk. The joint line profile and the observables $|V|^2$, $\delta\phi$ are also plotted.

Nonetheless the program is still far from being finished, because:

- **The program is slow:** Currently the computation of a single image of the simple toy model from the previous paragraph takes $\approx 10\,\mathrm{s}$ in low resolution — each panel in Fig. 3.2 has 128×128 points. To sample a spectral line, one should compute ≈ 20 images. Hence computations of one simple model takes 3 minutes. This makes automatic fitting of a model very difficult, because for 1000 iterations the whole procedure will take 2.1 d.

- **The radiative model is far too simple:** A more physical model is needed. A relative luminosity is not a satisfactory model for opaque objects and should be replaced by black-body radiation at least. Modelling of transparent parts is even more difficult, because their radiation can not be modelled as a black-body radiation.

- **A binary model is missing:** Roche model for stars, and Keplerian orbit are not implemented.

Hence *the program is not ready* for an application in the analysis of objects with complicated distribution of circumstellar matter such as β Lyr.

3.1.4 The normalised spectra

In Sect. 2.3 I discussed only the measurement of RVs, but a stellar spectrum provides much more information about the studied object. Here I describe a method for the determination of basic radiative properties of binary components from their spectra.

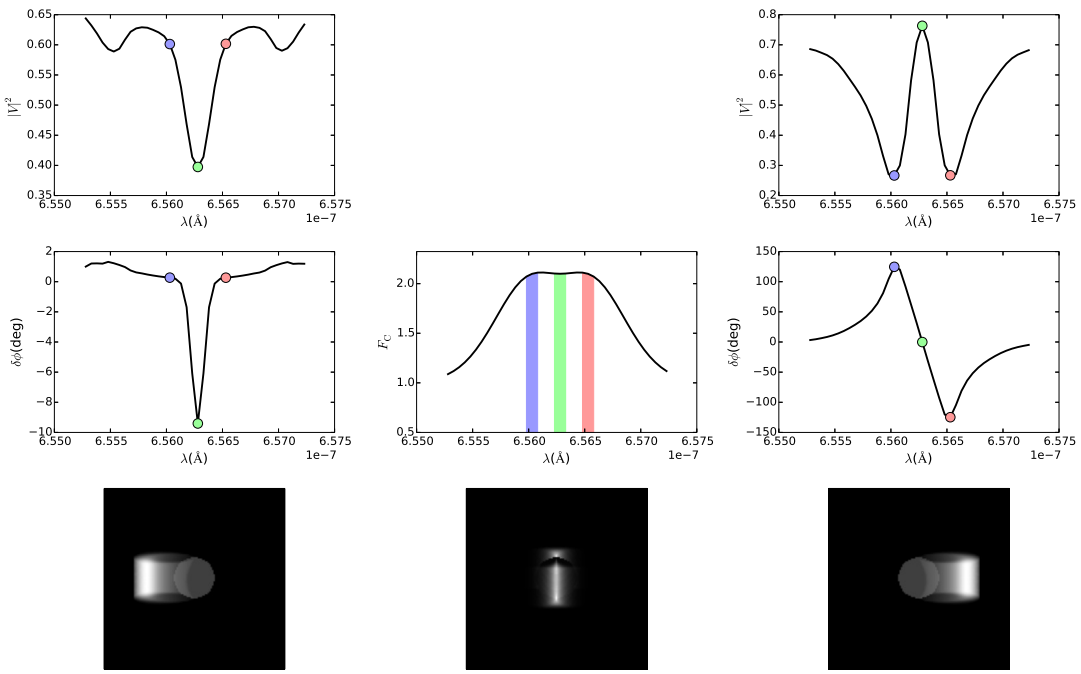

Figure 3.2: A demonstration of the program *DV*. Observables are computed for a simple model consisting of an opaque uniform sphere, whose relative luminosity is given by an absorption profile and a transparent disk, whose relative luminosity is given by an emission profile. Contents of individual panels are the following: *Top-left:* Black line denotes the squared visibility V^2 variations over the spectral line for a baseline oriented in the north-south direction. *Middle-left:* Black line denotes the differential phase $\delta\phi$ variations over the spectral line for a baseline oriented in the north-south direction. *Top-right:* Black line denotes the squared visibility V^2 variations over the spectral line for a baseline oriented in the east-west direction. *Middle-right:* Black line denotes the differential phase $\delta\phi$ variations over the spectral line for a baseline oriented in the east-west direction. *Middle-middle:* A joint line profile of the sphere and the disk. Blue band denotes the velocity channel $\Delta RV = [-140; -90]\,\mathrm{km.s^{-1}}$, green band the velocity channel $\Delta RV = [-24; 24]\,\mathrm{km.s^{-1}}$, and red band the velocity channel $\Delta RV = [90; 140]\,\mathrm{km.s^{-1}}$. *Bottom:* An image of the toy model as it would on the sky appear in the three velocity channels. Left panel corresponds to $\Delta RV = [-140; -90]\,\mathrm{km.s^{-1}}$, middle panel to $\Delta RV = [-24; 24]\,\mathrm{km.s^{-1}}$, and right panel to $\Delta RV = [90; 140]\,\mathrm{km.s^{-1}}$. Big points in the first four panels denote observables for the three velocity channels.

A spectrum of a well-behaved star can be satisfactorily approximated by a synthetic spectrum based on contemporary one-dimensional models of stellar atmospheres. These models depend on a relatively small number of parameters: the effective temperature $T_{\rm eff}$, the gravitational acceleration $\log g$, the metallicity Z, and the micro-turbulent velocity $v_{\rm MIC}$. The spectra are also broadened by various mechanisms. The most common ones are: the rotation $v_{\rm rot}$, and the macro-turbulence characterised by macro-turbulent velocity $v_{\rm MAC}$. A brief description of the parameters is given Sect. 2.1.2. A well-behaved star does not pulsate, has no spots, or strong magnetic fields, is not significantly deformed by either the rotation, or the presence of a companion, is not surrounded by any circumstellar matter, and is not evolved beyond the giant branch. A spectrum of a stellar misfit falling into one of the above-mentioned categories requires either a better atmospheric model or a better model of surface kinematics.

I have written a Python program (called *Pyterpol*), which interpolates in a pre-calculated grid of synthetic spectra and compares them to observed and/or disentangled ones to estimate parameters listed in the previous paragraph (or their subset). The search for the best-fitting model is carried out by minimisation of χ^2. *Pyterpol* is publicly available at `https://github.com/chrysante87/pyterpol`. Description of the program, its installation, basic tutorial, and demonstrations are at `https://github.com/chrysante87/pyterpol/wiki`.

The interpolation in a grid of synthetic spectra

Computation of a full-fledged one-dimensional model of a stellar atmosphere (including maximal possible number of species and their transitions) and the consecutive derivation of a synthetic spectrum still takes hours or even days. A simple minimisation routine such as simplex (Nelder and Mead, 1965) evaluates the χ^2 $10^2 - 10^3$ times before it converges. Hence it would be impossible to carry out fitting if a new atmospheric model was computed every time the routine evaluates the χ^2. Therefore I interpolate in a pre-computed rectangular grids of *normalised* synthetic spectra instead. Currently I am interpolating in four rectangular grids of synthetic spectra[2]:

- AMBRE (de Laverny et al., 2012) for effective temperatures from 4000 K to 8000 K.
- POLLUX (Palacios et al., 2010) for effective temperatures from 8000 K to 15000 K.
- BSTAR (Lanz and Hubený, 2007) for effective temperatures from 15000 K to 30000 K.
- OSTAR (Lanz and Hubený, 2003) for effective temperatures from 30000 K to 55000 K.

Each synthetic spectrum is characterised by a gravitational acceleration, metallicity and a micro-turbulent velocity. The step and range of values covered by each parameter differs from grid to grid, and for OSTAR and BSTAR grids it even differs from one effective temperature to another one. The parametric space covered by the grids *implemented* in the program *Pyterpol* is shown in Fig. 3.3. It is not as wide as the listed grids of synthetic spectra. This negligence is caused by a very difficult handling of grids in the old version of *Pyterpol*. This has been resolved in the new version and I plan to implement all spectra from listed grids.

The interpolation in the grid is carried out as a series of consecutive one-dimensional interpolations in one parameter (see Press et al., 2002, p.118-124). To illustrated it — say one wants to interpolate the relative intensity I linearly at $I\left(T_{\rm eff}, \log g\right) = I\left(10500, 3.8\right)$: The linear interpolation is the simplest method and requires only two points surrounding the value at which one interpolates. Therefore the program finds the smallest square, whose vertices surround the point at which we interpolate, e.g. $I\left(10000, 3.5\right)$, $I\left(10000, 4.0\right)$, $I\left(11000, 3.5\right)$, and $I\left(11000, 4.0\right)$. The program interpolates in the former two vertices in the gravitational acceleration to obtain $I\left(10000, 3.8\right)$, and in the latter two vertices to obtain $I\left(11000, 3.8\right)$. Then it interpolates in these two new points in the effective temperature to obtain $I\left(10500, 3.8\right)$. The algorithm is the same for more parameters and higher order interpolation methods. All grids that I implemented within *Pyterpol* have the same sampling in the wavelength (currently 0.01 Å) hence it is not necessary to interpolate in it as well. Even if they did not have the same sampling, the program changes the sampling of each spectrum before starting the interpolation.

[2] Although the authors of the listed grids of synthetic spectra made them publicly available, I do not have their consent to distribute them along with my code. Therefore the database is not available for download anywhere.

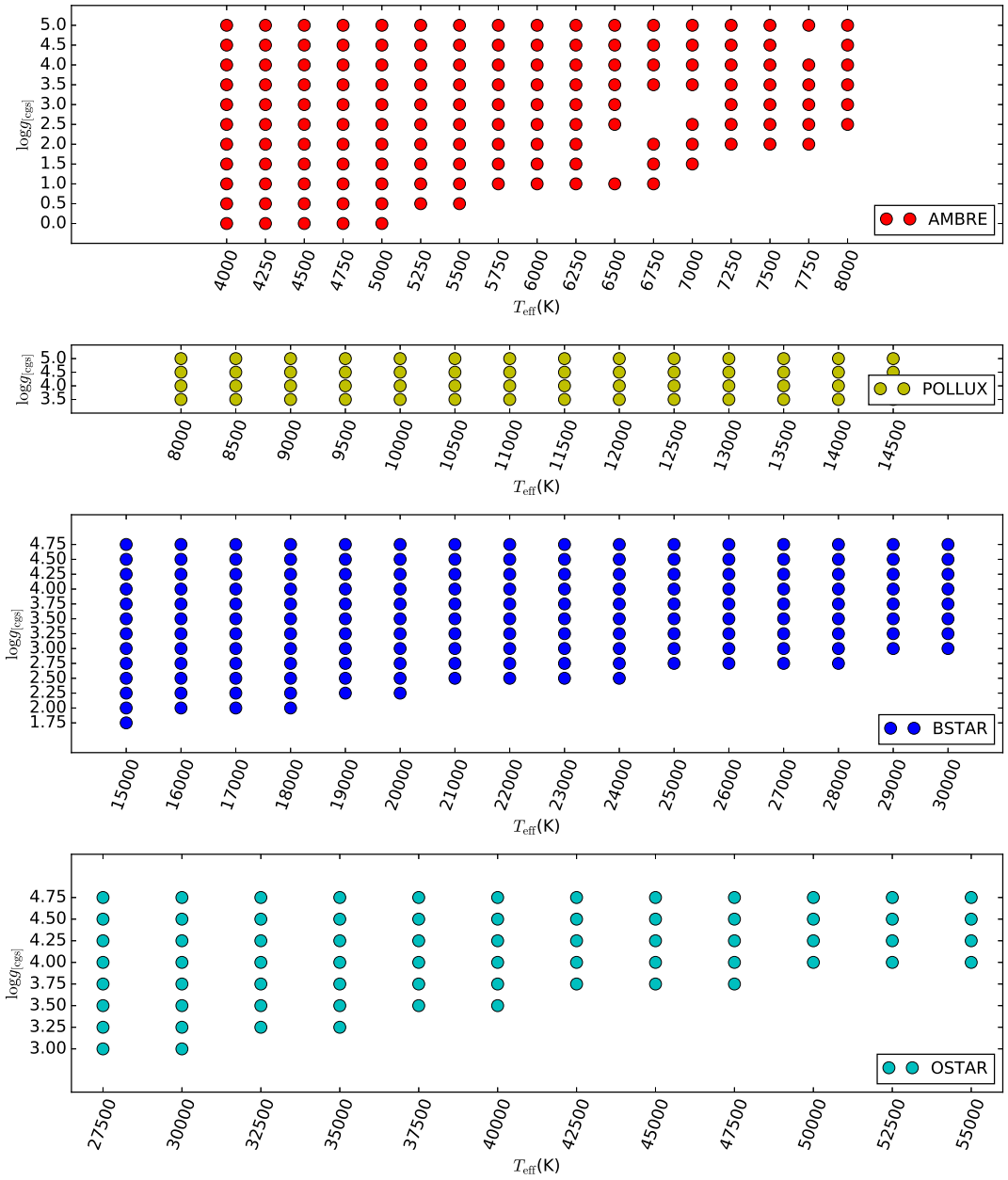

Figure 3.3: The coverage of the parametric space ($T_{\rm eff} \times \log g$) with the grids of synthetic spectra, that are implemented within *Pyterpol*. *The first panel* (starting from top): The coverage with spectra from the grid AMBRE developed by de Laverny et al. (2012). Only the solar metallicity is implemented and the micro-turbulent velocity $v_{\rm MIC} = 1\,{\rm km.s^{-1}}$ for $\log g > 3.0$, and $v_{\rm MIC} = 2\,{\rm km.s^{-1}}$ for $\log g \leq 3.0$. The grid AMBRE was computed for several values of the metallicity and even several values of α-enhancement. *The second panel*: The coverage with the synthetic spectra from the grid POLLUX developed by Palacios et al. (2010). Only solar metallicity and micro-turbulent velocity $v_{\rm MIC} = 2\,{\rm km.s^{-1}}$ is implemented within the program, but POLLUX grid also extends to metal-poor stars. *The third panel*: The coverage of synthetic spectra from the grid BSTAR developed by Lanz and Hubený (2003). Three metallicities are implemented in *Pyterpol* — $Z \in \{0.5, 1.0, 2.0\}\, Z_{\odot}$. The micro-turbulent velocity is $v_{\rm MIC} = 2\,{\rm km.s^{-1}}$ for all of them. The grid BSTAR is also available for lower metallicities, and one additional micro-turbulent velocity $v_{\rm MIC} = 10\,{\rm km.s^{-1}}$. *The fourth panel*: The coverage of synthetic spectra from the grid OSTAR developed by Lanz and Hubený (2007). Three metallicities are implemented in *Pyterpol* — $Z \in \{0.5, 1.0, 2.0\}\, Z_{\odot}$. The micro-turbulent velocity is $v_{\rm MIC} = 10\,{\rm km.s^{-1}}$ for all of them. The grid OSTAR is also available for lower metallicities.

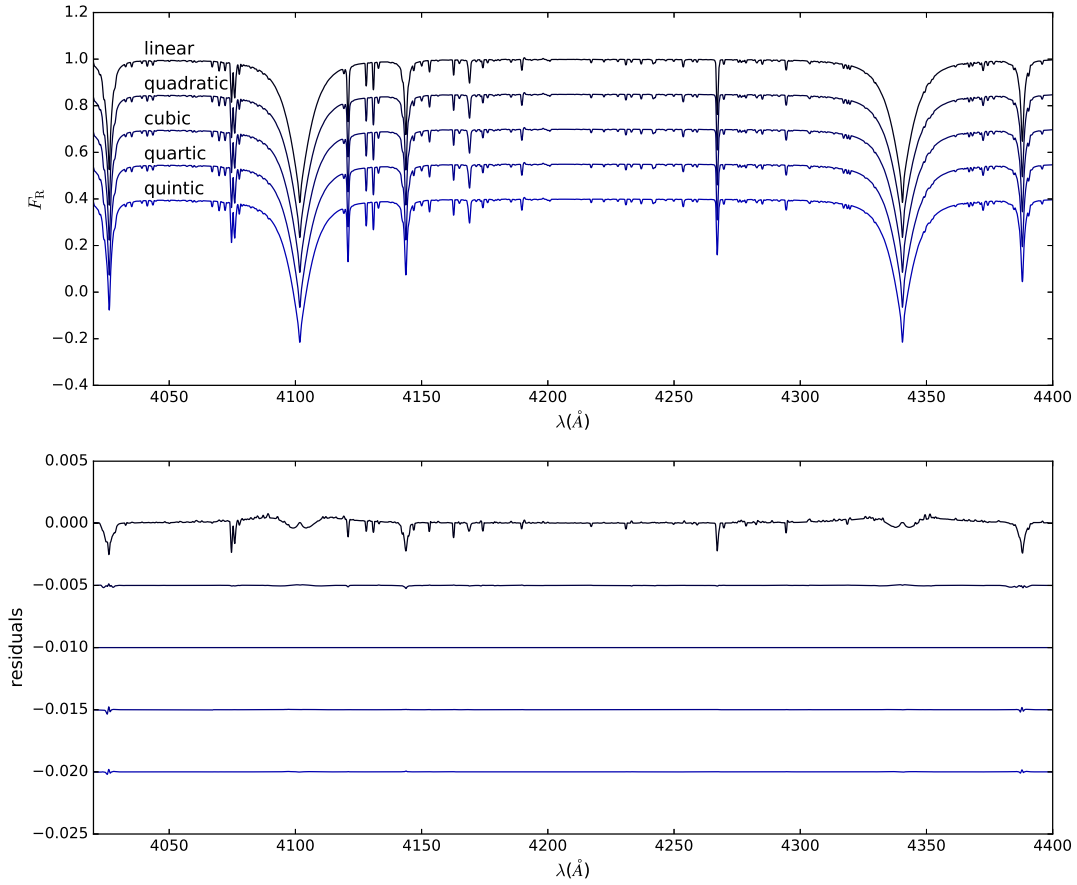

Figure 3.4: A comparison of synthetic spectra produced with *Pyterpol* using different order of the interpolation. The *upper panel* shows interpolated and normalised spectra for the following parameters: $T_{\rm eff} = 18250\,{\rm K}$, $\log g = 4.1$, $Z = 0.8\,Z_\odot$, $L_{\rm R} = 1$, $v_{\rm MIC} = 2\,{\rm km.s^{-1}}$, $v \sin i = 50\,{\rm km.s^{-1}}$, and $RV = 0\,{\rm km.s^{-1}}$. The interpolation order is given above each spectrum. The spectra were shifted with respect of each other in the relative flux $F_{\rm R}$ for better clarity of the plot. The *lower panel* shows the difference between the spectra from the upper panel and an interpolated spectrum produced with a cubic spline interpolation. Clearly the largest differences arise for the linear interpolation.

User is allowed to set the number of points N that will be used for each one-dimensional interpolation. This controls which interpolation algorithm will be used: $N = 2$ = linear interpolation, $N = 3$ = quadratic interpolation, $4 \leq N \leq 6$ = cubic spline interpolation, $N \geq 6$ = quintic spline interpolation. Fig. 3.4 shows an interpolated spectrum for the different orders of the interpolation and how much they differ from the cubic spline interpolation. The difference is the greatest for the linear interpolation. That is not surprising, because this method uses the bare minimum to estimate the shape of the function $I\,(T_{\rm eff}, \log g, Z, \dots)$ It also shows that already a cubic spline (even quadratic) estimates the shape of the relative intensity as a function of radiative properties very satisfactorily.

The post-processing of the interpolated spectrum

Before I compare an interpolated spectrum to an observed one, it is necessary to account for the broadening effects (rotational and instrumental), weigh each spectrum by its flux fraction, and shift it to the corresponding RV.

An interpolated spectrum I is first convolved with a Gaussian function. Its FWHM is the same as the resolution of the instrument which recorded the fitted observed spectrum. The

convolution is given by the following formula:

$$I_{\mathrm{I}} = \frac{1}{\sigma\sqrt{2\pi}} \int_{\mathbb{R}} I\left(x-y\right) \exp\left(-\frac{y^2}{2\sigma^2}\right) \mathrm{d}y, \tag{3.28}$$

where x, y are the wavelengths, and σ the standard deviation of the Gaussian. The relation between the FWHM and σ is $FWHM = 2\sqrt{2\ln 2}\sigma$. The spectrum I_{I} is then convolved with the rotational profile

$$I_{\mathrm{IB}} = \frac{\int_{\mathbb{R}} I_{\mathrm{I}}\left(x-y\right) K\left(y\right) \mathrm{d}y}{\int_{\mathbb{R}} K\left(y\right) \mathrm{d}y}, \tag{3.29}$$

where x, y are RVs, and K the rotational kernel defined by the following formula:

$$K\left(y\right) = \frac{2\left(1-\epsilon\right)\sqrt{1-\left(\frac{y}{v\sin i}\right)^2} + \frac{1}{2}\pi\epsilon\left[1-\left(\frac{y}{v\sin i}\right)^2\right]}{\pi v \sin i \left(1-\frac{\epsilon}{3}\right)}, \tag{3.30}$$

where $v \sin i$ is the projected rotational velocity, and ϵ the coefficient of the linear limb-darkening law. Then the spectrum is weighed by its relative luminosity $L\left(\lambda\right)$

$$I_{\mathrm{IBL}} = I_{\mathrm{IB}}\left(\lambda\right) L\left(\lambda\right). \tag{3.31}$$

The relative luminosity is a continuous function of the wavelength, but in *Pyterpol* it is set constant over a spectral range $\Delta\lambda$. Hence *the user has to choose the intervals short enough* for the variations of the relative luminosity to be negligible. Finally, each point of the spectrum is shifted in wavelength. This shift is given by its RV (see Eq. 2.33).

The procedure described in this section is repeated for every component of a binary and then the component spectra are summed. The composite spectrum is compared to an observed one. *Pyterpol* is able to fit the synthetic spectra to observed one by minimising the following χ^2:

$$\chi^2 = \sum_{i=1}^{N_{\mathrm{S}}} \left(\sum_{j=1}^{N} \frac{I_{\mathrm{OBS},i,j} - \sum_{k=1}^{N_{\mathrm{C}}} I_{\mathrm{IBLS},i,j,k}}{\sigma_{i,j}} \right)^2, \tag{3.32}$$

where I_{OBS} is the observed normalised spectrum I_{IBLS} is an interpolated spectrum, broadened by the instrumental and rotational profiles, weighed by the luminosity fraction and shifted according to its RV of k-th component of the studied binary, N_{C} the number of components of the system, N the number of points of the i-th observed digitised spectrum, N_{S} the number of observed spectra. σ is the uncertainty of the observed relative intensity.

Applications of the technique

The technique has been used in several studies, that I co-authored during my doctoral study. The program *Pyterpol* is an evolution of a C++ program, that I started writing during my master study. The program contained a similar model as *Pyterpol* (only instrumental broadening was not included), but was very cumbersome, that is why I re-wrote it in Python. A brief description of the original C++ program was published in the study of the triple system HD 152246 by Nasseri et al. (2014).

The C++ version of the program was used in several studies. In all these applications, the program was used to determine the effective temperature T_{eff}, gravitational acceleration $\log g$, and projected rotational velocity $v \sin i$ of components of the studied multiple systems. Ability to fit the metallicity Z was added later and hence applied only in one study. The applications[3] of the *old version* of the program were the following:

(i) The first application of the technique was in the study of an F0 Iae eclipsing binary with a dark disk ϵ Aur by Guinan et al. (2012). Here it was used to estimate effective temperatures of multiple systems lying within 2 deg × 2 deg square surrounding ϵ Aur. The effective temperatures of their components were further used to infer the distance of these objects, which was used to derive a calibration between the distance and central intensity of a few interstellar lines. This relation was then applied to estimate the distance of ϵ Aur.

[3] The C++ version of the program was very difficult to handle, so I remained its only user. Hence I carried out the analyses of objects listed in this section.

(ii) The second application was in the study of an eclipsing binary Y Cyg containing pair of two massive O9.5V by Harmanec et al. (2014). The program was used to estimate the effective temperatures of both components by fitting of the disentangled spectra.

(iii) The third application was in the study of a compact hierarchical triple system HD 152246 by Nasseri et al. (2014). The program was used to determine the effective temperature $T_{\rm eff}$, gravitational acceleration $\log g$, and projected rotational velocity $v \sin i$ of one component of the inner orbit and the tertiary. In this study, my results were independently verified by a similar program (compare Tabs. 7 and 8 in Nasseri et al., 2014) that uses the FASTWIND model atmosphere to obtain spectra and genetic algorithms to optimise its parameters (see Mokiem et al., 2005, for description of the program). The disagreement in the effective temperature between the models is very likely caused by the different atmospheric model. The FASTWIND model atmosphere contains hydrogen and helium only, while my fit was based on the grid OSTAR that was computed using plane-parallel non-LTE atmospheric models including the metal-line blanketing.

(iv) The fourth application was in the study of a semi-detached binary undergoing a mass transfer phase BR CMi by Harmanec et al. (2015). The binary is ellipsoidal only. We applied the program to determine the effective temperatures of both components by fitting the disentangled spectra. The resulting values were used in the light curve model to remove indeterminacy in the effective temperature $T_{\rm eff}$, Kopal potential $\Omega_{\rm K}$, mass ratio q, and inclination i, which has been already discussed in Sect. 3.1.2. I argued that the uncertainty estimates of the solution presented in Table 6 of Harmanec et al. (2015) are very severely underestimated in Sect. 2.3.3.

(v) The fifth application was in the study of an eclipsing binary, and a possible member of the putative δ Lyr cluster BD+36 3317 by Kıran et al. (2016). Here the program was used to estimate properties of both components by fitting of the disentangled spectra. The primary effective temperature was used to reduce the parametric space of the light curve model and reduce the degeneracy of the inverse problem.

(vi) The last application of the old program (although there is a reference to the new version in the paper) was in the study of an eclipsing binary with an apsidal motion V346 Cen by Mayer et al. (2016, accepted in A&A). The program was used to estimate properties of both binary components by fitting the disentangled spectra. Interestingly the secondary temperature was very inconsistent with the light curve solution. In the study the authors explained this discrepancy with an under-abundance of the oxygen in the secondary (see Fig. 6 in Mayer et al. 2016, accepted in A&A).

The analyses listed here suffered from two problems: The fitted spectra were not properly weighed given their SNR, and that mostly disentangled spectra were fitted. The former discrepancy caused that the formal χ^2 represented by Eq. (3.32) had no statistical meaning. Also if there were more regions fitted, this incorrect weighing probably caused that the minimum of the χ^2 moved slightly of the correct solution. The dangers resulting from the use of disentangled spectra are discussed in the next section.

On the use of disentangled spectra

The spectra produced by the disentangling are often warped. Degree of this warp depends on the quality and number of the observed spectra, but it is usually quite complicated and has to be removed manually, e.g. by fitting the continua with a convenient smooth function (I use a Hermite cubic spline). This approach changes line depths and their positions, hence introduces a systematic effect, whose quantification is very difficult. Another problem is that the observed spectra separated with the disentangling often do not come from the same instrument and are affected by a different instrumental profile. Then the disentangled spectra have a hybrid instrumental broadening, which is very hard to estimate. This becomes a problem especially when one is determining properties of a slowly rotating star. The disentangled spectra have very high SNR that is proportional to the total signal in all observed spectra. This SNR puts unrealistic demands on the re-normalisation causing that the reduced χ^2 (a χ^2 divided by the degrees of freedom) is too high and from a statistical point of view one should reject the synthetic spectrum as a completely wrong model. These problems were not admitted in any of

the studies listed in the previous paragraph — we actually did not present the χ^2 at all — but they are illustrated well in Nemravová et al. (2016) in Sects. 3.4, and 3.5.

In that study the new version of the program *Pyterpol* was used. One of the main features of this new version is its ability to fit a large number of observed spectra simultaneously. First I fitted 137 observed spectra of ξ Tau to estimate radiative properties, rotational broadening and RVs of its components. The synthetic spectra fitted the observed spectra very well, with the reduced chi-square close to one ($\chi^2_{\rm R} = 0.87$). Then I fitted disentangled spectra that were based on a similar set of observations. The credibility of the fit is lowered by two problems: (i) The unrealistic reduced chi-square $\chi^2_{\rm R} = 31.58$, and (ii) the sum of luminosity fractions was not equal to one. Clearly the use of the disentangled spectra introduced a systematic effect that was not present in observed spectra — a systematic effect that was not removed by the re-normalisation of disentangled spectra, because the parameters corresponding to the best fit of the disentangled spectra does not agree within error bars with the best-fit of the observed spectra (compare Tables 7 and 8 in Nemravová et al., 2016). The disentangled spectra of ξ Tau before and after re-normalisation and the best-fitting synthetic spectra are shown in Fig. 3.5.

Final remark to conclude this section, one should always be cautious when using disentangled spectra to infer properties of a studied system by comparing them to synthetic spectra. Ideally he or she should verify the results by fitting directly the observed spectra.

Caveats of the method

One should be always aware of the limits of the implemented model represented by the synthetic spectra and the simple broadening model.

Almost every spectrum will contain a signal, that will necessarily increase the χ^2, because the implemented model is unable to account for it, e.g. errors in the reduction (especially normalisation of observed spectra), telluric spectrum, interstellar lines, cosmics, ... One should always try to avoid fitting spectral regions affected by the above mentioned and other similar effects. If it is not possible, then it is necessary to evaluate their effect on the final solution.

A similar situation is when one uses the model for objects, for which the model is not sufficient. Here it is often even harder to evaluate the systematic effect of the phenomenon not included in the model on the final fit.

3.2 Models comparable to two or more types of observations

None of the models, which I have created is applicable to more than one type of observation. The only exception is the program for interpretation of interferometric fringe visibility $|V|^2$ together with the closure phase $T_3\phi$. In this section, I will briefly discuss general advantages and disadvantages of models applicable to more types of observables and list programs using such models.

Advantages and disadvantages of models applicable to more observation types

The advantages are the following:

+ **More advanced physics:** These models are usually physically more consistent and account for effects that are beyond reach of the simple (semi-)analytic models. For example: the *PHOEBE 1.0/WD* model of the light curve also includes a RV-curve model, which combines the RV of each component given by the motion on a Keplerian ellipse (given by Eq. 3.1) with the distribution of RV over the surfaces of both components and their projection into the line of sight. Hence it is able to consistently model the effects of inhomogeneous brightness distribution over the stellar surface or the Rossiter-McLaughlin effect, which is beyond the reach of the model presented in Sect. 3.1.1.

+ **Better estimation of model parameters:** Sect. 3.1 shows that parameter sets of models comparable only to one type of observations partially overlap. Generally a common parameter can be better constrained by one type of observable than by another. If "observation-specific" models are used, than an usual approach is to take the parameter value from the

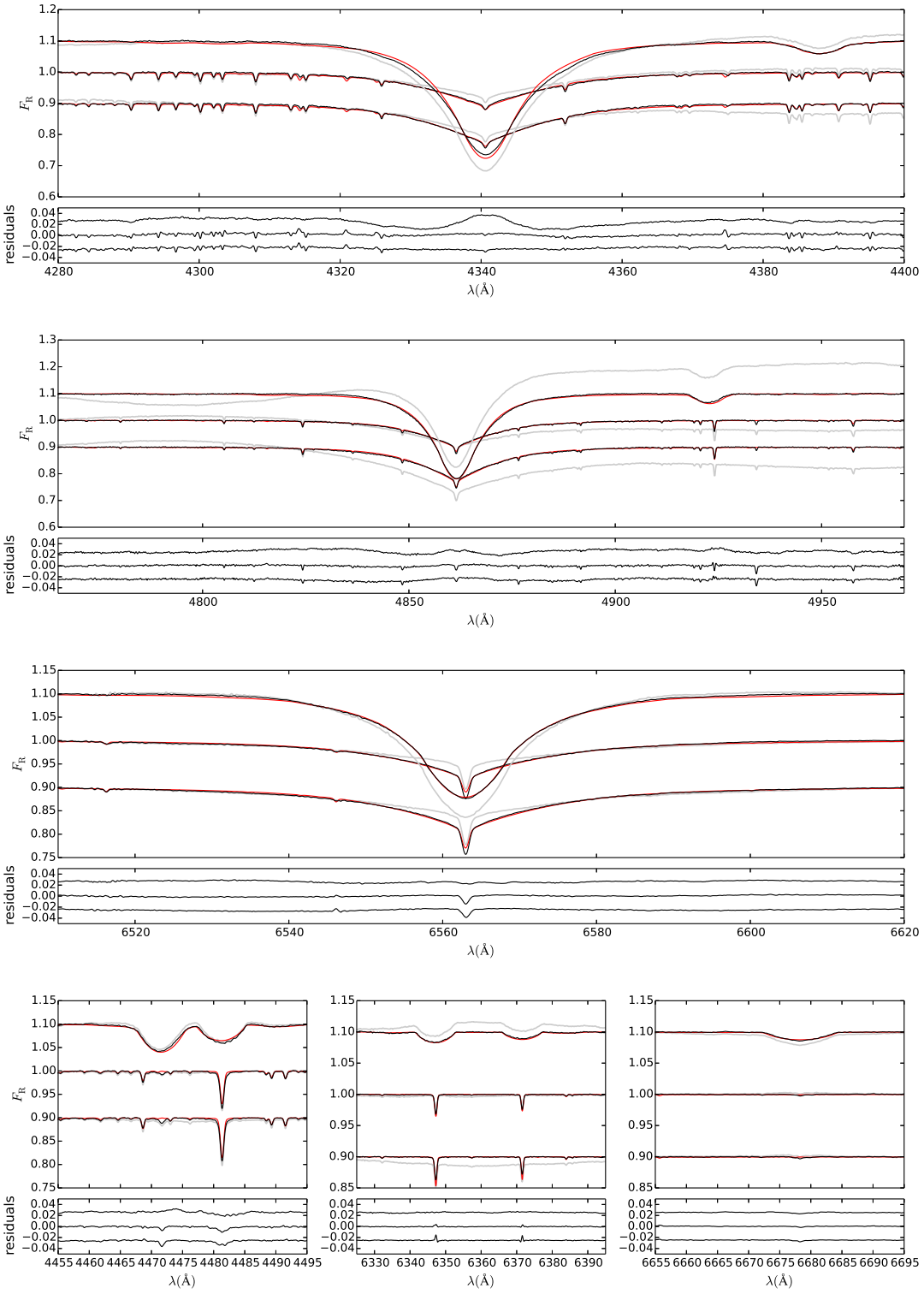

Figure 3.5: A comparison of disentangled and re-normalised disentangled spectra of the ξ Tau system, and synthetic spectra, which represent the best fit to the re-normalised disentangled spectra. Disentangled spectra are shown with the grey line, re-normalised disentangled spectra with the black line, and the synthetic spectra with the red line. The order of spectra in each panel is the following *top* component B, *middle* component Aa, and *bottom* component Ab. The notation of components is explained in Chapter 4. Below each panel there is a difference between the re-normalised disentangled spectrum and the best-fitting synthetic spectrum. The parameters defining the synthetic spectra are in Table 7 in Nemravová et al. (2016).

model, whose observable constrains the parameter better and fix it for another. For example: The periastron argument ω and eccentricity e are constrained by both RV and LC curves, but its determination is unambiguous for RV-curve only, while for $\omega \to k\pi, k \in \mathbb{Z}$ the eccentricity and also ω become ambiguous. If the parameters are taken from the RV-curve solution and fixed for the light-curve solution, the information held by the light curve is thrown away.

+ **Better error estimates:** If one is able to fit all model parameters together, the χ^2 minimisation routine can "explore" degeneracy of parametric space and correlations between individual parameters. Using an "observation-specific" model often requires that the user fixes one or more parameters and hence reduces the parametric space explored by a minimisation routine. This selection affects the shape of the χ^2 metric, but it is often forgotten that also the fixed value has an uncertainty. If it is not taken into account the uncertainties of the optimised parameters will be underestimated. A correct approach would be similar to that adopted for the measuring of RVs of ξ Tau using comparison of synthetic and observed spectra. There I have repeatedly carried out the fitting using synthetic spectra, whose parameters were randomly drawn from their posterior probability distribution approximated with the normal distribution (see Sect. 3.1 in Nemravová et al., 2016).

The disadvantages are the following:

- **Computational demands:** A model comparable to more types of observations is usually more complicated. One is often forced to partially (or fully) drop analytic formulas and use numerical models (e.g. 3D model of a star), or interpolate in pre-calculated tables (e.g. limb-darkening tables), or integrate differential equation (e.g. solving radiative transfer in a stellar atmosphere). The forward problem (i.e. creation of a model and computation of the observables) will be then more computationally demanding than a simple model

- **Difficult inverse task:** A model comparable to more observation types more likely relies on a larger number of parameters. A convergence time of a χ^2 minimisation routine is proportional to the number of fitted parameters. More complicated models are more likely numerical, hence one is forced to use methods that only evaluate χ^2 to find its minimum. Also an increased number of parameters increases the number of local minima, which can mislead the minimisation routine. Hence one is obliged to use a global minimisation method, whose computation time demands are higher than those of a local minimisation technique. This coupled with the first item may pose an impasse if the computation of χ^2 takes too much time.

- **Need for careful χ^2 analysis:** With several datasets one is obliged to evaluate contribution of each dataset to the total χ^2. This is so especially when the observation uncertainties are underestimated, or even worse — a dataset is affected by an unforeseen systematic errors. The former problem causes that χ^2 will prefer solutions that are in agreement with the dataset having underestimated errors. Unaccounted systematic errors mean that we have again underestimated the error of an observation set, but this time there is a signal, that we are not modelling properly and hence the affected dataset will drag the solution out of the correct one. This can be overlooked if the disagreement between datasets unaffected by systematics and those affected by systematics and the final model is not serious (χ^2_{R} is not very different from one). Then the researcher might neglect it as an error underestimation. This problem can be revealed by a bootstrap method (Efron, 1979), or by using the "observation-specific" methods as an independent check, because being independent, they would likely reveal a discrepancy between different types of data.

Illustration of the pros and cons on a quadruple system ξ Tau

These problems are illustrated by our analysis of the quadruple stellar system ξ Tau (see Chapter 4 for an overview of my research of this system and Nemravová et al., 2016).

In the study we used two methods to investigate the system. A set of (semi-)analytic "observation-specific" models mostly developed by me, and a complex N-body model developed able to produce RVs, astrometric positions, eclipse durations, eclipse minima timings, squared visibility moduli, and closure phases.

Although the two models work with two different kinds of orbital elements — mean (my models), and osculating (Dr. Brož's model) — their relatively fluent secular variations in case of ξ Tau allow their comparison. The N-body model combines overall information on the orbits, while the resulting orbital elements from my models are compared against each other and the most precise estimate is chosen. Hence the values and error estimates provided by N-body model are likely better.

Also the best solution obtained by the N-body model suffered from almost null ambiguities. The only orbital parameter that remained ambiguous in this model was the inclination of the outermost orbit i_3 (see Table 17 in Nemravová et al., 2016). Note that in case of the "observation-specific" models we sometimes had to constrain or directly fix a parameter using another model based on a different observable to force convergence to a plausible solution.

Although it was not that necessary in case of ξ Tau, because the "observation-specific" models provided a solid starting point for the N-body model we still carried out an extensive search of the parametric space by running a local minimisation technique from different starting points. The total number of fitted parameters was 23 and we computed $\simeq 10^7$ trials to exclude the possibility that we ended up in a local, not the global minimum. Degeneracy of the inverse problem is partially illustrated by a χ^2 map Fig. 10 in Nemravová et al. (2016). I say "partially" because the 1-d maps are often misleading because they show nothing about correlations of the displayed parameter with each other or the remaining parameters.

A demonstration, of how important is a complex analysis of contribution of individual datasets to the total χ^2, is the following. The N-body model provided and unexpected insight into orbital properties of ξ Tau. It is represented by Fig. 12 in Nemravová et al. (2016). There is a comparison between measured light curve minima timings and those predicted by the N-body model for two values of the longitude of the ascending node Ω of the innermost orbit shifted by 180 deg with respect to each other. Clearly only the solution $\Omega = 331$ deg is correct. Nonetheless the minima timings is the least numerous dataset and this could be overlooked, if only overall χ^2 was studied, because it would not increase significantly given that the remaining datasets were dominating (by factors 10 to 20).

4. A quadruple system ξ Tauri

In this chapter I summarise the analysis of the ξ Tau system, first a short introduction and then the results of a detailed investigation of the system, which has been published in a preliminary study by Nemravová et al. (2013) (N2013 hereafter), and a complex study by Nemravová et al. (2016) (N2016 hereafter).

4.1 Introduction of the ξ Tau system

ξ Tau is a bright ($V = 3.72$ mag) quadruple hierarchical system. The hierarchy is organised as follows: The inner orbit consists of a pair of eclipsing A0/B9 V type stars revolving around a common centre of gravity with a period 7.14664 d. The depth of the minima in Johnson V band is ≈ 0.1 mag. Components of the inner binary (labelled 1) are denoted Aa and Ab. The outer orbit (labelled 2) consists of the eclipsing pair and a B6/B5 V type star (denoted B). Its orbital period is 145.11 d. Component B is a rapid rotator and is probably responsible for the photometric micro-variability of the system with an amplitude of ≈ 0.0006 mag. The outermost orbit (labelled 3) consists of the close triple subsystem and a F V type star (denoted C), which is the least massive and the least luminous member of the system. Its orbital period is 51 yr. Properties of component C are uncertain, since it was only detected with speckle-interferometry and Hipparcos astrometry and its spectrum was not observed.

The notation of orbits and components of ξ Tau used here is identical to that used in N2016.

Figure 4.1 shows a sketch of the system as it would appear on the sky at epoch RJD = 56224.724705. Orbital elements of all orbits of ξ Tau are in Table 4.1 and properties of its components are in Table 4.2. The values listed in those two Tables represent our original results based on analyses that are outlined in Sects. 4.2.3 and 4.2.4.

The brightness of the object and comparable relative luminosities of its components, their orbital properties and the distance to the system $\pi = 15.60 \pm 1.04$ mas (van Leeuwen, 2007) make it an excellent target for contemporary optical (spectro)-interferometers. This, combined with the presence of an eclipsing subsystem, provides a unique opportunity to infer properties of the system with different techniques and critically confront them against each other. The accurate properties of the system make it a unique test-bed for models of binary formation and evolution and models of stellar evolution.

4.1.1 Historical overview

Multiplicity of ξ Tau was first discovered by Campbell (1909), who detected its RV variations. The orbit 3 was first resolved by Mason et al. (1999). Later, eight speckle-interferometric observations were analysed by Rica Romero (2010) who derived an astrometric orbit and inferred the total mass of the system. The properties of the compact triple subsystem of ξ Tau were first mentioned in Fekel (1981). They were based on the analyses of photographic plates acquired at the David Dunlap Observatory (DDO) by Dr. C.T. Bolton. Orbital elements of orbits 1 and 2 were first published in the catalogue by Tokovinin (1997). An abstract by Bolton and Grunhut (2007) lists accurate periods of orbits 1, and 2, and masses of components Aa, Ab, and B, but their estimate of the orbital inclination of orbit 2 is incorrect. Their results were based on long series of electronic and photographic spectra from the David Dunlap Observatory, and additional photographic plates from Lick and Perkins observatories. Authors also investigated the Hipparcos photometry of ξ Tau and noted that components of orbit 1 undergo mutual eclipses. Unfortunately the analysis standing behind their abstract has never been published in detail.

4.1.2 Preliminary study of ξ Tau

The first detailed study dedicated to this object by Nemravová et al. (2013) was a precursor to N2016, and much of the work presented in N2013 was refined in N2016. The study was based on series of spectroscopic, photometric, and spectro-photometric observations from CHARA/VEGA (ten Brummelaar et al., 2005; Mourard et al., 2009), and NPOI (Armstrong et al., 1998).

Table 4.1: The orbital elements of all three hierarchical orbits of ξ Tau. The results presented here are based on (semi-)analytic "observation-specific" models (see Sect. 4.2.3 and Table 14 in N2016). Hence these elements listed here should be taken as the mean ones. For a list of osculating elements inferred for a certain epoch with the N-body model see Table 15 in N2016. The parametric space of different "observation-specific" methods overlap – only the best estimate is listed here. See Table 12 in N2016 for a full list of results based on all "observation-specific" models. Nonetheless one result from the N-body model is adopted here — The sense of the motion of orbit 1 with respect to orbit 2 which was determined by the N-body model. — The elements given here are: a the semi-major axis, e the eccentricity, i the inclination, ω the periastron argument, $\dot{\omega}$ the apsidal advance given by Eq. (3.6), Ω the longitude of the ascending node, $T_{\rm p}$ the periastron epoch, $P_{\rm A}$ the anomalistic period — note that anomalistic period is equal to sidereal period for $\dot{\omega} = 0.0\,\mathrm{deg\,yr^{-1}}$, π the parallax of the system, γ the systemic velocity. [1]The element was kept fixed throughout the analyses. [2]A mirror solution $i_3 = -25.4$ is viable and has the same χ^2.

Orbit		3	2	1
Element	Unit		Value	
a	($\mathrm{R_\odot}$)	6350±220	229.0±7.7	25.550±0.090
e		0.5728±0.0028	0.2101±0.0053	0.0[1]
i	(deg)	25.4[2]±7.7	86.67±0.12	86.85±0.22
ω	(deg)	10.6±8.9	9.45±1.42	90[1]
$\dot{\omega}$	($\mathrm{deg\,yr^{-1}}$)	0.0[1]	2.02±0.31	0.0[1]
Ω	(deg)	106.4±2.2	148.453±0.066	148.4±1.9
$T_{\rm p}$	(RJD)	54620±250	55609.46±0.52	56224.72482±0.00022
$P_{\rm A}$	(d)	18630±260	145.579±0.048	7.14664±0.00002
π	(mas)		14.96 ± 0.51	
γ	($\mathrm{km.s^{-1}}$)		8.05 ± 0.18	

Table 4.2: A summary of properties of all components of ξ Tau. These estimates are based on "observation-specific" models (see Sect. 4.2.3 and Table 14 in N2016). The N-body model, (see Sect. 4.2.4) in the version that was applied to ξ Tau, was not comparable to either light curve or spectra. Hence it does not constrain radiative properties of its components well. The mass estimates based on the N-body model are listed in Table 15 in N2016. The parameters listed here are the following: m the mass, R the radius, θ the angular uniform-disk radius, $T_{\rm eff}$ the effective temperature, $\log g$ the gravitational acceleration, $v \sin i$ the projected rotational velocity, V the Johnson V magnitude, $B-V$, and $U-B$ are colour indices based on the Johnson UBV magnitudes, and "S. Type" shortens the spectral type. [1]The estimate is based on the Hipparcos parallax. [2]The spectral type is based on the Hipparcos measurements by ESA (1997). [3]The spectral type estimate is based on mass-spectral-type calibration by Harmanec (1988).

Parameter	Unit		Value		
Component		C	B	Aa	Ab
m	($\mathrm{M_\odot}$)	1.61±1.18	3.89±0.25	2.252±0.027	2.125±0.027
R	($\mathrm{R_\odot}$)	×	2.81±0.28	1.700±0.035	1.618±0.039
θ	(mas)	×	0.407±0.031	0.247[1]±0.017	0.235[1]±0.017
$T_{\rm eff}$	(K)	×	14190±150	10700±160	10480±130
$\log g$	(dex)	×	4.52±0.041	4.330±0.019	4.348±0.022
$v \sin i$	($\mathrm{km.s^{-1}}$)	×	229.2±1.7	12.6±2.6	14.3±3.1
V	(mag)	×	4.25±0.10	5.46±0.11	5.63±0.11
$B-V$	(mag)	×	-0.12±0.16	-0.05±0.16	-0.03±0.14
$U-B$	(mag)	×	-0.446±0.16	-0.09±0.14	-0.07±0.14
S. Type		F V[2]	B6 V[3]	A2 V-B9 V[3]	A2 V-B9 V[3]

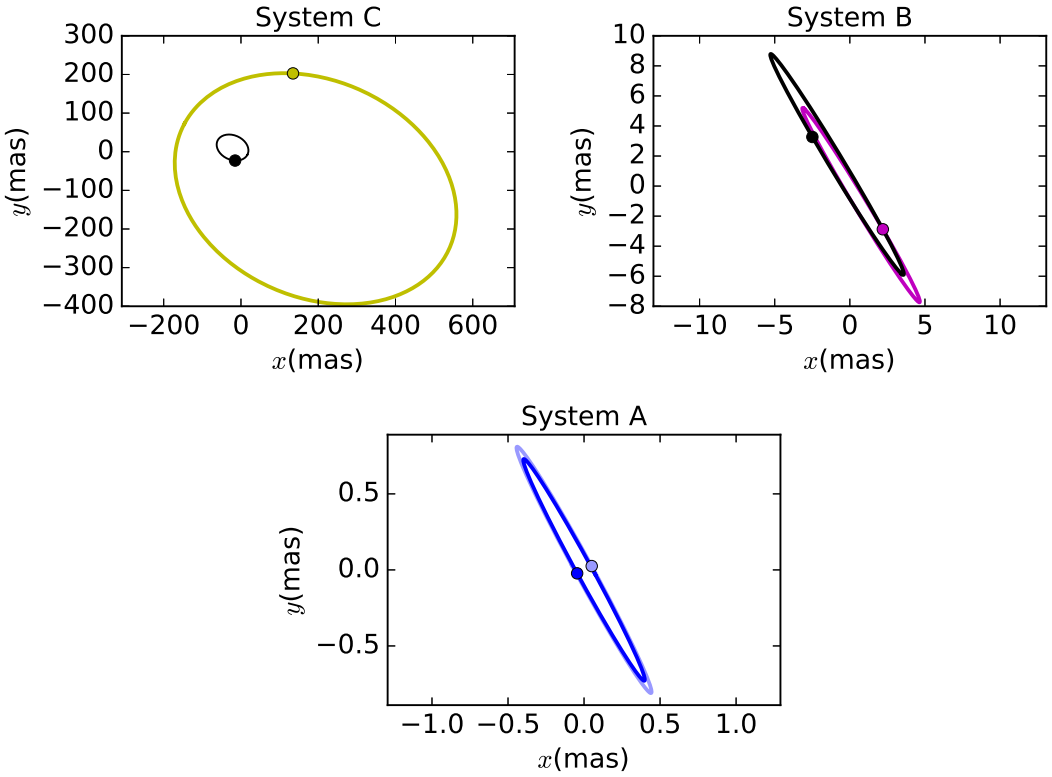

Figure 4.1: A sketch of orbits of the ξ Tau system as they would appear projected on the sky. These are osculating orbits at the epoch $RJD = 56224.724705$. The orbital elements correspond to the best fit of the N-body model to observations, which is in Table 15 in N2016. *Upper left panel:* The yellow line denotes the orbit of component C, and the black line the orbit of the barycentre of the triple subsystem (components Aa, Ab, B). The beginning of the coordinate system is identical to the centre of mass of the quadruple system. *Upper right panel:* The magenta line denotes the orbit of component B, and the black line the orbit of the barycentre of the eclipsing binary (components Aa, Ab). The beginning of the coordinate system is identical to the barycentre of the compact triple subsystem. *Lower panel:* The dark blue line denotes the orbit of component Aa, and the light blue line the orbit of component Ab. The beginning of the coordinate system is identical to the barycentre of the inner eclipsing binary. Points denote the position of a component or a centre of mass (depending on its colour) at the given epoch. All panels are in angular scale, x is the position in the east-west direction, and y the position in the north-south direction.

The studied observational material was the following:

- **The spectroscopic observations** consisted of electronic spectra from DDO, Ondřejov Observatory, and Lisbon Observatory, and RVs measured on photographic plates from DDO, Lick and Perkins observatories. The analysis of the RVs measured on the photographic plates were not used to estimate properties of ξ Tau in either N2013 or N2016. They only served as a consistency check of the orbital solution presented in N2013.
- **The photometric observations** consisted of series of Johnson's UBV measurements acquired at Hvar Observatory, South African Astronomical Observatory (SAAO), with Automatic Photometric Telescope (APT) at Four College in Villanova, and space-borne observations acquired with Hipparcos satellite.
- **The spectro-interferometric observations** consisted of five nights acquired in autumn 2011 with CHARA/VEGA instrument and 22 nights acquired with the NPOI instrument from 1991 to 2012.

For the analysis I used a set of "observation-specific" models. Those were *FOTEL* (Hadrava,

1990, 2004) for the analysis of the RVs, *KOREL* (Hadrava, 1995, 1997, 2009) for the spectral disentangling, *PHOEBE* (Prša and Zwitter, 2005, 2006) for the analysis of the photometric observations. The spectro-interferometric observations from NPOI were analysed by Christian Hummel, who used a simplified model consisting of two point sources bound by a common orbit, hence neglecting the visibility variations introduced by the inner orbit. The spectro-interferometric observations from CHARA/VEGA were analysed by Jordan Bencheikh who used a model consisting of three point sources, but only two observations had sufficient quality and the resolution needed to resolve orbit 1. Hence his solution suffered from a high uncertainty and he was forced to fix some parameters at values obtained from the fit to RVs. Finally the old C++ version of my program *Pyterpol* in one of its earliest versions was used to determine the radiative properties of all three components.

The key results of N2013 are the following: (i) physical sizes and orientations of orbits 1 and 2 (see Tables I, II and III in N2013), (ii) masses of components Aa, Ab, and B (see Sect. 4.1 in N2013), (iii) radii of components Aa, Ab (see Table II in N2013), (iv) radiative properties of components Aa, Ab, and B (see Table IV in N2013), (v) the detection of apsidal motion and its attribution to dynamical interaction between orbits 1 and 2 (see Sect. 4.2 in N2013). The study was published in conference proceedings, the page limit being ten pages only, hence we had to skip a number of details on the studied dataset, our models and results.

To a certain degree N2013 presents similar results as Sects. 3-6 in N2016, but the analysis presented in N2013 suffered from several deficiencies:

- The orbital model implemented in FOTEL does not allow an apsidal motion of the outer orbit. This effect is pronounced in ξ Tau and has major impact on the RVs over the studied time interval.

- The RVs were treated as having the same errors for components Aa, Ab, and B, although the applied method — comparison of direct and mirrored line profile in SPEFO — returned inaccurate estimates of RV of component B on the majority of eligible spectral lines.

- The light curve model relied only on relatively inaccurate UBV photometry, whose uncertainty is $\gtrsim 10\,\%$ of the relative light curve minima depth.

- Uncertainty of the orbital solution obtained by the disentangling was not properly evaluated. The disentangled spectra were plainly fitted with synthetic ones without verification by a fit to observed spectra. A possible danger arising from this approach was already discussed in Sect. 3.1.4. A comparison of Table IV in N2013 and Table 7 in N2016 shows a striking difference between the two models.

- A very simplified model was used to fit the spectro-interferometric observations. Also the observations were evaluated night-by-night instead of using a global model.

- The sum of squares was often fitted instead of χ^2. Therefore the goodness of individual fits could not be properly evaluated.

- Although derived orbital elements and properties of components Aa, Ab and B suffer from rather high uncertainties, there is a significant difference between masses inferred from the photometry and spectroscopy and those inferred from the spectroscopy and spectro-interferometry (e.g. mass of component B $m^{\rm B}_{\rm RV+LC} = 4.53 \pm 1.51\,{\rm M}_\odot$ vs. $m^{\rm B}_{\rm RV+IF} = 3.08 \pm 1.24\,{\rm M}_\odot$).

- In-depth analysis of the dynamical interaction between all three orbits of ξ Tau was not carried out.

- Orbital elements of the widest orbit and properties of component C were not studied at all. Its possible contribution to the spectroscopic, photometric and spectro-photometric observations was neglected.

Despite these issues the study N2013 provided a solid starting point for a detailed study, where all these issues were addressed.

4.2 A guide through the study N2016

In this section I provide an overview of the complex study of the ξ Tau system by Nemravová et al. (2016).

In the study I refined the (semi-)analytic "observation-specific" models, and used them to infer properties of ξ Tau system. During the analyses I attempted to carry out a thorough uncertainty analysis that resolved discrepancies between different methods.

The "observation-specific" models were then superseded with a complex N-body model (Brož, 2016, submitted to ApJL), developed and applied to ξ Tau by Dr. M. Brož, which models the motion of all components of the system by the integration of Newton's equations of motion starting from a set of osculating elements for a given epoch. The model is comparable to almost all observables which were studied with the observation-specific models. The N-body model also shows all possible effects arising from the gravitational interaction of the four components of ξ Tau if they were reduced to point masses.

Finally the most prominent secular and periodical effects are explained with the perturbation theory. The predictions of the theory are in agreement with the N-body model and provide dependencies of the dynamical effects on the orbital elements and masses of components.

4.2.1 The aims of the study

Our research was led by two principal goals: (i) Given the rich observational material we wanted to estimate properties of ξ Tau using "observation-specific" models independently and compare their performance. (ii) Then use this critical comparison to estimate orbital elements of the system and properties of its components with high accuracy. A full geometry of the system would then provide an excellent test-bed for models of binary formation, while the radiative properties and masses a test for the models of stellar evolution. (iii) In N2013 we only briefly touched the effects arising from the dynamical interaction of orbits 1 and 2. Therefore our last aim was to study these interaction by N-body simulation and by perturbation theory.

In N2016 the first goal is covered by Sects. 3-7, the second goal by Sects. 7 and 8 and the last goal by Sects. 8 and 9.

4.2.2 Overview of the observational material

A significant improvement of the result obtained by N2013 would not be possible if the observational material was not expanded. The observations used in N2013 were complemented with the following observations:

- The system was continually monitored from the Ondřejov observatory and additional slit spectra surrounding three major Balmer lines Hγ, Hβ, and Hα were obtained. Additional high-resolution echelle spectra were acquired with the spectrographs FEROS at the La Silla Observatory (Kaufer et al., 1999), and BESO at Cerro Amazones (Steiner et al., 2008; Fuhrmann et al., 2011). Four spectra were downloaded from the ELODIE archive (Moultaka et al., 2004). A journal of all studied spectra is in Table 4.3. Details on the reduction of the spectroscopic observations are in Appendix A in N2016.

- Additional Johnson UBV observations were secured at the Hvar observatory, but substantial for the study were the space-borne observations acquired with the satellite MOST (Walker et al., 2003). The instrument monitored ξ Tau almost continuously over 16 days and the precision of the all-sky magnitudes is $\approx 10^{-5} - 10^{-4}$ mag. Details on the reductions of the spectroscopic material are in Sect. 2.2 (MOST photometry), and in Appendix B (UBV photometry) in N2016. A journal of analysed photometric observations is in Table 4.4.

- Additional optical spectro-interferometric observations were taken during five nights in autumn 2012 with the instrument CHARA/VEGA and during ten nights in autumn 2012 and winter 2013 with the instrument NPOI. The latter observations were used to derive astrometric positions of the component B with respect to the photocentre of the eclipsing binary, but also the corresponding fringe visibilities and closure phases were analysed and compared to an orbital model. One additional IR observation acquired by the instrument VLTI/AMBER (Petrov et al., 2007) was downloaded from the ESO archive. A journal

Table 4.3: Journal of spectroscopic observations. For each instrument, ΔT refers to the time span between the first and the last measurement, N gives the number of RVs measured for components Aa, Ab, and B, $\Delta\lambda$ is the wavelength interval covered by the spectra in question, and R is the spectral resolution. Instruments: DDO - David Dunlap Observatory 1.9 m reflector, Cassegrain CCD spectrograph; ELO - Haute Provence Observatory 1.2 m reflector, echelle ELODIE CCD spectrograph; BES - Cerro Amazones Hexapod Telescope, BESO echelle CCD spectrograph; OND - Ondřejov Observatory 2 m reflector, coudé CCD spectrograph; LIS - Lisbon Observatory of the Instituto Geográfico do Exército, reflector, CCD spectrograph; FER - La Silla 2.2 m reflector, Feros echelle CCD spectrograph.

ΔT (RJD)	N Aa/Ab/B	$\Delta\lambda$ (Å)	R	Ins.
49300.7–52670.5	37/37/37	4357–4568	10800	DDO
51960.3–53637.6	04/04/04	4270–4523	42000	ELO
	04/04/04	4759–4991		
	04/04/04	6260–6735		
55041.9–55867.6	13/13/13	4270–4523	48000	BES
	13/13/13	4759–4991		
	13/13/13	6260–6735		
55579.4–56357.3	34/34/34	4270–4523	19200	OND
56579.4–56889.6	05/04/05	4274–4508	19200	OND
55579.3–55645.3	02/02/02	4378–4632	17700	OND
55579.3–56357.3	20/20/20	4753–5005	19300	OND
56527.6–56592.5	05/05/05	4759–4991	21500	OND
56527.6–56889.6	14/14/14	6260–6735	14000	OND
55561.3–56357.3	58/58/59	6255–6767	12700	OND
55597.4–55980.3	19/19/22	6497–6688	14000	LIS
56555.7–56564.7	12/12/12	4270–4523	48000	FER
	12/12/12	4759–4991		
	12/12/12	6260–6735		

Table 4.4: Journal of photometric observations. For each row, N is the number of observations in each of the filters used, ΔT is the time span covered by each dataset, column 'Passbands' shows the photometric filters used, column 'Comp/Check' lists the names of comparison and check star used. UBV denote the Johnson filters, and MO denotes the broad-band filter of the MOST satellite. Instruments: HVAR - Hvar Observatory 0.65 m Cassegrain reflector, photoelectric photometer; HIPP - The ESA Astrometric Mission; SAAO - South African Astronomical Observatory 0.5 m Cassegrain reflector, Lucy photoelectric photometer; VILL - the Four College 0.8 m reflector, photoelectric photometer; MOST - the Canadian MOST satellite. [1]Only three observations were taken before RJD = 54116, all at RJD = 46324. [2]The original Hipparcos $H_{\rm p}$ broad-band observations were transformed into the Johnson V filter following Harmanec (1998). However, for the light-curve solutions the limb-darkening coefficients corresponding to the original Hipparcos passband were used.

N	ΔT (RJD)	Passbands	Comp / Check	Instrument
441/451/452	46324.6–56882.6[1]	UBV	4 Tau / 6 Tau	HVAR
69	47909.6–48695.0	$V(H_{\rm p})$[2]	all-sky	HIPP
26/26/26	55569.3–55579.4	UBV	6 Tau / 4 Tau	SAAO
131/133/135	55883.9–55956.8	UBV	4 Tau / 6 Tau	VILL
18510	56222.0–56238.0	MO	all-sky	MOST

Table 4.5: Journal of the spectro-interferometric observations. ΔT is the time span RJD of the first and the last observation, ΔB the range of the projected baselines, $\Delta\lambda$ the wavelength range, N_{V^2} the total number of visibility observations, and $N_{\mathrm{T}_3\phi}$ the total number of closure phase observations. Instruments: 1 - Mark III, 2 - NPOI, 3 - CHARA/VEGA, 4 - VLTI/AMBER.

Instr.	ΔT (RJD)	ΔB (m)	$\Delta\lambda$ (nm)	$N_{\mathrm{V}^2}/N_{\mathrm{T}3_\phi}$
1	48275–48563	14–30	500–800	108/0
2	51093–56298	0–79	550–850	13461/4137
3	55825–56228	31–279	532–760	6132/0
4	56264–56264	41–139	1200–2600	2160/720

of the spectro-interferometric observations is in Table 4.5. A detailed description of the acquisition, calibration, and in case of NPOI also derivation of astrometric positions is given in Appendix C in N2016.

- Astrometric positions of component C with respect to the photocentre of the compact triple subsystem were downloaded from the Washington Double Star Catalogue (WDS hereafter) maintained at the U. S. Naval Observatory.

4.2.3 Summary of results based on observation-specific models

In the first part of the study N2016 (Sects. 3–7) we infer properties of ξ Tau system by comparing the individual types of observations to (semi-)analytic models, that are tailored to the specific types of observations. All these models contain only slightly modified Keplerian orbital model. A summary of the fitted types of observations and the applied models is the following:

Observation type	Model
Normalised flux	the program *Pyterpol* was used, the description of the model is in Sect. 3.1.4.
Radial velocity	the program *FRV* was used, the model is given by Eqs. (3.4), (3.5), and (3.6) in Sect. 3.1.1.
Magnitude	the program *PHOEBE* was used, the model implemented in it is roughly described in Sect. 3.1.2.
Astrometry	the program written by Dr. P. Zasche (Zasche and Wolf, 2007) was used, it is based on a orbital model given by Eqs. (3.16)–(3.18), but also contains terms accounting for the proper motion.
Visibility & Closure phase	the program *FV* was used, the model is represented by Eqs. (3.6), and (3.16)–(3.19).

Solution of the mass problem

In the preliminary study (see Sect 4.1.2) we reported a discrepancy between the mass of component B inferred from the combined solution of the light curve and the RV curve and the mass inferred from the solution of the RV curve and the inclination of orbit 2 from the interferometry.

The main problem turned out to be the measuring of RVs of broad lines of component B. The majority of orbital elements of orbit 2, relevant for the determination of component masses, can be estimated from the RV curve of components Aa and Ab, whose sharp lines provide accurate RVs. Nonetheless, one has to determine the semi-amplitude of *both* RV curves to obtain the masses of both components. Hence the issue transformed into a reliable determination of K_{B}. In my programs and KOREL the parametrisation using $K_{\mathrm{Aa+Ab}}$, and $q_2 = K_{\mathrm{Aa+Ab}}/K_{\mathrm{B}}$ is preferred.

We attempted to derive an orbital solution using the spectral disentangling (embodied by the program KOREL), but the data did not constrain the parameter well. This is demonstrated in Fig. 4.2, which shows the map of χ^2 of the semiamplitude of RV curve of the barycentre of the eclipsing binary $K_{\mathrm{Aa+Ab}}$ and the mass ratio q_2. This map shows that q_2 is poorly constrained by the disentangling. We also attempted to use the disentangled spectra for measuring of RVs, but we faced similar problems as we did for BR CMi (see Sect. 2.3.3).

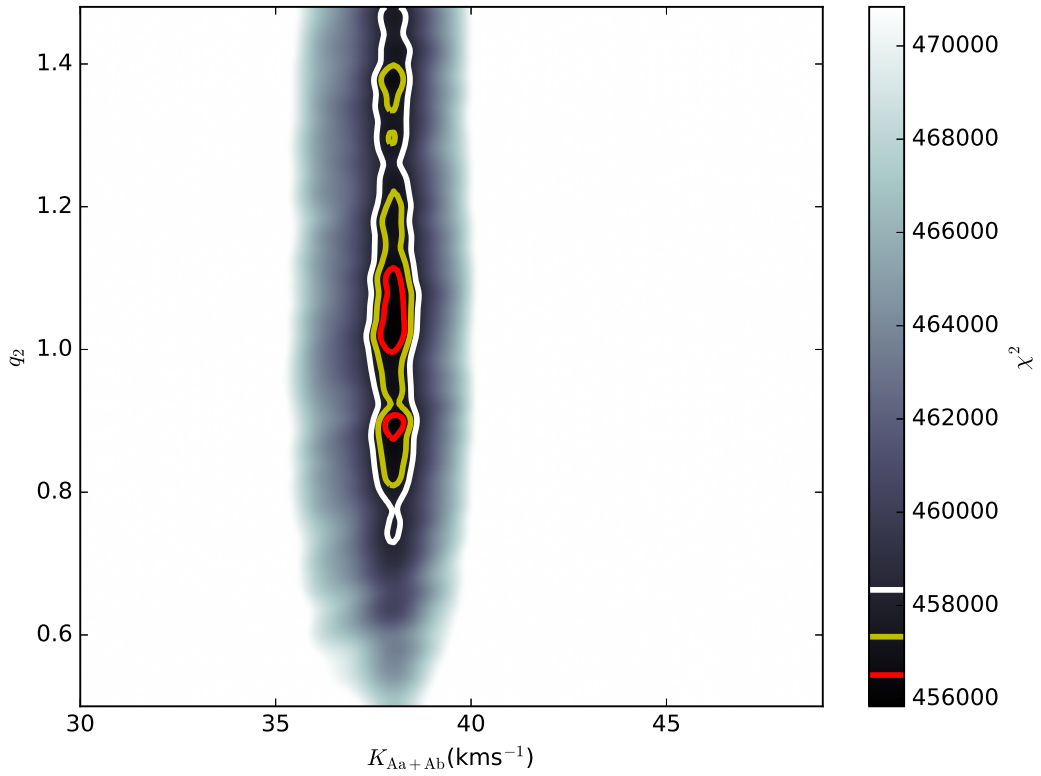

Figure 4.2: A χ^2 map of the mass ratio q_2 and the RV curve semiamplitude of barycentre of the eclipsing binary $K_{\mathrm{Aa+Ab}}$ surrounding the best fit found by KOREL (see Table 8 in N2016). The red line denotes one σ, the yellow line two σ, and the white line three σ confidence levels. Quite surprisingly, the 1-σ region surrounding the physically correct solution $q_2 \approx 0.9$ is smaller than the one surrounding the physically incorrect solution.

Comparison of direct and mirrored profiles did not turn out to be very useful, because we found only one spectral line (He I 4471Å) of component B that was strong and only weakly blended with lines of components Aa and Ab. Hence we were unable to estimate uncertainty of individual measurements properly.

A method that provided the best RV estimates of component B was comparison of synthetic spectra with the observed ones. First we optimised radiative properties of all three components by comparison of the synthetic spectra (mainly from the grid POLLUX) with 137 Ondřejov spectra. Second the RVs were measured by randomly drawing synthetic spectra based on the posterior distribution of parameters obtained in the first step. Their uncertainties (the statistical part only) were estimated from the distribution of results. Unexpectedly the uncertainty of RVs of component B turned out to be $\approx 5 - 10\,\mathrm{km.s^{-1}}$.

Nonetheless the fit of a synthetic RV curve (see Table 5 and Figs. 2, and 3 in N2016) to these measurements (with program *FRV*) provided a solution, which is not in conflict with the interferometry. The mass of component B based on combination of the RV and light curve solution is $m^{\mathrm{B}}_{\mathrm{RV+LC}} = 3.89 \pm 0.25\,\mathrm{M}_{\odot}$, and the same mass based on the RV curve solution and the interferometric inclination of orbit 2 $m^{\mathrm{B}}_{\mathrm{RV+LC}} = 3.60 \pm 0.52\,\mathrm{M}_{\odot}$.

Detection of rapid light oscillations

We discovered quasi-periodic light variations with a period $P_{\mathrm{R}} = 0.42 \pm 0.01\,\mathrm{d}$ and amplitude $A = 0.00060 \pm 0.00015\,\mathrm{mag}$ with the satellite MOST (see Figs. 5 and 7 in N2016). The period and the amplitude seem to be modulated with the period of the eclipsing binary P_1. A natural explanation would be that eclipsing binary causes a small ellipsoidal variation in between eclipses, which tilts the light curve of the oscillations slightly and introduces a phase-dependent period and amplitude shifts.

We were unable to identify the true physical cause of the 0.42 d light variations. The period is not similar to any instrumental period, hence it is unlikely an instrumental effect. Another explanation would be that component B has a close companion, orbiting the primary with an orbital period 0.84 d and distorting it, so it produces ellipsoidal variations. This scenario seems unlikely, because two consecutive minima (at phases 0.5 and 1.0) would have different depth, which was not seen in the data. This is shown in Fig. 4.3.

Other two causes that seem more likely are spots and pulsations. These two effects cannot be easily distinguished from each other since the period of 0.42 d is a plausible value for the rotational period of component B. Unfortunately the remaining periods, that we identified in the periodogram of the MOST light curve are aliases either with 1 d period, or with the orbital period of the satellite MOST. Spots seem a bit less likely, because the component B would have to be either chemically peculiar or have strong magnetic fields and we found no evidence for either of these in spectra. The component B could be a slowly pulsating B star. The first reason to attribute the pulsations to component B, is the fact that it fits better into instability strip in HR diagram for this type of pulsators (Waelkens et al., 1998), and second that it is simpler for it to produce the micro-variability, because it is the brightest member of ξ Tau.

Detection of eclipse-timing variations

One effect produced by the dynamical interaction of orbits 1 and 2 is the apsidal motion of orbit 2, which has already been reported in N2013. The eclipse-timing variations (ETV) were detected thanks to high-precision light curve from the satellite MOST. After we found that the two consecutive primary minima acquired with the satellite do not fold well, we measured the minima timings across the whole dataset. The amplitude of ETVs is roughly $A_{\mathrm{ETV}} = 0.025 \pm 0.01\,\mathrm{d}$ and they seem to vary on a timescale comparable to orbital period of orbit 2. The ETVs for all recorded minima (see Figs. B.1, and B.2 in N2016) are shown in Fig. 4.4.

At the beginning we attempted to explain the variations by fitting an eccentric orbit rather than the circular one, but this had not resolved the problem — a local value of orbital period was needed. Hence we suspected the LTTE produced by orbits 2 and 3 $\Delta t_2^{\mathrm{LTTE}} \simeq 0.006$, and $\Delta t_3^{\mathrm{LTTE}} \simeq 0.013$. The amplitude of the former is insufficient while the other varies with period equal to orbital period of orbit 3 ($\approx 51\,\mathrm{yr}$). Therefore LTTE is not a correct explanation.

The correct explanation was the dynamical interaction between orbits 1 and 2. An approximate formula derived by Rappaport et al. (2013) based on perturbation theory to the first order in the eccentricity gives an estimate for ξ Tau, which is in agreement with the observed

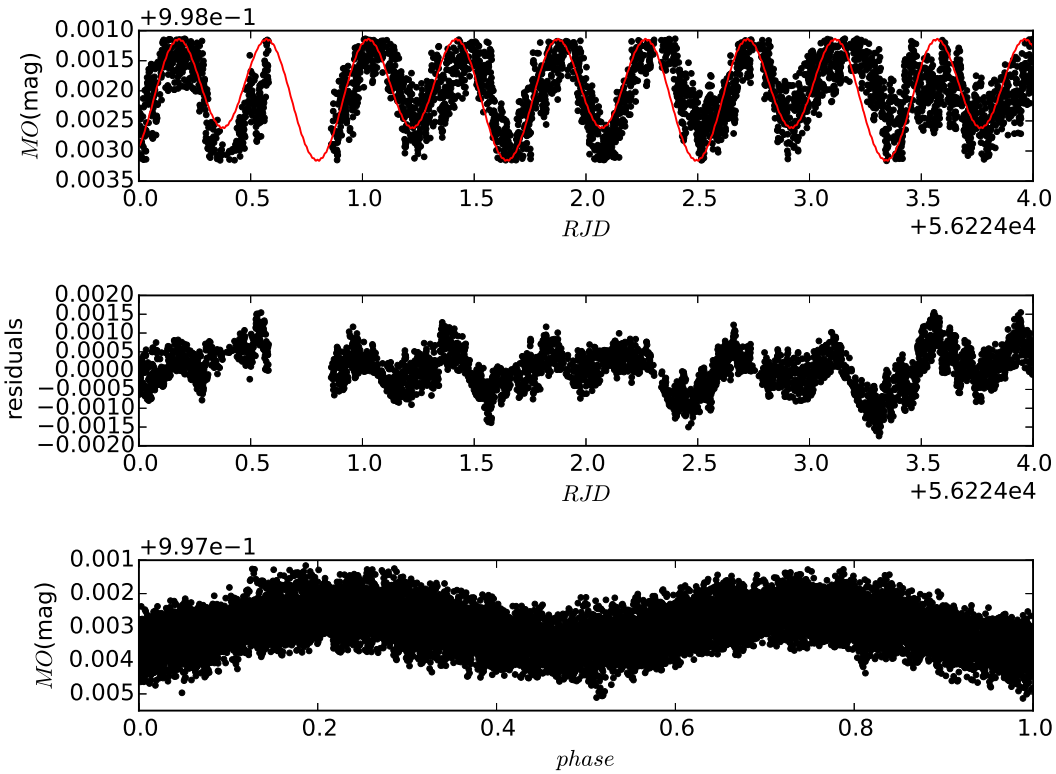

Figure 4.3: A fit of ellipsoidal variations to the MOST light curve outside the eclipses. The properties of component B were taken from the fit of synthetic spectra to observed ones (effective temperature, projected rotational velocity), and from the interferometry (radius). *Top panel*: The red line denotes the best-fitting model obtained with *PHOEBE* and the black points is the magnitude in the MOST passband *MO* outside the eclipses. *Middle panel*: The black points show residuals of the MOST light curve and the best fitting model. *Bottom panel*: The black points show a phase diagram of the MOST light curve for the period 0.848 d. Although the model is able to reproduce the amplitude of the rapid light variations, the shape of the model curve does not agree with observations.

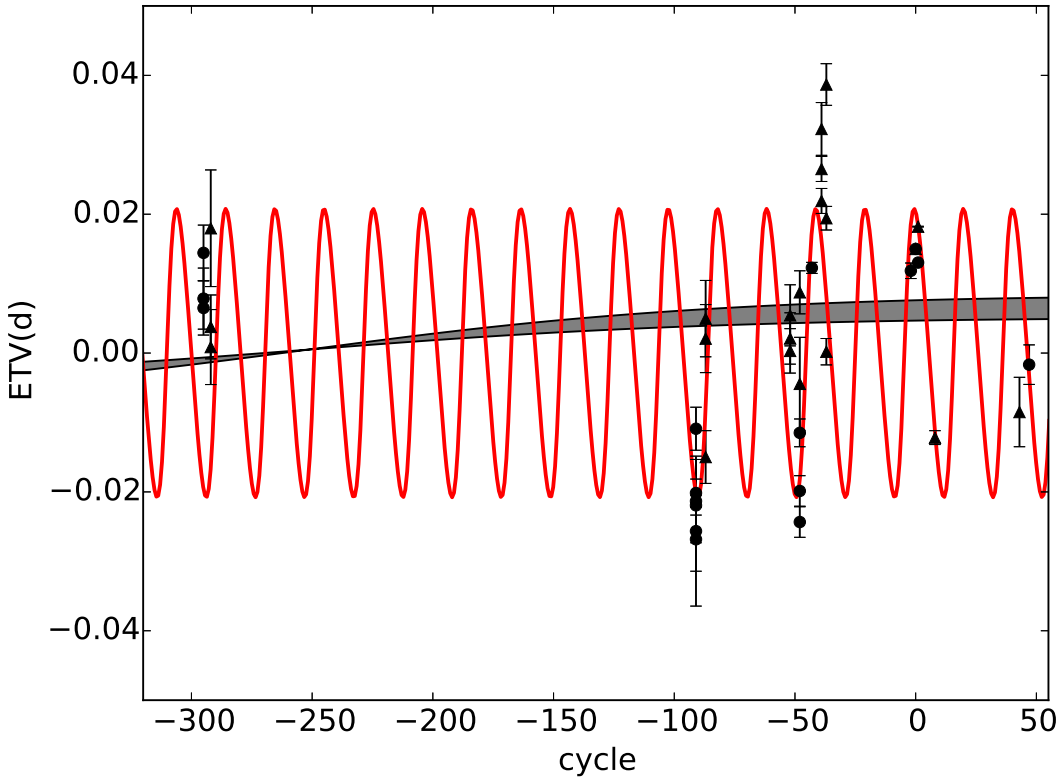

Figure 4.4: Eclipse-timing variations of the inner system of ξ Tau. The black points denote time difference measured minimum epoch and computed one using the ephemeris $T_{\min}(RJD) = 7.14664 \times E + 56224.72482$. Cycle denotes the time difference between the reference epoch and an arbitrary epoch divided by the reference period. The red line is a delay computed from a model represented by Eq. (8) in Rappaport et al. (2013). The grey band denotes the LTTE produced by orbit 3. *This comparison is not a fit.*

effect. A comparison of the observed delay and that produced by the approximate model is on Fig. 4.4.

Determination of mean orbital elements of ξ Tau and properties of its components

We were able to derive properties of the system. Our results include determination of the physical size and geometric orientation of all orbits of ξ Tau, masses of all components, radii and radiative properties of components of the compact triple, and the distance to the system. The best-fitting models inferred from the individual types of observations are mutually consistent.

A critical comparison of the results based on different models is in Sect. 7 of N2016. Here I present only a few remarks. (i) The properties of component C were solely estimated from the astrometry of the WDS catalogue. Hence we were only able to fit the projection of orbit 3 on the sky and estimate its mass with a great deal of uncertainty $m^{\mathrm{C}} = 1.61 \pm 1.18\,\mathrm{M}_{\odot}$. The mass is in agreement with the spectral type F V based on the Hipparcos measurements (ESA, 1997). (ii) The individual observation-specific models were not completely independent. The light-curve solution depended on the fit of the RV curve and the fit of observed spectra with synthetic ones — the temperature of component Aa, the mass ratio of orbit 1 and $a_1 \sin i_1$. Several parameters of the spectro-interferometric model had to be taken from the RV-curve solution, light-curve solution and the parallax — angular radii of components Aa, and Ab, mass ratio, and inclination of orbit 1 — because we lacked enough observations at very high spatial frequencies. (iii) The orbital solution based on observation-specific models still suffers from two ambiguities. The longitude of ascending node of orbit 1 has a mirror solution $\Omega_1' = \Omega_1 + \pi$. The inclination of orbit 3 has a mirror solution $i_3' = -i_3$.

Finally I note that all observation-specific models are incomplete and all contained simplifications of the orbital and radiative models. Fortunately these simplifications do not make the models invalid, because the reduced χ^2 of the best-fitting solution remained acceptable for all models with the exception of fit to spectro-interferometric observations, which suffer from the reduction and calibration systematics. The "observation-specific" models also provided a solid starting point for the complex N-body model, which is described in the next section.

4.2.4 The N-body model and the perturbation theory

The N-body model (Brož et al., 2010; Brož, 2016, submitted to ApJL) was applied to derive the orbital properties of all four components of ξ Tau as well as their basic radiative properties. After a brief description of the model I summarise its impact on the ξ Tau study N2016.

Description of the N-body model

The main features of the N-body model: (i) Trajectories of all components are determined by the integration of Newton's equations of motion. Each component is reduced to a point mass, hence the model includes effects that arise from their dynamical interaction. That means that tides, or relativistic effects are not included. For ξ Tau, these effects are negligible. The secular and periodic evolution of orbital elements of all four orbits of ξ Tau are shown in Figs. 4.5-4.7. (ii) When the trajectories are known, each component is represented with a homogeneous disk. The radiation of the disk is approximated with a black-body radiation. Then the eclipse-timings and eclipse durations can be determined from the model, and also the position of photocentre of each component. (iii) The model is comparable to several observables (the number of which has been growing steadily as Dr. Brož continues to improve his model). The observables that could be fitted in N2016 are the following: astrometric positions, closure phases, eclipse timings, eclipse durations, radial-velocities, and visibilities.

The trajectories can be determined in several coordinate systems. For the implemented integrator, the native coordinates are barycentric positions and velocities, but osculating orbital elements are directly comparable to the Keplerian models implemented in "observation-specific" models, that is why I will stick to those here (For a full definition of the N-body model that was applied in N2016 see Sects. 8.1 and 8.4 therein). Then the parameters defining the model are the following: $\{a_i, e_i, i_i, \omega_i, \Omega_i, M_i\}_{i=1}^{3}$ the osculating orbital elements for a certain epoch T_0, where a is the semi-major axis, e the eccentricity, i the inclination, ω the periastron argument, Ω the longitude of the ascending node, and M the mean anomaly. The remaining parameters

$\{R^j, m^j, T^j_{\rm eff}\}_{j\in\{\rm Aa,Ab,B,C\}}$ are the uniform-disk radius, the mass, and the effective temperature, and γ is the systemic velocity.

The model was applied to observations in two different ways based on how the interferometric data were treated. First only the astrometric positions of component B relative to the barycentre of the eclipsing binary from NPOI were used (see Table C.1 in N2016) and then the model was compared to all visibility and closure phase observations. This approach was applied because the visibilities and closure phases suffer from systematic errors, which increase the reduced chi-square of the best-fitting solution $\chi^2_{\rm R} \simeq 6$. This complicates their fitting along with the remaining observations, whose reduced χ^2 is comparable to one, because the interferometric observations completely dominate the overall χ^2. The astrometric observations from NPOI were estimated with the reduction package OYSTER by Hummel et al. (1998, 2003) which partially compensates for the instrumental effects. The resulting astrometric positions give a reduced χ^2 comparable to one.

Therefore first a steady orbital solution was found first using the NPOI astrometric positions and radii and luminosity ratios obtained by "observation-specific" models (see Sects 8.1-8.3 in N2016). Then the model was compared to visibility and closure phase measurements from CHARA/VEGA, NPOI, MARK III, and VLTI/AMBER instruments to resolve an ambiguity in the longitude of the ascending node of orbit 2 (see Sect. 8.4 in N2016). In this model the effective temperatures and the radius of the tertiary were free. Radii of the eclipsing binary were poorly constrained because the model does not exploit the light-curve.

Main results of the N-body model

First of all *the N-body model is physically more realistic.* The dynamical interaction (especially between orbits 1, and 2) produces a number of secular and periodic effects. The N-body model accounted for all of them. The secular and periodic variations of osculating orbital elements of all orbits over the time interval covered by observations are shown in Figs. 4.5-4.7. The best-fitting osculating elements found by the N-body model are in Table 15 of N2016.

Two main secular effects are the apsidal advance of orbit 2, and periodic variations of the longitudes of the ascending node and inclinations of orbits 1 and 2. These results partly justify the approximations made in "observation-specific" models. Clearly the advance of the apsidal line of orbit 2 is close to linear. The latter effect produces the following variations of the semiamplitude of RV curves ΔK, and depth of the primary minimum in Johnson V band: $\Delta K_{\rm Aa} \simeq \Delta K_{\rm Ab} \approx 0.4\,{\rm km.s^{-1}}$, $\Delta K_{\rm B} \simeq \Delta K_{\rm Aa+Ab} \approx 0.02\,{\rm km.s^{-1}}$, and $\Delta V_{\rm min} \approx 0.13\,{\rm mag}$, where $V_{\rm min}$ is the systemic magnitude in Johnson V filter at the primary minimum epoch. The variation of the semiamplitude of all RV curves is clearly beyond accuracy of our data, whose precision is $\gtrsim 1.0\,{\rm km.s^{-1}}$. On the other hand, such variations of the light-curve minima should be detectable given the accuracy of our UBV photometry, which is generally better than 0.02 mag. There is a hint of an eclipse-depth change in the UBV photometry, but the effect is comparable to the precision of the measurements. However the mutual inclination $\tilde{j}$ based on "observation-specific" models $\tilde{j} \lesssim 2\,{\rm deg}$ would produce minima-depth variations with a lower amplitude (eventually zero for co-planar orbits).

The N-body model *properly estimates periodic variations* of the osculating elements, hence *it is able to explain the ETVs produced by both LTTE and dynamical interaction* among ξ Tau components. It also provides the amplitude of periodic effects, and demonstrates that the inner interacting triple subsystem of ξ Tau is quite well-behaved and the ETVs could be easily included in the "observation-specific" models by using the approximate formula derived through the perturbation theory (see Sect. 9 of N2016).

An unexpected result came from the comparison of the N-body model and the ETVs. Using these data *N-body model allowed us to resolve the ambiguity in the longitude of the ascending node of orbit 1.* Fig. 12 in N2016 shows comparison of the four very accurate eclipse timings based on the observations from satellite MOST and the N-body model for two values of the $\Omega_1 = [151; 331]\,{\rm deg}$. Clearly the latter agrees with the measurements much better, hence the motion of components of orbit 1 is prograde with respect to motion of components of orbit 2. This is an excellent example of how the simplifications introduced in "observation-specific" models ignore some pieces of information contained in the observations.

The N-body model provides a better estimate of the orbital elements of ξ Tau and masses of its components not only because it implements a more physically correct orbital model, but

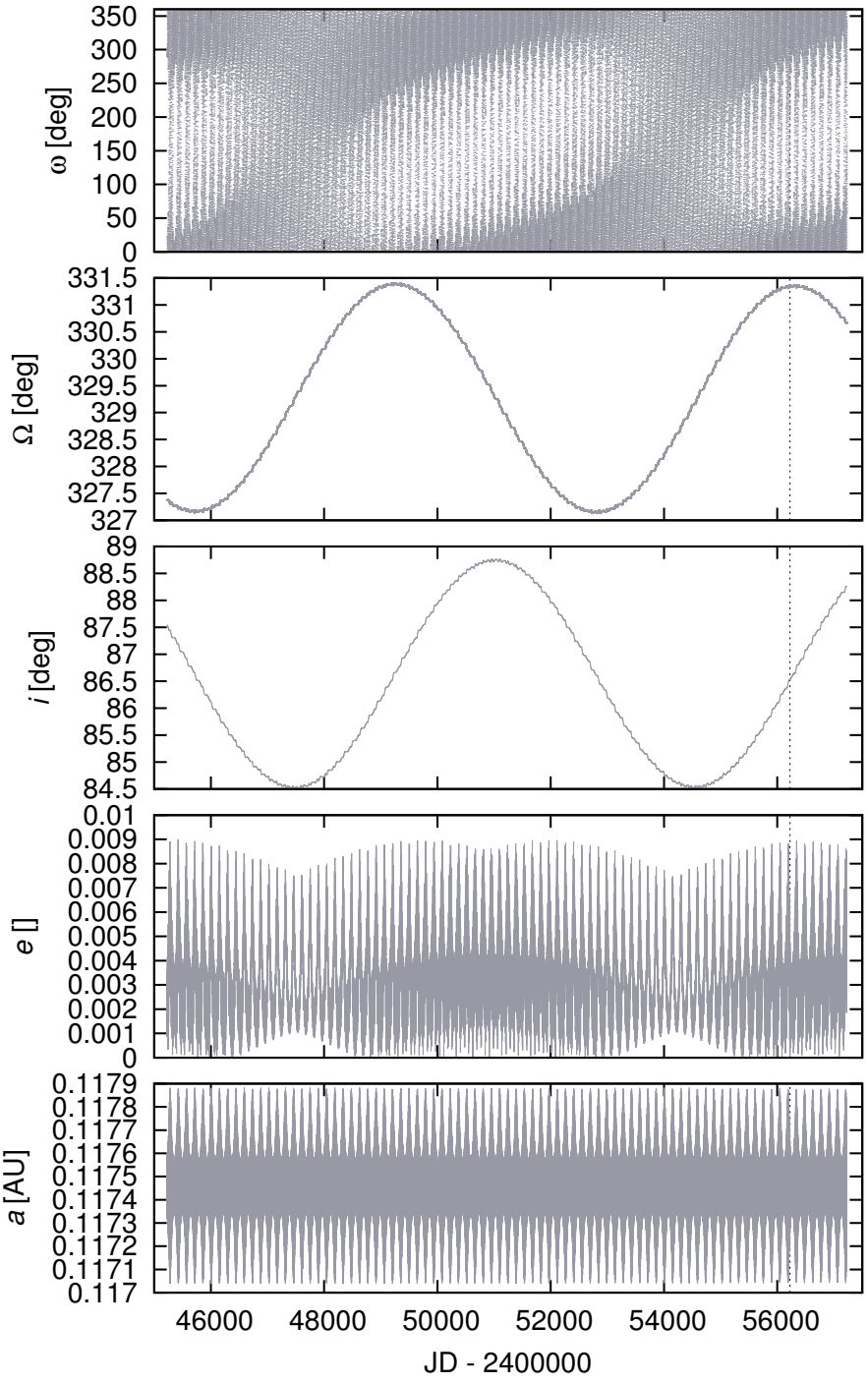

Figure 4.5: The evolution of osculating elements of orbit 1 of ξ Tau implied by the best-fitting N-body model. The orbital parameters are the following ω the periastron argument, Ω the longitude of the ascending node, i the inclination, e the eccentricity , and a the semi-major axis. The ω of orbit 1 is changing rapidly, because it is undefined for $e \longrightarrow 0$.

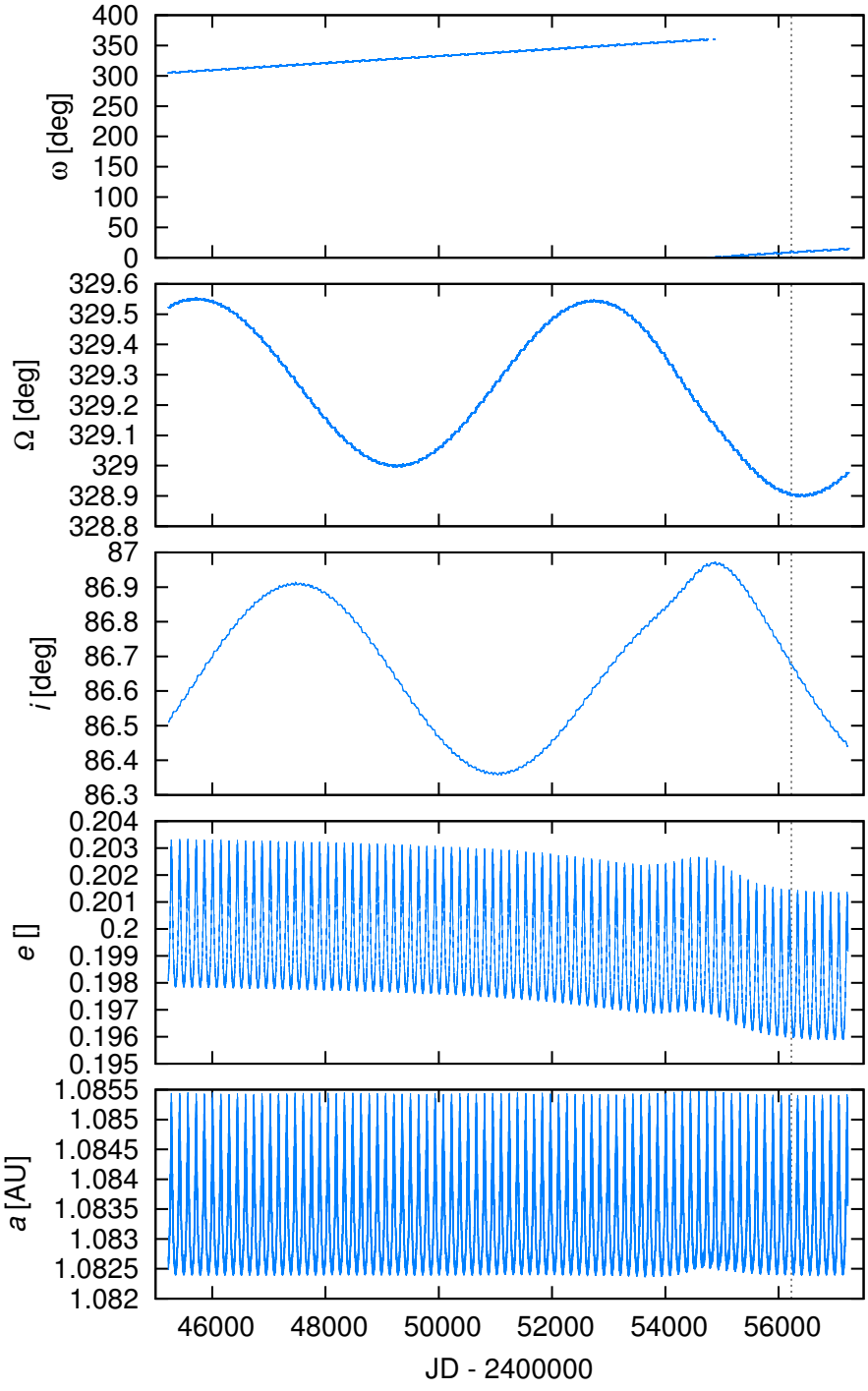

Figure 4.6: The evolution of osculating elements of orbit 2 of ξ Tau implied by the best-fitting N-body model. The orbital parameters are the following ω the periastron argument, Ω the longitude of the ascending node, i the inclination, e the eccentricity , and a the semi-major axis. The hump after RJD = 54000 is caused by the periastron passage of orbit 3.

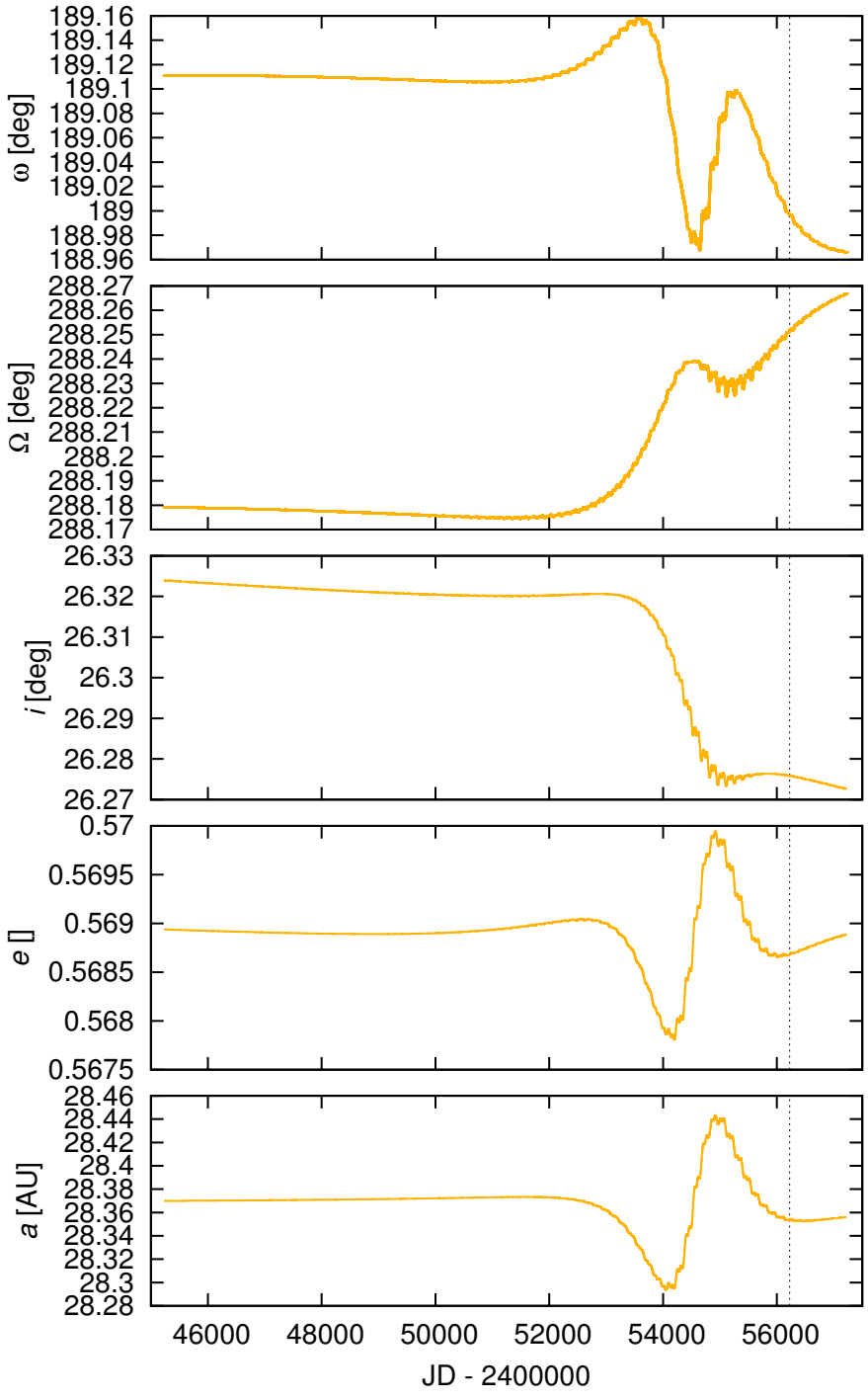

Figure 4.7: The evolution of osculating elements of orbit 3 of ξ Tau implied by the best-fitting N-body model. The orbital parameters are the following ω the periastron argument, Ω the longitude of the ascending node, i the inclination, e the eccentricity , and a the semi-major axis. The prominent changes starting around RJD = 53000 are caused by the periastron passage of orbit 3.

also because it is comparable to more types of observations simultaneously (see discussion in Sect. 3.2).

The main results of the perturbation theory

The N-body model detected a "jungle" full of secular and periodic variations of orbital elements, but their most prominent components are quite simple. Hence we turned to perturbation theory to estimate parametric dependencies of the most prominent periodic and secular effects. The approximate formulae were derived by Prof. Vokrouhlický. I present it here for a completeness of the description of the paper N2016.

In the ξ Tau study the dynamical interaction with component C is neglected. A glance at Fig. 4.6 reveals that dynamical effects introduced by interaction with this component are by at least an order lower than those produced by interaction of components Aa, Ab and B.

The secular evolution of ξ Tau is simple because the eccentricity of orbit 1 $e_1 \simeq 0$, and the mutual angle between orbits 1 and 2 in the Laplace frame $\tilde{j} \simeq 0\,\mathrm{deg}$. This plane is perpendicular to the total angular momentum. From now on, the orbital elements defined in this plane are denoted with a tilde. Here I (again) point out the completeness of our analysis — the mutual angle $\tilde{j}$ can be determined only if geometric orientation of both orbits is known. On a timescale of $\approx 10000\,\mathrm{d}$, only the quadrupole interaction is relevant. Then e_1, e_2 and $\tilde{j}$ are stable in time and the $\tilde{\Omega}_1$ and $\tilde{\Omega}_2$ linearly advance following Eq. (26) in N2016. This motion transcripts into sinusoidal variation of Ω_1, Ω_2, i_1, and i_2 in the observer frame, which is perpendicular to the sky, that are shown in Figs. 4.5, and 4.6. The interaction also introduces apsidal motion of orbit 2, which is given by Eq. (27) in N2016. The same approximations were already published by Soderhjelm (1975), and Breiter and Vokrouhlický (2015).

While the apsidal motion was clearly detected, we have not detected the variation of the inclination of orbit 1. The magnitude of this variation is comparable to the mutual angle $\tilde{j}$. This infers that the angle must be very small. The observations-specific models provide $\tilde{j} \lesssim 2\,\mathrm{deg}$ and N-body model $\tilde{j} \lesssim 5\,\mathrm{deg}$. This strengthens the assumptions under which the Eqs. (26), and Eqs. (27) were derived. The N-body model is in agreement with these equations. For observation-specific models the approximate model resolves the discrepancy between the linear apsidal motion given by the fit of the RV curve ($\dot{\omega}_2 = 2.90 \pm 0.33\,\mathrm{deg\,yr^{-1}}$) and the fit of spectro-interferometric observations ($\dot{\omega}_2 = 2.02 \pm 0.30\,\mathrm{deg\,yr^{-1}}$). The approximate model (Eq. 27 in N2016) gives $\dot{\omega}_2 = 2.11$, hence the latter model provides a correct value.

We have also investigated the main sources of the ETVs and identified the following two: (i) those with the orbital period of the outer orbit 2 (called long-periodic in N2016 and given by Eqs. 29 and 30 therein), and (ii) those with the half of the synodic orbital period of the inner orbit 1 (called short-periodic in N2016 and given by Eq. 31 therein). Both formulae are derived under the assumption that the orbits are co-planar. Similar or the same equations were already derived by (Soderhjelm, 1975; Borkovits et al., 2003; Rappaport et al., 2013). The long-periodic ETVs are caused by changes of the distance of the outer component with respect to the centre of mass of the inner system. Hence it is zero for a circular outer orbit. For ξ Tau they are the larger component of ETVs produced by the dynamical interaction $\delta t_{\mathrm{LP}} = 0.0168 \pm 0.007\,\mathrm{d}$. The short-periodic ETVs are caused by changes of distance of components Aa and Ab with respect to component B. Hence this effect is non-zero for circular orbit 2, but its magnitude depends on e_2. For ξ Tau, the amplitude of short-periodic ETVs is $\delta_{\mathrm{SP}} = 0.0068 \pm 0.0003\,\mathrm{d}$ at periastron of orbit 2 and by factor 4 smaller at apoastron of orbit 2. The sum of short-periodic and long-periodic ETVs is an excellent agreement with the amplitude of the measured delay $\delta = 0.025 \pm 0.010\,\mathrm{d}$.

4.2.5 Outlook for ξ Tau

We have derived a consistent picture of the system — we determined the size and orientation of all orbits, derived the basic physical and radiative properties of components Aa, Ab, and B, and the distance to the ξ Tau system. We detected traces of the dynamical interaction among its components and explained them using a complex N-body model and the perturbation theory. However more work remains to be done:

(i) The properties of component C still remain uncertain. High S/N spectra (preferably in the IR region) would provide its radiative properties and RVs that are needed for a reliable

determination of its mass and to resolve the ambiguity in the inclination of orbit 3.

(ii) High-S/N and high resolution spectra may allow the detection of line-profile variations or to prove their complete absence, thus helping to identify the true physical cause of the micro-variability of component B.

(iii) We demonstrated that the rotation of members of the eclipsing binary is synchronised with the orbital motion. The synchronicity ratios implied by results of "observation-specific" models are $F^{\mathrm{Aa}} = 0.95 \pm 0.20$, and $F^{\mathrm{Ab}} = 0.80 \pm 0.18$. We note that more accurate RV measurements of components Aa and Ab would allow a firm detection of the Rossiter-McLaughlin effect and would help to determine the sense of their rotations with respect to the orbital motion.

(iv) The sense of revolution of orbit 1 with respect to orbit 2 (found prograde by N-body model) can be verified either by interferometric observations at high spatial resolution including the closure phase, or by continuous photometric observations. Note that the retrograde solution ($\Omega_1 = 151\,\mathrm{deg}$) predicts that the eclipses should cease to exist in 2021.

(v) New series of spectro-interferometric observations would also help to resolve components of the eclipsing binary and its orbital properties providing an independent estimate to the light and RV curve solutions.

5. A binary undergoing mass transfer β Lyrae

β Lyr is a bright eclipsing semi-detached binary that is currently undergoing mass-transfer phase. Although the mass ratio has been already reversed, the mass transfer rate is still high. The mass emanating from the donor forms various circumstellar structures including an accretion disk, jets and a circumbinary cloud. All these structures can be both opaque and transparent. An overview of the investigation of this system is presented in Sect. 5.1.

As the system is in an evolutionary rare phase of mass transfer, knowledge of the geometrical distribution of the circumstellar matter and its properties (like density or temperature) is important for the understanding of the whole process of mass transfer.

Our first goal is to map the distribution of opaque and transparent circumstellar gas in β Lyr and to improve the orbital elements (mainly the mass ratio, inclination, and ascending node longitude). Our second goal is to compare the resulting picture to the contemporary models of mass transfer and draw general conclusions on the process.

β Lyr has been observed almost exclusively during a 12 d long campaign in 2013 with the spectro-interferometer CHARA/VEGA. These observations were accompanied by similar campaigns with instruments NPOI and CHARA/MIRC. New series of spectroscopic observations from the Ondřejov observatory and photometric observations from the Hvar observatory were also acquired. The observations are described in Sect. 5.2. We focus on the comparison of spectro-interferometric observables with (semi-analytic) models to confirm the existence of various gas structures reported in several previous studies, and to derive their shape and size. For that we intend to use tool *SIMTOI*, and develop a new tool for the interpretation of differential visibility and differential phase observations of binaries, which show traces of the circumstellar matter.

I reduced the extensive CHARA/VEGA observational material, and carried out its analysis in *SIMTOI*. The results show that in continuum the observations can be modelled with a Roche-lobe filling donor revolving around a common centre of gravity with a gainer hidden in an optically thick disk. The analysis is presented in Sect. 5.3.

Our analysis of β Lyr is still work in progress. A valuable information is held by the differential phases and differential visibilities, which provide information about the intensity and *velocity* distribution of the optically thin circumstellar gas. To extract this information I have to finish my program *DV*, that is outlined in Sect. 3.1.3. Part of the results presented in this chapter have been already reported by Nemravová et al. (2015).

5.1 Overview of previous studies

Here I briefly summarise results found by previous investigators of β Lyr system. A special attention is given to studies based on spectro-interferometric observations, because they form the principal part of the observational material that I analysed.

5.1.1 General overview

Photometric variations of the system were discovered by Goodricke and Englefield (1785), and the emission lines in its spectrum were first detected by Secchi (1866). The two hundreds years old history of investigation of this system were summarised by Sahade (1980) and later by Harmanec (2002). The system is a multiple star, but the name "β Lyr" usually refers to its eclipsing binary component β Lyr A with an orbital period $\simeq 12.94$ d. This binary consist of a Roche-lobe filling B6-8 II type ($m \simeq 3\,\mathrm{M}_\odot$) donor, and a B0 V type gainer ($m \simeq 13\,\mathrm{M}_\odot$), the latter being obscured by an opaque accretion disk whose spectrum resembles A5 III type spectrum (Skulskii and Topilskaya, 1991; Harmanec, 1992). The high mass transfer rate $\dot{m} \simeq 2.5 \times 10^{-5}\,\mathrm{M}_\odot\,\mathrm{yr}^{-1}$ (De Greve and Linnell, 1994) leads to a secular increase of the orbital period $\dot{P} = 19\,\mathrm{s\,yr}^{-1}$ (Harmanec and Scholz, 1993; Ak et al., 2007). The mass stream from the donor does not hit the gainer directly, but due to Coriolis force encircles the gainer and forms an accretion disk. Presence of an opaque accretion disk was first proposed by Huang

(1963). At the region of the interaction of the gas stream and the accretion disk (maybe even the mass stream with itself Bisikalo et al., 2000) the circumstellar gas is heated and forms a hotspot and two jets perpendicular to the orbital plane. A clear evidence for the mass loss from the system is the circumbinary cloud (Umana et al., 2000). The existence of jets was first proposed by Harmanec et al. (1996) from spectro-interferometry and independently confirmed by Hoffman et al. (1998) from spectropolarimetry and later by Bonneau et al. (2011) from H$\alpha$and Hβspectro-interferometry. The presence of a hotspot has been proposed by Bonneau et al. (2011); Lomax et al. (2012); Mennickent and Djurašević (2013). According to (Deschamps et al., 2013) it may play a crucial role in the formation of jets and mas-loss from a binary system.

5.1.2 (Spectro)-interferometric studies of β Lyr

β Lyr is bright ($V = 3.42$ mag) and moderately close (parallax $\pi = 3.39 \pm 0.17$ mas van Leeuwen, 2007). The angular size of its semimajor axis is $\tilde{a} \approx 0.92$ mas (based on physical size of the semimajor axis estimated by Linnell, 2000) make it resolvable with the contemporary optical interferometers, whose limiting spatial resolution is ≈ 0.1 mas. The system was first observed in 1991 with an optical spectro-interferometer GI2T (Mourard et al., 1994). A study based on these observations, which mainly demonstrated that the object is observable and resolvable by the GI2T instrument, was published by Mourard et al. (1992). It was observed again with GI2T during 11 nights in 1994, along with a large campaign of supporting spectral and photometric observations. A thorough analysis of this campaign was carried out by Harmanec et al. (1996). Besides other things, the authors inferred the existence of jets perpendicular to the orbital plane from the spectro-interferometric observations and from analysis of several emission-line profiles.

Later Umana et al. (2000) found a nebula with ≈ 40 AU across at 5 GHz with the Multi Element Radio Linked Interferometer Network (MERLIN). They also found that the nebula is aligned with the jets. The authors proved that the mass transfer is non-conservative, determined the mass-loss rate $\dot{m} = 10^{-7}\,\mathrm{M}_\odot\,\mathrm{yr}^{-1}$ and estimated the total mass lost from the system to $0.015\,\mathrm{M}_\odot$ from the beginning of the mass transfer.

Zhao et al. (2008) presented the first resolved images of β Lyr. Their analysis was based on series of H-band spectro-interferometric observations with the instrument CHARA/MIRC (Monnier et al., 2006). The images were fitted with a simple model (two uniform ellipses). The authors derived an astrometric orbit from the fit — the inclination $i = 92.25 \pm 0.82$ deg, the semimajor axis $\tilde{a} = 0.865 \pm 0.048$ mas, and the longitude of the ascending node $\Omega = 254.39 \pm 0.82$ deg.

Schmitt et al. (2009) studied the motion of the Hα emitting region with respect to the maximal continuum flux. Their study was based on series of observations with the optical spectro-interferometer NPOI (Armstrong et al., 1998). They found the semimajor axis $\tilde{a}_{H\alpha} = 0.46 \pm 0.03$ mas, and the longitude of ascending node $\Omega_{H\alpha} = 249 \pm 4$ deg. They also derived a solution based solely on continuum flux whose semimajor axis $\tilde{a} = 0.99 \pm 0.03$ mas, and the longitude of ascending node $\Omega = 255 \pm 7$ deg. The latter result is in better agreement with results presented by Zhao et al. (2008). The separation of Hα emitting region with respect to the continuum is too small even if an offset of jets with respect to the centre of gainer is taken into account. Schmitt et al. (2009) argued that they may have underestimated the continuum contribution to the Hα band.

Bonneau et al. (2011) carried out spectro-interferometric observations of β Lyr in Hα, and Hβ regions using the CHARA/VEGA instrument (Mourard et al., 2009). Although their resolution was too low to resolve the orbit (their resolution was similar to that of Schmitt et al., 2009), they studied visibility and differential visibility variations with the orbital phase in a direction perpendicular to the disk (aligned with the jets). They found that the extent of line-forming regions varies and tentatively suggested existence of a hotspot that is being obscured during the secondary eclipse.

5.2 Observational material

The available observational material consists of a large number of spectro-interferometric observations from CHARA/VEGA, CHARA/MIRC and NPOI. These are supplemented with earlier spectroscopic and photometric observations already used by Harmanec and Scholz (1993) and

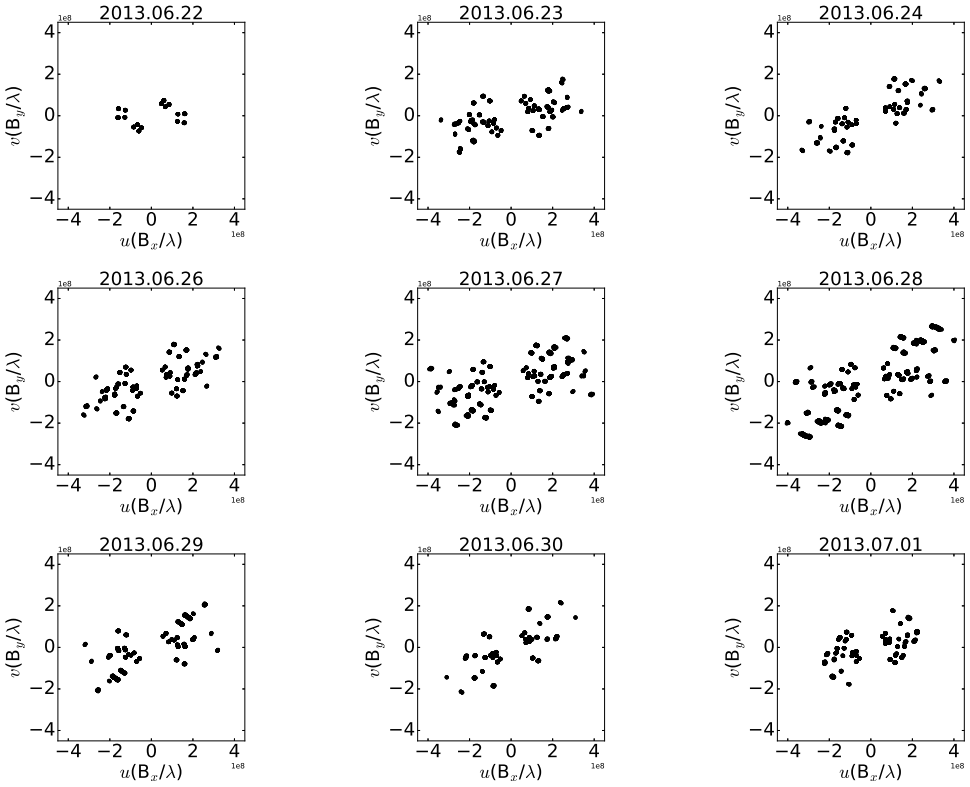

Figure 5.1: The Fourier plane coverage with CHARA/VEGA observations acquired during each night of the 2013 campaign. In each panel: u denotes the spatial frequency for a baseline oriented in east-west direction, and v denotes the spatial frequency for a baseline oriented in north-south direction. The acquisition date is given above each panel in format "yyyy-mm-dd".

Ak et al. (2007) and with series of new spectroscopic observations acquired at Ondřejov observatory and photometric observations at Hvar observatory.

5.2.1 Spectro-interferometric observations

I reduced the 2013 series of spectro-interferometric observations acquired with instrument CHARA/VEGA. These data have the highest spatial resolution. Therefore these data are introduced in greater detail here. A journal of β Lyr spectro-interferometric observations is in Table 5.2.

CHARA/VEGA observations

β Lyr was observed almost exclusively during nine nights with the CHARA/VEGA instrument. The coverage of the Fourier plane by each night's observations is given in Fig. 5.1. The orbital plane of β Lyr is oriented roughly in the east-west direction on the sky. The majority of baselines is aligned with the orbital plane, because in the perpendicular direction (aligned with jets) β Lyr is more extended ($\gtrsim 2$ mas according to Bonneau et al., 2011) and if the baselines were oriented in this direction, the object could be easily over-resolved (meaning that the overall visibility would be very close to zero) on long baselines.

Nine observations were taken with only two telescopes co-phased and 55 observations with three telescopes co-phased. The spectra were taken in four regions $\Delta\lambda \in \{[520, 550]\,, [640, 682]\,, [685, 725]\,, [805, 845]\}$ nm and in medium resolution $R \simeq 5000$. These regions contain three prominent spectral lines Hα, He I 6678 Å, and He I 7065 Å. The spectra were recorded with two cameras simultaneously, each pointed at one of the above-listed passbands. The observations were reduced using a standard procedure (see Sect. 2.2.2 and references therein). The frames were recorded with a frequency 100 Hz and were grouped into blocks of 2500 frames. Within

Table 5.1: A journal of calibrators that were used for the calibration of β Lyrspectro-interferometric observations acquired during the 2013 campaign with CHARA/VEGA instrument. The uniform-disk angular diameters were taken from Lafrasse et al. (2010). The listed parameters are the following: $T_{\rm eff}$ denotes the effective temperature, $\log g$ the surface gravitational acceleration, V (K) the magnitude in Johnson V (K) filter, and $\theta_{\rm V}$ ($\theta_{\rm K}$) the uniform disk diameter in Johnson V (K) filter.

Star	Spectral type	$T_{\rm eff}$ (K)	$\log g$ (dex)	V (mag)	K (mag)	$\theta_{\rm V}$ (mas)	$\theta_{\rm K}$ (mas)
HD 176437	B9 III	10500	3.4	3.234	3.122	0.650	0.669
HD 192640	A2 V	9000	4.2	4.946	4.422	0.450	0.466
HD 189849	A4 III	8750	3.3	4.652	4.179	0.439	0.511
HD 168914	A7 V	7600	4.2	5.119	4.477	0.445	0.464

Table 5.2: Journal of spectro-interferometric observations of β Lyr. ΔT denotes the time span of the whole dataset $\Delta\lambda$ the *effective wavelength* span of the whole dataset, ΔB the projected baseline span of the whole dataset, $N_{\rm V^2}$ the number of squared visibility measurements, and $N_{\rm T_3\phi}$ the number of closure phase measurements. [1]The 2007 β Lyr campaign that has been already studied by Zhao et al. (2008). [2]The 2013 β Lyr campaign.

Instrument	ΔT (RJD)	$\Delta\lambda$ (nm)	ΔB (m)	$N_{\rm V^2}$	$N_{\rm T_3\phi}$
CHARA/VEGA	56465–56476	530–832	54–246	7244	–
NPOI	56463–56471	561–861	12–53	6660	2182
CHARA/MIRC[1]	54024–54293	1515–1776	81–330	858	556
CHARA/MIRC[2]	56463–56471	1491–1736	33–330	4154	4978

these blocks the frames were coherently summed and the observables ($|V|^2$, δV, $\delta\phi$) were derived for the summed image. The majority of observations consists of 20 blocks.

For $|V|^2$ two narrow bands were chosen in each studied passband. Width of each passband ranges from 10 to 20 nm. Each passband lies outside the three prominent stellar spectral lines listed in previous paragraph. It contains weak spectral lines, but they are completely wiped out by the low spectral resolution. The region $[685, 725]$ nm is affected by atmospheric water vapour lines, but those are also blurred by the low spectral resolution. We did not estimate the closure phase, because the observations were either taken for only two telescopes, or because fringes were not detected for the longest baseline, because β Lyr was already over-resolved for this baseline. A calibrator was observed before and after each β Lyr observation (with a few exceptions). The transfer function was determined as the ratio between the theoretical squared visibility of a calibrator represented by a uniform disk and measured raw visibility. The transfer function at the mid-exposure of β Lyr was determined by linear interpolation between two surrounding calibrator observations (where available), or by the nearest calibrator. The calibrators were taken from Lafrasse et al. (2010) and chosen using the tool SearchCal (Bonneau et al., 2006). A journal of all calibrators is in Table 5.1.

The differential visibility and differential phase variations were estimated for all three major spectral lines. They were scanned with scientific channels 10, 5, and 2 Å wide with the step half the width of the scientific channel. After removal of the residual atmospheric piston, the continuum level of the differential visibility was calibrated with the $|V|^2$ estimated from the surrounding continuum channels. We could not increase the resolution of the differential visibility (by making the width of the scientific channel lower than 2 Å), because the signal in the scientific channel was too low.

NPOI and CHARA/MIRC observations

The observational campaign was joined by teams operating the CHARA/MIRC and NPOI instruments.

MIRC is an instrument capable of coherent combination of light from six telescopes (i.e. all telescopes of the CHARA array). The new observations were acquired in the H band. The low-resolution H-band spectrum ($R \simeq 300$) is split into eight pass-bands. Hence de-correlation

Table 5.3: Orbital elements of β Lyr based on previous studies that are listed in column "Source". Note that different authors came up with slightly different values (often not within one-σ). $T_{\rm min}$ denotes reference primary minimum epoch, $P(T_{\rm min})$ the period at the reference minimum epoch, $\dot{P}$ the linear change of the orbital period, a the semimajor axis, q the mass ratio, e the eccentricity, ω the argument of periastron, i the inclination, and Ω the longitude of the ascending node.

Element	Unit	Value	Source
$T_{\rm min}$	(RJD)	8247.968±0.015	Ak et al. (2007)
$P(T_{\rm min})$	(d)	12.913779±0.000016	Ak et al. (2007)
$\dot{P}$	(d d^{-1})	(5.9977±0.0057).10^{-7}	Ak et al. (2007)
a	($R_\odot$)	58.4±1.0	Linnell (2000)
q		0.223±0.010	Harmanec and Scholz (1993)
e		0.0	Harmanec and Scholz (1993)
ω	(deg)	90	Harmanec and Scholz (1993)
i	(deg)	92.25±0.82	Zhao et al. (2008)
Ω	(deg)	254.39±0.83	Zhao et al. (2008)

introduced by use of polychromatic light is negligible. We had also granted access to the observations that have been already analysed by Zhao et al. (2008). In case of the earlier observations, only four CHARA telescopes were co-phased.

NPOI observations were acquired simultaneously with those acquired by VEGA. The light from all telescopes is dispersed into 16 channels and recorded simultaneously (the so-called classic combiner). One of these bands $\lambda_{\rm eff} = 656.8$ nm unfortunately falls into Hα.

A journal of both CHARA/MIRC and NPOI observations is in Table 5.2.

5.3 Distribution of the optically thick circumstellar gas

A first step towards determination of gas distribution in β Lyr is determination of the geometry of its opaque parts, because the continuum radiation is almost exclusively formed in the dense optically thick medium, and it contributes also to line radiation. Hence it is beneficial to obtain the continuum image of β Lyr, and then fix it for the following analysis of the line-forming regions.

In my analysis I used orbital elements determined by previous investigators of β Lyr. They are listed in Table 5.3. Also throughout this section "primary" refers to the gainer and "secondary" to donor.

5.3.1 Night-by-night analysis of CHARA/VEGA observations

First we attempted to model the CHARA/VEGA observations only. We constructed a very simple model consisting of a homogeneous cylinder (representing the accretion disk around the gainer) and a homogeneous sphere (representing the donor). The radiative model was also very simple. Each object was assigned an effective temperature and the intensity was computed from the Planck law for a given effective temperature. The position of each object on the sky was given by orbital elements listed in Table 5.1.

This model was fitted to observations from each night separately. Five parameters were fitted: the donor radius, the donor temperature, the accretion disk radius, the accretion disk height, and the accretion disk temperature. The gainer was assumed to be completely obscured by the accretion disk. The results from this attempt are shown in Table 5.4. The best-fitting properties vary significantly from one night to another often reaching values which are completely inconsistent with the overall picture of β Lyr based on previous studies of the system. This is not encouraging because the best-fit was searched with a robust Bayesian global-minimisation technique MULTINEST (Feroz and Hobson, 2008; Feroz et al., 2009, 2013). The CHARA/VEGA observations might not constrain the geometry and the radiative properties well, although the baselines are well-distributed in both lengths and orientations (see Fig. 5.1). Also the observations were carried out in two different bands, which should constrain temperatures as well. This model was able to fit the general trend of the squared visibility well (see

Table 5.4: The best-fitting model to first four CHARA/VEGA observations of β Lyr. Data from each night (in format yyyy.mm.dd) were fitted separately with a simple analytic model (see Sect. 5.3.1 for details). ϕ_{orb} denotes the orbital phase based on the ephemeris from Ak et al. (2007), R_{d} the donor radius, T_{d} the donor temperature, R_{g} the accretion disk radius, H_{g} the accretion disk height, T_{g} the accretion disk temperature, and χ^2_{R} the reduced chi-square.

		Night			
Parameter	Unit	2013.06.22	2013.06.23	2013.06.24	2013.06.26
ϕ_{orb}		0.66	0.73	0.81	0.97
R_{d}	(mas)	0.350 ± 0.044	0.436 ± 0.059	0.269 ± 0.037	0.288 ± 0.034
T_{d}	(K)	15830 ± 1500	12130 ± 1350	18900 ± 3110	19900 ± 2300
R_{g}	(mas)	0.959 ± 0.040	0.802 ± 0.069	0.639 ± 0.023	0.700 ± 0.077
H_{g}	(mas)	0.374 ± 0.051	0.260 ± 0.051	0.37 ± 0.072	0.371 ± 0.140
T_{g}	(K)	9160 ± 700	10090 ± 1030	11330 ± 1850	7300 ± 800
χ^2_{R}		5.4	7.5	6.1	8.4

some selected fits in Fig. 5.2), but the results varying from night to night suggest that the model was given too much freedom. Purely from the statistical point of view the fits should be dismissed as incorrect, because the reduced chi-square $\chi^2_{\mathrm{R}} \in [5, 10]$.

5.3.2 A global model for β Lyrae

The results presented in Sect. 5.3.1 show that the radiative properties of β Lyr are not constrained well. Hence for the consecutive analysis we decided to improve the radiative model of the donor. The model that I describe here is implemented within the tool SIMTOI[1] (Kloppenborg and Baron, 2012b,a).

This tool was designed primarily for the interpretation of spectro-interferometric observations, but it is also able to model photometric observations. The software comes with a GUI, which makes the tool very easy to start with, but also with a minimal scripting environment only, which makes its usage a bit cumbersome. *SIMTOI* comes with models, which turned out to be a sufficient start for β Lyr in the continuum. The orbital model did not include the secular advance of the period, hence I had to add it myself, and my changes were later added to SIMTOI by Dr. Kloppenborg.

In the improved model the gainer remains the same, but the donor is represented by a Roche-lobe filling star. The emergent intensity is still given by the Planck law, but it now includes gravity brightening given by von Zeipel law (see Eq. 3.14), and limb-darkening represented by a quadratic limb-darkening law. The coefficients of the law were taken from Tables computed by Claret and Bloemen (2011) using the nearest grid point. The passband flux is not weighted by a corresponding transmission function, but only computed for a single effective wavelength. The offset between the synthetic and observed light curves is estimated from the magnitude difference between the first observation and the corresponding synthetic value.

5.3.3 Overview of preliminary analysis

I have made preliminary comparisons of the model that was described in Sect. 5.3.2 to the available spectro-interferometric and photometric observations. I have not carried out fitting, because it currently takes an excessive amount of time. Computation of χ^2 for all available spectro-interferometric data and a *subset* of photometric observations takes five to ten minutes. Therefore I intend to find a valid model and then optimise its parameters by an automatic χ^2 minimisation algorithm.

The model is very similar to that devised by Linnell (2000), the main difference between his and my model lies in the model for the accretion disk. His disk consists of two parts — hot inner disk with temperature $T_{\mathrm{eff}} = 30000\,\mathrm{K}$, and cool outer outer ring with temperature $T_{\mathrm{eff}} = 9000\,\mathrm{K}$. My disk is uniform with a temperature $T_{\mathrm{eff}} = 9000\,\mathrm{K}$. Our model should also account better for the limb-darkening of the donor, because the latest limb-darkening coefficients (Claret and

[1] The tool is available at `https://github.com/bkloppenborg/simtoi`

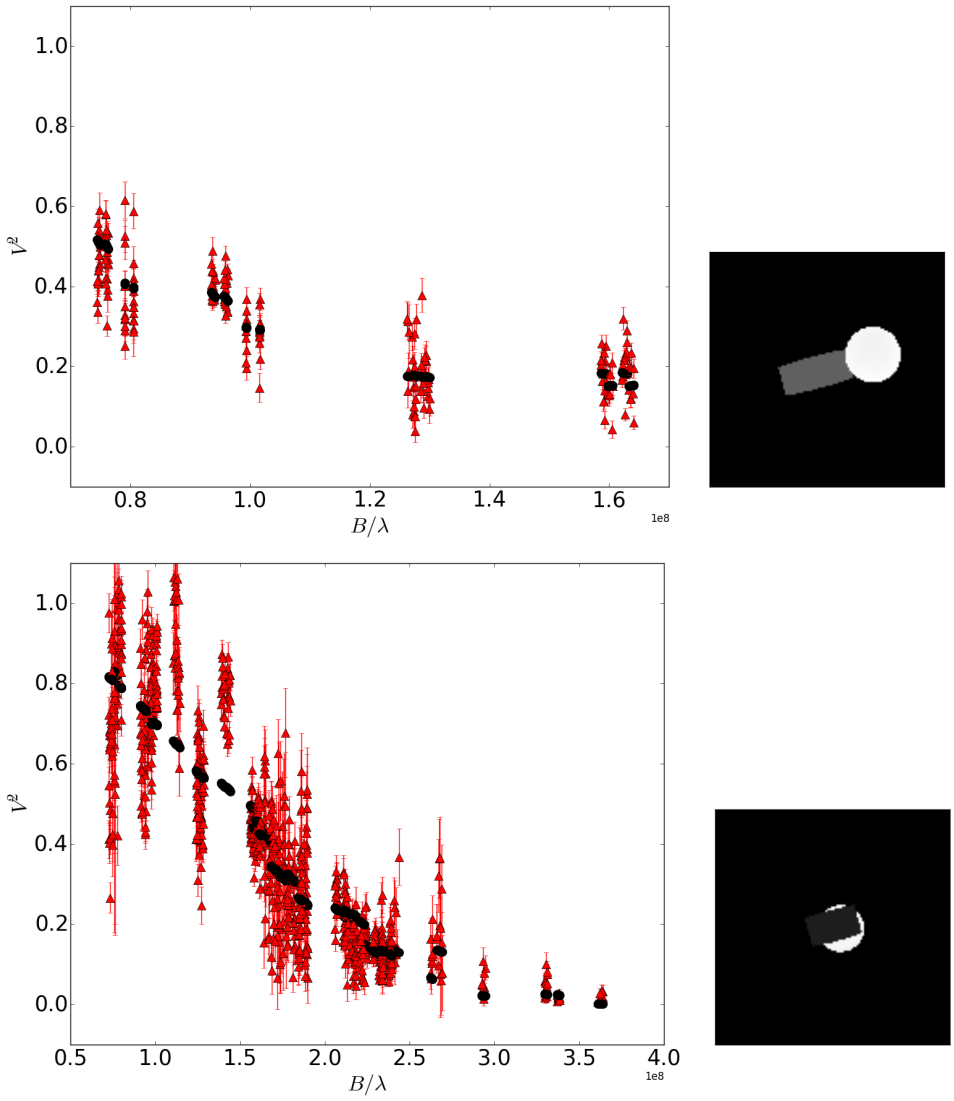

Figure 5.2: A fit of simple analytic model described in Sect. 5.3.1 to data from two nights. Diagrams on the left show observed squared visibility V^2 as a function of spatial frequency B/λ (B is the projected baseline length and λ the wavelength), and diagrams on the right show the β Lyr model as it would appear on the sky. The vertical axis is aligned with north-south direction and the horizontal axis with the east-west direction. The parameters corresponding to the best fitting model are in Table 5.4. *Upper panels* show the best fit of the model to CHARA/VEGA observations from night 2013.06.22 which have the mean orbital phase $\phi_{\rm orb} \simeq 0.66$, and *lower panels* the best fit of the model to CHARA/VEGA observations from night 2013.06.26, which have the mean orbital phase $\phi_{\rm orb} \simeq 0.97$.

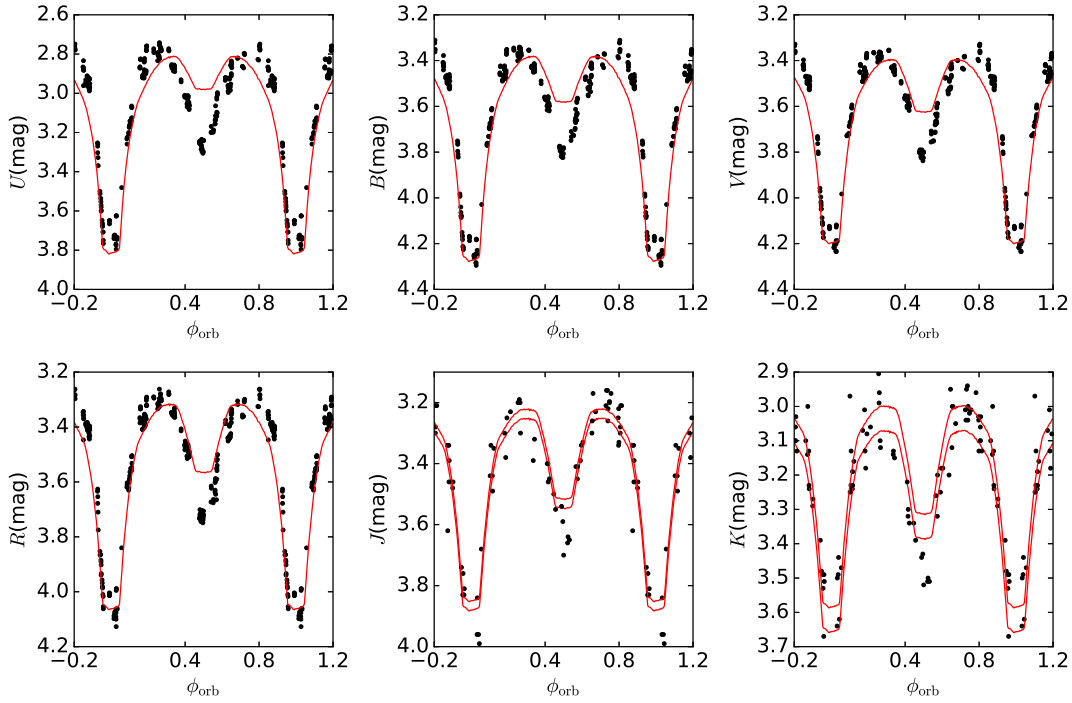

Figure 5.3: A comparison of visible and infrared light curves of β Lyr (denoted by the black dots) and a synthetic light curve produced for a model described in Sect. 5.3.2 in the program *SIMTOI*. U, B, V, R, J, K are the Johnson filters. There are two synthetic light curves plotted for J and K passbands, because these were acquired at two different observatories and were fitted independently. $\phi_{\rm orb}$ is the orbital mean phase based on the ephemeris determined by Ak et al. (2007).

Bloemen, 2011) were used. The absolute dimensions of the model were transformed to angular scale using the Hipparcos parallax.

A comparison of observed visible and infrared light curves and those produced with my model is in Fig. 5.3. The model is roughly able to explain the ellipsoidal variations, but it does not reproduce the observed depths of minima correctly, especially the secondary eclipse. This discrepancy is less pronounced in the infrared, which means that the uniform disk is insufficient model and we can clearly see inner parts of the accretion disk or even the star embedded in its centre. Infrared data suffer from a large scatter and have poor phase coverage. The scaling was more difficult here.

First I checked whether there are any ambiguities in the orbital inclination and the longitude of the ascending node. *SIMTOI* model clearly prefers $i \simeq 88\,\mathrm{deg}$ over $i \simeq 92\,\mathrm{deg}$ reported by Zhao et al. (2008). This is demonstrated by Fig. 5.4, where a comparison between the observed and synthetic closure phase for both inclinations is shown. This difference does not point at discrepancy in our model or that of Zhao et al. (2008), but likely at a difference in the choice of reference frames. Position of both components is determined following the Eqs. (3.16)–(3.18) with the beginning of the reference frame in the binary barycentre, while Zhao et al. (2008) used relative positions of the gainer with respect to the donor.

We performed a grid search of the χ^2 in the inclination i and the ascending node longitude Ω. The best fit was found for $i = 89\,\mathrm{deg}$ and $\Omega = 242\,\mathrm{deg}$. While the overall fit was not very sensitive to the inclination, the reduced chi-square varied significantly with the longitude of the ascending node. The $\Omega = 242$ is $\simeq 12\,\mathrm{deg}$ lower then the value reported by Zhao et al. (2008) and by $\simeq 7\,\mathrm{deg}$ lower than ascending node longitude reported by Schmitt et al. (2009). The low ascending node length is preferred by visible data (CHARA/VEGA, NPOI), while the infrared data prefer a value similar to that reported by Zhao et al. (2008). The reduced chi-square for data from individual instruments for two different ascending node longitudes are the following:

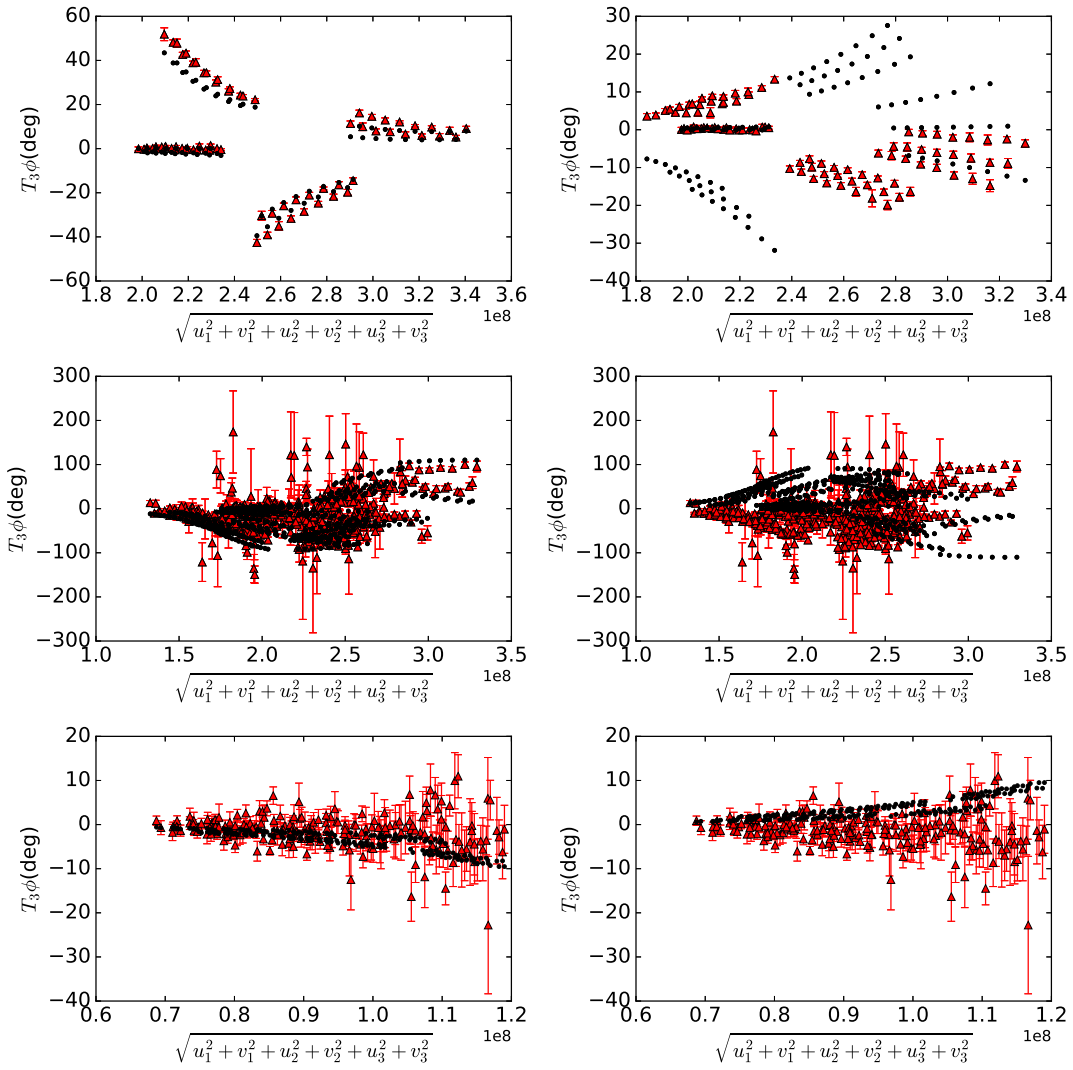

Figure 5.4: A comparison of the observed (red triangles) and synthetic (black points) closure phase. *Panels on the left* were computed for a model similar to that of Linnell (2000) and transformed to angular scale using the Hipparcos parallax (see Sect. 5.3.2 for description of the model). The orbital inclination was set to $i = 88\,\mathrm{deg}$. *Panels on the right* correspond to a mirror solution $i = 92\,\mathrm{deg}$, which is clearly inconsistent with the data. *Top panels:* MIRC H-band observations acquired on JD $\simeq$ 2454288.7 (7^{th} Jul 2007). *Middle panels:* MIRC H-band observations acquired on JD $\simeq$ 2456471.8 (28^{th} Jun 2013). *Bottom panels:* NPOI visible observations acquired on JD $\simeq$ 2456471.8 (28^{th} Jun 2013).

	Instrument		
Ω (deg)	CHARA/VEGA	NPOI	CHARA/MIRC
242	19	13	105
254	23	15	39

Although the increase of the reduced chi-square for the visible data is not as dramatic as the decrease for the infrared data, systematic discrepancies arise for short-baseline visible data. For short baselines, which lie in the orbital plane the model predicts much lower visibility than we actually see. This finding is demonstrated in Figs. 5.5 and 5.6. The effect is probably present even for long baselines, but it is not so pronounced since the overall visibility is low.

This discrepancy again suggests that the radiative model of the accretion disk is too simple, which is not that surprising, because already Linnell (2000) reported that a homogeneous disk is an insufficient model for the photometric observations. The data suggests that in the visible the photocentre of the accretion disk is shifted with respect to that in the infrared. Also the object might be less resolved in the visible, because the overall synthetic visibility is below the observations.

One possible explanation (and possibly the simplest one) is that due to non-zero orbital inclination, we can see inner hot parts of the disk. Such an effect would produce a shift of the photocentre and would make the disk more point-like, especially in the visible. A two-component (or more complex) model is not implemented within *SIMTOI*. The program cannot be cheated by embedding a hotter disk into cooler one, because it led to errors in the rendering of the model. Hence we have to implement a two-component disk, or to create my own model. The latter scenario is more likely because there are some debatable design choices in *SIMTOI* such as:

- Each object has its own completely independent set of orbital elements. Hence one is obliged to fit more parameters than necessary.
- Each object is decoupled from its orbit. The Roche-lobe model is independent of its orbital elements. This again forces the user to fit additional, unnecessary parameters.
- The program can only be handled through a GUI which makes its modification difficult, because any change has to be also propagated into the GUI.
- The program writes/plots an excessive amount of information on the standard output. This necessarily slows down the computation.

Additional effects that may change the intensity distribution on the accretion disk and which are wavelength-dependent are the scattering and opacity. The opacity drops significantly towards the infrared, meaning that the opaque part of the disk may appear less extended in the infrared. On a possible role of the scattering may point the fact that the night-by-night analysis predicted a smaller accretion disk around the primary eclipse. Nonetheless I have not evaluated the role of these effects yet.

Throughout the Sects. 5.3.1 and 5.3.2 I have presented fits whose $\chi^2_{\mathrm{R}} \simeq 10$ and statistically speaking these models are wrong. At least for CHARA/VEGA the uncertainty of the calibrated visibilities is severely underestimated by the automatic reduction procedure. This can be seen in Figs. 5.5, and 5.6 the variations of the visibility due to diurnal motion are redundant, but the visibility (vertical) spread of an observation is higher than a typical uncertainty of one point. The true uncertainty should be comparable to this spread.

5.4 Future work on β Lyrae

As already mentioned, β Lyr is still work in progress. My primary goal now is to prepare a program in which different models of the opaque parts could be easily implemented and adapted to our needs and which would not suffer from the problematic design choices made in *SIMTOI* and listed in Sect. 5.3.2. Given the complexity of the object we shall see if it is possible to create a "toy model" of the accretion disk, which would fit the observations sufficiently in both the visible and infrared passbands.

The analysis of the differential visibility and phase measured by CHARA/VEGA instrument will follow the analysis of the continuum radiation. I started preparing a model for the

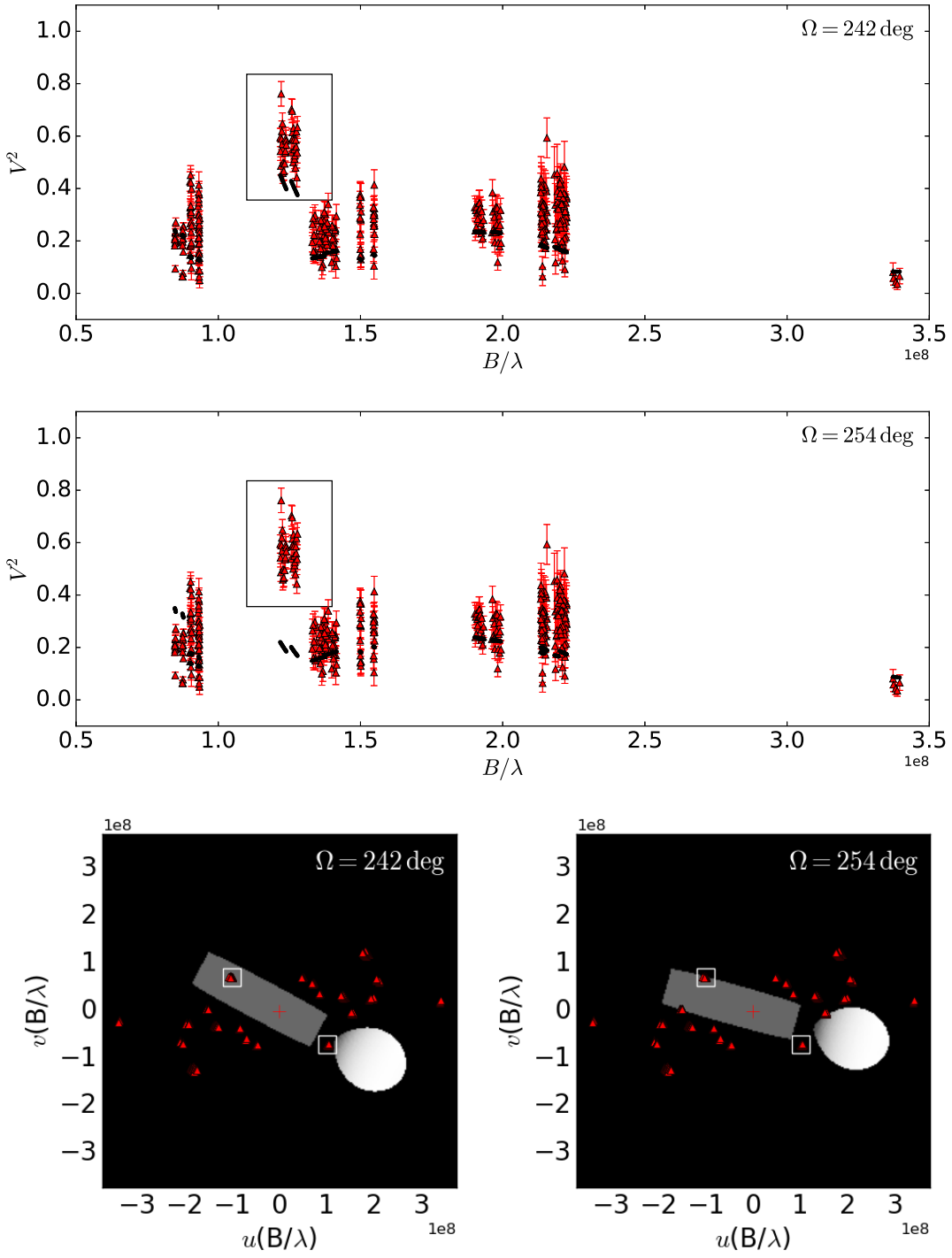

Figure 5.5: A comparison of observed and synthetic squared visibility for CHARA/VEGA observations for $JD \simeq 2456467$ (night of the 23$^{\text{rd}}$ Jun, 2013). *Top panel* shows comparison of the β Lyr model described in Sect. 5.3.2 for the longitude of the ascending node $\Omega = 242$ deg. The model as it would appear on the sky is shown in the *bottom left panel*. The baseline showing a systematic difference is emphasised by a black box. *Middle panel* shows the comparison of the same β Lyr model the longitude of the ascending node $\Omega = 254$ deg. The model as it would appear on the sky is shown in the *bottom right panel*. The baseline showing a systematic difference is emphasised by a black box. *Bottom panels* show the on-sky model. The vertical axis is aligned with the north-south direction and the horizontal axis with the east-west direction. Over these images the the coverage of the Fourier plane is plotted as a function of spatial frequencies (u, v). The baseline that is producing the error is emphasised by a white box.

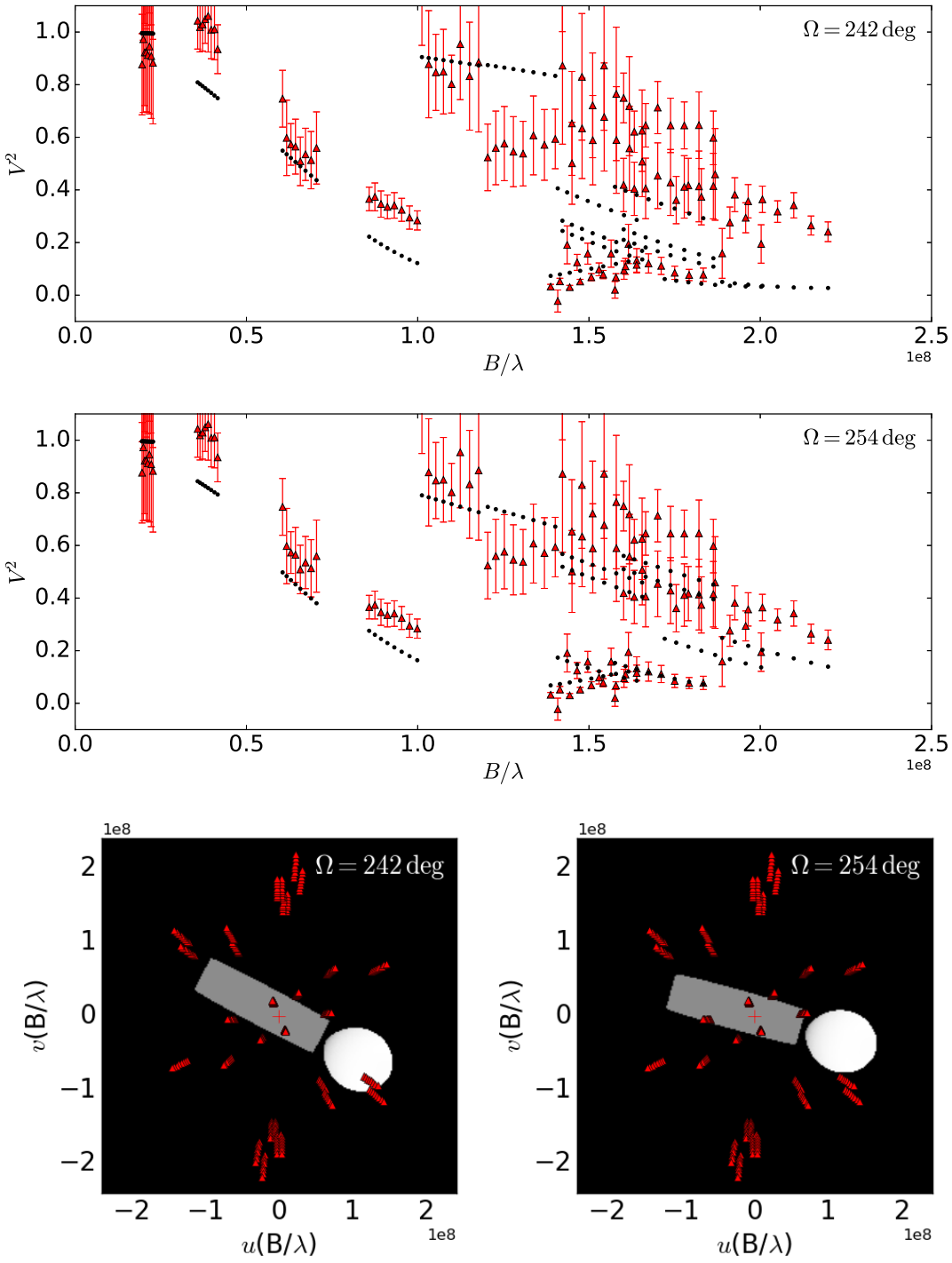

Figure 5.6: A comparison of observed and synthetic squared visibility for CHARA/MIRC observations for $JD \simeq 2456466$ (night of the 22$^{\rm rd}$ Jun, 2013). *Top panel* shows comparison of the β Lyr model described in Sect. 5.3.2 for the longitude of the ascending node $\Omega = 242$ deg. The model as it would appear on the sky is shown in the *bottom left panel*. *Middle panel* shows comparison of the same β Lyr model the longitude of the ascending node $\Omega = 254$ deg. The model as it would appear on the sky is shown in the *bottom right panel*. *Bottom panels* show the on-sky model. The vertical axis is aligned with the north-south direction and the horizontal axis with the east-west direction. Over these images the the coverage of the Fourier plane is plotted as a function of spatial frequencies (u, v). The improvement is seen especially for high visibility and spatial frequencies ($\gtrsim 10^8$). Those are generally baselines that are perpendicular to the orbital plane.

transparent medium and its current state is outlined in Sect. 3.1.3. For the moment, it has not been finished or tested on real data.

If I am successful, and the model turns out to be a sufficient representation of the data, the geometrical distribution of the circumstellar matter in β Lyr would provide and excellent test object for models of the binary mass transfer.

6. Program description

In the course of my master and doctoral studies I developed a few tools for the interpretation and/or reduction of binary observations. In this chapter I briefly describe three tools that I developed to a degree which makes them applicable to more objects and not just the one for which they were originally designed. The tools are the following: (i) Program *ERV* for the measuring of RVs through comparison of the observed and template spectra. (ii) Program *FRV* for the interpretation of RV-curves of hierarchical multiple stellar systems. (iii) *FV* for the interpretation of interferometric fringe visibility and closure phase of detached binaries and triple systems.

All these tools were originally tailored to application on ξ Tau system (see Chap. 4). Although I carried out basic debugging of the program, all these tools carry out only small-to-none check of the input. Hence it may still contain minor bugs and inputting and incorrect input may not always result into crash of the program but to incorrect results. As the development was driven by "need", the manipulation with the programs, readability of the code, and format of the input and output are sometimes not very user-friendly. The source code of all programs is commented on though. Since all these tools are written in Python a basic knowledge of this programming language is helpful when dealing with problems or adapting the program to one's needs. Python is a multi-platform interpreted language, hence the program should work on any operating system with the required version of the interpreter and libraries installed.

I have also developed a more complex tool for the estimation of radiative properties of multiple systems through comparison of observed and synthetic spectra called *Pyterpol*. A thorough description of the tool along with installation directions, and tutorials can be found at `https://github.com/chrysante87/pyterpol`. This is thus the only program, which was designed to be used by other people and I encourage anyone interested to try it.

6.1 Measuring of radial velocities through a comparison of observed and template spectra

The program *ERV* compares *any* template spectra with observed normalised spectra in order to estimate RV of its components. In contrast to *Pyterpol*, which can also estimate RV, but only through comparison of *synthetic* and observed spectra, *ERV* can use any template, e.g. disentangled or observed spectra. The search for the optimal parameters is carried out through minimisation of the χ^2 given by Eq. (2.36). Arbitrary number of wavelength intervals and components can be fitted.

6.1.1 Execution of the program

The program *ERV* is compatible with Python in version 2.6.x or 2.7.x. The program also requires three Python libraries: (i) NumPy (version $\geq$ 1.10.x), (ii) SciPy (version $\geq$ 0.15.x), and (iii) Matplotlib (version $\geq$ 1.2.x). The program is controlled through a few arguments. Their list is the following:

Execution		python ERV.py -f *arg1* -rv0 *arg2* -korel
Argument	Type	Description
-f	M	Name of the control file including path.
-rv0	O	List of initial RVs.
-korel	O	Indicates that template spectra come from the spectral disentangling.

M denotes *mandatory* argument, and O *optional* argument. Description of the control file and the initial list of radial velocities is in Sect. 6.1.2. The minimum of the χ^2 is searched either globally by the differential evolution algorithm (Storn and Price, 1997) if the user does not provide a list of initial RVs, or locally by Powell's conjugate directions method (Powell, 1964) if the list is supplied. If the optional flag "-korel" is not provided the template spectra representing individual components are summed according to Eq. (2.36). Otherwise $k-1$ is subtracted from the combined disentangled template spectra, where k is the number of template spectra.

6.1.2 Description of input files

The program is controlled through a control file, whose structure is the following:

```
 1  WORKDIR                  hemg
 2  OBSERVEDSPECTRALISTFILE  d43604570.lis
 3  TEMPLATEFILELIST         3
 4  DE.free.03.dat
 5  DE.free.01.dat
 6  DE.free.02.dat
 7  LIMITS                   2
 8  4455  4495
 9  6330  6600
10  RESULTFILE               d43604570hemg.lis
11  PLOTLIMITS               4455  4495  0.80  1.05
```

The format of the control file is mandatory. The upper case words identify individual keys within the control file. Here is a line-by-line description of the input file:

Line	Description
1	Name of a folder, where the output will be stored. If the folder does not exist, it will be created.
2	An ASCII list of observed spectra. The list contains two columns: column1 = filename, column2 = hjd. Each observed spectrum has to be in ASCII format and contain three columns: column1 = wavelength, column2 = relative flux, column3 = uncertainty of the relative flux.
3	Number of template spectra.
4–6	A list of names of files containing template spectra. Each template has to be in ASCII format and contain two columns: column1 = wavelength, column2 = relative flux.
7	Number of fitted wavelength intervals.
8–9	Each line contains the lower and upper wavelength limit of one fitted passband.
10	Name of the output file. The measured RVs are stored in this file.
11	Limits of the plot. The first two records are the minimal and maximal wavelength and the latter two are limits in the relative flux.

The observed spectra do not have to be equidistant or even sorted in the wavelength. Template spectra have to be sorted in wavelength, but do not have to be equidistant. The format of the (optional) file containing initial estimates of RV is the same as that of the output file containing the RV measurements (line 10). Its format is described in Sect. 6.1.3.

6.1.3 Description of output files

The format of the output file (whose name is defined in the control file), where the measured RVs are stored, is the following:

Column	Description
1	Name of the observed file.
2	Time of observation (e.g. HJD, BJD, RJD, years).
3–k+2	These columns contain RV measurements for the k templates. The order of RVs is the same as the order of templates in the control file.
k+3	The initial χ^2.
k+4	The final χ^2.

The program also plots a comparison of observed spectra and the best fitting combined template spectra in the wavelength range specified in the control file.

6.2 Orbital solution of multiple systems

The program *FRV* was developed for the interpretation of RVs of hierarchical multiple systems consisting of up to three orbits. The orbital model is given by Eqs. (3.4)–(3.6) which represent a slightly modified Keplerian model. The optimal model is searched by the minimisation of the χ^2 given by Eq. (3.7).

6.2.1 Execution of the program

The program *FRV* is compatible with the Python interpreter in versions 2.6.x and 2.7.x. The program also requires two Python libraries: (i) NumPy (version $\geq$ 1.10.x), and (ii) SciPy (version $\geq$ 0.15.x). The program is controlled through several arguments. Their list is the following:

Execution		python FRV.py -pf *arg1* -df *arg2* -o *arg3* -d
Argument	Type	Description
-pf	M	Name of the control file.
-df	M	Name of the file containing list of files with measured RVs. Each line of the file contains name of a file with RV measurements.
-o	M	Name of the output file.
-d	O	Turns on debug mode, in which more pieces of information on the run of the program are printed to the standard output. The user unfamiliar with the source code should not use this flag.

M denotes *mandatory* argument, and O *optional* argument. Description of the control file and the input files containing measured RVs is in Sect. 6.2.2. The minimum of the χ^2 is searched with the sequential least square method (Kraft, 1988) and Newton's conjugate gradient method (see Press et al., 2002, p.515-519). Both these methods are local and allow the user to set boundaries for each optimised parameter. The program performs several optimisation runs always starting from the best point from the previous run. This way it is partially secured that the program does not end up in a local minimum, while a global (or a deeper local minimum at least) is nearby. Uncertainties of the fitted parameters are determined from a Hessian constructed at the χ^2 minimum.

6.2.2 Description of input files

The input files consist of a control file and a list of ASCII data files containing the RV measurements. An example of the control file for a triple system is the following:

```
 1  K        10      38.39253        30      50      0.0     1
 2  q        10      0.86227         0       10      0.0     1
 3  e        10      0.20303         1e-05   0.4     0.0     0
 4  o        10      5.07227         0       50      0.0     0
 5  T0       10      55608.3419      55600   55615   0.0     0
 6  P        10      145.63805       145.1   146     0.0     0
 7  do       10      3.27591         0       10      0.0     0
 8  K        0       87.97996        75      100     0.0     0
 9  q        0       0.94614         0       10      0.0     0
10  e        0       0               1e-08   0.98    0.0     0
11  o        0       90              0       360     0.0     0
12  T0       0       56224.70726     56223   56225   0.0     0
13  P        0       7.14665         7.14    7.15    0.0     0
14  do       0       0               -10     10      0.0     0
15  gamma    0       9.056187988     -20     20      0.0     1
16  gamma    1       9.201670744     -20     20      0.0     1
17  gamma    2       9.722777694     -20     20      0.0     1
```

The order of columns is mandatory the order of rows is arbitrary. Description of the columns is the following:

Column	Description
1	Identification of an orbital element. K is the semiamplitude of RV-curve (typically) in km.s^{-1}, q the mass ratio, e the eccentricity, o the periastron argument in deg, $T0$ the periastron passage epoch, P the period, do the linear apsidal advance in deg yr^{-1}, and γ the systemic RV. For each fitted orbit, initial values of all listed orbital elements must be given.
2	For all orbital elements except the systemic velocity (i.e. K, q, e, o, $T0$, P, and do) the number denotes an orbit in the hierarchy. The innermost orbit is labelled 0, the intermediate orbit 10, the outermost orbit 20. When building a multiple system the labelling always starts from the inner orbit. Hence a binary will contain only one orbit labelled 0, a triple system two orbits labelled 0 (inner orbit) and 10 (outer orbit). For systemic velocity this number serves as an identification of a dataset. Hence for this particular example our data are split into three datasets. An independent systemic velocity is derived for each dataset.
3	The initial value of the parameter.
4	Lower bound of the interval searched by the minimisation routine.
5	Upper bound of the interval searched by the minimisation routine.
6	Uncertainty of a parameter.
7	Flag saying which parameter is fitted (1) and which remains fixed (0).

The format of the ASCII file containing the RV measurements, which is similar to that used in the programs SPEL, FOTEL and several reduction programs HEC, is the following:

Column	Description
1	Observation time which has the same unit as the the period and the periastron passage epoch defined in the control file.
2	RV having same unit as the semiamplitude of the RV-curve in the control file.
3	Uncertainty of the RV.
4	Dataset number. The identification number of gamma velocity (column 2 in control file) refers to this number.
5	Component number. Primary component of an orbit has the same number as the orbit, and the secondary component number is increased by one. If an orbit contains a star and centre of mass of an orbit or hierarchy, the latter is always considered primary. Hence notation of components for a binary would be: 0 = primary, 1 = secondary, and for a triple system it would be: 0 = primary of the inner orbit, 1 = secondary of the inner orbit, 11 = tertiary = secondary of the outer orbit.

The program *FRV* fits only those datasets that are defined in the control file, meaning that there is a line in the file defining a systemic velocity for the dataset (lines 15-17 in the example).

6.2.3 Description of output files

The program *FRV* produces two types of output. The first one contains the elements corresponding to the χ^2 minimum found by the minimisation technique and their locally estimated uncertainties. Its structure is *exactly the same* as the structure of the input control file. Hence the output file can be readily used as an input file for another run. The second output consists of files, where the measured and synthetic RVs, orbital phase and residuals are stored. The exact structure of these files depends on the configuration of the studied object. Each column of these files is labelled and the file structure is quite self-explanatory. An independent file is produced for each component and dataset, so the user can evaluate the separately.

6.3 Visibility variations

The program *FV* was developed for the interpretation of squared visibilities and closure phases of interferometric fringes of binaries and triple systems. The orbits are given by a slightly modified Keplerian orbital model (Eqs. 3.16–3.18). The "slight modification" lies in the inclusion

of linear apsidal advance given by Eq. (3.6). Each component is represented by a uniform disk. The synthetic complex visibility for this model is computed through Eq. (3.19). The computation of squared visibility is straightforward, synthetic closure phase is computed according to Eqs. (2.31), and (2.32). The best-fitting model is searched through χ^2 optimisation either locally using the sequential least squares algorithm (Kraft, 1988), and the Newton conjugate gradient method (see Press et al., 2002, p.515-519), or globally through differential evolution algorithm (Storn and Price, 1997). Uncertainties of the fitted parameters are estimated locally from the Hessian matrix.

6.3.1 Execution of the program

The program *FV* is compatible with the Python interpreter in version 2.6.x or 2.7.x. The program also requires three Python libraries: (i) NumPy (version $\geq$ 1.10.x), (ii) SciPy (version $\geq$ 0.15.x), and (iii) Matplotlib (version $\geq$ 1.2.x). The program is controlled through several arguments their list is the following:

Execution		python FV.py -f *arg1* -o *arg2* -m *arg3* -nprint *arg4* -np -debug -chi2only
Argument	Type	Description
-f	M	Name of the control file.
-o	O	Name of the output file.
-m	O	Minimisation engine. The available options are: (i) "slsqp" the sequential least square method, (ii) "tnc" the Newton conjugate gradients method, (iii) "diffevol" the differential evolution method. By default "slsqp" is used.
-nprint	O	Print each nprint-th iteration on the standard output. By default each iteration is printed.
-np	O	Do not plot the final model.
-debug	O	Turns on the debugging mode. The amount information corresponding to the run of the program that is printed on the standard output is greatly increased. This flag should be used only if the user is familiar with the source code.
-chi2only	O	Computes only one comparison for the parameters that are currently stored within the control file.

M denotes *mandatory* argument, and O *optional* argument. Description of the control file and the input files containing records with individual observations are described in Sect. 6.3.2.

6.3.2 Description of input files

The input of the program *FV* consists of a control file and data files. *They have different structure for visibilities and closure phases.* An example of the control file for a triple system[1] is the following:

```
1  #-------------------------------------------------------------
2  NMODEL  3
3  NORBIT  2
4  #-------------------------------------------------------------
5  M1      uniform_disk    0
6         theta       0.3837      0.3200      0.4400  0.0028   1
7            L0       0.6349      0.5500      0.6800  0.0012   1
8            L0       0.6349      0.5500      0.6800  0.0012   1
9  M2      uniform_disk    1
10        theta       0.2510      0.1000      1.0000  0.0000   0
11           L0       0.2005      0.1300      0.2800  0.0019   1
12           L0       0.2349      0.5500      0.6800  0.0012   1
13 M3      uniform_disk    2
14        theta       0.2220      0.1000      1.0000  0.0000   0
15           L0       0.1646      0.1000      0.2500  0.0000   0
16           L0       0.1649      0.5500      0.6800  0.0012   1
```

[1] The positions of individual components can be also unbound. Then each object is assigned two additional parameters x and y defining position of each object on the sky in mas. More powerful tools for the fitting of unbound stars exist (e.g. Tallon-Bosc et al., 2008).

```
17  M4       orbit   0
18               a     15.8249      15.0000      16.5000  0.0073   1
19               e      0.2155       0.1900       0.2400  0.0003   1
20               i     86.6688      85.0000      88.0000  0.0102   1
21               o      9.3695       5.0000      15.0000  0.0436   1
22               O    148.4300     140.0000     152.0000  0.0070   1
23              T0  55609.6941  55608.0000  55611.0000  0.1210   1
24               P    145.4780     145.4000     145.7000  0.0019   1
25              do      2.0435       1.5000       3.0000  0.0132   1
26  M5       orbit   1
27               a      1.7081       1.4000       2.0000  0.0052   1
28               q      0.9155       0.8000       1.1000  0.0242   1
29               e      0.0000       0.0000       0.3000  0.0000   0
30               i     88.9025      80.0000      98.0000  0.3145   1
31               o     90.0000       0.0000     360.0000  0.0000   0
32               O    146.2670     140.0000     153.0000  0.1448   1
33              T0  56224.2787  56224.0000  56224.4000  0.7637   1
34               P      7.1466       0.0000    1000.0000  0.0000   0
35  0
36  #------------------------------------------------------------
37  DATAFILE - WEIGHT, FILTER, TYPE, FILE
38  1.0  filterA  vis  data/vis.dat
39  1.0  filterB  cp   data/cp.dat
40  0
41  #------------------------------------------------------------
42  FITLOG  fit.log
43  RESFILE temp.res
44  METHOD  SLSQP
45  NITER   2000
46  #------------------------------------------------------------
```

The file is divided by dashed lines into four blocks: (i) a header, (ii) a definition of the model, (iii) a list of observations, and (iv) parameters controlling the χ^2 minimisation.

The header consists of two keys NMODEL that says how many stars will be fitted, and NORBIT that determines the number of orbits. NORBIT=0 means that the objects are unbound, NORBIT=1 means that there is at least one orbit binding two objects, and NORBIT=2 means that there are two orbits binding three objects.

In the second block the objects (uniform disks) and their orbits are defined. They are defined separately, because arbitrary number of unbound objects can be added (e.g. a star that is not a member of the studied system, but its angular separation is too small). The block is divided into five parts, three of the defining objects, and two orbits. Each part starts with a header, which has the same structure as the following line:

```
M1 uniform_disk 0
```

The first key indicates that a model will be read. "M" and the counter number (starting from one) are both mandatory. The second key sets the model (eligible options are "orbit", "uniform_disk", and "point_source"). The third key is an integer placing objects into orbits (hence it is not used for model "orbit"). If the object is a binary key3 = 0 denotes primary, and key3 = 1 the secondary. If the object is a triple system then key3 = 0 denotes the tertiary (primary in the outer orbit), key3 = 1 the primary of the inner orbit, and key3 = 2 the secondary of the inner orbit. It is not mandatory to define first the objects and then the orbits, but the order of labels ("M1", "M2", ...) is mandatory. The header is followed by a set of parameters defining the object. Their structure is the following:

Column	Description
1	Identification of a parameter. Parameters of a *uniform-disk* are: *theta* is the uniform disk diameter, and L the relative luminosity. The number of fitted relative luminosities depends on the number of spectral passbands defined in the observation part of the control file. Parameters of an *orbit* are: a is the semi-major axis in mas, q the mass ratio, e the eccentricity, i the inclination in deg, o the argument of periastron in deg, O the ascending node longitude in deg, $T0$ the periastron passage epoch in the units of time used, P the period, *do* the linear apsidal advance in $\mathrm{deg\,yr^{-1}}$. Note that the complex visibility is invariant of the shift of the whole system. Hence the mass ratio of the outer orbit of a triple or the mass ratio of a binary cannot be determined.
2	Value of the parameter.
3	Lower bound of the interval searched by the minimisation routine.
4	Upper bound of the interval searched by the minimisation routine.
5	Uncertainty of a parameter.
6	Flag saying which parameter is fitted (=1) and which remains fixed (=0).

The block ends with a line containing only "0"to indicate that no additional model will be read.

The structure of the third block defining the fitted observations is the following:

Column	Description
1	Global weight for the set of observations.
2	A user-defined name of a spectral region. A separate set of relative luminosities is fitted for each spectral region. Their number depends only on the number of passbands defined in this part of control file.
3	Identification of the observation type. Files containing squared visibilities are denoted "vis" and those containing closure phases "cp".
4	Name of the file containing observations.

Note that the order of filters determines the order of relative luminosities in the second block, where the model is defined. The block ends with a line containing only "0". This signals that no additional observations will be read.

The fourth block contains these parameters: *FITLOG* denotes name of the file, where each iteration is stored, *RESFILE* name of the file, where the the parameters corresponding to the best solution are written, this file is overridden by the command-line argument "-o", *METHOD* the minimisation engine, this parameter is overridden by command-line argument "-m", and *NITER* is the maximal allowed number of iterations. This number does not apply to the global minimisation algorithm, the differential evolution, which requires much larger number of iterations before it converges.

The observation files containing the squared visibility measurements have the following structure:

Column	Description
1	Projection of the baseline into east-west direction in m.
2	Projection of the baseline into north-south direction in m.
3	Time in the same unit as P and $T0$ in the control file.
4	Squared visibility.
5	Uncertainty of squared visibility.
6	Effective wavelength in m.

The observation files containing closure phase measurements have the following structure:

Column	Description
1	Projection of the first baseline into east-west direction in m.
2	Projection of the first baseline into north-south direction in m.
3	Projection of the second baseline into east-west direction in m.
4	Projection of the second baseline into north-south direction in m.
5	Time in the same unit as $T0$ and P in the parameter definition.
6	Closure phase in deg.
7	Uncertainty of closure phase in deg.
8	Effective wavelength in m.

6.3.3 Description of input files

Program *FV* produces several output files. The best-fitting model is written into user-defined output file (flag '-o'). The structure of this file is the same as that of control file and can be readily used as an input file for another run. The program also creates the following additional file, which can help the user to evaluate the result: (i) output_file + suffix ".chi2" contains condensed list of the parameters for the best fitting model along with their uncertainties and the corresponding χ^2. (ii) output_file + suffix ".synth" contains all measured squared visibilities and closure phases and also synthetic values based on the best-fitting model. (iii) output_file + suffix ".rms" contains a list of reduced χ^2 for each individual observation file. (iv) A fitting log, where each evaluation of χ^2 is stored.

Bibliography

H. A. Abt. Normal and abnormal binary frequencies. *Annu. Rev. Astron. Astrophys.*, 21:343–372, 1983. doi: 10.1146/annurev.aa.21.090183.002015.

C. Aerts, M. de Pauw, and C. Waelkens. Mode identification of pulsating stars from line profile variations with the moment method. an example - The Beta Cephei star Delta Ceti. *Astronomy&Astrophysics*, 266:294–306, December 1992.

C. Aerts, J. Puls, M. Godart, and M.-A. Dupret. Collective pulsational velocity broadening due to gravity modes as a physical explanation for macroturbulence in hot massive stars. *Astronomy&Astrophysics*, 508:409–419, December 2009. doi: 10.1051/0004-6361/200810471.

C. Aerts, J. Christensen-Dalsgaard, and D. W. Kurtz. *Asteroseismology*. 2010.

H. Ak, P. Chadima, P. Harmanec, O. Demircan, S. Yang, P. Koubský, P. Škoda, M. Šlechta, M. Wolf, H. Božić, D. Ruždjak, and D. Sudar. New findings supporting the presence of a thick disc and bipolar jets in the β Lyrae system. *Astronomy and Astrophysics*, 463:233–241, February 2007. doi: 10.1051/0004-6361:20065536.

E. J. Aldoretta, S. M. Caballero-Nieves, D. R. Gies, E. P. Nelan, D. J. Wallace, W. I. Hartkopf, T. J. Henry, W.-C. Jao, J. Maíz Apellániz, B. D. Mason, A. F. J. Moffat, R. P. Norris, N. D. Richardson, and S. J. Williams. The Multiplicity of Massive Stars: a High Angular Resolution Survey With the Guidance Sensor. *Astronomical Journal*, 149:26, January 2015. doi: 10.1088/0004-6256/149/1/26.

J. Andersen. Accurate masses and radii of normal stars. *Astronomy and Astrophysics Reviews*, 3:91–126, 1991. doi: 10.1007/BF00873538.

J. T. Armstrong, D. Mozurkewich, L. J. Rickard, D. J. Hutter, J. A. Benson, P. F. Bowers, II N. M. Elias, C. A. Hummel, K. J. Johnston, D. F. Buscher, III J. H. Clark, L. Ha, L.-C. Ling, N. M. White, and R. S. Simon. The Navy Prototype Optical Interferometer. *Astrophysical Journal*, 496:550–571, March 1998. doi: 10.1086/305365.

D. Baade. Nonradial Pulsations and the be Phenomenon. In G. Cayrel de Strobel and M. Spite, editors, *The Impact of Very High S/N Spectroscopy on Stellar Physics*, volume 132 of *IAU Symposium*, page 217, 1988.

P. Berio, D. Mourard, D. Bonneau, O. Chesneau, P. Stee, N. Thureau, F. Vakili, and J. Borgnino. Spectrally resolved Michelson stellar interferometry. I. Exact formalism in the multispeckle mode. *Journal of the Optical Society of America A*, 16:872–881, April 1999. doi: 10.1364/JOSAA.16.000872.

P. Berio, Y. Bresson, J. M. Clausse, D. Mourard, J. Dejonghe, A. Duthu, S. Lagarde, A. Meilland, K. Perraut, I. Tallon-Bosc, N. Nardetto, A. Spang, C. Bailet, A. Marcotto, O. Chesneau, P. Stee, P. Feautrier, P. Balard, and J. L. Gach. Long baseline interferometry in the visible: the FRIEND project. In *Optical and Infrared Interferometry IV*, volume 9146 of *Proceedings of the SPIE*, page 914616, July 2014. doi: 10.1117/12.2054890.

M. S. Bessell. Standard Photometric Systems. *Annu. Rev. Astron. Astrophys.*, 43:293–336, September 2005. doi: 10.1146/annurev.astro.41.082801.100251.

D. V. Bisikalo, A. A. Boyarchuk, V. M. Chechetkin, O. A. Kuznetsov, and D. Molteni. Three-dimensional numerical simulation of gaseous flow structure in semidetached binaries. *Mon. Not. of Royal Astr. Soc.*, 300:39–48, October 1998. doi: 10.1046/j.1365-8711.1998.01815.x.

D. V. Bisikalo, P. Harmanec, A. A. Boyarchuk, O. A. Kuznetsov, and P. Hadrava. Circumstellar structures in the eclipsing binary eta Lyr A. Gasdynamical modelling confronted with observations. *Astronomy&Astrophysics*, 353: 1009–1015, January 2000.

J. E. Bjorkman and J. P. Cassinelli. Equatorial disk formation around rotating stars due to Ram pressure confinement by the stellar wind. *Astrophysical Journal*, 409:429–449, May 1993. doi: 10.1086/172676.

C. T. Bolton and J. H. Grunhut. The Orbit and Properties of the Spectroscopic-Eclipsing- Interferometric Trips System ξ Tauri. In W. I. Hartkopf, P. Harmanec, and E. F. Guinan, editors, *IAU Symposium*, volume 240 of *IAU Symposium*, page 66, August 2007.

D. Bonneau, J.-M. Clausse, X. Delfosse, D. Mourard, S. Cetre, A. Chelli, P. Cruzalèbes, G. Duvert, and G. Zins. SearchCal: a virtual observatory tool for searching calibrators in optical long baseline interferometry. I. The bright object case. *Astronomy&Astrophysics*, 456:789–789, September 2006. doi: 10.1051/0004-6361:20054469.

D. Bonneau, O. Chesneau, D. Mourard, P. Bério, J. M. Clausse, O. Delaa, A. Marcotto, K. Perraut, A. Roussel, A. Spang, P. Stee, I. Tallon-Bosc, H. McAlister, T. ten Brummelaar, J. Sturmann, L. Sturmann, N. Turner, C. Farrington, and P. J. Goldfinger. A large Halpha line forming region for the massive interacting binaries beta Lyrae and upsilon Sagitarii. *Astronomy&Astrophysics*, 532:A148, August 2011. doi: 10.1051/0004-6361/201116742.

T. Borkovits, B. Érdi, E. Forgács-Dajka, and T. Kovács. On the detectability of long period perturbations in close hierarchical triple stellar systems. *Astronomy&Astrophysics*, 398:1091–1102, February 2003. doi: 10.1051/0004-6361:20021688.

T. Borkovits, S. Rappaport, T. Hajdu, and J. Sztakovics. Eclipse timing variation analyses of eccentric binaries with close tertiaries in the Kepler field. *Mon. Not. of Royal Astr. Soc.*, 448:946–993, March 2015. doi: 10.1093/mnras/stv015.

H. Božić, P. Harmanec, J. Horn, P. Koubsky, G. Scholz, D. McDavid, A.-M. Hubert, and H. Hubert. Toward a consistent model of the B0.5IVe + sdO binary ϕ Persei. *Astronomy&Astrophysics*, 304:235, December 1995.

H. Božić, J. Nemravová, and P. Harmanec. Standard UBV photometry and improved physical properties of TW Dra. *Information Bulletin on Variable Stars*, 6086:1, December 2013.

S. Breiter and D. Vokrouhlický. Secular motion in a hierarchic triple stellar system. *Mon. Not. of Royal Astr. Soc.*, 449:1691–1703, May 2015. doi: 10.1093/mnras/stv361.

M. Brož. An advanced n-body model for interacting multiple systems (using SWIFT and WD codes). 2016.

M. Brož, P. Mayer, T. Pribulla, P. Zasche, D. Vokrouhlický, and R. Uhlář. A Unified Solution for the Orbit and Light-time Effect in the V505 Sgr System. *Astronomical Journal*, 139:2258–2268, June 2010. doi: 10.1088/0004-6256/139/6/2258.

W. W. Campbell. *Astrophysical Journal*, 29:224–228, April 1909. doi: 10.1086/141644.

F. Castelli and R. L. Kurucz. New Grids of ATLAS9 Model Atmospheres. *ArXiv Astrophysics e-prints*, May 2004.

X. Che, L. Sturmann, J. D. Monnier, T. A. Ten Brummelaar, J. Sturmann, S. T. Ridgway, M. J. Ireland, N. H. Turner, and H. A. McAlister. Optical and Mechanical Design of the CHARA Array Adaptive Optics. *Journal of Astronomical Instrumentation*, 2:1340007, 2013. doi: 10.1142/S2251171713400072.

R. Chini, V. H. Hoffmeister, A. Nasseri, O. Stahl, and H. Zinnecker. A spectroscopic survey on the multiplicity of high-mass stars. *Mon. Not. of Royal Astr. Soc.*, 424:1925–1929, August 2012. doi: 10.1111/j.1365-2966.2012.21317.x.

A. Claret. Comprehensive tables for the interpretation and modeling of the light curves of eclipsing binaries. *Astronomy&Astrophysics Suppl.*, 131:395–400, September 1998. doi: 10.1051/aas:1998278.

A. Claret. A new non-linear limb-darkening law for LTE stellar atmosphere models. Calculations for -5.0 <= log[M/H] <= +1, 2000 K <= T_{eff} <= 50000 K at several surface gravities. *Astronomy&Astrophysics*, 363:1081–1190, November 2000.

A. Claret. The evolution of the theoretical bolometric albedo in close binary systems. *Mon. Not. of Royal Astr. Soc.*, 327:989–994, November 2001. doi: 10.1046/j.1365-8711.2001.04783.x.

A. Claret and S. Bloemen. VizieR Online Data Catalog: Limb-darkening coefficients (Claret+, 2011). *VizieR Online Data Catalog*, 352, March 2011.

A. Claret and A. Gimenez. The Apsidal Motion Test of the Internal Stellar Structure - Comparison Between Theory and Observations. *Astronomy&Astrophysics*, 277:487, October 1993.

A. D. Code, R. C. Bless, J. Davis, and R. H. Brown. Empirical effective temperatures and bolometric corrections for early-type stars. *Astrophysical Journal*, 203:417–434, January 1976. doi: 10.1086/154093.

T. J. Cornwell. Radio-interferometric imaging of weak objects in conditions of poor phase stability - the relationship between speckle masking and phase closure methods. *Astronomy&Astrophysics*, 180:269–274, June 1987.

T. J. Cornwell and K. F. Evans. A simple maximum entropy deconvolution algorithm. *Astronomy&Astrophysics*, 143:77–83, February 1985.

T. G. Cowling. On the motion of the apsidal line in close binary systems. *Mon. Not. of Royal Astr. Soc.*, 98:734, June 1938. doi: 10.1093/mnras/98.9.734.

J. P. Cox. Pulsating stars. *Reports on Progress in Physics*, 37:563–698, 1974. doi: 10.1088/0034-4885/37/5/001.

J. A. Crawford. On the Subgiant Components of Eclipsing Binary Systems. *Astrophysical Journal*, 121:71, January 1955. doi: 10.1086/145965.

J. Davis, W. J. Tango, and A. J. Booth. Limb-darkening corrections for interferometric uniform disc stellar angular diameters. *Monthly Notices of the Royal Astronomical Society*, 318(2):387–392, 2000. doi: 10.1046/j.1365-8711.2000.03701.x. URL `http://mnras.oxfordjournals.org/content/318/2/387.abstract`.

J. P. De Greve and A. P. Linnell. Origin and evolution of semi-detached binaries: Beta Lyrae and SV Centauri. *Astronomy&Astrophysics*, 291:786–794, November 1994.

P. de Laverny, A. Recio-Blanco, C. C. Worley, and B. Plez. The AMBRE project: A new synthetic grid of high-resolution FGKM stellar spectra. *Astronomy&Astrophysics*, 544:A126, August 2012. doi: 10.1051/0004-6361.

R. Deschamps, L. Siess, P. J. Davis, and A. Jorissen. Critically-rotating accretors and non-conservative evolution in Algols. *Astronomy&Astrophysics*, 557:A40, September 2013. doi: 10.1051/0004-6361/201321509.

A. Duquennoy and M. Mayor. Multiplicity among solar-type stars in the solar neighbourhood. II - Distribution of the orbital elements in an unbiased sample. *Astronomy&Astrophysics*, 248:485–524, August 1991.

A. S. Eddington. The reflection effect in eclipsing variables. *Mon. Not. of Royal Astr. Soc.*, 86:320–327, March 1926. doi: 10.1093/mnras/86.5.320.

B. Efron. Bootstrap Methods: Another Look at the Jackknife. *Ann. Statist.*, 7(1):1–26, 01 1979. doi: 10.1214/aos/1176344552. URL `http://dx.doi.org/10.1214/aos/1176344552`.

P. P. Eggleton and L. Kiseleva-Eggleton. Orbital Evolution in Binary and Triple Stars, with an Application to SS Lacertae. *Astrophysical Journal*, 562:1012–1030, December 2001. doi: 10.1086/323843.

P. P. Eggleton, L. G. Kiseleva, and P. Hut. The Equilibrium Tide Model for Tidal Friction. *Astrophysical Journal*, 499:853–870, May 1998.

ESA, editor. *The HIPPARCOS and TYCHO catalogues. Astrometric and photometric star catalogues derived from the ESA HIPPARCOS Space Astrometry Mission*, volume 1200 of *ESA Special Publication*, 1997.

T. Eversberg and K. Vollmann. *Spectroscopic Instrumentation: Fundamentals and Guidelines for Astronomers*. 2015.

D. Fabrycky and S. Tremaine. Shrinking Binary and Planetary Orbits by Kozai Cycles with Tidal Friction. *Astrophysical Journal*, 669:1298–1315, November 2007. doi: 10.1086/521702.

Jr. F. C. Fekel. The properties of close multiple stars. *Astrophysical Journal*, 246:879–898, June 1981. doi: 10.1086/158981.

F. Feroz and M. P. Hobson. Multimodal nested sampling: an efficient and robust alternative to Markov Chain Monte Carlo methods for astronomical data analyses. *Mon. Not. of Royal Astr. Soc.*, 384:449–463, February 2008. doi: 10.1111/j.1365-2966.2007.12353.x.

F. Feroz, M. P. Hobson, and M. Bridges. MULTINEST: an efficient and robust Bayesian inference tool for cosmology and particle physics. *Mon. Not. of Royal Astr. Soc.*, 398:1601–1614, October 2009. doi: 10.1111/j.1365-2966.2009.14548.x.

F. Feroz, M. P. Hobson, E. Cameron, and A. N. Pettitt. Importance Nested Sampling and the MultiNest Algorithm. *ArXiv e-prints*, June 2013.

E. L. Fitzpatrick. Interstellar Extinction in the Milky Way Galaxy. In A. N. Witt, G. C. Clayton, and B. T. Draine, editors, *Astrophysics of Dust*, volume 309 of *Astronomical Society of the Pacific Conference Series*, page 33, May 2004.

Y. Frémat, J. Zorec, A.-M. Hubert, and M. Floquet. Effects of gravitational darkening on the determination of fundamental parameters in fast-rotating B-type stars. *Astronomy&Astrophysics*, 440:305–320, September 2005. doi: 10.1051/0004-6361:20042229.

D. L. Fried. Optical Resolution Through a Randomly Inhomogeneous Medium for Very Long and Very Short Exposures. *Journal of the Optical Society of America (1917-1983)*, 56:1372, October 1966.

K. Fuhrmann, R. Chini, V. H. Hoffmeister, R. Lemke, M. Murphy, W. Seifert, and O. Stahl. BESO échelle spectroscopy of solar-type stars at Cerro Armazones. *Mon. Not. of Royal Astr. Soc.*, 411:2311–2318, March 2011. doi: 10.1111/j.1365-2966.2010.17850.x.

J. Goodricke and H. C. Englefield. Observations of a New Variable Star. By John Goodricke, Esq.; Communicated by Sir H. C. Englefield, Bart. F. R. S. and A. S. *Philosophical Transactions of the Royal Society of London Series I*, 75:153–164, 1785.

R. Gratton, C. Sneden, and E. Carretta. Abundance Variations Within Globular Clusters. *Annu. Rev. Astron. Astrophys.*, 42:385–440, September 2004. doi: 10.1146/annurev.astro.42.053102.133945.

D. F. Gray. Atmospheric turbulence measured in stars above the main sequence. *Astrophysical Journal*, 202:148–164, November 1975. doi: 10.1086/153960.

D. F. Gray. *The Observation and Analysis of Stellar Photospheres*. September 2005.

E. F. Guinan, P. Mayer, P. Harmanec, H. Božić, M. Brož, J. Nemravová, S. Engle, M. Šlechta, P. Zasche, M. Wolf, D. Korčáková, and C. Johnston. *Astronomy&Astrophysics*, 546:A123, October 2012. doi: 10.1051/0004-6361.

P. Hadrava. Eclipsing binaries-light curve solutions. *Contributions of the Astronomical Observatory Skalnate Pleso*, 20:23, 1990.

P. Hadrava. Orbital elements of multiple spectroscopic stars. *Astronomy&Astrophysics Suppl.*, 114:393, December 1995.

P. Hadrava. Relative line photometry of eclipsing binaries. *Astronomy&Astrophysics Suppl.*, 122:581–584, May 1997. doi: 10.1051/aas:1997102.

P. Hadrava. FOTEL 4 - User's guide. *Publications of the Astronomical Institute of the Czechoslovak Academy of Sciences*, 92:1–14, 2004.

P. Hadrava. Disentangling of spectra - theory and practice. *ArXiv e-prints*, September 2009.

R. Hanbury Brown. A Test of a New Type of Stellar Interferometer on Sirius. *Nature*, 178:1046–1048, November 1956. doi: 10.1038/1781046a0.

R. Hanbury Brown, J. Davis, and L. R. Allen. The angular diameters of 32 stars. *Mon. Not. of Royal Astr. Soc.*, 167:121–136, April 1974. doi: 10.1093/mnras/167.1.121.

R. H. Hardie. Potential Improvements in Photometric Accuracy. In K. Loden, L. O. Loden, and U. Sinnerstad, editors, *Spectral Classification and Multicolour Photometry*, volume 24 of *IAU Symposium*, page 243, 1966.

P. Harmanec. Review of observational facts about Be stars. *Hvar Observatory Bulletin*, 7:55–88, 1983.

P. Harmanec. Stellar masses and radii based on modern binary data. *Bulletin of the Astronomical Institutes of Czechoslovakia*, 39:329–345, December 1988.

P. Harmanec. One less puzzle in Beta Lyrae? *Astronomy&Astrophysics*, 266:307–312, December 1992.

P. Harmanec. A reliable transformation of HIPPARCOS H_p magnitudes into Johnson V and B magnitudes. *Astronomy&Astrophysics*, 335:173–178, July 1998.

P. Harmanec. Physical Properties and Evolutionary Stage of Be Stars. In M. A. Smith, H. F. Henrichs, and J. Fabregat, editors, *IAU Colloq. 175: The Be Phenomenon in Early-Type Stars*, volume 214 of *Astronomical Society of the Pacific Conference Series*, page 13, 2000.

P. Harmanec. The ever challenging emission-line binary beta Lyrae. *Astronomische Nachrichten*, 323:87–98, July 2002. doi: 10.1002/1521-3994(200207)323:2⟨87::AID-ASNA87⟩3.0.CO;2-P.

P. Harmanec and H. Božić. Useful transformations between photometric systems. *Astronomy&Astrophysics*, 369: 1140–1142, April 2001. doi: 10.1051/0004-6361:20010205.

P. Harmanec and J. Horn. A set of Fortran77 programs for reductions of photoelectric measurements, reliable transformation to standard systems, data archiving and retrieval. *Journal of Astronomical Data*, 4:5, December 1998.

P. Harmanec and G. Scholz. Orbital elements of beta Lyrae after the first 100 years of investigation. *Astronomy&Astrophysics*, 279:131–147, November 1993.

P. Harmanec, J. Horn, and K. Juza. Reliable photometric reductions to the standard UBV (or uvby) system and accurate UBV magnitudes of bright standard stars from the northern part of the international Be program. *Astronomy&Astrophysics Suppl.*, 104:121–143, April 1994.

P. Harmanec, F. Morand, D. Bonneau, Y. Jiang, S. Yang, E. F. Guinan, D. S. Hall, D. Mourard, P. Hadrava, H. Bozic, C. Sterken, I. Tallon-Bosc, G. A. H. Walker, G. P. McCook, F. Vakili, P. Stee, and J. M. Le Contel. Jet-like structures in β Lyrae. Results of optical interferometry, spectroscopy and photometry. *Astronomy&Astrophysics*, 312:879–896, August 1996.

P. Harmanec, D. V. Bisikalo, A. A. Boyarchuk, and O. A. Kuznetsov. On the role of duplicity in the Be phenomenon. I. General considerations and the first attempt at a 3-D gas-dynamical modelling of gas outflow from hot and rapidly rotating OB stars in binaries. *Astronomy&Astrophysics*, 396:937–948, December 2002. doi: 10.1051/0004-6361:20021534.

P. Harmanec, D. E. Holmgren, M. Wolf, H. Božić, E. F. Guinan, Y. W. Kang, P. Mayer, G. P. McCook, J. Nemravová, S. Yang, M. Šlechta, D. Ruždjak, D. Sudar, and P. Svoboda. Revised physical elements of the astrophysically important O9.5+O9.5V eclipsing binary system Y Cygni. *Astronomy&Astrophysics*, 563:A120, March 2014. doi: 10.1051/0004-6361/201323230.

P. Harmanec, P. Koubský, J. A. Nemravová, F. Royer, D. Briot, P. North, P. Lampens, Y. Frémat, S. Yang, H. Božić, L. Kotková, P. Škoda, M. Šlechta, D. Korčáková, M. Wolf, and P. Zasche. Properties and nature of Be stars. 30. Reliable physical properties of a semi-detached B9.5e+G8III binary BR CMi = HD 61273 compared to those of other well studied semi-detached emission-line binaries. *Astronomy&Astrophysics*, 573:A107, January 2015. doi: 10.1051/0004-6361/201424640.

R. S. Harrington. Dynamical evolution of triple stars. *Astronomical Journal*, 73:190–194, April 1968. doi: 10.1086/110614.

J. B. Hearnshaw. *The Measurement of Starlight, Two Centuries of Astronomical Photometry*. 1996.

J. L. Hoffman, K. H. Nordsieck, and G. K. Fox. Spectropolarimetric Evidence for a Bipolar Flow in beta Lyrae. *Astronomical Journal*, 115:1576–1591, April 1998. doi: 10.1086/300274.

J. A. Högbom. Aperture Synthesis with a Non-Regular Distribution of Interferometer Baselines. *Astronomy&Astrophysics Suppl.*, 15:417, June 1974.

J. Horn, P. Koubsky, P. Hadrava, K. Juza, S. Kriz, P. Skoda, and S. Stefl. The orbit of the spectroscopic binary ρ Aurigae. *Astronomy&Astrophysics Suppl.*, 105, May 1994.

J. Horn, J. Kubat, P. Harmanec, P. Koubsky, P. Hadrava, V. Simon, S. Stefl, and P. Skoda. Spectroscopic orbit of the triple star 55 Ursae Majoris. *Astronomy&Astrophysics*, 309:521–529, May 1996.

S.-S. Huang. An Interpretation of Beta Lyrae. *Astrophysical Journal*, 138:342, August 1963. doi: 10.1086/147648.

I. Hubený and M. J. Plavec. Can a disk model explain Beta Lyrae? *Astronomical Journal*, 102:1156–1170, September 1991. doi: 10.1086/115942.

C. A. Hummel, D. Mozurkewich, J. T. Armstrong, A. R. Hajian, II N. M. Elias, and D. J. Hutter. Navy Prototype Optical Interferometer Observations of the Double Stars Mizar A and Matar. *Astronomical Journal*, 116:2536–2548, November 1998. doi: 10.1086/300602.

C. A. Hummel, J. A. Benson, D. J. Hutter, K. J. Johnston, D. Mozurkewich, J. T. Armstrong, R. B. Hindsley, G. C. Gilbreath, L. J. Rickard, and N. M. White. First Observations with a Co-phased Six-Station Optical Long-Baseline Array: Application to the Triple Star η Virginis. *Astronomical Journal*, 125:2630–2644, May 2003. doi: 10.1086/374572.

John W. Tukey James W. Cooley. An Algorithm for the Machine Calculation of Complex Fourier Series. *Mathematics of Computation*, 19(90):297–301, 1965. ISSN 00255718, 10886842. URL `http://www.jstor.org/stable/2003354`.

H. L. Johnson, R. I. Mitchell, B. Iriarte, and W. Z. Wisniewski. Ubvrijkl Photometry of the Bright Stars. *Communications of the Lunar and Planetary Laboratory*, 4:99, 1966.

J. Kallrath and E. F. Milone. *Eclipsing Binary Stars: Modeling and Analysis*. 2009. doi: 10.1007/978-1-4419-0699-1.

A. Kaufer, O. Stahl, S. Tubbesing, P. Nørregaard, G. Avila, P. Francois, L. Pasquini, and A. Pizzella. Commissioning FEROS, the new high-resolution spectrograph at La-Silla. *The Messenger*, 95:8–12, March 1999.

P. Kervella, N. Nardetto, D. Bersier, D. Mourard, and V. Coudé du Foresto. Cepheid distances from infrared long-baseline interferometry. I. VINCI/VLTI observations of seven Galactic Cepheids. *Astronomy&Astrophysics*, 416: 941–953, March 2004. doi: 10.1051/0004-6361:20031743.

R. Kippenhahn and A. Weigert. Entwicklung in engen Doppelsternsystemen I. Massenaustausch vor und nach Beendigung des zentralen Wasserstoff-Brennens. *Zeitschrift für Astrophysik*, 65:251, 1967.

E. Kıran, P. Harmanec, Ö. L. Değirmenci, M. Wolf, J. Nemravová, M. Šlechta, and P. Koubský. The orbital elements and physical properties of the eclipsing binary BD+36 3317, a probable member of Delta Lyrae cluster. *Astronomy&Astrophysics*, 587:A127, March 2016. doi: 10.1051/0004-6361/201527211.

Brian Kloppenborg and F. Baron. LibOI: The OpenCL Interferometry Library. 2012a.

Brian Kloppenborg and Fabien Baron. SIMTOI: SImulation and Modeling Tool for Optical Interferometry. 2012b.

D. G. Koch, W. J. Borucki, G. Basri, N. M. Batalha, T. M. Brown, D. Caldwell, J. Christensen-Dalsgaard, W. D. Cochran, E. DeVore, E. W. Dunham, III T. N. Gautier, J. C. Geary, R. L. Gilliland, A. Gould, J. Jenkins, Y. Kondo, D. W. Latham, J. J. Lissauer, G. Marcy, D. Monet, D. Sasselov, A. Boss, D. Brownlee, J. Caldwell, A. K. Dupree, S. B. Howell, H. Kjeldsen, S. Meibom, D. Morrison, T. Owen, H. Reitsema, J. Tarter, S. T. Bryson, J. L. Dotson, P. Gazis, M. R. Haas, J. Kolodziejczak, J. F. Rowe, J. E. Van Cleve, C. Allen, H. Chandrasekaran, B. D. Clarke, J. Li, E. V. Quintana, P. Tenenbaum, J. D. Twicken, and H. Wu. Kepler Mission Design, Realized Photometric Performance, and Early Science. *Astrophysical Journal Letters*, 713:L79–L86, April 2010. doi: 10.1088/2041-8205/713/2/L79.

Z. Kopal. The classification of close binary systems. *Annales d'Astrophysique*, 18:379, January 1955.

Z. Kopal. *Close binary systems*. 1959.

Y. Kozai. Secular perturbations of asteroids with high inclination and eccentricity. *Astronomical Journal*, 67:591, November 1962. doi: 10.1086/108790.

D. Kraft. *A software package for sequential quadratic programming*. Deutsche Forschungs- und Versuchsanstalt für Luft- und Raumfahrt Köln: Forschungsbericht. Wiss. Berichtswesen d. DFVLR, 1988. URL `http://books.google.cz/books?id=4rKaGwAACAAJ`.

S. Kriz and P. Harmanec. A hypothesis of the binary origin of Be stars. *Bulletin of the Astronomical Institutes of Czechoslovakia*, 26:65–81, 1975.

G. P. Kuiper. On the Interpretation of β Lyrae and Other Close Binaries. *Astrophysical Journal*, 93:133, January 1941. doi: 10.1086/144252.

A. Labeyrie. Attainment of Diffraction Limited Resolution in Large Telescopes by Fourier Analysing Speckle Patterns in Star Images. *Astronomy&Astrophysics*, 6:85, May 1970.

A. Labeyrie. Interference fringes obtained on VEGA with two optical telescopes. *Astrophysical Journal Letters*, 196: L71–L75, March 1975. doi: 10.1086/181747.

A. Labeyrie, S. G. Lipson, and P. Nisenson. *An Introduction to Optical Stellar Interferometry*. June 2006.

S. Lafrasse, G. Mella, D. Bonneau, G. Duvert, X. Delfosse, and A. Chelli. JMMC Stellar Diameters Catalogue - JSDC (Lafrasse+, 2010). *VizieR Online Data Catalog*, 2300:0, June 2010.

T. Lanz and I. Hubený. A Grid of Non-LTE Line-blanketed Model Atmospheres of O-Type Stars. *Astrophysical Journal Supplement*, 146:417–441, June 2003. doi: 10.1086/374373.

T. Lanz and I. Hubený. A Grid of NLTE Line-blanketed Model Atmospheres of Early B-Type Stars. *Astrophysical Journal Supplement*, 169:83–104, March 2007. doi: 10.1086/511270.

A. P. Linnell. Progress on a model for β Lyrae. *Mon. Not. of Royal Astr. Soc.*, 319:255–266, November 2000. doi: 10.1046/j.1365-8711.2000.03898.x.

A. P. Linnell, I. Hubený, and P. Harmanec. New Light Synthesis and Spectrum Synthesis Constraints on a Model for β Lyrae. *Astrophysical Journal*, 509:379–391, December 1998. doi: 10.1086/306484.

J. R. Lomax, J. L. Hoffman, II N. M. Elias, F. A. Bastien, and B. D. Holenstein. Geometrical Constraints on the Hot Spot in Beta Lyrae. *Astrophysical Journal*, 750:59, May 2012. doi: 10.1088/0004-637X/750/1/59.

L. B. Lucy. Gravity-Darkening for Stars with Convective Envelopes. *Zeitschrift für Astrophysik*, 65:89, 1967.

L. B. Lucy. An analysis of the variable radial velocity of alpha Cygni. *Astrophysical Journal*, 206:499–508, June 1976. doi: 10.1086/154405.

B. D. Mason, C. Martin, W. I. Hartkopf, D. J. Barry, M. E. Germain, G. G. Douglass, C. E. Worley, G. L. Wycoff, T. ten Brummelaar, and O. G. Franz. Speckle Interferometry of New and Problem HIPPARCOS Binaries. *Astronomical Journal*, 117:1890–1904, April 1999. doi: 10.1086/300823.

B. D. Mason, W. I. Hartkopf, D. R. Gies, T. J. Henry, and J. W. Helsel. The High Angular Resolution Multiplicity of Massive Stars. *Astronomical Journal*, 137:3358–3377, February 2009. doi: 10.1088/0004-6256/137/2/3358.

P. Mayer, H. Drechsel, J. Kubát, and M. Šlechta. The O-type eclipsing binary SZ Camelopardalis revisited. *Astronomy&Astrophysics*, 524:A1, December 2010. doi: 10.1051/0004-6361/200913472.

A. Meilland, P. Stee, M. Vannier, F. Millour, A. Domiciano de Souza, F. Malbet, C. Martayan, F. Paresce, R. G. Petrov, A. Richichi, and A. Spang. First direct detection of a Keplerian rotating disk around the Be star α Arae using AMBER/VLTI. *Astronomy&Astrophysics*, 464:59–71, March 2007. doi: 10.1051/0004-6361:20064848.

A. Meilland, O. Delaa, P. Stee, S. Kanaan, F. Millour, D. Mourard, D. Bonneau, R. Petrov, N. Nardetto, A. Marcotto, A. Roussel, J. M. Clausse, K. Perraut, H. McAlister, T. ten Brummelaar, J. Sturmann, L. Sturmann, N. Turner, S. T. Ridgway, C. Farrington, and P. J. Goldfinger. The binary Be star δ Scorpii at high spectral and spatial resolution. I. Disk geometry and kinematics before the 2011 periastron. *Astronomy&Astrophysics*, 532:A80, August 2011. doi: 10.1051/0004-6361/201116798.

A. Meilland, F. Millour, S. Kanaan, P. Stee, R. Petrov, K.-H. Hofmann, A. Natta, and K. Perraut. First spectro-interferometric survey of Be stars. I. Observations and constraints on the disk geometry and kinematics. *Astronomy&Astrophysics*, 538:A110, February 2012. doi: 10.1051/0004-6361/201117955.

R. E. Mennickent and G. Djurašević. On the accretion disc and evolutionary stage of β Lyrae. *Mon. Not. of Royal Astr. Soc.*, 432:799–809, June 2013. doi: 10.1093/mnras/stt515.

A. A. Michelson. Measurement of Jupiter's Satellites by Interference. *Nature*, 45:160–161, December 1891. doi: 10.1038/045160a0.

A. A. Michelson and F. G. Pease. *Astrophysical Journal*, 53, May 1921. doi: 10.1086/142603.

M. R. Mokiem, A. de Koter, J. Puls, A. Herrero, F. Najarro, and M. R. Villamariz. Spectral analysis of early-type stars using a genetic algorithm based fitting method. *Astronomy&Astrophysics*, 441:711–733, October 2005. doi: 10.1051/0004-6361:20053522.

J. D. Monnier, E. Pedretti, N. Thureau, J.-P. Berger, R. Millan-Gabet, T. ten Brummelaar, H. McAlister, J. Sturmann, L. Sturmann, P. Muirhead, A. Tannirkulam, S. Webster, and M. Zhao. Michigan Infrared Combiner (MIRC): commissioning results at the CHARA Array. In *Society of Photo-Optical Instrumentation Engineers (SPIE) Conference Series*, volume 6268 of *Society of Photo-Optical Instrumentation Engineers (SPIE) Conference Series*, page 1, June 2006. doi: 10.1117/12.671982.

J. Moultaka, S. A. Ilovaisky, P. Prugniel, and C. Soubiran. The ELODIE Archive. *Publications of the Astronomical Society of the Pacific*, 116:693–698, July 2004. doi: 10.1086/422177.

D. Mourard, D. Bonneau, A. Biazit, A. Labeyrie, F. Morand, I. Percheron, I. Tallon-Bosc, and F. Vakili. Simultaneous Spectroscopic and Interferometric Measurements of Binaries with the GI2T. In H. A. McAlister and W. I. Hartkopf, editors, *IAU Colloq. 135: Complementary Approaches to Double and Multiple Star Research*, volume 32 of *Astronomical Society of the Pacific Conference Series*, page 510, 1992.

D. Mourard, I. Tallon-Bosc, A. Blazit, D. Bonneau, G. Merlin, F. Morand, F. Vakili, and A. Labeyrie. The GI2T interferometer on Plateau de Calern. *Astronomy&Astrophysics*, 283:705–713, March 1994.

D. Mourard, J. M. Clausse, A. Marcotto, K. Perraut, I. Tallon-Bosc, P. Bério, A. Blazit, D. Bonneau, S. Bosio, Y. Bresson, O. Chesneau, O. Delaa, F. Hénault, Y. Hughes, S. Lagarde, G. Merlin, A. Roussel, A. Spang, P. Stee, M. Tallon, P. Antonelli, R. Foy, P. Kervella, R. Petrov, E. Thiebaut, F. Vakili, H. McAlister, T. ten Brummelaar, J. Sturmann, L. Sturmann, N. Turner, C. Farrington, and P. J. Goldfinger. *Astronomy and Astrophysics*, 508: 1073–1083, December 2009. doi: 10.1051/0004-6361/200913016.

A. Nasseri, R. Chini, P. Harmanec, P. Mayer, J. A. Nemravová, T. Dembsky, H. Lehmann, H. Sana, and J.-B. Le Bouquin. HD 152246: a new high-mass triple system and its basic properties. *Astronomy&Astrophysics*, 568:A94, August 2014. doi: 10.1051/0004-6361/201424382.

J. A. Nelder and R. Mead. A Simplex Method for Function Minimization. *The Computer Journal*, 7(4):308–313, 1965. doi: 10.1093/comjnl. URL `http://comjnl.oxfordjournals.org/content/7/4/308.abstract`.

J. Nemravová, P. Harmanec, J. Kubát, P. Koubský, L. Iliev, S. Yang, J. Ribeiro, M. Šlechta, L. Kotková, M. Wolf, and P. Škoda. Properties and nature of Be stars. 27. Orbital and recent long-term variations of the Pleiades Be star Pleione = BU Tauri. *Astronomy&Astrophysics*, 516:A80, June 2010. doi: 10.1051/0004-6361/200913885.

J. Nemravová, P. Harmanec, P. Koubský, and A. Miroshnichenko. Methods of the Long-term Radial-Velocity Variation Removal and their Application to Detect Duplicity of Several Be Stars. In M. T. Richards and I. Hubený, editors, *From Interacting Binaries to Exoplanets: Essential Modeling Tools*, volume 282 of *IAU Symposium*, pages 319–320, April 2012a. doi: 10.1017/S1743921311027700.

J. Nemravová, P. Harmanec, P. Koubský, A. Miroshnichenko, S. Yang, M. Šlechta, C. Buil, D. Korčáková, and V. Votruba. Properties and nature of Be stars. 29. Orbital and long-term spectral variations of γ Cassiopeiae. *Astronomy&Astrophysics*, 537:A59, January 2012b. doi: 10.1051/0004-6361/201117922.

J. Nemravová, D. Mourard, P. Harmanec, and A. Meilland. Yet Another Spectro-Interferometric Study of The Gas Distribution in The Enigmatic Semi-Detached Binary β Lyrae. In *EAS Publications Series*, volume 71 of *EAS Publications Series*, pages 175–179, December 2015. doi: 10.1051/eas/1571039.

J. A. Nemravová, P. Harmanec, J. Bencheikh, C. T. Bolton, H. Božić, M. Brož, S. Engle, J. Grunhut, E. F. Guinan, C. A. Hummel, D. Korčáková, P. Koubský, P. Mayer, D. Mourard, J. Ribeiro, M. Šlechta, D. Vokrouhlický, V. Votruba, M. Wolf, P. Zasche, Chara/Vega Team, and Npoi Team. An Unusual Quadruple System ξ Tauri. *Central European Astrophysical Bulletin*, 37:207–216, 2013.

J. A. Nemravová, P. Harmanec, M. Brož, D. Vokrouhlický, D. Mourard, C. A. Hummel, E. Cameron, J. Matthews, C. T. Bolton, H. Božić, R. Chini, T. Dembsky, S. Engle, C. Farrington, J. Grunhut, D. B. Guenther, E. F. Guinan, D. Korčáková, P. Koubský, R. Kříček, R. Kuschnig, P. Mayer, G. P. McCook, A. F. J. Moffat, N. Nardetto, A. Prša, J. Ribeiro, J. F. Rowe, S. Rucinski, P. Škoda, M. Šlechta, I. Tallon-Bosc, V. Votruba, W. Weiss, M. Wolf, P. Zasche, and R. T. Zavala. Xi Tauri: a unique laboratory to study dynamic interaction in a compact hierarchical quadruple system. *Astronomy&Astrophysics*, `http://dx.doi.org/10.1051/0004-6361/201628860`, 2016.

B. Paczyński. Evolutionary Processes in Close Binary Systems. *Annu. Rev. Astron. Astrophys.*, 9:183, 1971. doi: 10.1146/annurev.aa.09.090171.001151.

A. Palacios, M. Gebran, E. Josselin, F. Martins, B. Plez, M. Belmas, and A. Lèbre. POLLUX: a database of synthetic stellar spectra. *Astronomy&Astrophysics*, 516:A13, June 2010. doi: 10.1051/0004-6361.

L. Pasquini, G. Avila, A. Blecha, C. Cacciari, V. Cayatte, M. Colless, F. Damiani, R. de Propris, H. Dekker, P. di Marcantonio, T. Farrell, P. Gillingham, I. Guinouard, F. Hammer, A. Kaufer, V. Hill, M. Marteaud, A. Modigliani, G. Mulas, P. North, D. Popovic, E. Rossetti, F. Royer, P. Santin, R. Schmutzer, G. Simond, P. Vola, L. Waller, and M. Zoccali. Installation and commissioning of FLAMES, the VLT Multifibre Facility. *The Messenger*, 110:1–9, December 2002.

M. A. C. Perryman, L. Lindegren, J. Kovalevsky, E. Hoeg, U. Bastian, P. L. Bernacca, M. Crézé, F. Donati, M. Grenon, M. Grewing, F. van Leeuwen, H. van der Marel, F. Mignard, C. A. Murray, R. S. Le Poole, H. Schrijver, C. Turon, F. Arenou, M. Froeschlé, and C. S. Petersen. The HIPPARCOS Catalogue. *Astronomy&Astrophysics*, 323, July 1997.

R. G. Petrov, F. Malbet, G. Weigelt, P. Antonelli, U. Beckmann, Y. Bresson, A. Chelli, M. Dugué, G. Duvert, S. Gennari, L. Glück, P. Kern, S. Lagarde, E. Le Coarer, F. Lisi, F. Millour, K. Perraut, P. Puget, F. Rantakyrö, S. Robbe-Dubois, A. Roussel, P. Salinari, E. Tatulli, G. Zins, M. Accardo, B. Acke, K. Agabi, E. Altariba, B. Arezki, E. Aristidi, C. Baffa, J. Behrend, T. Blöcker, S. Bonhomme, S. Busoni, F. Cassaing, J.-M. Clausse, J. Colin, C. Connot, A. Delboulbé, A. Domiciano de Souza, T. Driebe, P. Feautrier, D. Ferruzzi, T. Forveille, E. Fossat, R. Foy, D. Fraix-Burnet, A. Gallardo, E. Giani, C. Gil, A. Glentzlin, M. Heiden, M. Heininger, O. Hernandez Utrera, K.-H. Hofmann, D. Kamm, M. Kiekebusch, S. Kraus, D. Le Contel, J.-M. Le Contel, T. Lesourd, B. Lopez, M. Lopez, Y. Magnard, A. Marconi, G. Mars, G. Martinot-Lagarde, P. Mathias, P. Mège, J.-L. Monin, D. Mouillet, D. Mourard, E. Nussbaum, K. Ohnaka, J. Pacheco, C. Perrier, Y. Rabbia, S. Rebattu, F. Reynaud, A. Richichi, A. Robini, M. Sacchettini, D. Schertl, M. Schöller, W. Solscheid, A. Spang, P. Stee, P. Stefanini, M. Tallon, I. Tallon-Bosc, D. Tasso, L. Testi, F. Vakili, O. von der Lühe, J.-C. Valtier, M. Vannier, and N. Ventura. AMBER, the near-infrared spectro-interferometric three-telescope VLTI instrument. *Astronomy&Astrophysics*, 464:1–12, March 2007. doi: 10.1051/0004-6361:20066496.

M. Plavec. Mass Exchange in Binary Stars. *Publications of the Astronomical Society of the Pacific*, 82:957, October 1970. doi: 10.1086/128996.

J. M. Porter and T. Rivinius. Classical Be Stars. *Publications of the Astronomical Society of the Pacific*, 115: 1153–1170, October 2003. doi: 10.1086/378307.

M. J. D. Powell. An efficient method for finding the minimum of a function of several variables without calculating derivatives. *The Computer Journal*, 7(2):155–162, 1964. doi: 10.1093/comjnl/7.2.155. URL `http://comjnl.oxfordjournals.org/content/7/2/155.abstract`.

W. H. Press, S. A. Teukolsky, W. T. Vetterling, and B. P. Flannery. *Numerical recipes in C++ : the art of scientific computing*. 2002.

G. W. Preston. The chemically peculiar stars of the upper main sequence. *Annu. Rev. Astron. Astrophys.*, 12:257–277, 1974. doi: 10.1146/annurev.aa.12.090174.001353.

A. Prša and T. Zwitter. A Computational Guide to Physics of Eclipsing Binaries. I. Demonstrations and Perspectives. *Astrophysical Journal*, 628:426–438, July 2005. doi: 10.1086/430591.

A. Prša and T. Zwitter. Disentangling Effective Temperatures of Individual Eclipsing Binary Components by Means of Color-Index Constraining. *Astrophysics and Space Science*, 304:347–350, August 2006. doi: 10.1007/s10509-006-9154-4.

S. Rappaport, K. Deck, A. Levine, T. Borkovits, J. Carter, I. El Mellah, R. Sanchis-Ojeda, and B. Kalomeni. Triple-star Candidates among the Kepler Binaries. *Astrophysical Journal*, 768:33, May 2013. doi: 10.1088/0004-637X/768/1/33.

G. Raskin, H. van Winckel, H. Hensberge, A. Jorissen, H. Lehmann, C. Waelkens, G. Avila, J.-P. de Cuyper, P. Degroote, R. Dubosson, L. Dumortier, Y. Frémat, U. Laux, B. Michaud, J. Morren, J. Perez Padilla, W. Pessemier, S. Prins, K. Smolders, S. van Eck, and J. Winkler. HERMES: a high-resolution fibre-fed spectrograph for the Mercator telescope. *Astronomy&Astrophysics*, 526:A69, February 2011. doi: 10.1051/0004-6361/201015435.

F. M. Rica Romero. Orbital elements for eight binaries. Study of the nature of wide components. I. *Revista Mexicana de Astronomía y Astrofísica*, 46:263–277, October 2010.

J. B. Rice. Doppler imaging of stellar surfaces (review). In K. G. Strassmeier and J. L. Linsky, editors, *Stellar Surface Structure*, volume 176 of *IAU Symposium*, page 19, 1996.

J. Rickard, W. Nees, and F. Middelburg. The Grant machine. *European Southern Observatory ESO Bulletin*, 12, June 1975.

T. Rivinius, A. C. Carciofi, and C. Martayan. Classical Be stars. Rapidly rotating B stars with viscous Keplerian decretion disks. *Astronomy and Astrophysics Reviews*, 21:69, October 2013. doi: 10.1007/s00159-013-0069-0.

E. Roche. Recherches sur les atmospheres des cometes. *Annales de l'Observatoire de Paris*, 5:353–393, 1859.

F. Roddier and P. Lena. Long-baseline Michelson interferometry with large ground-based telescopes operating at optical wavelengths. I - General formalism: Interferometry at visible wavelengths. *Journal of Optics*, 15:171–182, August 1984. doi: 10.1088/0150-536X/15/4/002.

K. Rousselet-Perraut, J. B. Le Bouquin, D. Mourard, F. Vakili, O. Chesneau, D. Bonneau, J. L. Chevassut, A. Crocherie, A. Glentzlin, S. Jankov, S. Ménardi, R. Petrov, and C. Stehlé. First sky validation of an optical polarimetric interferometer. *Astronomy&Astrophysics*, 451:1133–1137, June 2006. doi: 10.1051/0004-6361:20054296.

D. Ruždjak, H. Božić, P. Harmanec, R. Fiřt, P. Chadima, K. Bjorkman, D. R. Gies, A. B. Kaye, P. Koubský, D. McDavid, N. Richardson, D. Sudar, M. Šlechta, M. Wolf, and S. Yang. Properties and nature of Be stars. 26. Long-term and orbital changes of ζ Tauri. *Astronomy&Astrophysics*, 506:1319–1333, November 2009. doi: 10.1051/0004-6361/200810526.

J. Sahade. The system of Beta Lyrae. *Space Science Reviews*, 26:349–389, August 1980. doi: 10.1007/BF00217387.

H. Sana, J.-B. Le Bouquin, S. Lacour, J.-P. Berger, G. Duvert, L. Gauchet, B. Norris, J. Olofsson, D. Pickel, G. Zins, O. Absil, A. de Koter, K. Kratter, O. Schnurr, and H. Zinnecker. Southern Massive Stars at High Angular Resolution: Observational Campaign and Companion Detection. *Astrophysical Journal Supplement*, 215:15, November 2014. doi: 10.1088/0067-0049/215/1/15.

H. R. Schmitt, T. A. Pauls, C. Tycner, J. T. Armstrong, R. T. Zavala, J. A. Benson, G. C. Gilbreath, R. B. Hindsley, D. J. Hutter, K. J. Johnston, A. M. Jorgensen, and D. Mozurkewich. Navy Prototype Optical Interferometer Imaging of Line Emission Regions of β Lyrae Using Differential Phase Referencing. *Astrophysical Journal*, 691: 984–996, February 2009. doi: 10.1088/0004-637X/691/2/984.

A. Secchi. Schreiben des Herrn Prof. Secchi, Directors der Sternwarte des Collegio Romano, an den Herausgeber. *Astronomische Nachrichten*, 68:63, October 1866. doi: 10.1002/asna.18670680405.

T. Semaan, J. Gutiérrez-Soto, Y. Frémat, A. M. Hubert, C. Martayan, and J. Zorec. A Pulsational Study of a Sample of CoRoT Faint Be Stars. In J. C. Suárez, R. Garrido, L. A. Balona, and J. Christensen-Dalsgaard, editors, *Stellar Pulsations: Impact of New Instrumentation and New Insights*, volume 31 of *Astrophysics and Space Science Proceedings*, page 261, 2013. doi: 10.1007/978-3-642-29630-7_47.

N. I. Shakura and K. A. Postnov. Doppler-effect modulation of the observed radiation flux from ultracompact binary stars. *Astronomy&Astrophysics*, 183:L21, September 1987.

S. M. Simkin. Measurements of Velocity Dispersions and Doppler Shifts from Digitized Optical Spectra. *Astronomy&Astrophysics*, 31:129, March 1974.

P. Škoda. SPEFO—A Simple, Yet Powerful Program for One-Dimensional Spectra Processing. In G. H. Jacoby and J. Barnes, editors, *Astronomical Data Analysis Software and Systems V*, volume 101 of *Astronomical Society of the Pacific Conference Series*, page 187, 1996.

M. Y. Skulskii and G. P. Topilskaya. Secondary Component Lines in the Spectrum of Beta-Lyrae. *Soviet Astronomy Letters*, 17:263, July 1991.

M. A. Smith, R. Lopes de Oliveira, C. Motch, G. W. Henry, N. D. Richardson, K. S. Bjorkman, P. Stee, D. Mourard, J. D. Monnier, X. Che, R. Bücke, E. Pollmann, D. R. Gies, G. H. Schaefer, T. ten Brummelaar, H. A. McAlister, N. H. Turner, J. Sturmann, L. Sturmann, and S. T. Ridgway. The relationship between γ Cassiopeiae's X-ray emission and its circumstellar environment. *Astronomy&Astrophysics*, 540:A53, April 2012. doi: 10.1051/0004-6361/201118342.

S. Soderhjelm. The three-body problem and eclipsing binaries - Application to algol and lambda Tauri. *Astronomy&Astrophysics*, 42:229–236, August 1975.

P. Stee, O. Delaa, J. D. Monnier, A. Meilland, K. Perraut, D. Mourard, X. Che, G. H. Schaefer, E. Pedretti, M. A. Smith, R. Lopes de Oliveira, C. Motch, G. W. Henry, N. D. Richardson, K. S. Bjorkman, R. Bücke, E. Pollmann, J. Zorec, D. R. Gies, T. ten Brummelaar, H. A. McAlister, N. H. Turner, J. Sturmann, L. Sturmann, and S. T. Ridgway. The relationship between γ Cassiopeiae's X-ray emission and its circumstellar environment. II. Geometry and kinematics of the disk from MIRC and VEGA instruments on the CHARA Array. *Astronomy&Astrophysics*, 545:A59, September 2012. doi: 10.1051/0004-6361/201219234.

I. Steiner, O. Stahl, W. Seifert, R. Chini, and A. Quirrenbach. BESO: first light at the high-resolution spectrograph for the Hexapod-Telescope. In *Society of Photo-Optical Instrumentation Engineers (SPIE) Conference Series*, volume 7014 of *Society of Photo-Optical Instrumentation Engineers (SPIE) Conference Series*, page 4, July 2008. doi: 10.1117/12.788182.

Rainer Storn and Kenneth Price. Differential Evolution – A Simple and Efficient Heuristic for global Optimization over Continuous Spaces. *Journal of Global Optimization*, 11(4):341–359, 1997. ISSN 0925-5001. doi: 10.1023/A:1008202821328. URL `http://dx.doi.org/10.1023/A%3A1008202821328`.

B. Strömgren. Spectral Classification Through Photoelectric Narrow-Band Photometry. *Annu. Rev. Astron. Astrophys.*, 4:433, 1966. doi: 10.1146/annurev.aa.04.090166.002245.

O. Struve. On the Origin of Bright Lines in Spectra of Stars of Class B. *Astrophysical Journal*, 73:94, March 1931. doi: 10.1086/143298.

I. Tallon-Bosc, M. Tallon, E. Thiébaut, C. Béchet, G. Mella, S. Lafrasse, O. Chesneau, A. Domiciano de Souza, G. Duvert, D. Mourard, R. Petrov, and M. Vannier. LITpro: a model fitting software for optical interferometry. In *Society of Photo-Optical Instrumentation Engineers (SPIE) Conference Series*, volume 7013 of *Society of Photo-Optical Instrumentation Engineers (SPIE) Conference Series*, July 2008. doi: 10.1117/12.788871.

T. A. ten Brummelaar, H. A. McAlister, S. T. Ridgway, Jr. W. G. Bagnuolo, N. H. Turner, L. Sturmann, J. Sturmann, D. H. Berger, C. E. Ogden, R. Cadman, W. I. Hartkopf, C. H. Hopper, and M. A. Shure. First Results from the CHARA Array. II. A Description of the Instrument. *Astrophysical Journal*, 628:453–465, July 2005. doi: 10.1086/430729.

D. Tody. The IRAF Data Reduction and Analysis System. In D. L. Crawford, editor, *Instrumentation in astronomy VI*, volume 627 of *Society of Photo-Optical Instrumentation Engineers (SPIE) Conference Series*, page 733, January 1986.

D. Tody. IRAF in the Nineties. In R. J. Hanisch, R. J. V. Brissenden, and J. Barnes, editors, *Astronomical Data Analysis Software and Systems II*, volume 52 of *Astronomical Society of the Pacific Conference Series*, page 173, January 1993.

A. Tokovinin. Comparative statistics and origin of triple and quadruple stars. *Mon. Not. of Royal Astr. Soc.*, 389:925–938, September 2008. doi: 10.1111/j.1365-2966.2008.13613.x.

A. Tokovinin. From Binaries to Multiples. II. Hierarchical Multiplicity of F and G Dwarfs. *Astronomical Journal*, 147:87, April 2014. doi: 10.1088/0004-6256/147/4/87.

A. Tokovinin, S. Thomas, M. Sterzik, and S. Udry. Tertiary companions to close spectroscopic binaries. *Astronomy&Astrophysics*, 450:681–693, May 2006. doi: 10.1051/0004-6361:20054427.

A. A. Tokovinin. MSC - a catalogue of physical multiple stars. *Astronomy&Astrophysics Suppl.*, 124:75–84, July 1997. doi: 10.1051/aas:1997181.

G. Torres, D. W. Latham, and R. P. Stefanik. Cross-Correlation in Four Dimensions: Application to the Quadruple-lined Spectroscopic System HD 110555. *Astrophysical Journal*, 662:602–612, June 2007. doi: 10.1086/516836.

G. Torres, J. Andersen, and A. Giménez. Accurate masses and radii of normal stars: modern results and applications. *Astronomy and Astrophysics Reviews*, 18:67–126, February 2010. doi: 10.1007/s00159-009-0025-1.

R. H. D. Townsend, S. P. Owocki, and I. D. Howarth. Be-star rotation: how close to critical? *Mon. Not. of Royal Astr. Soc.*, 350:189–195, May 2004. doi: 10.1111/j.1365-2966.2004.07627.x.

G. Umana, P. F. L. Maxted, C. Trigilio, R. P. Fender, F. Leone, and S. K. Yerli. Resolving the radio nebula around beta Lyrae. *Astronomy&Astrophysics*, 358:229–232, June 2000.

W. van Hamme. New limb-darkening coefficients for modeling binary star light curves. *Astronomical Journal*, 106: 2096–2117, November 1993. doi: 10.1086/116788.

W. van Hamme and R. E. Wilson. Stellar atmospheres in eclipsing binary models. In U. Munari, editor, *GAIA Spectroscopy: Science and Technology*, volume 298 of *Astronomical Society of the Pacific Conference Series*, page 323, 2003.

F. van Leeuwen. Validation of the new Hipparcos reduction. *Astronomy&Astrophysics*, 474:653–664, November 2007. doi: 10.1051/0004-6361:20078357.

H. von Zeipel. The radiative equilibrium of a rotating system of gaseous masses. *Mon. Not. of Royal Astr. Soc.*, 84: 665–683, June 1924. doi: 10.1093/mnras/84.9.665.

C. Waelkens, C. Aerts, E. Kestens, M. Grenon, and L. Eyer. Study of an unbiased sample of B stars observed with Hipparcos: the discovery of a large amount of new slowly pulsating B stars. *Astronomy&Astrophysics*, 330:215–221, February 1998.

G. Walker, J. Matthews, R. Kuschnig, R. Johnson, S. Rucinski, J. Pazder, G. Burley, A. Walker, K. Skaret, R. Zee, S. Grocott, K. Carroll, P. Sinclair, D. Sturgeon, and J. Harron. The MOST Asteroseismology Mission: Ultraprecise Photometry from Space. *Publications of the Astronomical Society of the Pacific*, 115:1023–1035, September 2003. doi: 10.1086/377358.

W. F. Welsh, J. A. Orosz, C. Aerts, T. M. Brown, E. Brugamyer, W. D. Cochran, R. L. Gilliland, J. A. Guzik, D. W. Kurtz, D. W. Latham, G. W. Marcy, S. N. Quinn, W. Zima, C. Allen, N. M. Batalha, S. Bryson, L. A. Buchhave, D. A. Caldwell, III T. N. Gautier, S. B. Howell, K. Kinemuchi, K. A. Ibrahim, H. Isaacson, J. M. Jenkins, A. Prsa, M. Still, R. Street, B. Wohler, D. G. Koch, and W. J. Borucki. KOI-54: The Kepler Discovery of Tidally Excited Pulsations and Brightenings in a Highly Eccentric Binary. *Astrophysical Journal Supplement*, 197:4, November 2011. doi: 10.1088/0067-0049/197/1/4.

M. W. Werner, T. L. Roellig, F. J. Low, G. H. Rieke, M. Rieke, W. F. Hoffmann, E. Young, J. R. Houck, B. Brandl, G. G. Fazio, J. L. Hora, R. D. Gehrz, G. Helou, B. T. Soifer, J. Stauffer, J. Keene, P. Eisenhardt, D. Gallagher, T. N. Gautier, W. Irace, C. R. Lawrence, L. Simmons, J. E. Van Cleve, M. Jura, E. L. Wright, and D. P. Cruikshank. The Spitzer Space Telescope Mission. *Astrophysical Journal Supplement*, 154:1–9, September 2004. doi: 10.1086/422992.

R. E. Wilson and E. J. Devinney. Realization of Accurate Close-Binary Light Curves: Application to MR Cygni. *Astrophysical Journal*, 166:605, June 1971. doi: 10.1086/150986.

R. E. Wilson and W. Van Hamme. Unification of Binary Star Ephemeris Solutions. *Astrophysical Journal*, 780:151, January 2014. doi: 10.1088/0004-637X/780/2/151.

M. Wittkowski, C. A. Hummel, K. J. Johnston, D. Mozurkewich, A. R. Hajian, and N. M. White. Direct multi-wavelength limb-darkening measurements of three late-type giants with the Navy Prototype Optical Interferometer. *Astronomy&Astrophysics*, 377:981–993, October 2001. doi: 10.1051/0004-6361:20011124.

G. Woan and P. J. Duffett-Smith. Determination of Closure Phase in Noisy Conditions. *Astronomy&Astrophysics*, 198:375, June 1988.

K. Wood, K. S. Bjorkman, and J. E. Bjorkman. Deriving the Geometry of Be Star Circumstellar Envelopes from Continuum Spectropolarimetry. I. The Case of ζ Tauri. *Astrophysical Journal*, 477:926–939, March 1997.

A. T. Young. Improvements in photometry. V - High-order moments in transformation theory. *Astronomy&Astrophysics*, 257:366–388, April 1992.

P. Zasche and M. Wolf. Combining astrometry with the light-time effect: The case of VW Cep, ζ Phe and HT Vir. *Astronomische Nachrichten*, 328:928, November 2007. doi: 10.1002/asna.200710828.

M. Zhao, D. Gies, J. D. Monnier, N. Thureau, E. Pedretti, F. Baron, A. Merand, T. ten Brummelaar, H. McAlister, S. T. Ridgway, N. Turner, J. Sturmann, L. Sturmann, C. Farrington, and P. J. Goldfinger. First Resolved Images of the Eclipsing and Interacting Binary β Lyrae. *Astrophysical Journal Letters*, 684:L95–L98, September 2008. doi: 10.1086/592146.

S. Zucker and T. Mazeh. Study of spectroscopic binaries with TODCOR. 1: A new two-dimensional correlation algorithm to derive the radial velocities of the two components. *Astrophysical Journal*, 420:806–810, January 1994. doi: 10.1086/173605.

S. Zucker, G. Torres, and T. Mazeh. Study of Spectroscopic Binaries with TODCOR. III. Application to Triple-lined Systems. *Astrophysical Journal*, 452:863, October 1995. doi: 10.1086/176354.

List of Figures

5.6 A comparison of observed and synthetic squared visibility for CHARA/MIRC observations for $JD \simeq 2456466$ (night of the 22$^{\text{rd}}$ Jun, 2013). *Top panel* shows comparison of the β Lyr model described in Sect. 5.3.2 for the longitude of the ascending node $\Omega = 242$ deg. The model as it would appear on the sky is shown in the *bottom left panel*. *Middle panel* shows comparison of the same β Lyr model the longitude of the ascending node $\Omega = 254$ deg. The model as it would appear on the sky is shown in the *bottom right panel*. *Bottom panels* show the on-sky model. The vertical axis is aligned with the north-south direction and the horizontal axis with the east-west direction. Over these images the the coverage of the Fourier plane is plotted as a function of spatial frequencies (u, v). The improvement is seen especially for high visibility and spatial frequencies ($\gtrsim 10^8$). Those are generally baselines that are perpendicular to the orbital plane. 82

List of Tables

List of Abbreviations

3D	Three Dimensions.
BESO	Bochum Echelle Spectroscopic Observer, spectroscopic detector.
CCD	Charge-Coupled Device, a device for the movement of electrical charge.
CHARA	Center for High Angular Resolution Astronomy, American scientific facility.
DFT	Discrete Fourier Transform.
ETV	Eclipse-Timing Variation.
FEROS	Fibre-fed, Extended Range, Échelle Spectrograph, spectroscopic detector.
FFT	Fast Fourier Transform, an efficient algorithm for the Fourier transform computation.
FLAMES	Fibre Large Array Multi Element Spectrograph, spectroscopic detector.
FOV	Field Of View.
FWHM	Full Width at Half Maximum.
GUI	Graphical User Interface.
HERMES	High Efficiency and Resolution Mercator Echelle Spectrograph, spectroscopic detector.
HJD	Heliocentric Julian Date.
IR	InfraRed, electromagnetic radiation covering wavelengths from 700 nm to 1 mm.
IRAF	Image Reduction and Analysis Facility, a package for reduction and analysis of astronomical observations.
KCT	Kozai-cycles with tides, an effect responsible for formation of very close binaries.
LTTE	Light-Time Travel Effect, a time delay arising from the variations of the distance travelled by a signal.
MERLIN	Multi Element Radio Linked Interferometer Network, an interferometric array.
MIRC	Michigan InfraRed Combiner, an infrared spectro-interferometer.
NPOI	Navy Precision Optical Interferometer, an optical spectro-interferometer.
OPD	Optical Path Difference, difference in path of two beams.
PHOEBE	PHysics Of Eclipsing BinariEs, an enhanced wrapper around WD featuring a GUI and scripting environment.
PoP	Pipes of Pan, a part of a delay lines of an interferometer.
PSF	Point Spread Function, a wavefront convolved with the transfer function of an imaging device.
PSR	Phoebe Scientific Reference, a manual to the program PHOEBE.
RJD	Reduced Julian Date (RJD = HJD − 2 400 000 unless specified otherwise.)
RME	Rossiter-McLaughlin effect, an effect causing deformation of an eclipsing binary RV curve.
RV	Radial Velocity, projection of the velocity of a body in the direction to the observer.
SED	Spectral Energy Distribution, dependency of flux on the wavelength.
SNR	Signal to Noise Ratio, ratio between the acquired signal and its uncertainty.
SN	supernova, terminal stage of a massive star (type II) or a binary interaction, where the gainer is a white dwarf (type I).
TF	Transfer Function, ratio between visibility measure by an interferometer and the real visibility.
TTV	Transit-Timing Variations variations of time between two adjacent transits.
UV	UltraViolet, electromagnetic radiation covering wavelengths from 10 nm to 400 mm.

VEGA	Visible spEctroGraph and polArimeter, an instrument, which is described in Mourard et al. (2009).
WD	Wilson-Devinney code, a program for the light-curve inversion.

BU Tauri study

Astronomy & Astrophysics manuscript no. 13885TEX
November 20, 2013

Properties and nature of Be stars ⋆

27. Orbital and recent long-term variations of the Pleiades Be star Pleione = BU Tauri

J. Nemravová[1], P. Harmanec[1], J. Kubát[2], P. Koubský[2], L. Iliev[3], S. Yang[4], J. Ribeiro[5], M. Šlechta[2], L. Kotková[2], M. Wolf[1], and P. Škoda[2]

[1] Astronomical Institute of the Charles University, Faculty of Mathematics and Physics, V Holešovičkách 2, CZ-180 00 Praha 8, Czech Republic
[2] Astronomical Institute of the Academy of Sciences, CZ-251 65 Ondřejov, Czech Republic
[3] Institute of Astronomy, Bulgarian Academy of Sciences, BG-1784, 72 Tsarigradsko Chaussee Blvd., Sofia, Bulgaria
[4] Physics & Astronomy Department, University of Victoria, PO Box 3055 STN CSC, Victoria, BC, V8W 3P6, Canada
[5] Observatório do Instituto Geográfico do Exército, R. Venezuela 29, 3 Esq. 1500-618, Lisboa, Portugal

Release November 20, 2013

ABSTRACT

Radial-velocity variations of the Hα emission measured on the steep wings of the Hα line, prewhitened for the long-time changes, vary periodically with a period of $218^{\rm d}.025 \pm 0^{\rm d}.022$, confirming the suspected binary nature of the bright Be star BU Tau, a member of the Pleiades cluster. The orbit seems to have a high eccentricity over 0.7, but we also briefly discuss the possibility that the true orbit is circular and that the eccentricity is spurious owing to the phase-dependent effects of the circumstellar matter. The projected angular separation of the spectroscopic orbit is large enough to allow the detection of the binary with large optical interferometers, provided the magnitude difference primary – secondary is not too large. Since our data cover the onset of a new shell phase up to development of a metallic shell spectrum, we also briefly discuss the recent long-term changes. We confirm the formation of a new envelope, coexisting with the previous one, at the onset of the new shell phase. We find that the full width at half maximum of the Hα profile has been decreasing with time for both envelopes. In this connection, we briefly discuss Hirata's hypothesis of precessing gaseous disk and possible alternative scenarios of the observed long-term changes.

Key words. stars: early-type – stars: binaries – stars: Be – stars: individual: BU Tau

1. Introduction

Pleione (BU Tau, 28 Tau, HD 23862) is a well-known Be star and a member of the Pleiades cluster. It underwent several phase transitions between B, Be, and Be shell phases, accompanied by pronounced light variations; see, e.g. Gulliver (1977), Sharov & Lyuty (1976), Iliev et al. (1988), Sharov & Lyutyj (1992), Hirata & Kogure (1976), Hirata & Kogure (1977), Hirata (1995), Doazan et al. (1988), Iliev et al. (2007), and Tanaka et al. (2007).

There is a rather complicated history of attempts to study the radial-velocity (RV hereafter) variations of this star. Struve & Swings (1943) measured RVs on the photographic spectra taken in the years 1938-1943 and tentatively concluded that the RV of BU Tau varies with a possible period of 142 days or – less likely – 106 days. Merrill (1952) studied RVs from 1941 to 1951 and found clear long-term variations with some overlapping changes on a shorter time scale. Gulliver (1977) analyzed a large collection of digitized photographic spectra from 1938-1954 and from 1969-1975 and concluded that there are no significant RV changes. Ballereau et al. (1988) carried out an analysis of a homogeneous series of Haute Provence high-dispersion photographic spectra from 1978-1987 and once more concluded that the shell RVs vary with periods of 136.0 and 106.7 days. Katahira et al. (1996a,b) analyzed shell RVs from the two consecutive shell phases separated some 34 years, using published as well as new RVs and concluded that BU Tau is a spectroscopic binary with an orbital period of $218^{\rm d}.0$, semi-amplitude of 5.9 km s^{-1}, and a large orbital eccentricity of 0.60. However, Rivinius et al. (2006) – analyzing a series of electronic spectra – were unable to confirm the 218-d period and concluded that BU Tau is not a spectroscopic binary. Hirata (2007) analyzed a long series of polarimetric observations and presented a model of a slowly precessing disk to explain the long-term B – Be – Be shell phase transition. He argued that the disk precession is caused by the attractive force of the secondary in the 218-d binary. Harmanec (1982) compiled the majority of at that time available RVs of BU Tau and averaged them over about 100 days. This resulted in a smooth RV curve with a period of about 13000 days (35.6 years), in phase with the recorded shell episodes. Harmanec (1982) speculated that BU Tau could be a long-periodic binary with shell phases occurring always at the same orbital phases. A more distant companion with an angular distance of $0\farcs22$ was indeed discovered from speckle interferometry by McAlister et al. (1989). Gies et al. (1990) studied a sequence of low-dispersion Hα spectra of BU Tau taken

Send offprint requests to: J. Nemravová,
e-mail: : janicka.ari@seznam.cz

⋆ Based on new spectral and photometric observations from the following observatories: Dominion Astrophysical Observatory, Herzberg Institute of Astrophysics, National Research Council of Canada, Haute Provence, IGeoE-Lisbon, Astronomical Institute AS CR Ondřejov, and Rozhen.

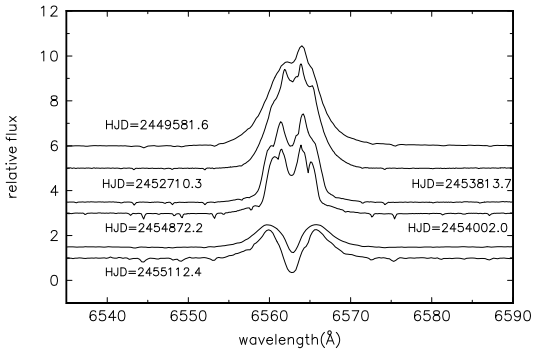

Fig. 1. Comparison of Hα profiles from different stages of the long-term changes.

with a sampling rate of 7 ms during a lunar occultation on 1987 March 6. They detected an asymmetry of the envelope in agreement with the observed long-term V/R changes. They speculated that the speckle-interferometric component could have an eccentric orbit and that the recurrent shell phases could be caused by its periastron passages. Luthardt & Menchenkova (1994) compiled RVs from the years 1938-1990 and confirmed a period of 12450-12860 days. They advocated an eccentric orbit and mass transfer resulting in a release of a new shell during periastron passages, but the gaps in their RV curve do not allow one to conclude that the orbit has a high eccentricity. Finally, using the technique of adaptive optics photometry and astrometry, Roberts et al. (2007) report discovery of a new companion to BU Tau at a separation of 4.″66 with a spectral type M5. They also confirm a companion at 0.″24 and discuss other suggested companions.

Table 1. Journal of new spectroscopic observations for BU Tau.

Station Source	Time interval (HJD−2400000)	No. of. obs.	Wavelength region (Å)
Ondřejov	49581 - 54872	101	6200 - 6800
DAO	49786 - 54912	26	6150 - 6700
OHP	51569 - 52664	21	6200 - 6700
Rozhen	52710 - 54108	23	6520 - 6610
Lisboa	54874 - 54881	4	6520 - 6600

We succeeded in collecting a rich series of electronic spectra at several observatories, covering many cycles of the suspected 218-d period. The main goal of this study is, therefore, to resolve the issue of whether BU Tau is a spectroscopic binary. Katahira et al. (1996a,b) based their orbit on the RV measurements of shell lines that may be affected by possible asymmetries in the circumstellar matter. Moreover, their RV curve has a rather small amplitude and is based on a collection of heterogeneous data. It naturally shows a rather large scatter around the mean curve. The spectra at our disposal all cover the red spectral region near Hα. They were taken over the time interval when the star had fairly strong Hα emission. Therefore, our study is based on the RV measurements of the steep wings of the emission, which is a procedure that turned out to be

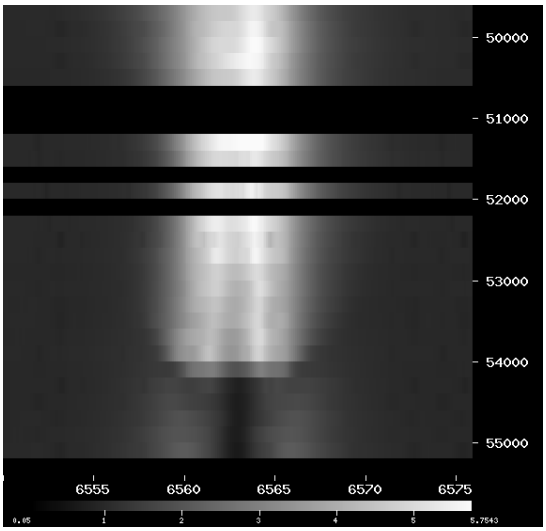

Fig. 2. A complete series of our Hα profiles in a gray representation (only a few saturated or underexposed spectra were omitted). Abscissa shows the wavelength scale in Å, while the time on ordinate is shown in JD-2400000. Each horizontal strip represents an average of spectra secured within 200 days, and dark horizontal belts correspond to time intervals from which no spectra are available. At the bottom, there is a scale showing the correspondence between the flux level in the units of continuum and the gray scale.

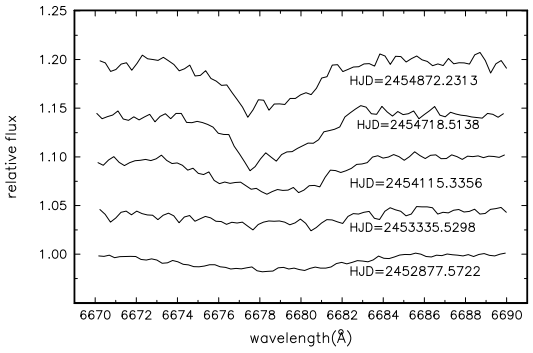

Fig. 3. Selected He I 6678 Å line profiles, ordered in time, with corresponding HJDs.

successful for detecting the duplicity of several other Be stars (Božić et al. 1995; Koubský et al. 2000; Harmanec et al. 2000; Miroshnichenko et al. 2001, 2002).

Since very pronounced long-term spectral variations occurred over the time interval covered by our spectra, we also briefly describe these changes and discuss them, especially in relation to the model put forward by Hirata (2007).

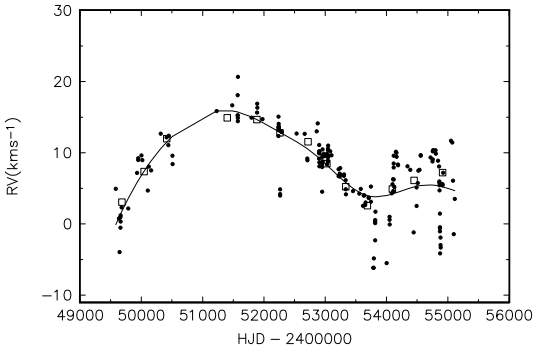

Fig. 4. Measured RVs of the Hα emission wings plotted vs. time. Prewhitening for the long-term changes, carried out with the help of the program HEC13, is shown by a line. Empty squares show the alternate way to remove long-term RV changes via individual γ velocities for subsets spanning no more than a year. See the text for details.

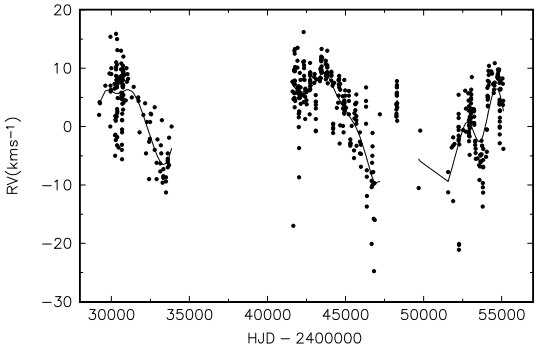

Fig. 5. Measured Hα absorption core plotted vs. time. We also included the RV measurements of shell lines by Katahira et al. (1996b) and Rivinius et al. (2006) to this plot. Prewhitening for the long-term changes, carried out with the help of the program HEC13, is shown by a line. See the text for details.

2. Spectroscopic observations and their reductions

The red spectra at our disposal were obtained at five observatories and their overview is in Table 1. Details about the instruments and data reduction can be found in Appendix A where also Table A.1 with our RV measurements of the steep wings of the Hα emission and of the Hα absorption core is provided. The latter was measured for comparison with the RVs collected and analyzed by Katahira et al. (1996b), but only for those spectra where the absorption was clearly visible.

Over the interval of the more than 5000 days covered by our observations, the strength of the Hα emission gradually declined and the shape of the Hα profile underwent notable changes. Typical examples for several distinct stages are shown in Fig. 1, and the whole development of a new shell and metallic-shell phase is shown as a gray-scale representation of all usable Hα profiles in Fig. 2.

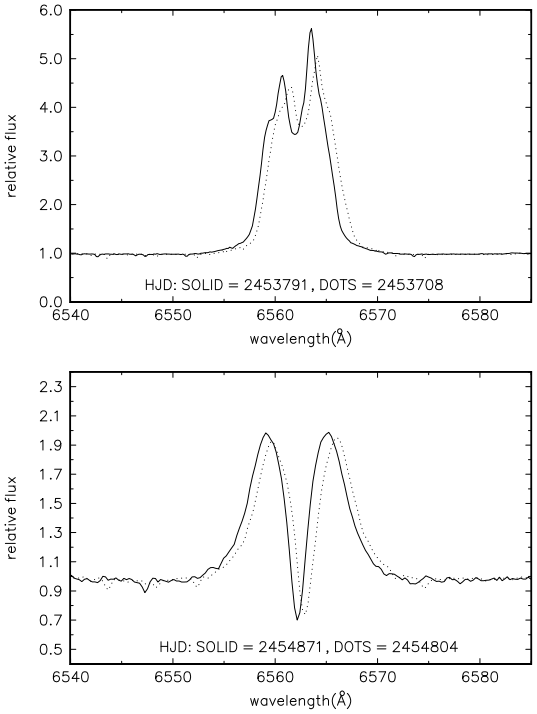

Fig. 6. A comparison of two pairs of the Hα line profiles from the locally recorded velocity extrema (HJDs of the profiles are indicated).

The fading of the Hα emission was accompanied by a light decrease in the *J*, *H*, *K*, and *L* IR photometric bands that started around JD 2451500 (Taranova et al. 2008). This clearly corresponds to the gradual development of the hydrogen shell spectrum according to our spectra – see also Tanaka et al. (2007). Emission has been slowly fading from JD 2453000 until now, when its peak intensity represents only about 30% of the intensity seen in our earliest spectra. During the transition from a single-peaked to double-peaked emission, there is some time interval when the Hα profile has a characteristic wine-bottle shape. The occasional presence of additional absorption components has been already noted by Iliev et al. (2007) or Tanaka et al. (2007) and is typical of all recorded shell phases of BU Tau. Besides the occasional presence of one or more additional absorptions, extended red emission wings are seen on some Hα profiles. This makes the emission wings asymmetric and hard to measure for RV. We also note that all double-peaked profiles recorded prior to about JD 24540000 always have a red peak stronger than the violet one. Figure 2 shows that the *width* of the Hα emission has remained more or less constant over the whole time interval covered by our observations. The same figure also shows that the metallic shell phase appeared rather abruptly.

Figure 3 shows the gradual development of the He I 6678 Å line profile. It illustrates well how shallow the line is at the beginning of a new shell phase. A very interesting finding is that, even for the B8 star, a presumably photospheric He I line can develop a shell component. The profile clearly gets stronger and

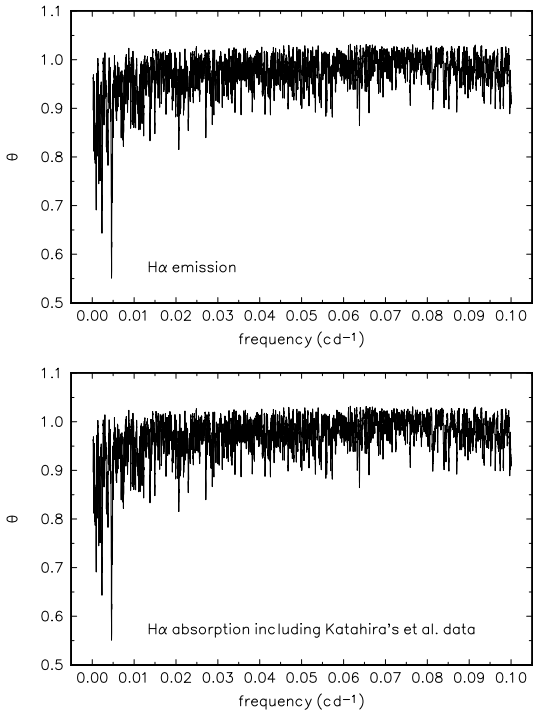

Fig. 7. Stellingwerf (1978) PDM θ statistics for all emission-wing RVs (top) and shell absorption-core RVs including Katahira et al. (1996b). The dominant frequency of 0.004587 c d^{-1} corresponds to the 218-d period.

narrower as the hydrogen shell line gets deeper. The additional absorption at the blue wing of the line seen on more recent spectra is the Fe II 6677.305 Å shell line.

3. Radial-velocity changes

Figures 4 and 5 are the time plots of the measured RVs vs. time for the Hα emission wings and the absorption core. In the later, we also included all shell RVs used and published by Katahira et al. (1996b) and Rivinius et al. (2006). One can see systematic RV changes on at least two distinct time scales: a smooth change on a longer time scale and overlapping more rapid changes, especially the occasional steep decreases in RV.

Considering the uncertainties in accurate RV measurements combined with the fact that the full amplitude of the changes is low, it was deemed useful to convince readers that the RV changes are not only a result of changing asymmetry of the profiles, but they also represent a real shift of the whole line. To this end, we compare in Fig. 6 two pairs of the Hα line profiles obtained near the local RV extrema. The upper pair comes from the beginning of a new shell phase and the bottom one from a more recent time when a weaker emission and deeper shell cores are present in the profiles (note a large difference in the flux scale of the two plots). The RV shift of the whole emission and absorption core is seen beyond any doubt. We, therefore, conclude that our RV measurements reflect *real RV variations* of BU Tau.

In accordance with Katahira et al. (1996b), we find that the evolution of the emission episode is accompanied by long-term RV changes that need to be removed prior to a search for possible periodic RV changes. To also make this step as objective as possible, we used two different procedures.

One is that we smoothed the long-term changes using the program HEC13, written by PH and based on a smoothing technique developed by Vondrák (1969, 1977).[1] For both emission and absorption RVs, optimal smoothings were obtained for the smoothing parameter $\varepsilon = 10^{-16}$ fitted through 200-d normals. (Inspecting the time plots of RVs, we identified $\sim$ 200 days as a time scale on which more rapid changes were observed, and this was the reason for the choice of 200-d normals. We have verified, however, that the result of smoothing is not sensitive to the particular choice of the averaging interval for the smoothing within reasonable limits.) The RV residuals from the smoothing were subjected to a period search based on the Stellingwerf (1978) PDM technique over a period range from 5000 down to 0.05 d. The dominant frequency found in both searches was 0.004587 c d^{-1} and its integer submultiples. The one-day aliases were largely supressed thanks to having data from observatories, that have a large difference in their local time, producing much shallower minima in the θ statistics ($\sim$ 0.75 – 0.82) and scattered phase diagrams. To make the diagrams readable, we show the corresponding θ statistics in Fig. 7 for the emission (top) and absorption (bottom) RVs only for a limited frequency interval down to 0.1 c d^{-1}. The result seems to confirm the 218-d periodicity discovered by Katahira et al. (1996b).

As another demonstration that the 218-d period is real, we show phase plots in Fig. 8 for the original RVs (without prewhitening for the long-term changes) for several subsets of data covering time intervals no longer than one year. Clearly similar RV curves, with sharp minima, rather flat maxima, and a mutual phase coherence, are seen in all cases. The first subset is based solely on the RVs from the Ondřejov spectra secured with Reticon detector, which were already investigated by Rivinius et al. (2006).

4. BU Tau as a spectroscopic binary

Our findings, and especially the fact that the Hα Balmer emission line moves in RV as a whole in spite of very large secular changes of its strength, indicate that BU Tau is indeed a single-line spectroscopic binary that moves in a highly eccentric orbit. We therefore used the program SPEL (written by the late Dr. Jiří Horn and never published) to derive the orbital elements. For comparison with Katahira et al. (1996b), we first derived orbital elements for Balmer *absorption* RVs, using the data from their study, RVs published by Rivinius et al. (2006), and our own Hα absorption RVs, prewhitened with HEC13 as shown in Fig. 5. The resulting orbital elements are given as solution 1 in Table 2 and the corresponding phase plots are shown in Fig. 9. For more clarity, we plot there the photographic RVs, Heros RVs from Rivinius et al. (2006), and our Hα absorption RVs in three separate panels. Although Rivinius et al. (2006) write that the suspected binary nature of BU Tau could not be confirmed on the basis of their data, their RVs also nicely follow the 218-d period. This constitutes yet another support for the reality of this period. Our solution 1 agrees well with the result of Katahira et al. (1996b).

[1] The program HEC13 with brief instructions how to use it is available to interested users at *http://astro.troja.mff.cuni.cz/ftp/hec/HEC13*.

Next, we analyzed the emission RVs that we consider as most realistically describing the true orbital motion. To see how sensitive the result is to the manner of prewhitening the data we derived the elements not only for the RVs prewhitened with the help of HEC13 (see above) but also from the original data. To this end, we divided the data into subsets spanning no more than one year and allowed SPEL to derive separate γ velocities for individual data subsets. The results are summarized in Table 2, and the corresponding RV curves compared in Fig. 10.

Table 2. Several sets of orbital elements: Solution 1... Katahira, Rivinius and this paper, prewhitened with HEC13; Solution 2... New emission-line RVs prewhitened with HEC13; Solution 3... New emission-line RVs with allowance for locally derived γ velocities.

Solution:	1	2	3
Orbital element	Old & new Hα abs.	Hα emis. wings	Hα emis. wings
P (d)	218.023±0.023	218.099±0.050	218.053±0.053
$T_{\rm periastr.}$ (d)	40040.4±1.6	52039.34±0.69	52039.73±0.73
$T_{\rm super.c.}$ (d)	40032.3	52035.50	52034.79
$T_{\rm min.\,RV}$ (d)	40044.5	52040.64	52041.11
e	0.596±0.035	0.774±0.028	0.745±0.026
ω(°)	147.7±4.5	154.2±4.0	157.3±3.5
K_1 (km s^{-1})	5.41±0.35	6.30±0.63	6.39±0.46
γ (km s^{-1})	-0.15±0.1	0.35±0.15	–
rms (km s^{-1})	3.21	1.93	1.58

The inspection of Fig. 10 shows that even the Hα emission-wing RVs are indeed indicative of an orbit with high eccentricity but that there is also an alternative possibility that the observed deep RV minimum could be a consequence of some unspecified effect of circumstellar matter, reminiscent of "an inverse rotational or Rossiter effect". In this case, the true orbit could essentially be circular. To this end, we derived yet another, a circular-orbit solution for the Hα emission RVs prewhitened for long-term changes via HEC13, omitting all RVs from the phase interval around phase zero with the most negative RVs. This resulted in the following elements: $P = 218\overset{\rm d}{.}34 \pm 0.62$, $T_{\rm super.c.}$ = HJD 2452009.9 ± 4.8, $K_1 = 1.72 \pm 0.21$ km s^{-1}.

Using the eliptical-orbit elements for the Hα emission RVs from Table 2, we estimated the basic properties of the binary from the mass function $f(m) = 0.00165$ M$_\odot$ for several plausible orbital inclinations, assuming a normal mass of the primary corresponding to its spectral type after Harmanec (1988) to be $M_1 = 2.9$ M$_\odot$.

The results of Table 3 show that the binary properties, especially the low mass ratio, are quite similar to other binaries discovered so far with Be primaries. For the estimates, we only considered higher orbital inclinations since BU Tau is one of the cases of an inverse correlation between the brightness and emission-line strength, which indicates that we see the system roughly equator-on – cf, e.g., Harmanec (1983).

If we adopt the distance to Pleiades $d = 138$ pc after Groenewegen et al. (2007), we estimate that the projected angular distance of the binary components should be $\theta = 0\overset{''}{.}0075$, dropping down to $0\overset{''}{.}0018$ at periastron. This angular separation is certainly within reach of existing large optical interferometers. The only problem is the luminosity ratio primary/secondary. If the secondary would be a normal late M dwarf corresponding to its mass, it would be fainter in the visual region by more than 10 magnitudes and the only chance to search for it would be in the far IR region, where, however, the IR excess from the Be envelope can complicate the detection. However – if it were a hot subdwarf, similar to the one found for another Be binary φ Per by Gies et al. (1998) – it might be observable in the optical region since the absolute visual magnitude of BU Tau is fainter for some 2 magnitudes than for the φ Per B0.5e primary. Finally, a cool Roche-lobe filling secondary seems improbable since it would probably produce binary eclipses.

Table 3. Basic physical properties of BU Tau as a single-line binary based on elliptical-orbit solution for the Hα emission RVs – cf. Table 2. The estimates are derived assuming the primary mass of $M_1 = 2.9$ M$_\odot$, A and $A_{\rm peri.}$ denote the semi-major axis and the binary separation at periastron, respectively.

i (°)	M_2/M_1	M_2 (M$_\odot$)	A (R$_\odot$)	$A_{\rm peri.}$ (R$_\odot$)
90	0.0876	0.254	223.5	53.0
70	0.0936	0.272	223.9	53.1
50	0.1164	0.338	225.5	53.4

In any case, attempts to resolve the 218-d binary system with some large interferometer are very desirable since a visual orbit would help not only to estimate the true orbital inclination but also to clarify whether the orbit has a high eccentricity or is nearly circular.

5. Comments on Hirata's model

We have postponed a detailed study of the long-term changes for a later work (Iliev et al. in prep.), but we wish to comment briefly on the hypothesis put forward recently by Hirata (2007). He obtained systematic spectroscopy and polarimetry of BU Tau from 1974 to 2003 and finds a change in the polarization angle from about 60° to 130° over that time interval. He interprets this change as evidence of the precession of the circumstellar disk that is responsible for the observed Hα emission. He further argues that also the change in the Hα profiles from a weak double emission with a strong central absorption core to a strong emission with a wine-bottle shape indicates that the disk was first seen more or less edge-on and later more face-on. Tanaka et al. (2007) studied the spectra of BU Tau from Nov. 2005 until April 2007, which cover the period of a formation of the new shell phase. They argue that a new disk was formed in the equatorial plane of the B star while the old disk was decaying but still present. According to their interpretation, the old disk was precessing in space as suggested by Hirata (2007). Our spectra cover a much longer time interval, including the one studied by Tanaka et al. (2007), and as Fig. 2 shows, the change of the Hα profile was smooth. We thus measured the full width at half maximum (FWHM) of a representative selection of our Hα emission-line profiles and the variation in FWHM with time is shown in Fig. 11. It was already demonstrated by Struve (1931) in his first model of Be stars as rapidly rotating objects that there is a clear correlation between the width of presumably photospheric He I lines and the width of the Balmer emission lines, which is preserved during the long-term changes. This correlation has been confirmed by a number of later studies – see, e.g., Fig. 5 of Slettebak (1979). One would therefore expect that, if the appearance of a new shell phase of BU Tau is primarily a con-

sequence of a geometrical effect, namely a gradual precession of a flat disk that becomes to be seen equator-on, the FWHM should gradually grow as the new shell phase is approaching. In contrast, Fig. 11 shows that the FWHM of Hα *was slowly decreasing* during the last 15 years. Its dramatic increase is related to the formation of a new envelope, which our spectra clearly confirm – see Fig. 12. The apparent discontinous increase in the FWHM occurs at the moment when the strength of the broader emission from the new envelope rises to a half of the peak intensity of the original emission. All this indicates that the observed variations are primarily due to physical changes in the circumstellar matter and cannot be reduced to a simple geometrical cause – a precession of the original gaseous disk. There has been a rather widespread tendency in recent years to intepret the presence of shell absorption lines as evidence of an equator-on view, since many investigators are picturing the Be star disk as a flat structure located at the stellar equator with a (rather small) opening angle (Waters 1986; Bjorkman & Cassinelli 1993; Hanuschik 1995, 1996). It is true that this model can lead to theoretical Balmer profiles similar to the observed ones, see, e.g., the 3D radiative line transfer models by Hummel (1994). One should be aware, however, that there is no unique proof of a specific geometry on the level of various simplifications of current models. For instance, Höflich (1987,1988) succeeded in modeling several Balmer emission-line profiles of particular Be stars with his model consisting of an NLTE atmosphere and a *spherical* envelope. It is then conceivable that strong shell lines could also develop in the spectrum of a Be star seen more or less pole-on in situations where a very extended *spheroidal envelope* forms around it. Similarly, it might be worth considering whether the asymmetry detected by the gradual change in the polarimetric angle is indeed caused by the precession of a flat disk or by some other effect, e.g. by a slowly revolving elongated (non-axisymmetric) disk.

Acknowledgements. We profited from the use of the program SPEL, written by our late colleague Dr. Jiří Horn. We acknowledge the use of the publicly available Elodie spectra from the electronic archive of the Haute Provence Observatory. Our thanks go to Drs. M. Ceniga, P. Hadrava, A. Kawka, D. Korčáková, J. Krtička, M. Netolický, S. Štefl, and V. Votruba, who secured some of the Ondřejov spectrograms used in this study. We also thank the referee, Dr. A.F. Gulliver, for his comments on the first version of the paper. The research of the Czech authors was supported by the grant 205/06/0304 and 205/08/H005 of the Czech Science Foundation and also from the Research Programs MSM0021620860 *Physical study of objects and processes in the solar system and in astrophysics* of the Ministry of Education of the Czech Republic, and AV0Z10030501 of the Academy of Sciences of the Czech Republic. The research of PK was supported by the ESA PECS grant 98058. In its final stages, the research of JN, PH, and MW was also supported by the grant P209/10/0715 of the Czech Science Foundation. We acknowledge the use of the electronic database from the CDS, Strasbourg and electronic bibliography maintained by the NASA/ADS system.

References

Ballereau, D., Chauville, J., & Mekkas, A. 1988, A&AS, 75, 139
Bjorkman, J. E. & Cassinelli, J. P. 1993, ApJ, 409, 429
Božić, H., Harmanec, P., Horn, J., et al. 1995, A&A, 304, 235
Doazan, V., Bourdonneau, B., & Thomas, R. N. 1988, A&A, 205, L11
Gies, D. R., Bagnuolo, Jr., W. G., Ferrara, E. C., et al. 1998, ApJ, 493, 440
Gies, D. R., McKibben, W. P., Kelton, P. W., Opal, C. B., & Sawyer, S. 1990, AJ, 100, 1601
Groenewegen, M. A. T., Decin, L., Salaris, M., & De Cat, P. 2007, A&A, 463, 579
Gulliver, A. F. 1977, ApJS, 35, 441
Hanuschik, R. W. 1995, Be Star Newsletter, 30, 17
Hanuschik, R. W. 1996, A&A, 308, 170
Harmanec, P. 1982, in IAU Symp. 98: Be Stars, 279–293
Harmanec, P. 1983, Hvar Observatory Bulletin, 7, 55
Harmanec, P. 1988, Bulletin of the Astronomical Institutes of Czechoslovakia, 39, 329
Harmanec, P., Habuda, P., Štefl, S., et al. 2000, A&A, 364, L85
Hirata, R. 1995, PASJ, 47, 195
Hirata, R. 2007, in Astronomical Society of the Pacific Conference Series, Vol. 361, Active OB-Stars: Laboratories for Stellare and Circumstellar Physics, ed. A. T. Okazaki, S. P. Owocki, & S. Stefl, 267–271
Hirata, R. & Kogure, T. 1976, PASJ, 28, 509
Hirata, R. & Kogure, T. 1977, PASJ, 29, 477
Horn, J., Kubát, J., Harmanec, P., et al. 1996, A&A, 309, 521
Hummel, W. 1994, A&A, 289, 458
Iliev, L., Koubský, P., Kubát, J., & Kawka, A. 2007, in Astronomical Society of the Pacific Conference Series, Vol. 361, Active OB-Stars: Laboratories for Stellare and Circumstellar Physics, ed. A. T. Okazaki, S. P. Owocki, & S. Stefl, 440–442
Iliev, L., Kovachev, B., & Ruusalepp, M. 1988, Information Bulletin on Variable Stars, 3204, 1
Katahira, J.-I., Hirata, R., Ito, M., et al. 1996a, in Revista Mexicana de Astronomia y Astrofisica, vol. 27, Vol. 5, Revista Mexicana de Astronomia y Astrofisica Conference Series, ed. V. Niemela, N. Morrell, P. Pismis, & S. Torres-Peimbert, 114–116
Katahira, J.-I., Hirata, R., Ito, M., et al. 1996b, PASJ, 48, 317
Koubský, P., Harmanec, P., Hubert, A. M., et al. 2000, A&A, 356, 913
Luthardt, R. & Menchenkova, E. V. 1994, A&A, 284, 118
McAlister, H. A., Hartkopf, W. I., Sowell, J. R., Dombrowski, E. G., & Franz, O. G. 1989, AJ, 97, 510
Merrill, P. W. 1952, ApJ, 115, 145
Miroshnichenko, A. S., Bjorkman, K. S., & Krugov, V. D. 2002, PASP, 114, 1226
Miroshnichenko, A. S., Fabregat, J., Bjorkman, K. S., et al. 2001, A&A, 377, 485
Moultaka, J., Ilovaisky, S. A., Prugniel, P., & Soubiran, C. 2004, PASP, 116, 693
Rivinius, T., Štefl, S., & Baade, D. 2006, A&A, 459, 137
Roberts, Jr., L. C., Turner, N. H., & ten Brummelaar, T. A. 2007, AJ, 133, 545
Sharov, A. S. & Lyuty, V. M. 1976, in IAU Symposium, Vol. 70, Be and Shell Stars, ed. A. Slettebak, 105–106
Sharov, A. S. & Lyutyj, V. M. 1992, AZh, 69, 544
Škoda, P. 1996, in ASP Conf. Ser. 101: Astronomical Data Analysis Software and Systems V, 187–189
Slettebak, A. 1979, Space Science Reviews, 23, 541
Stellingwerf, R. F. 1978, ApJ, 224, 953
Struve, O. 1931, ApJ, 73, 94
Struve, O. & Swings, P. 1943, ApJ, 97, 426
Tanaka, K., Sadakane, K., Narusawa, S.-Y., et al. 2007, PASJ, 59, L35
Taranova, O., Shenavrin, V., & Nadjip, A. D. 2008, Peremennye Zvezdy Prilozhenie, 8, 6
Vondrák, J. 1969, Bull. Astron. Inst. Czechosl., 20, 349
Vondrák, J. 1977, Bull. Astron. Inst. Czechosl., 28, 84
Waters, L. B. F. M. 1986, A&A, 162, 121

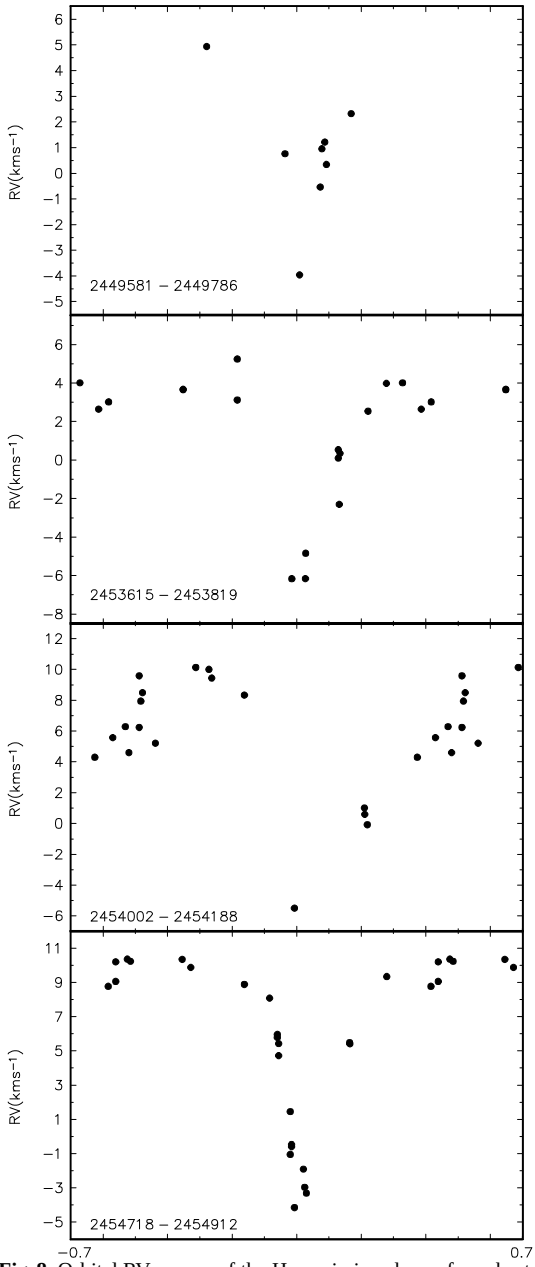

Fig. 8. Orbital RV curves of the Hα emission shown for subsets of data spanning less than a year. For all plots, period $218^{d}.053$ was used, with phase zero at HJD 2452041.11, which corresponds to the RV minimum (see Table 2).

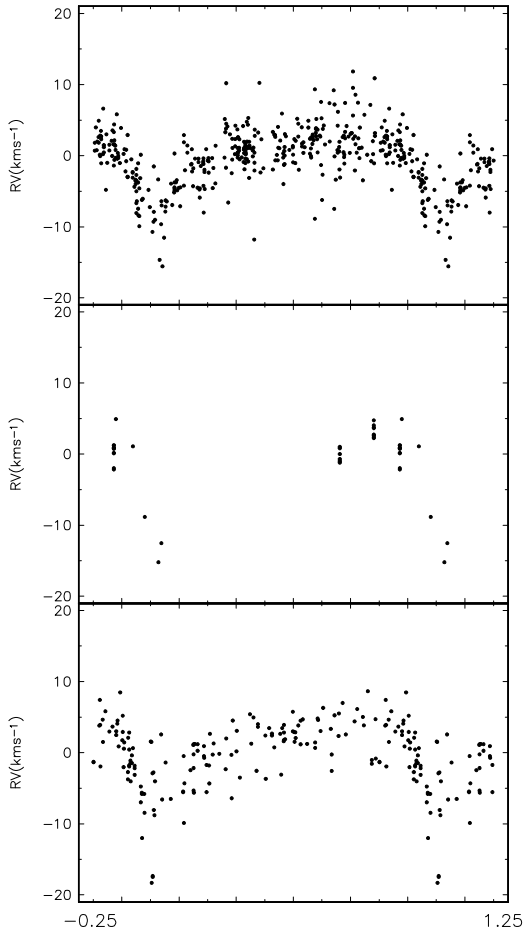

Fig. 9. *Top:* The phase plots of all available Balmer absorption RVs, prewhitened for the long-term RV variations with HEC13 (as shown in Fig. 5). Elements from solution 1 of Table 2 were used, with phase zero at minimum RV. For clarity, we show three different data subsets separately: *Top panel:* Photographic RVs from Katahira et al. (1996b); *Central panel:* RVs from electronic Heros spectra published by Rivinius et al. (2006); *Bottom panel:* RVs from electronic spectra used in this paper.

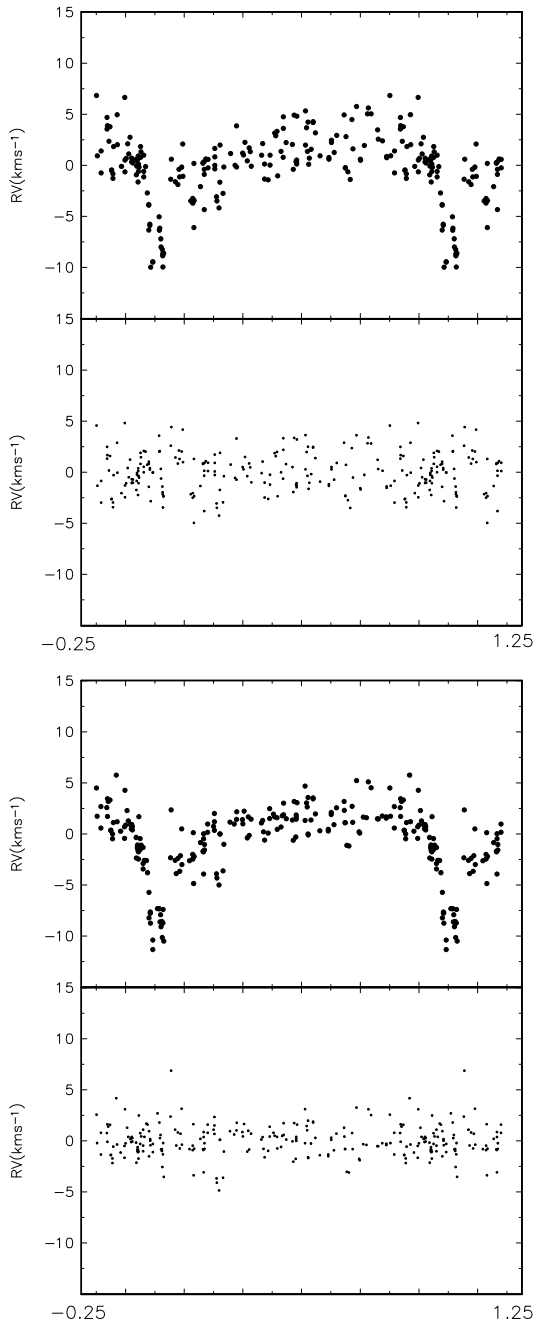

Fig. 10. The orbital RV curves of BU Tau based on the Hα emission RVs plotted for the solutions 2 and 3 of Table 2. Phase zero corresponds to the respective epoch of minimum RV and the O-C deviations from the solutions are shown by small circles in separate panels. *Top two panels:* RVs prewhitened via HEC13 (solution 2); *Two bottom panels:* original RVs minus locally derived systemic γ RVs (solution 3). See the text for details.

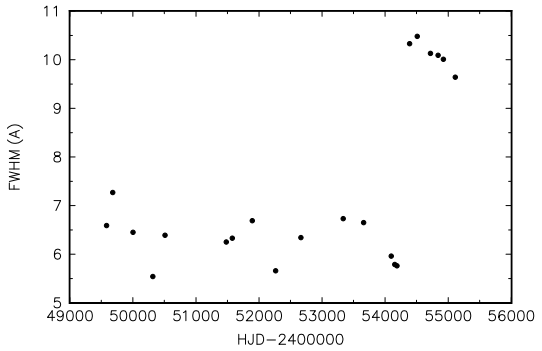

Fig. 11. A time development of the FWHM (in Å) of the Hα emission. The rapid increase is caused by the formation and a fast strengthening of another double emission due to a newly formed envelope.

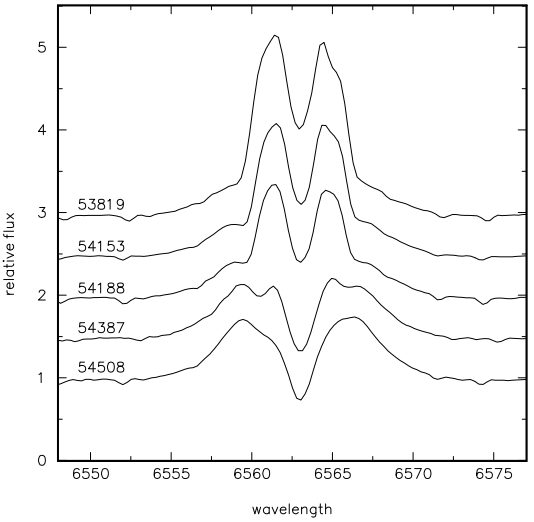

Fig. 12. A series of the Hα profiles over the time interval of the formation of a new shell. The HJDs-2400000 of individual spectra are shown and the time runs from the top to the bottom. One can see how the new broad emission gradually rises in intensity and how its blending with the decaying previous double (but narrower) emission creates a profile with four emission peaks for some time. Then the new emission gets so strong that it merges with the original one.

Appendix A: Overview of available spectroscopic observations

Here, we provide some details on the spectra used in this study and listed in Table 1 and on their reduction:

1. *Ondřejov spectra:* All 101 electronic spectrograms were obtained in the coudé focus of the 2.0-m reflector and have a linear dispersion of 17.2 Å mm^{-1} and a 2-pixel resolution 12600 (11-12 km s^{-1} per pixel). The first 35 spectra were taken with a Reticon 1872RF linear detector and cover a spectral region from 6300 to 6730 Å. Complete reductions of these spectrograms were carried out by JN with the program SPEFO, written by the late Dr. J. Horn and further developed by Dr. P. Škoda and more recently by Mr. J. Krpata – see Horn et al. (1996) and Škoda (1996). The remaining spectra were secured with an SITe-5 800 × 2000 CCD detector and cover a slightly longer wavelength interval 6260–6760 Å. Their initial reductions (bias subtraction, flatfielding, creation of 1-D images, and wavelength calibration) were carried out by MŠ in IRAF.
2. *DAO spectra:* These spectrograms were obtained in the coudé focus of the 1.22-m reflector of the Dominion Astrophysical Observatory by SY, who also carried out their initial reductions (bias subtraction, flatfielding, and creation of 1-D images). Their wavelength calibration was carried out by JN in SPEFO. The spectra were obtained with the 32121H spectrograph with the IS32R image slicer. The detectors were UBC-1 4096x200 CCD for data before May 2005 and SITe-4 4096x2048 CCD for data after May 2005. They cover a wavelength region from 6150 to 6750 Å, have a linear dispersion of 10 Å mm^{-1} and 2-pixel resolution of 21700 (∼ 7 km s^{-1} per pixel).
3. *OHP spectra:* The public ELODIE archive of the Haute Provence Observatory (Moultaka et al. 2004) contains 30 spectra listed as BU Tau, but some of them are actually spectra of 27 Tau. We were able to recover 21 usable spectra. For the purpose of this study, we extracted, rectified, and measured only the red parts of these spectrograms.
4. *Rozhen spectra:* All 23 spectra from Rozhen observatory were obtained in the coudé spectrograph of the 2-m RCC telescope. A CCD camera Photometrics AT200 with SITe SI003AB 1024x1024 chip was used. The spectrograph was used in a configuration providing high-resolution spectra suitable for revealing fine details and the structure of the spectral lines. A Bausch&Lomb 632/22.3 grating was used in its 2nd order, giving a linear dispersion of 4.2 A/mm with 2-pixel resolution of 33000 (∼ 4.5 km/s per pixel). Wavelength coverage is about 100 Å around Hα. The initial reduction (bias subtraction, flatfielding, creation of 1-D images and wavelength calibration) was carried out by LI in MIDAS.
5. *Lisboa spectra:* These 4 CCD spectra were obtained with the IGeoE 0.356-m SC telescope working at F/11. The spectrograph is a Littrow LHIRESIII with a 2400 grooves per mm grating and a spectral resolution of about 14.000. The initial reduction (bias subtraction, flatfielding, creation of 1-D images, and wavelength calibration) of the spectra was made by JR.

The rectification and removal of cosmics and flaws of *all spectrograms* were carried out in a uniform way by JN in SPEFO. The program SPEFO was also used to RV measurements, based on a comparison of direct and flipped images of the spectral line profiles. Since we were searching for small RV variations and since the setting on the steep wings of the emission-line profiles was not always straightforward (see below), these RV measurements were carried out independently by JN and PH. Besides the settings on the steep wings of the Hα emission, we also measured the Hα absorption core on all spectra where such absorption was present to have a comparison with the results of Katahira et al. (1996b). We also tried to measure RV of the He I 6678 Å absorption wings but due to weakness of this line and its possible structure, these measurements turned out to be useless so we did not use them. Following Horn et al. (1996), we also measured selected stronger and unblended telluric lines in all spectra and used them to a correction of the RV zero point. Thanks to that, the spectra from all observatories can be treated as coming from one instrument for all practical purposes.

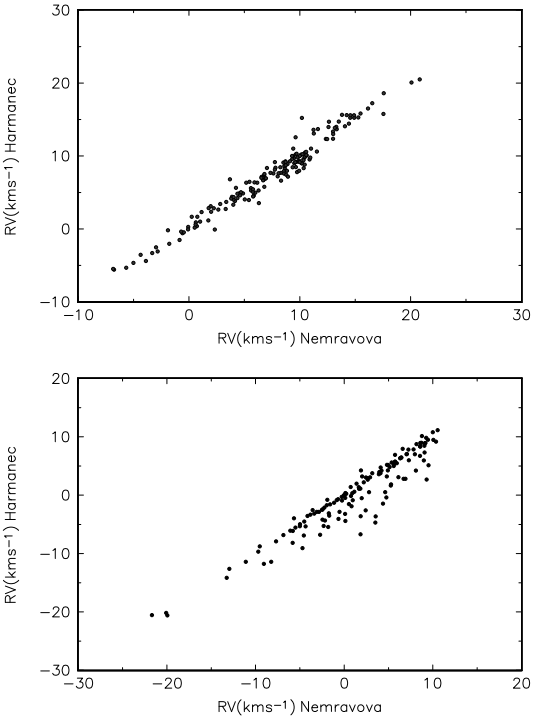

Fig. A.1. A comparison of independent RV measurements of the steep Hα emission wings (upper panel) and shell core absorption (bottom panel).

A comparison of the two sets of independent RV measurements is shown in Fig. A.1. In general, the agreement is good. A formal regression between the measurements of PH and JN was derived. Its slope is 0.98 ± 0.01 for the emission and 0.94 ± 0.01 for the absorption. For the absorption line, it is conceivable that in specific cases one or the other measurer was confused by a telluric line blended with the stellar absorption core. For analysis, we used the mean RVs of the two independent measurements. All our RVs with the corresponding HJDs of their mid-exposures are provided in Table A.1.

Table A.1. Radial velocities of the Hα emission wings and shell absorption core obtained via averaging the independent measurements by J. Nemravová and P. Harmanec; DAO = Dominion Astrophysical Observatory, Victoria; ROZ = Rozhen National Observatory ; OND = Ondřejov Observatory; LIS = IGeoE-Lisbon; OHP = Haute Provence Observatory;

Time of obs. (HJD-2400000)	RV(Hα em.) [km s^{-1}]	RV(Hα abs.) [km s^{-1}]	Source	Time of obs. (HJD-2400000)	RV(Hα em.) [km s^{-1}]	RV(Hα abs.) [km s^{-1}]	Source
49581.5875	4.94	–	OND	52957.5296	8.80	-0.28	OND
49634.6281	0.76	–	OND	52978.2960	9.86	0.06	ROZ
49644.5439	-3.96	–	OND	52992.4704	9.53	5.72	OND
49658.4732	-0.54	–	OND	53027.3770	8.36	2.20	OND
49659.4898	0.95	–	OND	53029.2971	9.82	3.96	OND
49661.4455	1.21	–	OND	53042.2717	8.90	1.48	ROZ
49662.5208	0.34	–	OND	53042.2776	8.73	0.74	ROZ
49679.3450	2.32	-10.53	OND	53044.2905	10.57	4.86	ROZ
49786.7179	2.17	-0.69	DAO	53044.3017	10.35	4.64	ROZ
49930.5573	7.16	–	OND	53046.3601	9.36	3.09	ROZ
49948.5677	9.24	–	OND	53048.3209	11.01	6.33	OND
49949.6057	8.98	–	OND	53060.2802	9.59	5.48	OND
50001.5337	9.63	–	OND	53082.2765	10.21	8.46	OND
50015.4509	8.96	–	OND	53103.2588	9.65	2.68	ROZ
50104.4137	4.68	–	OND	53216.5807	7.69	2.99	OND
50122.3298	8.05	–	OND	53216.5841	6.72	2.61	OND
50159.3244	7.52	–	OND	53236.5388	7.07	0.62	OND
50316.5313	12.67	–	OND	53236.5418	6.67	1.69	OND
50410.5517	12.17	–	OND	53236.5444	6.85	2.75	OND
50439.3454	11.07	–	OND	53244.5837	7.85	0.32	ROZ
50448.4556	12.39	–	OND	53303.4677	6.89	-3.16	ROZ
50508.3366	9.58	–	OND	53303.4734	6.76	-2.61	ROZ
50509.3213	8.40	–	OND	53306.4628	6.94	-2.43	ROZ
51227.6834	15.86	–	DAO	53332.2934	6.14	-3.80	ROZ
51481.5805	16.66	–	OND	53335.5298	4.87	-4.51	OND
51570.2954	18.09	-11.26	OHP	53335.5058	4.15	-5.53	OND
51572.2713	15.23	–	OHP	53452.2425	4.60	-5.45	ROZ
51572.2823	15.27	-7.80	OHP	53555.5651	4.25	-6.60	OND
51573.3101	14.43	–	OHP	53579.5663	4.92	-9.15	OND
51573.3184	14.89	–	OHP	53615.5628	2.54	-6.85	OND
51576.2801	20.66	–	OND	53628.0077	3.98	-4.82	DAO
51797.5902	14.92	-3.58	OND	53638.9848	4.01	-5.96	DAO
51888.4738	15.65	-12.79	OHP	53651.5938	2.64	-4.98	OND
51889.4120	16.89	-1.85	OHP	53658.5135	3.02	-6.07	OND
51892.4705	16.33	-3.26	OHP	53708.8482	3.65	-2.43	DAO
51975.3321	14.73	-2.98	OND	53708.8552	3.68	-4.75	DAO
52236.4148	12.34	-0.05	OHP	53745.4308	3.12	-3.33	OND
52236.4313	13.49	-0.60	OHP	53745.4444	5.25	-3.26	OND
52237.4193	13.64	1.47	OHP	53782.3483	-6.17	-13.71	ROZ
52238.4212	15.07	-2.16	OHP	53791.3420	-6.16	-9.69	OND
52239.4098	14.07	5.44	OHP	53791.6955	-4.84	-10.42	DAO
52241.4048	13.66	2.18	OHP	53813.6682	0.54	-6.90	DAO
52241.4168	13.28	-0.09	OHP	53813.6731	0.10	-7.00	DAO
52242.3968	13.50	-2.44	OHP	53814.3319	-2.30	-11.32	ROZ
52242.4088	13.17	-1.56	OHP	53814.7058	0.35	-5.74	DAO
52263.3571	4.86	-21.12	OHP	53819.2800	1.72	-3.85	OND
52264.3598	3.99	-20.28	OHP	54002.0002	-5.50	-5.17	DAO
52264.3759	4.19	-20.14	OHP	54049.4053	1.00	-0.49	ROZ
52287.7753	12.91	-3.06	DAO	54049.5688	0.59	-4.32	ROZ
52533.0560	12.70	-0.59	DAO	54051.3857	-0.08	-0.54	ROZ
52664.2587	12.66	6.15	OHP	54085.1936	4.30	6.64	OND
52706.7375	9.20	3.07	DAO	54097.3352	5.58	5.29	OND
52710.2434	8.94	-0.88	ROZ	54105.7532	6.28	4.59	DAO
52860.5294	13.01	5.71	ROZ	54108.3564	4.60	3.58	ROZ
52877.5835	14.12	4.46	OND	54115.3230	9.59	7.83	OND
52899.5953	9.18	2.73	OND	54115.3365	6.24	5.07	OND
52900.5672	10.16	1.06	OND	54116.3092	7.94	5.01	OND
52900.5694	9.91	3.46	OND	54117.3291	8.49	4.97	OND
52902.4322	11.08	0.23	OND	54126.2227	5.21	3.45	OND
52902.4376	10.01	-0.84	OND	54153.2844	10.13	9.55	OND
52904.6492	10.21	-1.22	OND	54162.3401	10.00	7.07	OND
52904.6537	8.10	-1.58	OND	54164.2850	9.44	8.85	OND
52904.6581	8.64	-2.50	OND	54186.2921	8.34	10.40	OND
52949.6009	4.53	-4.85	OND	54188.3212	8.24	7.65	OND
52949.6044	7.99	-1.69	OND	54341.0107	8.10	9.45	DAO
52949.6091	8.48	0.25	OND	54387.5177	7.60	9.07	OND
52952.5541	9.42	1.66	ROZ	54442.9976	-1.19	7.27	DAO
52952.5619	8.61	0.73	ROZ	54490.2613	2.53	5.75	OND

Table A.2. (cont.) Radial velocities of the Hα emission wings and shell absorption core obtained via averaging the independent measurements by J. Nemravová and P. Harmanec; DAO = Dominion Astrophysical Observatory, Victoria; ROZ = Rozhen National Observatory ; OND = Ondřejov Observatory; LIS = IGeoE-Lisbon; OHP = Haute Provence Observatory;

Time of obs. (HJD-2400000)	RV(Hα em.) [km s^{-1}]	RV(Hα abs.) [km s^{-1}]	Source	Time of obs. (HJD-2400000)	RV(Hα em.) [km s^{-1}]	RV(Hα abs.) [km s^{-1}]	Source
54519.6647	7.47	7.46	DAO	54871.4085	1.45	0.87	OND
54537.3145	7.61	7.02	OND	54871.4347	-1.05	-1.35	OND
54557.3011	9.58	7.53	OND	54872.2313	-0.59	0.00	OND
54557.3179	9.66	10.86	OND	54872.2523	-0.47	-0.18	OND
54718.5138	9.34	8.46	OND	54874.3436	-4.15	-2.85	LIS
54748.4616	8.77	8.77	OND	54880.3360	-1.91	2.66	LIS
54753.4457	10.20	9.03	OND	54881.3230	-2.97	2.77	LIS
54753.4540	9.06	8.76	OND	54882.3222	-3.32	1.51	LIS
54761.4009	10.36	9.77	OND	54911.6519	5.48	6.32	DAO
54763.4827	10.24	8.19	OND	54911.6904	5.42	6.43	DAO
54798.4322	10.35	9.47	OND	54912.6793	5.60	6.45	DAO
54804.2374	9.88	8.46	OND	54924.3033	7.18	7.77	OND
54840.4814	8.89	9.77	OND	55050.5248	11.68	8.25	OND
54857.4154	8.08	7.49	OND	55071.5298	11.44	7.33	OND
54862.6448	5.96	3.92	DAO	55083.6501	6.07	3.72	OND
54862.6812	5.78	3.76	DAO	55097.4911	-1.45	4.41	OND
54863.6276	5.43	4.58	DAO	55112.4081	3.52	-3.81	OND
54863.6627	4.72	4.21	DAO				

γ Cas study

Astronomy & Astrophysics manuscript no. 17922tex
November 17, 2011

Properties and nature of Be stars ⋆,⋆⋆

29. Orbital and long-term spectral variations of γ Cassiopeiæ

J. Nemravová[1], P. Harmanec[1], P. Koubský[2], A. Miroshnichenko[3], S. Yang[4], M. Šlechta[2], C. Buil[5], D. Korčáková[1], and V. Votruba[2]

[1] Astronomical Institute of the Charles University, Faculty of Mathematics and Physics, V Holešovičkách 2, CZ-180 00 Praha 8, Czech Republic
[2] Astronomical Institute of the Academy of Sciences, CZ-251 65 Ondřejov, Czech Republic
[3] Department of Physics and Astronomy, University of North Carolina at Greensboro, Greensboro, NC 27402, USA
[4] Physics & Astronomy Department, University of Victoria, PO Box 3055 STN CSC, Victoria, BC, V8W 3P6, Canada
[5] Association des Utilisateurs de Détecteurs Électroniques (AUDE), 28 rue du Pic du Midi, 31130 Quint-Fonsegrives, France

Release November 17, 2011

ABSTRACT

A detailed analysis of more than 800 electronic high-resolution spectra of gamma Cas, which were obtained during a time interval of over 6000 days (16.84 yrs) at several observatories, documents the smooth variations in the density and/or extend of its circumstellar envelope. We found a clear anticorrelation between the peak intensity and FWHM of the Hα emission, which seems to agree with recent models of such emission lines. The main result of this study is a confirmation of the binary nature of the object, determination of a reliable linear ephemeris $T_{\rm min.RV}$ = HJD (2452081.9 ± 0.6) + (203$^{\rm d}$.52 ± 0$^{\rm d}$.08) × E, and a rather definitive set of orbital elements. We clearly demonstrated that the orbit is circular within the limits of accuracy of our measurements and has a semi-amplitude of radial-velocity curve of 4.30±0.09 km s^{-1}. No trace of the low-mass secondary was found. The time distribution of our spectra does not allow a reliable investigation of rapid spectral variations, which are undoubtedly present in the spectra. We postpone this investigation for a future study, based on series of dedicated whole-night spectral observations.

Key words. stars: early-type – stars: binaries – stars: Be – stars: individual: gamma Cas

1. Introduction

The well–known Be star of spectral type B0IVe γ Cassiopeiæ (27 Cas, HR 264, HD 5394, HIP 4427, MWC 9, ADS 782A), is one of the first two Be stars ever discovered (see Secchi 1866) and a member of a visual multiple system. It exhibits spectral and brightness variations on several timescales. It underwent two major shell phases in 1935–36 and 1939–40. Afterwards, it appeared briefly as a normal B star. Emission strength of the Balmer lines and the brightness of the star in the visual region had been rising slowly during the rest of the 20$^{\rm th}$ century. The observational history of the star has been summarized in detail by Harmanec (2002).

In 1976, γ Cas was identified as an X-ray source. This discovery started a long debate over whether the source of X-rays is the star itself or whether γ Cas is an X-ray binary with a mass accreting compact binary companion. In an effort to prove the duplicity of γ Cas, Cowley et al. (1976) measured radial velocities (RVs hereafter) on a rich collection of photographic spectra obtained in the years 1941–1967. They were unable to find any RV changes exceeding 20 km s^{-1} or to detect any coherent periods between 2$^{\rm d}$.5 and 4000$^{\rm d}$.0. Jarad (1987) measured RVs on 81 medium-dispersion (30 Å mm^{-1}) photographic spectra using the cross-correlation technique. They concluded that the RVs vary with a short period of 1$^{\rm d}$.16885, a semi-amplitude of 27.7 km s^{-1}, and a well-defined phase curve. Combining their RVs with those measured by Cowley et al. (1976), they found a period of 0$^{\rm d}$.705163 with a semi-amplitude of only 8.6 km s^{-1}. They preferred the shorter period, which they interpreted as either a rotational or pulsation period of the star. Robinson & Smith (2000) published a detailed study of the X-ray flux of γ Cas. They found that the X-ray flux varied with a period P = 1$^{\rm d}$.12277, which they tentatively interpreted as the rotational period of γ Cas. They used this finding as one of the arguments against the binary scenario for the X-ray flux. More recently, Smith et al. (2006) have reported a coherent periodicity of 1$^{\rm d}$.21581±0$^{\rm d}$.00004 from the 1998-2006 optical photometry, prewhitened for variations on longer time scales. The latter authors pointed out that the initial period estimate of 1$^{\rm d}$.12277 was probably an alias of the correct period near 1$^{\rm d}$.21581.

Harmanec et al. (2000) measured RVs of the steep Hα emission wings in a series of 295 Ondřejov Reticon spectra spanning nearly 2500 days from 1993 to 2000. After removing the long-term RV changes, they discovered periodic RV variations with a period P = 203$^{\rm d}$.59±0$^{\rm d}$.29, semi-amplitude K_1 = 4.68 km s^{-1}, and eccentricity e = 0.26, which they interpreted as the binary motion around a common centre of gravity with a low-mass companion. They demonstrate that the published RVs from the photographic spectra can also be reconciled with the 203$^{\rm d}$.59 period and discuss

Send offprint requests to: J. Nemravová,
e-mail: janicka.ari@seznam.cz

⋆ Based on new spectral and photometric observations from the Castanet-Tolosan, Dominion Astrophysical, Haute Provence, Hvar, Ondřejov, and Ritter Observatories.

⋆⋆ Tables 2 and 3 are available only in electronic form at the CDS via anonymous ftp to cdarc.u-strasbg.fr (130.79.128.5) or via http://cdsweb.u-strasbg.fr/cgi-bin/qcat?J/A+A/

the possible properties of the system. Their result was confirmed by Miroshnichenko et al. (2002), who also measured the RVs of the Hα emission wings in a series of 130 electronic echelle spectra, secured with the 1 m reflector of the Ritter Observatory between 1993 and 2002. These two studies differ in the technique of RV measurements. While Harmanec et al. (2000) measured the RVs manually, sliding the direct and reversed continuum-normalized line profiles within a range of intensities on the computer screen until the best match was obtained, Miroshnichenko et al. (2002) also matched the original and reversed profiles, but used an automatic procedure. They arrived at a period of $205\overset{\mathrm{d}}{.}50\pm0\overset{\mathrm{d}}{.}38$, semi-amplitude of 3.80±0.12 km s^{-1}, and a *circular* orbit. They discuss several possible reasons why their results differ significantly from those of Harmanec et al. (2000). Miroshnichenko et al. (2002) also document the cyclic long-term spectral variations of γ Cas over a time interval from 1973 to 2002.

To shed more light on the differences between these two RVs studies, to obtain truly reliable orbital elements of γ Cas, and to exclude possible 1 d aliases of the 204 d period, we combined our efforts and analysed the two sets of spectra, complemented by more recent observations from Ondřejov and additional spectra from the Dominion Astrophysical (DAO), Haute Provence (OHP) and Castanet-Tolosan Observatories. The RVs in all these spectra were measured by both measuring techniques – alternatively used by Harmanec et al. (2000) and Miroshnichenko et al. (2002) – and analysed in several different ways. Here we present the results of our investigation. We also studied the long-term and rapid spectral variations of γ Cas in our data.

2. Spectral variations

We have collected and analysed series of electronic spectra from five observatories. They cover the time interval from 1993 to 2010. The journal of the observations is in Table 1, where the wavelength range, time interval covered, the number of spectra, and the spectral lines are given. For more details on the individual datasets, readers are referred to Appendix A.

Table 1. Journal of spectral observations.

Origin of spectra	$\Delta\lambda$ (Å)	ΔT (RJD)	Lines	N
Ond	6300–6730	49279–55398	Ha, He, Si	439
Rit	6528–6595	49272–52671	Ha	204
OHP	4000–6800	50414–52871	Ha, He, Si	34
DAO	6155–6755	52439–54911	Ha, He, Si	136
OHP/Cst	various	53997–55422	Ha	13

Notes. Ond = 2 m reflector of the Astronomical Institute AS CR Ondřejov, Rit = 1 m reflector of the Ritter Observatory of the University of Toledo, DAO = 1.22 m reflector of the Dominion Astrophysical Observatory, OHP = 1.52 m reflector of the Haute Provence Observatory, Cast = Castanet-Tolosan; $\Delta\lambda$ = the wavelength region covered, ΔT = the time interval spanned by each dataset, where times are given in the *reduced* Julian dates RJD = HJD-2400000, Lines: Ha = Hα, He = He I 6678 Å, Si = Si II 6347 Å, and Si II 6371 Å.

We focused our study on the lines in the Hα region, which are available for all spectra, although several echelle spectra cover almost the whole visible region of the electromagnetic spectrum. In particular, we studied the following spectral lines: Hα, He I 6678 Å, Si II 6347 Å, and Si II 6371 Å. No dramatic changes were found in these line profiles. The He I 6678 Å and Si II lines exhibit double-peaked emissions with the well-known V/R variations (changes in the relative strength of the shorter wavelength, "violet", to the longer wavelength, "red", peak) on the timescale of several years. Over the whole time interval covered by our spectra, the Hα line was observed as a strong, basically single–peaked emission, having a peak intensity between 3.5 and 5.0 in the units of the continuum level. Its V/R variations manifest themselves as a relative shift in the emission peak with respect to the centre of the emission profile. Several shallow absorptions can be noted in the Hα line in some of the studied spectra, but most of them are the telluric water vapour lines. Ocassionally, some weak shallow absorptions of probably stellar origin were seen, but they disappeared in less than several tens of days, and we found no regularity in their appearance and disappearance. The He I 6678 Å line consists of a double–peaked emission filling a large part of the rotationally broadened photospheric (or pseudophotospheric) absorption. The whole line is very weak and can only be measured reliably on the spectra with high S/N. The emission peaks rise only a few percent above the continuum level. Nevertheless, the time variations are seen most prominently in this line. The red peak of the He I 6678 Å emission disappeared almost completely at certain times. It is hard to say whether these variations represent only real long-term changes or whether they are partly caused by line blending. The Si II 6347 Å and Si II 6371 Å double emission lines are even weaker than the He I 6678 Å line, and their peak intensity never exceeds 5% of the continuum level. The more recent evolution of the Hα line profile is shown in Fig. 1. All line profiles shown were obtained after RJD = 52225 and were not included in the study by Harmanec et al. (2000). A similar sequences of the He I 6678 Å, Si II 6347 Å, and Si II 6371 Å line profiles are shown in Fig. 2. All displayed spectra are from Ondřejov, to compare the data with the same resolution. There are, however, the huge differences in the flux scale between Hα, He I 6678 Å, Si II 6347 Å, and Si II 6371 Å lines.

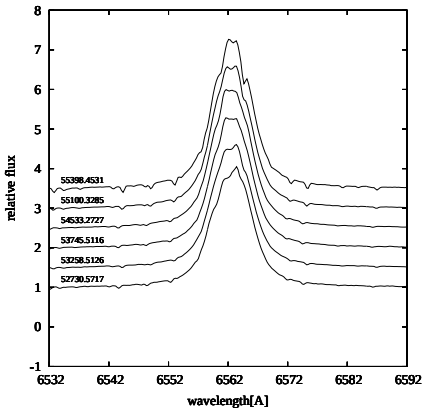

Fig. 1. Recent evolution of the Hα line profile. Mid–exposure times of the displayed spectra are in RJD = HJD–2400000.

We fitted the Hα line profiles with a Gaussian profile to obtain their peak intensity (I_{p} hereafter) and full width at half maximum (FWHM hereafter). This procedure naturally returns a value of I_{p}, which is slightly less than the very maximum of the emission profile, which is affected by both the V/R varia-

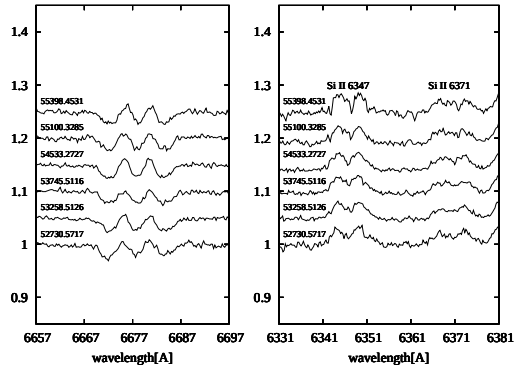

Fig. 2. Recent evolution of the He I 6678 Å (left), Si II 6347 Å, and Si II 6371 Å (right) line profiles. Mid–exposure times of the displayed spectra are in RJD = HJD–2400000. The vertical axis is in the units of the continuum flux.

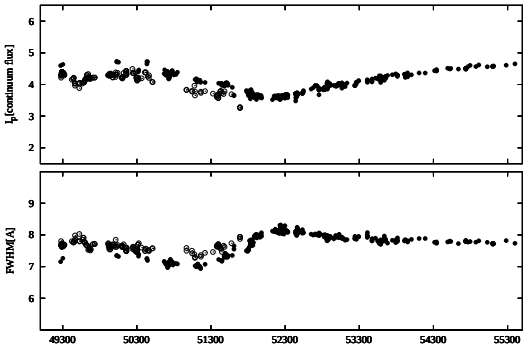

Fig. 4. The secular time variations of I_p (upper panel) and FWHM (bottom panel) of the Hα line. The time on abscissa is in RJD = HJD-2400000. The open symbols denote measurements from the Ondřejov Reticon detector, capable of distinguishing only 4000 intensity steps, which is why these measurements deviate systematically from the rest. See the text for details.

tions and blending with the neighbouring telluric lines. We do believe, however, that the fitted Gaussian provides an objective measure of the gradual changes in the emission-line strength. We omitted the saturated Hα line profiles, of course. One example of a Gaussian fit is in Fig. 3 to show where the FWHM and I_p were measured.

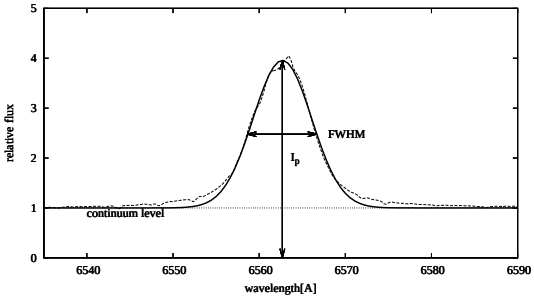

Fig. 3. An example of the Gaussian fit to an Hα line profile, which also shows the derived quantities I_p and FWHM. Dashed line: the observed Hα profile; solid line: the Gaussian fit to it; dotted line: the continuum level.

Figure 4 shows the time variations of the FWHM and I_p. An interesting finding is that the secular variations of these two quantities are anticorrelated with each other. The apparently increased scatter of both dependencies between RJDs $\approx$ 50000 and 52000 is caused solely by the lower resolution in intensity of the Ondřejov Reticon spectra taken prior RJD = 52000. [1]

[1] Although the original Reticon detector and the currently used CCD detector were attached to the same camera of the coudé spectrograph and have the same *spectral* resolution, the control electronics of the Reticon detector allowed distinguishing only 4000 steps in intensity, while the CCD detector recognizes 60000 intensity steps. This leads to a systematic difference for strong emission lines.

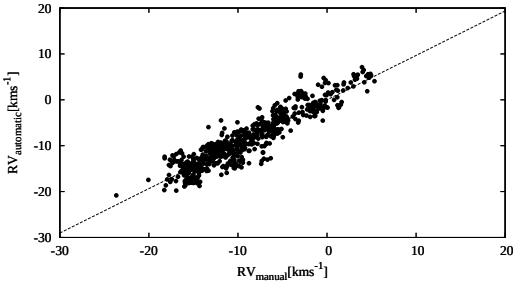

Fig. 5. Comparison of the automatically measured Hα emission-wing RVs (ordinate = y) with those measured manually (abscissa = x). The dashed line is a fitted linear function $y = 0.968\,x$.

3. RV changes

3.1. Long–term and periodic RV changes and the new orbital solutions

Similar to Harmanec et al. (2000) and Miroshnichenko et al. (2002), we measured the steep wings of the Hα emission in all unsaturated profiles. The reasons the emission wings should provide a good estimate of the true orbital motion of the Be primary around the common centre of gravity with the secondary were recently summarized in detail by Ruždjak et al. (2009). To them, we can add that Poeckert & Marlborough (1978) modelled the Hα emission of γ Cas, and their model showed that the Hα emission wings originate in regions that are much closer to the star than the radiation that is forming the upper part of the line.

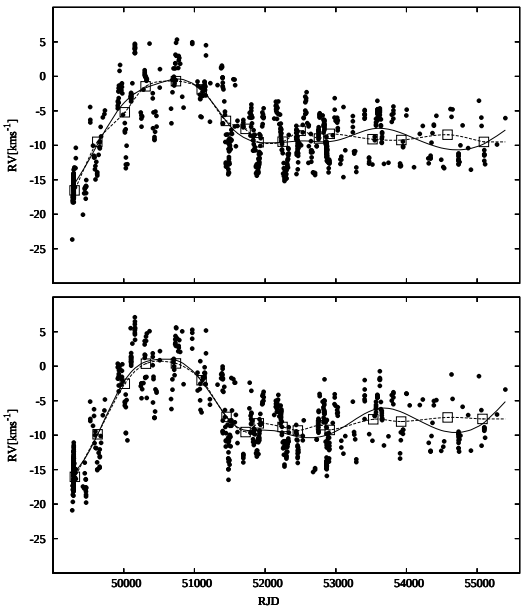

Fig. 6. Plots of RVs vs. RJD = HJD-2400000: *Top panel:* Manually measured Hα emission-wing RVs. *Bottom panel:* Automatically measured Hα emission-wing RVs. The solid lines in all panels represent the long–term RV change as derived with the program HEC13. The squares in both panels denote the local 'systemic' velocities calculated with the program SPEL for individual data subsets. The dashed line represents Hermite–polynomial fit computed with program HEC36. See the text for details.

Moreover, we also attempted to measure the RVs of other available spectral lines (He I 6678 Å, Si II 6347 Å and Si II 6371 Å) to see if they undergo similar time changes. We primarily measured also the outer emission wings of these lines, but for the He I 6678 Å line it was possible to obtain a relatively accurate RV of the central absorption core. The RVs measured on the emission wings of the Si II 6347 Å and Si II 6371 Å lines were averaged.

Two methods of RV measurement were used as follows.

1. *Manual measurements* were carried out in the program SPEFO, written by Dr. J. Horn and more recently improved by Dr. P. Škoda and Mr. J. Krpata (see Horn et al. 1996; Škoda 1996). The user can slide the direct and reversed line profile on the computer screen until a perfect match of the selected parts of the profiles is achieved. The advantage of this, admittedly a bit tedious procedure, is that the user actually sees all measured line profiles and can avoid any flaws and blends with the telluric or weak stellar lines. It is invaluable for measurements of weak spectral lines, where any automatic method can be easily fooled by the noise. The same measuring technique has also been used by Harmanec et al. (2000). One of us, JN, also re-measured all Reticon spectra used in their study. Plots of the old vs. new measurements are available as Fig. A.4 in Appendix A. Considering the good agreement of both measurements, we used the mean value of the original and new RV measurements for each studied feature. All lines (whenever available) were measured with this technique.
2. *Automatic measurements* were obtained with a program written by AM, which also shifts the direct and reversed line-profile images for a selected range of relative intensities in the continuum units to find a minimum difference between them. The advantages of this method are that it is fast and impersonal. A potential danger is that it can be fooled by flaws and blends in some particular cases. Only the Hα emission wings were measured with this method.

We denote the RVs measured by the first method as *manual* and those measured by the second method as *automatic* to distinguish them in following sections. In Fig. 5 the automatic Hα emission RVs are plotted vs. the manually measured ones to see whether there is any systematic difference between the two methods. We fitted the data with a linear relation and somewhat surprisingly the slope was found to be 0.968±0.009; i.e., the automatic method finds a slightly narrower total range of RV variations than the manual one. All individual RV measurements on the steep wings of the Hα emission are published in detail in Table 2 for the manual, and in Table 3 for the automatic measurements.[2]

The Hα emission RVs measured manually and automatically are plotted vs. time in Fig. 6. Additional time plots for other measured features can be found in Appendix A. Figure 6 shows that γ Cas exhibits long-term RV variations over several years, which seem to correlate with those of the peak intensity of the emission. To be able to search for periodic RV changes on a shorter timescale, one has first to remove the long-term ones. To check how robust the result is or how much it depends on the specific way of secular-changes removal, we applied three different approaches to this goal.

The first was to use the program HEC13 written by PH, which is based on the smoothing technique developed by Vondrák (1969, 1977) and which uses some subroutines kindly provided by Dr. Vondrák[3]. The level of smoothing is controlled by a smoothing parameter ϵ (the lower the value of ϵ, the higher the smoothing), and the smoothing routine can operate either through individual data points or through suitably chosen normal points, which are the weighted mean values of the observed quantity (RV in our case) over the chosen constant time intervals. In both cases, the $O-C$ residua are provided for all individual observations. In these particular cases the following specifications for smoothing were used: $\epsilon = 5\times10^{-16}$ and 200 d normals for the Hα emission-wing RVs measured by both methods, and $\epsilon = 1\times10^{-16}$ and 200 d normals for the RVs measured on the He I 6678 Å absorption core. These particular choices of ϵ make the smoothing function follow only the secular RV variations. The solid lines in the three panels of Fig. 6 show the estimated long-term changes, which were then substracted from the original RVs. These prewhitened RVs were than searched for periodicity from $3000\overset{d}{.}0$ down to $0\overset{d}{.}5$ with the program HEC27 (also written by PH), based on the PDM technique developed by Stellingwerf (1978). The θ-statistics periodograms for the manually and automatically measured Hα emission RVs are plotted in Figs. 7 and 8, respectively. The upper panels in both plots show

[2] Tables 2 and 3 are published only in the electronic form.

[3] The program HEC13 with brief instructions how to use it is available to interested users at http://astro.troja.mff.cuni.cz/ftp/hec/HEC13.

the range of periods from $3000\overset{d}{.}0$ down to $50\overset{d}{.}0$, while the periods from $2\overset{d}{.}0$ down to $0\overset{d}{.}5$ are shown in the lower panels. The periodograms are flat, with θ close to a value of 1 for all periods between 2 and 50 d, which is why we do not show these parts of the periodograms in the figures. One can see that the combination of RVs from several observatories, which are different from each other in their local times, safely excluded the one-day aliases.

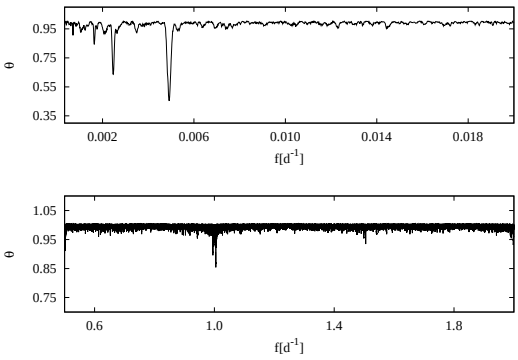

Fig. 7. Stellingwerf's θ statistics for the manually measured RVs of the Hα emission wings plotted vs. frequency f. *Upper panel:* Periods from $3000\overset{d}{.}0$ down to $50\overset{d}{.}0$. *Bottom panel:* Periods from $2\overset{d}{.}0$ downto $0\overset{d}{.}5$. The panels have a different scale on the ordinate.

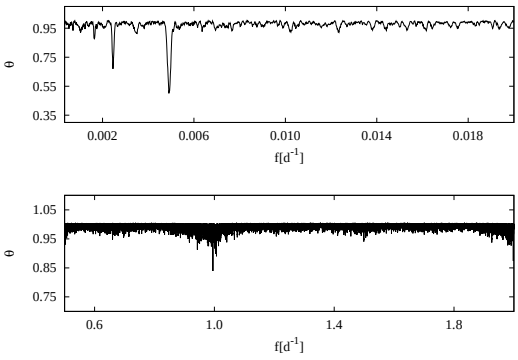

Fig. 8. Stellingwerf's θ statistics for the automatically measured RVs of the Hα emission wings plotted vs. frequency f. *Upper panel:* Periods from $3000\overset{d}{.}0$ down to $50\overset{d}{.}0$. *Bottom panel:* Periods from $2\overset{d}{.}0$ downto $0\overset{d}{.}5$. The panels have a different scale on the ordinate.

The deepest minimum in both periodograms at a frequency $f \approx 0.004910$ d^{-1} corresponds to a period of $P \approx 203\overset{d}{.}0$. The two shallower peaks at lower frequencies in Figs. 7 and 8 correspond to the integer multiples of the 203 d period. The 203 d period was also detected in the measured RVs of other spectral lines, though with a larger scatter in the RV curves. These additional results are presented in the online Appendix.

Since no obvious signs of the secondary companion are seen in the spectrum, we adopted γ Cas as a single-line spectroscopic binary. We derived a number of orbital solutions for the Hα emission RVs, prewhitened for the long-term changes with HEC13. We used the program SPEL (written by Dr. J. Horn and never published) for this purpose. The program has already been used in several previous studies, e.g., Harmanec (1983, 1984), Koubský et al. (1985), Štefl et al. (1990), and Horn et al. (1992, 1994).

Our first goal was to decide whether the orbital eccentricity found by Harmanec et al. (2000) is real or whether the orbit is actually circular as concluded by Miroshnichenko et al. (2002). In Table 4 the eccentric-orbit solutions for the manually and automatically measured Hα emission-wing RVs are compared. Lucy & Sweeney (1971) have pointed out that observational uncertainties may cause the estimated eccentricity to be biased when the eccentricity is low. The probability that the true eccentricity is zero can be calculated, and this is given in the column "L-S test". If this probability is greater than 0.05 we accept the hypothesis that the true eccentricity is zero at a 5% confidence level.

To shed more light on the problem, we split both manually and automatically measured RVs into a number of data subsets, each of them covering a time interval not longer than three consecutive orbital periods and containing enough observations to define the orbital RV curve. We used the original, not the prewhitened RVs. The phase diagrams for a period $P = 203\overset{d}{.}52$ for all selected data subsets are shown in Fig. 9. We derived the elliptical-orbit solutions for them, again testing the reality of the non-zero orbital eccentricity after Lucy & Sweeney (1971). To always find the solution with the smallest rms error, we started the trial solutions for each subset with initial values of ω for four possible orientations of the orbit, namely 45°, 135°, 225°, and 315°.

The corresponding orbital elements for the selected subsets, together with the Lucy-Sweeney test, are summarized in Table 5 for manually measured RVs and in Table 6 for automatically measured RVs. The results show very convincingly that the true orbit must be circular (or has a very low eccentricity, which is beyond the accuracy limit of our data). Although the L–S test detected a definite eccentricity for several subsets, the individual values of the longitude of periastron are basically accidental, and that is probably the strongest argument for the eccentric-orbit solutions not being trusted.

Table 4. Eccentric-orbit solutions based on the Hα emission-wing RVs measured manually and automatically and prewhitened for the long-term changes with the program HEC13.

Solution No.:	1)	2)
Element	Manual	Automatic
P (d)	203.36±0.10	203.08±0.11
T_{RVmin} (RJD)	52083±17	52080±13
ω (°)	19±30	147±22
e	0.048±0.027	0.072±0.030
K_1 (km s^{-1})	3.88±0.10	3.93±0.12
γ (km s^{-1})	0.164±0.071	0.180±0.081
rms (km s^{-1})	1.772	1.948
L–S test	0.183	0.064
No. of RVs	757	700

Table 5. The eccentric-orbit solutions for the subsets of manually measured Hα emission-wing RVs, shown as phase plots in Fig.9.

N_s	e	ω (°)	K_1 (km s^{-1})	L–S test	N
2	0.052±0.073	141±38	4.30±0.24	0.734	25
3	0.313±0.082	165±12	5.43±0.44	0.001	42
4	0.416±0.083	108.9±8.3	6.46±0.58	0.000	42
5	0.14±0.14	160±41	4.37±0.60	0.672	25
7	0.10±0.11	322±47	6.88±0.88	0.674	50
9	0.109±0.067	201±36	4.10±0.30	0.299	42
10	0.120±0.040	263±16	5.20±0.20	0.026	61
12	0.086±0.055	149±28	4.64±0.26	0.353	46
13	0.18 ±0.10	308±29	3.56±0.36	0.270	70
14	0.102±0.040	147±22	4.31±0.21	0.038	59
16	0.116±0.067	105±31	3.87±0.22	0.287	30

Notes. N_s = a number of RV subset (the same numbering being also used in Fig. 9), L–S test = probability that the eccentricity found is false, N = number of RVs in the subset.

Table 6. The eccentric-orbit solutions for the subsets of automatically measured Hα emission-wing RVs.

N_s	e	ω (°)	K_1 (km s^{-1})	L–S test	N
2	0.30±0.14	322±24	4.57±0.81	0.174	24
4	0.42±0.11	285±17	5.82±0.78	0.004	44
5	0.34±0.10	6±20	4.74±0.62	0.014	25
7	0.16±0.12	87±49	6.0±1.1	0.311	52
9	0.15±0.19	92±53	3.38±0.50	0.583	40
10	0.098±0.050	48±23	4.12±0.19	0.147	60
12	0.40±0.21	336.0±9.5	5.9±1.2	0.054	36
13	0.21±0.14	82±44	3.94±0.53	0.157	59
14	0.167±0.068	111±20	4.57±0.33	0.026	46
16	0.26±0.13	227±24	4.61±0.56	0.201	27

Notes. N_s = a number of a RV subset (the same numbering being also used in Fig. 9), L–S test = probability that the eccentricity found is false, N = number of RVs in the subset.

Adopting the circular orbit from now on, we attempted to remove the long-term RV variations with a different approach. Using the manually measured Hα emission-wing RVs, we treated each data subset spanning no more than three orbital periods (last four subsets) and two orbital periods (remaining subsets) as data coming from separate spectrographs, allowing SPEL to derive individual 'systemic velocities' for each subset. This way, the orbital solution was again free of the long-term changes but they were removed in discrete velocity steps. The corresponding orbital solution is in Table 7, and individual velocity levels (γ's) are shown in the top panel of Fig. 6 and listed in Table A.2 in Appendix A. At first sight, this way of removing the long-term changes might seem less accurate, but it leads to smaller rms error for the solution than the removal via HEC13. There are two reasons for that:

1. The HEC13 program computes normal points from RV subsets covering constant time intervals, while for γ velocities the length of subsets was chosen more suitably to our data distribution in time.
2. The HEC13 program computes the normal points as weighted means, but the γ velocities computed with the SPEL program are elements of the Keplerian orbital model.

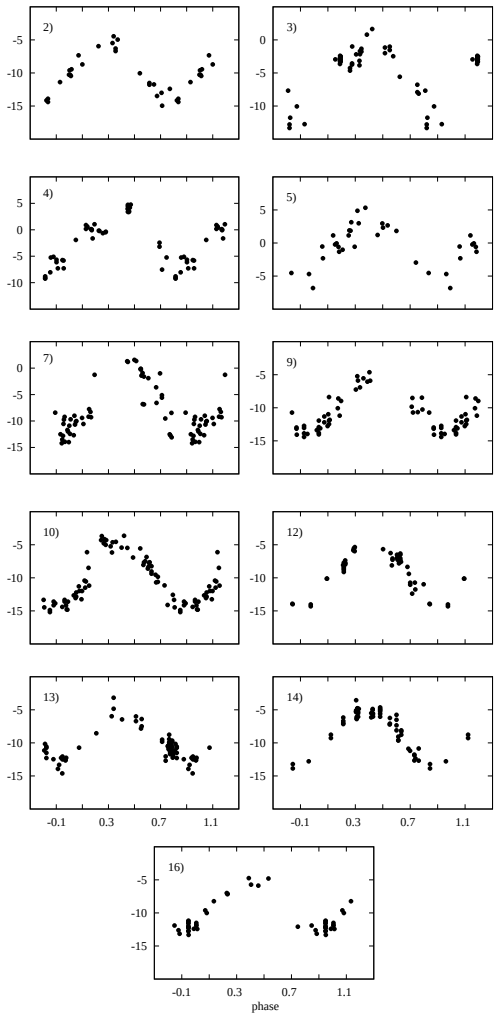

Fig. 9. Phase diagrams for subsets of Hα emission-wing RVs measured manually. The ordinates of all plots are RVs in km s^{-1}and the individual subsets vertical axis is in RV and the different ranges reflect the fact that the original, not prewhitened RVs are used. Trial orbital solutions for these subsets are in Tabs. 5 and 6.

For completeness, a solution for an eccentric orbit was also derived but the L-S test gave the probability of 0.18, reassuring us that the eccentricity is spurious. Also for this method of the long-term removal the rms error of the orbital solution is better for the manually than for the automatically measured RVs.

We tested yet another method of removing the long–term variations. It can only be used when one has a RV curve uniformly enough covered by observations. The RVs are averaged over chosen time intervals, and the Hermite polynomials are fitted through these averaged (normal) points. We used the pro-

Table 7. Orbital elements obtained using RVs measured manually (3) and automatically (4) on the Hα line, with the removal of the long–term changes using different γ velocities for individual data subsets.

Solution No.:	3)	4)
Element	Manual	Automatic
P(d)	203.65±0.13	203.47±0.14
$T_{\rm RVmin}$(RJD)	52081.42±0.81	52081.99±0.95
K_1(km s^{-1})	4.084±0.10	4.14±0.13
rms(km s^{-1})	1.657	1.908
No. of RVs	757	700

gram HEC23 to compute the normal points and program HEC36 to fit them[4]. We tentatively averaged the RVs over a 300 d and a 400 d interval. New orbital solutions were derived using RVs prewhitened this way. The rms error of the resulting solution was approximately the same as the rms error of the solution for RVs prewhitened HEC13. We decided to use this approach in another way. We used the systemic velocities derived with SPEL as normal points and fitted them with the Hermite polynomials using HEC36. The RJDs of RVs in a subset were averaged and the mean RJD was used as the epoch of the γ velocity. The same approach to computing epochs of normal points is also used in the program HEC13. This way we effectively removed one of the disadvantages of the previous method since HEC36 connects the normal points with a smooth curve, thus removing the discontinuous shifts introduced with the second method. The Hermite–polynomial fit is shown in the first two panels of Fig. 6. The $O-C$ residua were again used to derive circular-orbit solutions with SPEL. These are presented in Table 8. As expected, the improvement in the resulting rms errors with the second method is relatively small.

Table 8. Orbital elements obtained using the Hα RVs measured manually (5) and automatically (6) and removing the long–term RV variations via a Hermite–polynomial fit through the locally derived γ velocities.

Solution No.:	5)	6)
Element	Manual	Automatic
P(d)	203.523±0.076	203.371±0.089
$T_{\rm RVmin}$(RJD)	52081.89±0.62	52082.07±0.76
K_1(km s^{-1})	4.297±0.090	4.26±0.11
γ(km s^{-1})	0.018±0.064	-0.018±0.075
rms (km s^{-1})	1.592	1.825
No. of RVs	757	700

The net orbital RV curves and the corresponding $O-C$ residua from the orbital solutions are shown in Fig. 10 for the manual and in Fig. 11 for the automatically measured Hα RVs. The rms errors per one observation of the Keplerian fit no. 5 based on manually measured RVs (no. 6 in the case of automatic measurements) are shown as short abscissæ in the upper right corners of both figures. The RVs prewhitened for the long-term changes, on which these best solutions 5 and 6 are based, are also presented in Tables 2 and 3.

We did several preliminary tests of the possible rapid variations of γ Cas. Although the results clearly demonstrated their presence, the quantitative results were inconclusive so we decided to postpone analysis of rapid spectral changes for a future study, based on dedicated series of whole-night spectral observations.

[4] Both programs, written by PH, and the instructions how to use them, are available at *http://astro.troja.mff.cuni.cz/ftp/hec/HEC36*.

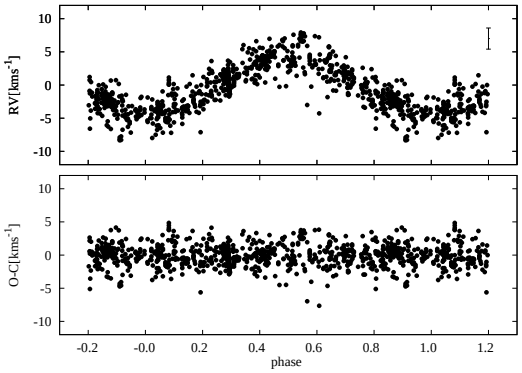

Fig. 10. *Top panel:* The net orbital RV curve corresponding to the circular-orbit solution (5) of Table 8. *Bottom panel:* The $O-C$ residua from the orbital solution. Both plots have the same velocity scale, and the epoch of RV$_{\rm min}$ is used as a reference epoch. The short abcissa in the right upper corner of the top panel denotes the rms of 1 observation for the Keplerian fit no. 5.

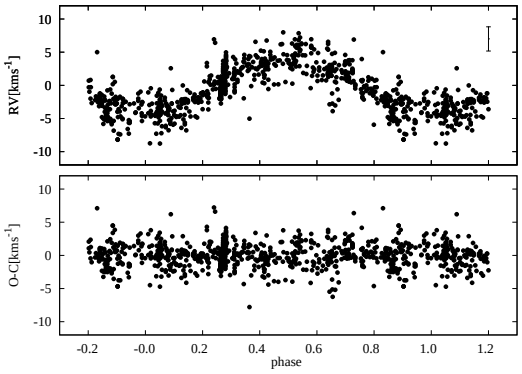

Fig. 11. *Top panel:* The net orbital RV curve corresponding to the circular-orbit solution (6) of Table 8. *Bottom panel:* The $O-C$ residua from the orbital solution. Both plots have the same velocity scale, and the epoch of RV$_{\rm min}$ is used as a reference epoch. The short abcissa in the right upper corner of the top panel denotes the rms of 1 observation for the Keplerian fit no. 6.

4. Interpretation of results

4.1. Spectral variations

We have confirmed the continuing presence of long–term variations in the Hα emission profile using the Gaussian fit and RV measurements. The former procedure gives more objective results than a direct measurement of the peak height and the full width of the line at half maximum (FWHM), because the observed height of the highest peak of a very strong emission line partly reflects the long-term V/R changes, while the measured

FWHM can be affected by the presence of several telluric water vapour-lines of variable strength. Figure 4 shows that the I_p and FWHM of the Hα emission are *anti–correlated* over the interval covered by our observations and seem to also show some variability on shorter time scales. We carried out period searches for both these quantities prewhitened for the long-term changes, but no significant periodicities were detected, and trial plots of prewhitened data did not show any evidence of variations connected with the orbital period.

It is probable that the observed long-term changes reflect some variations in the density and/or the extent of the circumstellar disk around the Be primary. Using optical interferometry, Quirrenbach et al. (1997) and Tycner et al. (2006) were able to resolve the envelope around the primary component of γ Cas and estimate that its inclination must be higher than 46° and 55°, respectively. Adopting a reasonable assumption that the rotational axis of the disk is roughly perpendicular to the binary orbit, we can conclude that the binary system is also seen under an orbital inclination higher than some 45°. We then suggest the following possible interpretation of the observed changes.

It is very probable that the envelope around the Be primary is rotationally supported and that its linear rotational velocity decreases with the axial distance from the star. Regardless of the process causing secular variations of the disk, one can assume that the increase in the height of the emission peak reflects the presence of more emission power at lower rotational velocities, thus implying either an increase in the density of the outer parts of the disk and/or an increase in the geometrical extent of the disk. This must naturally decrease the observed FWHM of the emission as observed. This qualitative scenario seems to be supported by the line-profile calculations published by Silaj et al. (2010).

4.2. Orbital motion

As mentioned in Sect. 1, one of the principal motivations of this study was to resolve the differences in the orbital solutions obtained by Harmanec et al. (2000) and by Miroshnichenko et al. (2002) and to arrive at a more definitive set of the orbital elements. We were able to combine both independent datasets and complement them with more recent spectra. In Sect. 3 we carried out a number of various tests, analysing separately the RVs measured by a manual and an automatic technique. We also tested the effect of the different ways of data prewhitening on the resulting elements. Special attention was payed to the test of whether the orbit is actually circular or has a significant eccentricity.

The principal results are the following.

1. The binary orbit of γ Cas is circular, at least within the limits of the accuracy of our data, as concluded by Miroshnichenko et al. (2002).
2. The resulting value of the orbital period is now well constrained by the data at hand, and it is robust with respect to different ways of analysis. From all experiments, we were finding values between $203\overset{d}{.}0$ and $203\overset{d}{.}6$, close to the value already found by Harmanec et al. (2000). An inspection of all trial solutions shows that the solutions based on manually measured RVs have rms errors that are systematically lower for $\approx 15\%$ in comparison to the solutions for the automatically measured Hα emission-wing RVs. We therefore conclude that solution 5 of Table 8 is the best we can offer and suggest the following linear ephemeris for the epoch of RV minimum to be used in the future studies of this binary:

$$T_{\mathrm{min.RV}} = \mathrm{HJD}\,(2452081.89 \pm 0.62) + (203\overset{d}{.}523 \pm 0\overset{d}{.}076) \times E. \quad (1)$$

3. The semiamplitude of the orbital motion is close to 4 km s^{-1} for all solutions. The recommended value from solution 5 is $K_1 = 4.297 \pm 0.090$ km s^{-1}, implying the mass function $f(M) = 0.00168$ M$_\odot$. For comparison, Harmanec et al. (2000) and Miroshnichenko et al. (2002) obtained semi-amplitudes of 4.68 ± 0.25 km s^{-1}and 3.80 ± 0.12 km s^{-1}, respectively. If we adopt the inclination value $i = 45°$ and the primary star mass $M_1 = 13$ M$_\odot$ suggested by Harmanec et al. (2000), we can estimate the secondary star mass $M_2 = 0.98$ M$_\odot$. If the system is at a post mass-transfer phase, then the secondary might be a hot helium star that could be directly detectable in the UV region of the electromagnetic spectrum.

Note: After our paper was accepted for publication, we had the privilege to read a preliminary version of another study of γ Cas kindly communicated to us by Dr. Myron A. Smith and his coauthors. They analysed in particular a smaller and partly independent set of RVs to obtain their own orbital solution. Their results are compatible with our final solution within the respective error bars.

Acknowledgements. We gratefully acknowledge the use of spectrograms of γ Cas from the public archives of the Elodie spectrograph of the Haute Provence Observatory. Our thanks are also due to Drs. P. Chadima, M. Dovčiak, P. Hadrava, J. Kubát, P. Mayer, P. Škoda, S. Štefl, M. Wolf, and P. Zasche, who obtained some of the spectra used in this study. Constructive criticism and a careful proofreading of the original version by an anonymous referee helped to improve the paper and are gratefully acknowledged. We thank Dr. M.A. Smith and his collaborators for allowing us to see a preliminary version of their new complex study of γ Cas before it was submitted for publication and for useful comments. This research was supported by the grants 205/06/0304, 205/08/H005, and P209/10/0715 of the Czech Science Foundation, from the Research Programme MSM0021620860 *Physical study of objects and processes in the solar system and in astrophysics* of the Ministry of Education of the Czech Republic, and from the research project AV0Z10030501 of the Academy of Sciences of the Czech Republic. The research of JN was supported from the grant SVV-263301 of the Charles University of Prague, while PK was supported from the ESA PECS grant 98058. We acknowledge the use of the electronic database from the CDS Strasbourg, and the electronic bibliography maintained by the NASA/ADS system.

References

Cowley, A. P., Rogers, L., & Hutchings, J. B. 1976, PASP, 88, 911
Harmanec, P. 1983, Bull. astr. Inst. Czechosl., 34, 324
Harmanec, P. 1984, Bull. astr. Inst. Czechosl., 35, 164
Harmanec, P. 2002, in ASP Conf. Ser., Vol. 279, Exotic Stars as Challenges to Evolution, ed. C. A. Tout & W. van Hamme (Astron. Soc. Pacific, San Francisco: USA), 221
Harmanec, P., Habuda, P., Štefl, S., et al. 2000, A&A, 364, L85
Horn, J., Hubert, A. M., Hubert, H., Koubský, P., & Bailloux, N. 1992, A&A, 259, L5
Horn, J., Koubský, P., Hadrava, P., et al. 1994, A&AS, 105, 119
Horn, J., Kubát, J., Harmanec, P., et al. 1996, A&A, 309, 521
Jarad, M. M. 1987, Journal of Space Astronomy Research, 4, 87
Koubský, P., Horn, J., Harmanec, P., et al. 1985, Information Bulletin on Variable Stars, 2778, 1
Lucy, L. B. & Sweeney, M. A. 1971, AJ, 76, 544
Miroshnichenko, A. S., Bjorkman, K. S., & Krugov, V. D. 2002, PASP, 114, 1226
Moultaka, J., Ilovaisky, S. A., Prugniel, P., & Soubiran, C. 2004, PASP, 116, 693
Poeckert, R. & Marlborough, J. M. 1978, ApJ, 220, 940
Quirrenbach, A., Bjorkman, K. S., Bjorkman, J. E., et al. 1997, ApJ, 479, 477
Robinson, R. D. & Smith, M. A. 2000, ApJ, 540, 474
Ruždjak, D., Božić, H., Harmanec, P., et al. 2009, A&A, 506, 1319
Secchi, A. 1866, Astronomische Nachrichten, 68, 63

Silaj, J., Jones, C. E., Tycner, C., Sigut, T. A. A., & Smith, A. D. 2010, ApJS, 187, 228
Škoda, P. 1996, in ASP Conf. Ser., Vol. 101, Astronomical Data Analysis Software and Systems V, ed. G. H. Jacoby & J. Barnes, 187–190
Smith, M. A., Henry, G. W., & Vishniac, E. 2006, ApJ, 647, 1375
Štefl, S., Harmanec, P., Horn, J., et al. 1990, Bull. astr. Inst. Czechosl., 41, 29
Stellingwerf, R. F. 1978, ApJ, 224, 953
Tycner, C., Gilbreath, G. C., Zavala, R. T., et al. 2006, AJ, 131, 2710
Vondrák, J. 1969, Bull. astr. Inst. Czechosl., 20, 349
Vondrák, J. 1977, Bull. astr. Inst. Czechosl., 28, 84

Appendix A: Details of spectroscopic observations and their analyses

A.1. Observational equipment

Here we provide more details on the spectra used in this study (see Table 1) and their reduction:

1. Ondřejov spectra: All 439 spectra were obtained in the coudé focus of the 2.0 m reflector and have a linear dispersion 17.2 Å.mm^{-1} and a 2–pixel resolution $R \sim 12600$ ($\sim$ 11–12 km s^{-1}per pixel). The first 318 spectra were taken with a Reticon 1872RF detector. Complete reductions of these spectrograms were carried out by Mr. Josef Havelka, Mr. Pavol Habuda and by PH in the program SPEFO. The remaining spectra were secured with an SITe–5 800×2000 CCD detector. Their initial reductions (bias substraction, flatfielding, extraction of 1–D image and wavelength calibration) were done by MŠ with the IRAF program.
2. DAO spectra: All 136 spectra were obtained in the coudé focus of the 1.22 m Dominion Observatory reflector by SY, who carried out initial reductions (bias substraction, flatfielding, extraction of 1–D image). The wavelength calibration of the spectra was carried out by JN in SPEFO. The spectra were obtained with the 32121H spectrograph with the IS32R image slicer. The detectors were UBC–1 4096×200 CCD for the data prior to May 2005 and SITe–4 4096×2048 CCD for the data after May 2005. The spectra have a linear dispersion of 10 Å.mm^{-1} and 2–pixel resolution $R \sim 21700$ ($\sim$ 7 km s^{-1}per pixel).
3. OHP spectra: Public ELODIE archive[5] of the Haute Provence Observatory (Moultaka et al. 2004) contains 35 echelle spectra obtained at the 1.93 m telescope. They have resolution $R \sim 42000$. Initial reductions (bias substraction, flatfielding, extraction of 1–D image, and wavelength calibration) was carried out at the OHP. We only extracted and studied the red parts of the spectra.
4. Ritter spectra: All 204 spectra were obtained with a fiber–fed echelle spectrograph at the 1 m telescope of the Ritter Observatory of the University of Toledo. We obtained spectra in form of ASCII table covering only region close to Hα spectra line. The resolution of the spectra is $R \sim 26000$. Initial reductions of spectra (bias substraction, flatfielding, extraction of 1–D image and wavelength calibration) were carried out at the Ritter Observatory with the IRAF program.
5. Castanet Tolosan and OHP spectra: We downloaded these spectra from the Be Star Spectra database[6]. All of them were obtained by CB with several different spectrographs[7]. Only spectra with a resolution comparable to spectra obtained at the rest of observatories were used in the study. Initial reductions (bias substraction, flatfielding, extraction of 1–D image, and wavelength calibration) were carried out by CB.

For all individual spectrograms, the zero point of the heliocentric wavelength scale was corrected via the RV measurements of selected unblended telluric lines in SPEFO (see Horn et al. 1996, for details).

[5] URL: http://atlas.obs-hp.fr/elodie/

[6] URL: http://basebe.obspm.fr/basebe/

[7] For detailed information on the spectrographs used, see the CB homepage at http://astrosurf.com/buil/

Table A.1. Orbital elements obtained using RVs measured on the emission wings of He I 6678 Å line, absorption core of the He I 6678 Å line, and emission wings of the Si II 6347 Å and Si II 6371 Å lines. RJD = HJD–2400000

spectral line	He I 6678 Å emission	He I 6678 Å absorption	Si II emission
P(d)	203.52(fixed)	203.52(fixed)	203.52(fixed)
T_{min}(RJD)	52085.3±3.1	52081.4±2.6	52096.4±3.5
K_1(km s^{-1})	3.60±0.43	5.22±0.50	3.14±0.45
γ(km s^{-1})	0.16±0.27	0.18±0.32	0.29±0.28
rms(km s^{-1})	6.179	7.548	6.357
N	560	572	550

A.2. Additional RV measurements

We measured RVs on emission wings and absorption core of He I 6678 Å and emission wings of Si II 6347 Å and Si II 6371 Å lines. The program SPEFO was used to the task. The precision of these RV measurements is quite low, since the relative flux in the lines is only several percent greater than in surrounding continuum (see Fig. 2). One could be easily misled during measurements, because measured lines are deformed with continuum fluctuations, and they blend with telluric lines. Despite these complications RVs measured on these lines exhibit long–term variations very similar to the variations that can be seen in Fig. 6. RVs measured on emission wings of He I 6678 Å line, absorption core of He I 6678 Å line, and emission wings of Si II 6347 Å and Si II 6371 Å lines are shown in Fig. A.1.

The long–term variations were removed with the program HEC13, using the 200 d normals and $\epsilon = 5\times10^{-16}$. The model of long-term variations derived by HEC13 is shown in Fig. A.1. The residua were searched for periodicity using the HEC27 program. A period near 200 d was detected in all cases, although with a lower significance than the Hα emission RV (see Figs. 7 and 8. The θ statistics periodograms for trial periods from $3000\overset{d}{.}0$ down to $50\overset{d}{.}0$ are shown in Fig. A.2, where the period $P = 203\overset{d}{.}0$ is denoted. The θ mininum for this period is not the dominant one only in the case of RV measured on the silicon lines. It is probably due to their low precision and/or incomplete removal of the long-term changes via HEC13.

The circular-orbit solutions were computed for all prewhitened RVs, keeping the orbital period fixed at the value $P = 203\overset{d}{.}52$. The corresponding orbital elements are in Table A.1.

Data smoothing with different γ velocities derived with the SPEL program was tested as well. It led to none or a slight (lower than 5%) improvement in rms for the Keplerian fit.

In passing, we wish to mention that the Gaussian fits of the Hα line also provided individual RVs of this line. Not surprisingly, a Keplerian fit of these RVs resulted in a semiamplitude lower than was obtained for the directly measured RVs and for some 40% greater rms than that for our preferred solution 5.

A.3. Comparison

PH and JN measured RVs independently on spectra obtained with Reticon detector at Ondřejov observatory. Comparison of their results is shown in Fig. A.4. Dependency was fitted with linear function $y = a.x$. The resulting parameters are emission wings of Hα line $a = 1.024\pm0.006$, emission wings of He I 6678 Å line $a = 1.038\pm0.024$, absorption core of

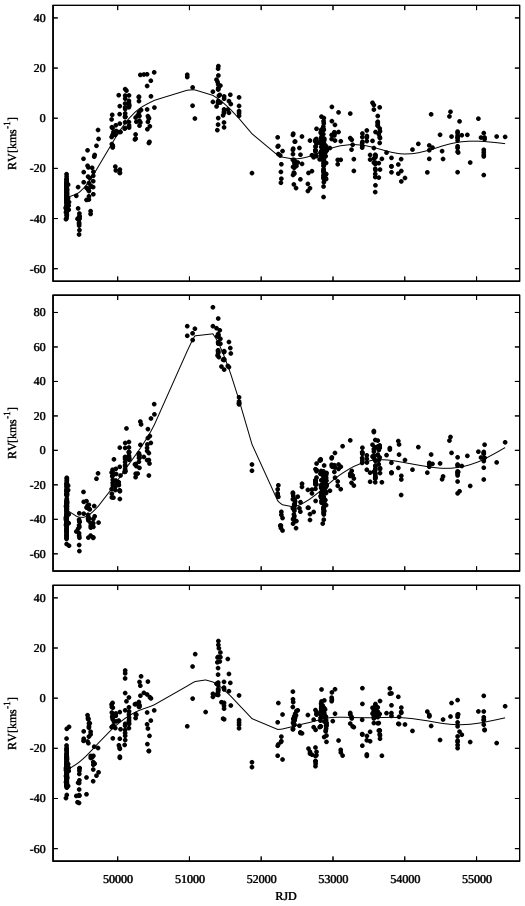

Fig. A.1. A time plot of the RVs measured manually in SPEFO. *Top panel*: The emission wings of the He I 6678 Å line, *Middle panel*: The absorption core of the He I 6678 Å line, *Bottom panel*: The emission wings of Si II 6347 Å and Si II 6371 Å lines. The HEC13 model of the long-term variations is shown by a solid line in each panel.

He I 6678 Å line $a = 1.022 \pm 0.008$. Differences between the measurements of both authors are quite high for He I 6678 Å line emission wings measurements. It is probably because wings of the line are affected by the background noise and because the red peak of the He I 6678 Å line is very low at some point in the V/R cycle.

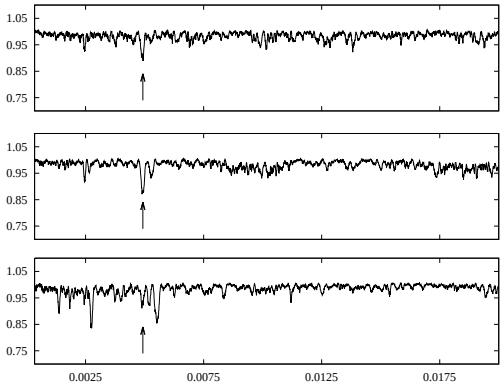

Fig. A.2. The θ statistics periodograms. *Top panel:* the emission wings of He I 6678 Å line, *Middle panel:* the absorption core of He I 6678 Å line, *Bottom panel:* the emission wings of Si II 6347 Å and Si II 6371 Å lines. The period $P = 203\overset{d}{.}0$ is marked with an arrow. Vertical axis: normalized phase scatter θ; Horizontal axis: frequency(d^{-1}).

Table A.2. γ velocities obtained through the same orbital solution as orbital elements in Table 7.

method No. of subset	automatic γ(km s^{-1})	manual γ(km s^{-1})
1	-16.04±0.29	-16.54±0.26
2	-9.88±0.40	-9.50±0.34
3	-2.54±0.30	-5.21±0.26
4	0.37±0.29	-1.45±0.26
5	0.39±0.39	-0.70±0.34
6	-2.04±0.38	-1.89±0.36
7	-7.36±0.27	-6.46±0.24
8	-9.55±0.36	-7.89±0.32
9	-8.29±0.31	-9.56±0.26
10	-8.81±0.25	-9.47±0.22
11	-9.32±0.43	-7.89±0.24
12	-8.55±0.32	-9.01±0.25
13	-9.25±0.27	-8.34±0.22
14	-7.69±0.29	-9.12±0.22
15	-7.02±0.45	-9.24±0.39
16	-7.43±0.39	-8.46±0.32
17	-7.65±0.53	-9.51±0.48

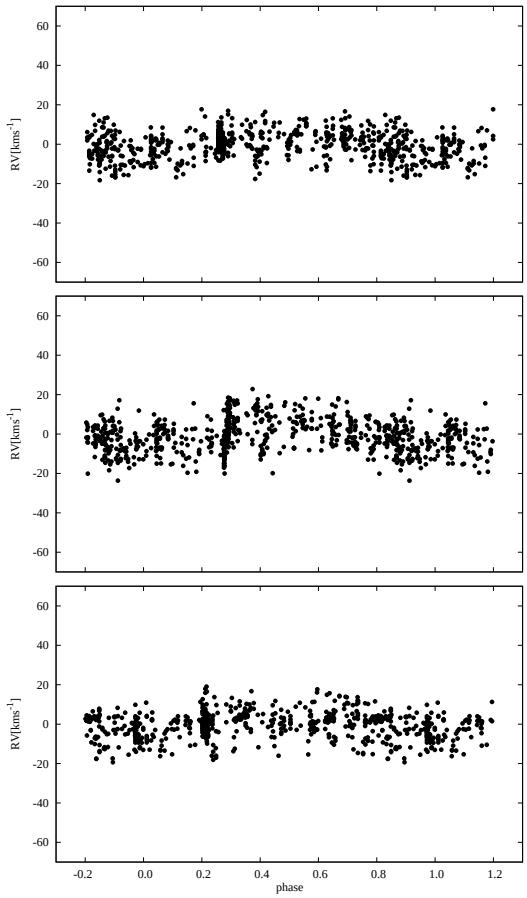

Fig. A.3. Phase diagrams of RVs prewithened with HEC13. *Top panel*: the emission wings of the He I 6678 Å line, *Middle panel*: the absorption core of the He I 6678 Å line, *Bottom panel*: the emission wings of the Si II 6347 Å and Si II 6371 Å lines. The period $P = 203\overset{d}{.}52$ was used.

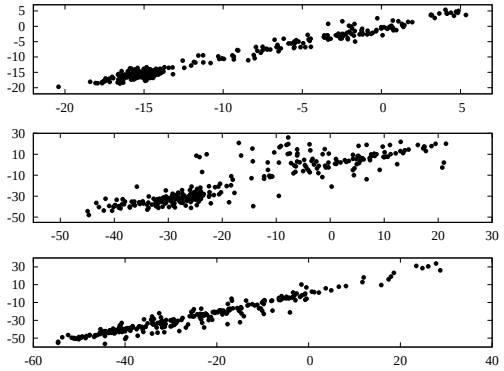

Fig. A.4. RVs measured by JN plotted vs. RVs measured by PH on spectra obtained at Ondřejov Observatory with Reticon detector. *Top panel*: emission wings of Hα line, *Middle panel*: emission wings of He I 6678 Å line, *Bottom panel*: absorption core of He I 6678 Å line.

Preliminary ξ Tau study

ISSN 1845–8319

AN UNUSUAL QUADRUPLE SYSTEM ξ TAURI

J. A. NEMRAVOVÁ[1], P. HARMANEC[1], J. BENCHEIKH[2], C. T. BOLTON[3], H. BOŽIĆ[4], M. BROŽ[1], S. ENGLE[5], J. GRUNHUT[6], E. F. GUINAN[5], C. A. HUMMEL[7], D. KORČÁKOVÁ[1], P. KOUBSKÝ[8], P. MAYER[1], D. MOURARD[2], J. RIBEIRO[9], M. ŠLECHTA[8], D. VOKROUHLICKÝ[1], V. VOTRUBA[8], M. WOLF[1], P. ZASCHE[1], the CHARA/VEGA and the NPOI teams.

[1]*Astronomical Institute, Faculty of Mathematics and Physics, Charles University in Prague, V Holešovičkách 2, Praha 8, Czech Republic*
[2]*Laboratoire Lagrange, OCA/UNS/CNRS UMR7293, BP4229, 06304 Nice Cedex*
[3]*David Dunlap Observatory, University of Toronto, Richmond Hill, Canada*
[4]*Hvar Observatory, Faculty of Geodesy, Kačićeva 26, Zagreb, Croatia*
[5]*Department of Astronomy & Astrophysics, Villanova University, 800 Lancaster Ave. Villanova, PA 19085, USA*
[6]*Department of Physics, Engineering Physics & Astronomy, Queens University, Kingston, Ontario, Canada*
[7]*European Southern Observatory, Karl–Schwarzschild–Str. 2, 85748 Garching bei München, Germany*
[8]*Astronomical Institute of the Academy of Sciences, Ondřejov, Czech Republic*
[9]*Observatório do Instituto Geográfico do Exército, R. Venezuela, Lisboa, Portugal*

Abstract. A preliminary analysis of spectroscopic, photometric and interferometric observations of the triple subsystem of a hierarchical quadruple system ξ Tau is presented. The triple system consists of a close eclipsing binary ($P^{\rm A} = 7\overset{\rm d}{.}146651$), revolving around a common centre of gravity with a distant tertiary ($P^{\rm B} = 145\overset{\rm d}{.}17$). All three stars have comparable brightness. The eclipsing pair consists of two slowly-rotating A stars while the tertiary is a rapidly-rotating B star. The outer orbit is eccentric ($e^{\rm B} = 0.237 \pm 0.022$). Available electronic radial velocities indicate an apsidal advance of the outer orbit with a period $P^{\rm B}_{\rm APS} = 224 \pm 147\,{\rm yr}$.

Key words: binary stars - hot stars

1. Introduction

ξ Tau (2 Tau, HD 21364, HIP 16083, HR 1038) is a hierarchical quadruple system, consisting of sharp-lined A stars, undergoing binary eclipses, a more distant broad-lined B star and a much more distant (the semi-major

axis $a^{\mathrm{C}} = 0''.441 \pm 0''.027$, Rica Romero 2010) F star. Here, we shall denote the components as follows: C (F-type), B (B-type), Aa, Ab (A-types) and the orbits: C (F-type), B (B-type), A (A-types). The visual magnitude of ξ Tau ($V = 3^{\mathrm{m}}.72$) and its declination $9°44'$ make it an easy target for a wide range of instruments and observational techniques. The binary nature of the system was discovered by Campbell (1909). The outermost orbit C was resolved using speckle-interferometry by Mason *et al.* (1999). All speckle-interferometric observations of the system were analysed by Rica Romero (2010), who found an orbital period $P^{\mathrm{C}} = 52 \pm 15$ yrs. The orbital elements of the triple subsystem were published by Bolton and Grunhut (2007). The Hipparcos parallax of the system is $p = 15.6 \pm 1.04$ mas (van Leeuwen, 2007a,b). As we were unable to detect either spectral or light variations of the distant and faint F component, we do not deal with the orbit C in this study.

2. Observations and Data Reduction

We have collected a rich series of spectroscopic, photometric and interferometric observations spanning more than two decades.

2.1. Spectroscopy

The 131 electronic slit spectra cover the time interval RJD = 49300 to 55971[1]. They were secured at three observatories: 1) Ondřejov Observatory, Czech Republic, 2) David Dunlap Observatory, Canada, and 3) Observatory of the Army Geographic Institute, Portugal.

Spectral lines of the three components are visible in the spectra. We studied the Hγ, Hβ, and Hα Balmer lines and also stronger metallic lines (Mg II 4481 Å, Si II 6347 Å and Si II 6371 Å), in which the contribution of the A–type stars is dominant. The B-type component contributes about 60 % to the total flux in the optical region and its spectral lines are significantly rotationally broadened ($v_{\mathrm{R}} \sin i \geq 200\,\mathrm{km\,s^{-1}}$). The spectral lines of both A-type stars are sharp and very similar to each other.

2.2. Photometry

Altogether, 1786 *UBV* observations (spanning RJD = 54116 to 55956) were secured at three observatories: 1) Hvar Observatory, Croatia, 2) South

[1] RJD = JD - 2400000

African Astronomical Observatory, South Africa, and 3) Villanova APT, USA. We also used 69 Hipparcos $H_{\rm p}$ observations (Perryman and ESA, 1997) spanning RJD = 47909 to 48695. These were transformed to the Johnson V using a formula found by Harmanec (1998).

2.3. Spectro-interferometry

The ξ Tau system was observed with the NPOI interferometer (Armstrong *et al.*, 1998) between 1991 and 2012, the bulk of observations being taken during the last decade, and also with the VEGA/CHARA spectro-interferometer (Mourard *et al.*, 2009) in 2011 and 2012. [2]

3. Data Analysis and Preliminary Results

3.1. Orbital Solution

We measured RVs by an automatic comparison of suitably chosen synthetic and observed spectra. The measurements were then divided into two subsets well-separated in time from each other. We used the program FOTEL Hadrava (2004a) (release on the 25$^{\rm the}$ of June, 2003) to compute the orbital solution. This release of the program does not allow modelling of apsidal motion for the outer orbit. Therefore the RVs measured on the A-type stars had to be fitted on each subset separately. This does not apply to the RVs of the B-type star. This component can be considered moving in a binary system and its apsidal motion can be treated properly in FOTEL.

Elements published by Bolton and Grunhut (2007) were used as an initial estimate. The orbital period of the inner orbit $P^{\rm A}$ was kept fixed at the value given by the light curve solution (see below). The orbital elements corresponding to the best-fit of the RVs measured on the lines of the B-type star are: the anomalous period $P^{\rm B}_{\rm an} = 145.42 \pm 0.15\,$d, the periastron epoch $T^{\rm B}_{\rm p}\,({\rm RJD}) = 55608.9 \pm 2.3$, the eccentricity $e^{\rm B} = 0.237 \pm 0.022$, the periastron longitude $\omega^{\rm B} = 187.0 \pm 6.9\,$deg, and semi-amplitude $K^{\rm B}_1 = 38.44 \pm 0.90\,{\rm km\,s^{-1}}$. The results also revealed presence of an apsidal motion of the orbit B with a period of $P^{\rm B}_{\rm APS} = 224 \pm 147\,$yrs. The RV curve of the tertiary and the best-fit model are shown in Figure 1.

The spectral-disentangling program KOREL (Hadrava, 2004b) was used for the final orbital solution and the corresponding orbital elements are listed

[2] Only observations from 2011 being reported here.

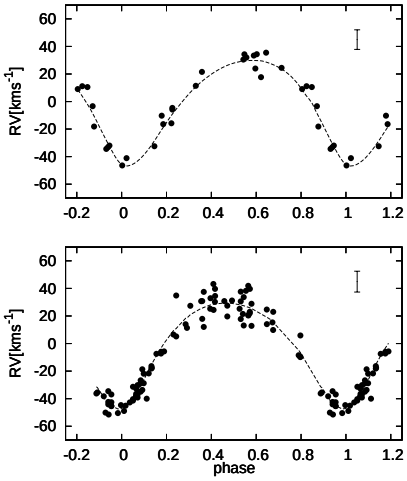

Figure 1: A secular evolution of the orbit B. The RVs measured on the spectral lines of the B-type star in between: upper panel: RJD = 49300 to 50500 and lower panel: RJD = 55560 to 55981. The mean RV curve of the time interval is shown with a dashed line. The typical uncertainty of one measurement is denoted by line segments.

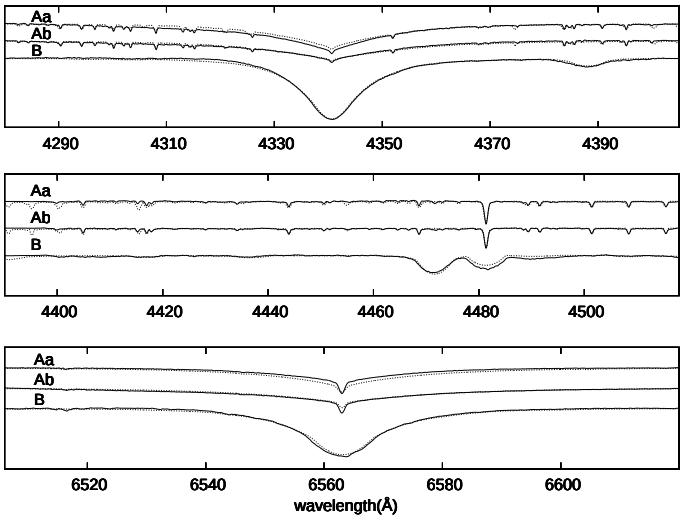

Figure 2: Spectra of the triple subsystem components obtained by means of disentangling (full line) and synthetic spectra fitted to the disentangled ones (dotted line). With the exception of the spectrum covering the wavelength interval $\Delta\lambda = 4390 - 4518$ Å all disentangled spectra did not have perfectly flat continua and we had to re-normalize them.

Table I: The orbital solution resulting from spectral-disentangling of the spectroscopic observations, where $P_{\rm S}$ denotes the sidereal orbital period, $P_{\rm An}$ the anomalous orbital period, $T_{\rm P}$ the epoch of periastron, e the eccentricity, ω the longitude of periastron, K_1 the semiamplitude, q the mass ratio, and $P_{\rm APS}$ the period of the apsidal advance.

Element	Outer orbit (B)	Inner orbit (A)
$P_{\rm An}$ (d)	145.44 ± 0.10	–
$P_{\rm S}$ (d)	145.17 ± 0.10	7.146651 ± 0.000010
$T_{\rm P}$ (RJD)	55609.88 ± 0.01	–
$T_{\rm conj.}$ (RJD)	55580.77 ± 0.01	48299.075 ± 0.010
e	0.22 ± 0.15	$0.0 + 0.05$
ω (deg)	189.7 ± 5.0	90 ± 10
$P^{\rm B}_{\rm APS}$ (yr)	214 ± 100	–
K_1 (km s^{-1})	38.02 ± 5.0	89.1 ± 10.0
q	1.01 ± 0.20	0.96 ± 0.10

in Table I. The disentangled component spectra are shown in Figure 2.

3.2. Light-curve solution

We used the program PHOEBE (Prša and Zwitter, 2005) for modelling of the brightness variations of ξ Tau. The limb-darkening coefficients were taken from Claret (2000). The semi-major axis and the mass ratio obtained with spectral-disentangling were kept fixed. The light contribution of the B-type star had to be considered as the third light, its relative luminosity in the V band being $L^{\rm V}_{\rm r} = 0.60 \pm 0.02$. As the secondary minimum occurs a bit earlier than half of the period after the primary one, we had to allow for a small orbital eccentricity. The elements of the solution are presented in Table II. The observed and the best-fit synthetic light curve are shown in Figure 3.

3.3. Interferometric solution

Interferometric observations were fitted in Fourier space in order to obtain positions of the stars. Then the positions of stars were fitted in order to obtain the orbital properties. Results are presented in Table III. In case of the VEGA/CHARA interferometer, the spectroscopic solution presented in this paper was used to obtain an initial model of the system for the mod-

Table II: Light curve solution for the inner orbit of ξ Tau. P denotes the orbital period, $T_{\rm min}$ the epoch of the primary light curve minimum, i the orbital inclination, e the eccentricity, ω the periastron longitude, r the radius, $T_{\rm eff}$ the effective temperature and $L_{\rm r}^{\rm V}$ the relative brightness in the Johnson V-band.

Orbital properties		
Parameters	Values	
$P^{\rm A}$ (d)	7.146656 ± 0.000020	
$T_{\rm min}^{\rm A}$ (RJD)	48302.6374 ± 0.0010	
$i^{\rm A}$ (deg)	86.2 ± 0.5	
$e^{\rm A}$	0.016 ± 0.010	
$\omega^{\rm A}$ (deg)	110 ± 10	
Properties of the close binary components		
Parameters	Aa	Ab
r ($R_\odot$)	2.0 ± 0.2	1.5 ± 0.2
$T_{\rm eff}$ (K)	9250 ± 100	9200(fixed)*
$L_{\rm r}^{\rm V}$	0.26 ± 0.02	0.14 ± 0.02

*Taken from the fit of the disentangled spectra to the synthetic ones.

Table III: List of the best-fit interferometric orbital elements. $T_{\rm p}$ denotes the periastron epoch, $P_{\rm S}$ the sidereal orbital period, i the inclination, Ω the longitude of the ascending node, e the eccentricity, ω the periastron longitude, a the angular size of the semi-major axis, $P_{\rm APS}$ the period the apsidal motion, N the number of the interferometric observations.

	Instrument		
Element	VEGA/CHARA		NPOI
$T_{\rm p}$(RJD)**	55755.04 ± 0.1		53712.90 ± 0.34
N	5		22
	Inner Orbit (A)	Outer Orbit (B)	Outer Orbit (B)
$P_{\rm S}$(d)	7.146656(fixed)	145.17(fixed)	145.12 ± 0.055
i (deg)	97.5 ± 5.0	85.0 ± 4.0	87.07 ± 0.19
Ω (deg)*	350.5 ± 4.0	329.2 ± 2.0	328.63 ± 0.38
e	–	0.24 ± 0.04	0.213 ± 0.007
ω (deg)	–	182.0 ± 5.0	163.07 ± 0.13
a (mas)	–	15.5 ± 0.4	16.09 ± 0.18
$P_{\rm APS}^{\rm B}$ (yr)	–	–	266 ± 65

*Values of $\Omega + 180\,^\circ$ are also possible.**$T_{\rm p}$ denotes the reference epoch in the case of the inner orbit.

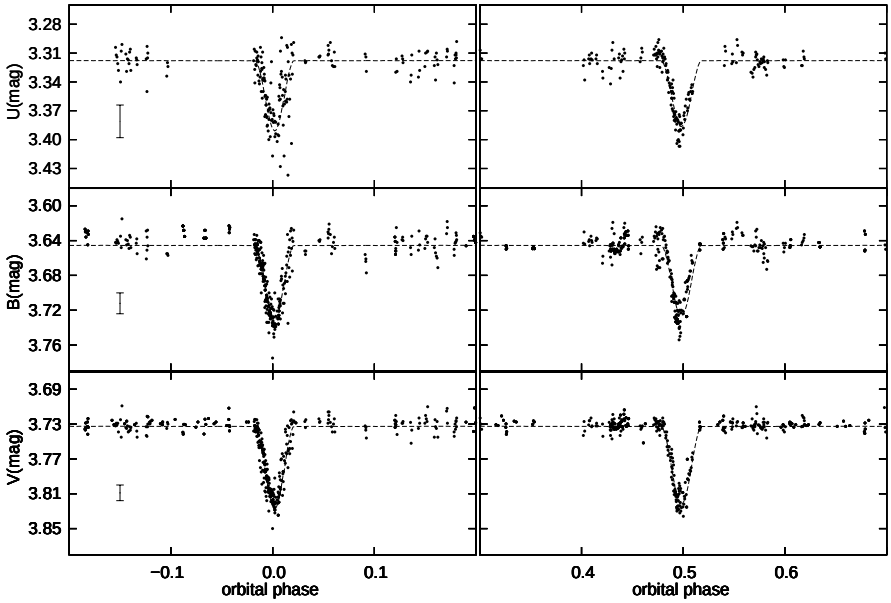

Figure 3: The *UBV* light curves of ξ Tau. Top panel: U filter, middle panel: B filter, bottom panel: V filter. Data sources, number of observations N, typical uncertainties $(\delta U, \delta B, \delta V)$ of an observation in each filter are: 1) Hvar Observatory, $N = 1308$, $\delta U = 0.019$ mag, $\delta B = 0.012$ mag, $\delta V = 0.009$ mag. 2) South African Astronomical Observatory $N = 76$, $\delta B = 0.010$ mag, $\delta V = 0.008$ mag. 3) Villanova APT $N = 401$, $\delta B = 0.010$ mag, $\delta V = 0.008$ mag. 4) Hipparcos satellite $N = 401$, $\delta V = 0.008$ mag. The SAAO and the Villanova APT observations in the U filter were excluded from study, because their zero point was significantly shifted with respect to the Hvar observations, which represent the bulk of our photometric data. The rest of the data is transformed to the same zero point. Therefore there are no differences in residuals between observatories. The shape of the light curves in regions which are not displayed is the same as it is in the surroundings of minima. The synthetic light curve is denoted by the dashed line. The typical uncertainty of Hvar observations, which have the highest uncertainty, is denoted by line segments.

elling of the star positions. NPOI interferometer is unable to resolve the inner system.

3.4. Comparison of the observed and synthetic spectra

We have used a program, which interpolates in grids of synthetic spectra and compares the synthetic spectrum to observed ones using the least-square method. The elements, which can be optimized, are: the effective temper-

Table IV: The Result of the observed spectra fitting to the synthetic spectra. $T_{\rm eff}$ denotes the effective temperature, $\log g$ the logarithm of gravitational acceleration, $v_{\rm R} \sin i$ the projected rotational velocity, $L_{\rm r}$ the relative luminosity, RV_γ the systemic radial velocity and Z the metallicity. $\Delta\lambda\,\epsilon$ [4380, 4500] Å region was fitted.

Parameter	System component		
	B	Aa	Ab
$T_{\rm eff}$ (K)	15100 ± 200	9400 ± 500	9200 ± 500
$\log(g)_{\rm [cgs]}$	4.3 ± 0.1	4.2(fixed)	4.2(fixed)
$v_{\rm R} \sin i\,({\rm km\,s^{-1}})$	246 ± 10	33 ± 2	34 ± 2
$L_{\rm r}$	0.73 ± 0.02	0.14 ± 0.02	0.13 ± 0.02
$RV_\gamma\,({\rm km\,s^{-1}})$	2.4 ± 5.0	7.7 ± 5.0	6.9 ± 5.0
$Z\,({\rm Z_\odot})$	2(fixed)	2(fixed)	2(fixed)

ature $T_{\rm eff}$, the logarithm of gravitational acceleration $\log g$, the projected rotational velocity $v_{\rm R} \sin i$, the relative luminosity $L_{\rm R}$, and the radial velocities of the components $RV_{\rm i}$. The grids of synthetic spectra by Lanz and Hubený (2003, 2007), and Palacios *et al.* (2010) were used. The best-fit synthetic spectra are shown in Figure 2 and the corresponding optimal parameters are in Table IV.

4. Discussion

4.1. Derived properties of the system

An estimated precision of the RV measurements on the electronic spectra is approximately 2 $\rm km\,s^{-1}$ for the A-type stars and 5 $\rm km\,s^{-1}$ for the B-type star. A good phase coverage for both orbital periods led to reliable RV-curve solutions with FOTEL (giving the rms error of one observation $\leq 7\,\rm km\,s^{-1}$). The FOTEL orbital elements provided good initial values for the final solution with KOREL. We mapped χ^2 around the minimum of the sum of squares in order to get estimates of the uncertainties of the elements. We did only basic uncertainty analysis and the uncertainties given in the Table I were estimated on basis of the above-mentioned maps.

The light curve solution exhibits a high degeneracy in the diameters of the stars. This is due to very shallow and almost identical eclipse minima. The light curve solution also indicates a small eccentricity of the orbit A $e^{\rm A} \leq 0.03$. The mutual interaction between the close binary A and the ter-

tiary should also cause a secular nodal motion. If the orbits are not coplanar, the depths of the eclipses should change in the course of time. We compared observations from two seasons, but we cannot confirm such an effect yet. Data from more epochs are needed.

The orbital solutions based on the interferometric observations from the CHARA/VEGA (which depend heavily on the spectroscopic solution in Table I) and the NPOI do not agree with each other in the longitude of periastron. The value of longitude of periastron based on the ephemeris obtained on the NPOI data would be $\omega^{\mathrm{B}}\,(RJD = 55755) = 171 \pm 2\,\mathrm{deg}$. However, the discrepancy may result from underestimation of the uncertainties of the NPOI fit, because only a preliminary uncertainty analysis was done.

The combined orbital elements of the inner orbit imply masses of the components of the system: $M^{\mathrm{Aa}} = 2.29 \pm 0.91\,\mathrm{M}_\odot$, $M^{\mathrm{Ab}} = 2.20 \pm 0.78\,\mathrm{M}_\odot$, $M^{\mathrm{B}} = 4.53 \pm 1.51\,\mathrm{M}_\odot$ and semi-major axes of the orbits: $a^{\mathrm{A}} = 25.77 \pm 3.95\,\mathrm{R}_\odot$ and $a^{\mathrm{B}} = 213 \pm 51\,\mathrm{R}_\odot$, while the combined orbital elements of the outer orbit leads to masses: $M^{\mathrm{B}} = 3.08 \pm 1.24\,\mathrm{M}_\odot$, $M^{\mathrm{Aa+Ab}} = 3.11 \pm 0.65\,\mathrm{M}_\odot$. Although both results agree with each other within uncertainty boxes, the difference between the expected values might suggest discrepancy in our model of the triple subsystem.

4.2. Apsidal motion

The detected apsidal motion is most likely caused by an interaction between the pair of the A-type stars and the B-type star. The large semi-major axis of the orbit B $a^{\mathrm{B}} = 213 \pm 51\,\mathrm{R}_\odot$ and the relatively low eccentricity $e^{\mathrm{B}} = 0.2 \pm 0.15$ exclude a possibility that the apsidal advance would be caused either by the stellar internal structure or by a relativistic effect.

We calculated the periods of the apsidal motion $P_{\mathrm{B}}^{\mathrm{APS}} \in [142, 352]\,\mathrm{yr}$ and the nodal motion $P^{\mathrm{NOD}} \in [16, 24]\,\mathrm{yr}$ with the formulæ derived by Soderhjelm (1975) and independently by a direct integration of Lagrange equations (high uncertainty in the mass ratio q^B was taken into account). These periods are possible (from the point of view of dynamics) if our model of the system given by the spectroscopic solution is correct. Both intervals of periods depend heavily on the angle between the orbital planes. Values of the angle in the range $j \in [0, 35]\,\mathrm{deg}$ were evaluated.

5. Future Plans and Expectations

The ultimate goal of our effort will be the determination of very accurate masses and radii of all components and of dynamical properties and possible evolution of the system. We plan to obtain additional high-precision light curve of the eclipsing pair with the MOST satellite, and continue observations with the VEGA/CHARA interferometer as well as ground-based photometric and spectroscopic observations.

Acknowledgements

The Czech authors were supported by the grants No. 703812 (PH and JN) of the Grant Agency of the Charles University in Prague and P209/10/0715 (PH, PM, JN, MW, PZ) of the Czech Science Foundation as well as from the Research programs MSM0021620860 (MB, PH, DV, PM, MW, PZ) and AV0Z10030501 (PK, VV, MŠ).

References

Armstrong, J. T., Mozurkewich, D., Rickard, L. J., *et al.*: 1998, *Astrophys. J.* **496**, 550.
Bolton, C. T. and Grunhut, J. H.: 2007, *in* W. I. Hartkopf, E. F. Guinan, and P. Harmanec (eds.), *IAU Symposium*, Vol. 240, p. 66.
Campbell, W. W.: 1909, *Astrophys. J.* **29**, 224.
Claret, A.: 2000, *Astron. Astrophys.* **363**, 1081.
Hadrava, P.: 2004a, *Publ. Astron. Inst. Acad. Sci. Czech Rep.* **92**, 1.
Hadrava, P.: 2004b, *Publ. Astron. Inst. Acad. Sci. Czech Rep.* **92**, 15.
Harmanec, P.: 1998, *Astron. Astrophys.* **335**, 173.
Lanz, T. and Hubený, I.: 2003, *Astrophys. J., Suppl. Ser.* **146**, 417.
Lanz, T. and Hubený, I.: 2007, *Astrophys. J., Suppl. Ser.* **169**, 83.
Mason, B. D., Martin, C., Hartkopf, W. I., *et al.*: 1999, *Astron. J.* **117**, 1890.
Mourard, D., Clausse, J. M., Marcotto, A., *et al.*: 2009, *Astron. Astrophys.* **508**, 1073.
Palacios, A., Gebran, M., Josselin, E., Martins, F., Plez, B., Belmas, M., and Lèbre, A.: 2010, *Astron. Astrophys.* **516**, A13.
Perryman, M. A. C. and ESA: 1997, ESA SP Series 1200, Noordwijk, Netherlands.
Prša, A. and Zwitter, T.: 2005, *Astrophys. J.* **628**, 426.
Rica Romero, F. M.: 2010, *Rev. Mex. Astron. Astrofis.* **46**, 263.
Soderhjelm, S.: 1975, *Astron. Astrophys.* **42**, 229.
van Leeuwen, F.: 2007a, *in* F. van Leeuwen (ed.), *Astrophysics and Space Science Library*, Vol. 350, Springer, Germany.
van Leeuwen, F.: 2007b, *Astron. Astrophys.* **474**, 653.

Detailed ξ Tau study

Astronomy & Astrophysics manuscript no. xitau
June 17, 2016

ξ Tauri: a unique laboratory to study the dynamic interaction in a compact hierarchical quadruple system ⋆ ⋆⋆

J.A. Nemravová[1], P. Harmanec[1], M. Brož[1], D. Vokrouhlický[1], D. Mourard[2], C.A. Hummel[3], C. Cameron[4], J.M. Matthews[5], C.T. Bolton[6], H. Božić[7], R. Chini[8,9], T. Dembsky[8], S. Engle[10], C. Farrington[11], J.H. Grunhut[3], D.B. Guenther[12], E.F. Guinan[10], D. Korčáková[1], P. Koubský[13], R. Kříček[1], R. Kuschnig[14], P. Mayer[1], G.P. McCook[10], A.F.J. Moffat[15], N. Nardetto[2], A. Prša[10], J. Ribeiro[16], J. Rowe[17], S. Rucinski[6], P. Škoda[13], M. Šlechta[13], I. Tallon-Bosc[18], V. Votruba[13], W.W. Weiss[14], M. Wolf[1], P. Zasche[1], and R.T. Zavala[19]

(Affiliations can be found after the references)

Release June 17, 2016

ABSTRACT

Context. Compact hierarchical systems are important because the effects caused by the dynamical interaction among its members occur on a human timescale. These interactions play a role in the formation of close binaries through Kozai cycles with tides. One such system is ξ Tauri: it has three hierarchical orbits: 7.14 d (eclipsing components Aa, Ab), 145 d (components Aa+Ab, B), and 51 yr (components Aa+Ab+B, C).
Aims. We aim to obtain physical properties of the system and to study the dynamical interaction between its components.
Methods. Our analysis is based on a large series of spectroscopic photometric (including space-borne) observations and long-baseline optical and infrared spectro-interferometric observations. We used two approaches to infer the system properties: a set of observation-specific models, where all components have elliptical trajectories, and an N-body model, which computes the trajectory of each component by integrating Newton's equations of motion.
Results. The triple subsystem exhibits clear signs of dynamical interaction. The most pronounced are the advance of the apsidal line and eclipse-timing variations. We determined the geometry of all three orbits using both observation-specific and N-body models. The latter correctly accounted for observed effects of the dynamical interaction, predicted cyclic variations of orbital inclinations, and determined the sense of motion of all orbits. Using perturbation theory, we demonstrate that prominent secular and periodic dynamical effects are explainable with a quadrupole interaction. We constrained the basic properties of all components, especially of members of the inner triple subsystem and detected rapid low-amplitude light variations that we attribute to co-rotating surface structures of component B. We also estimated the radius of component B. Properties of component C remain uncertain because of its low relative luminosity. We provide an independent estimate of the distance to the system.
Conclusions. The accuracy and consistency of our results make ξ Tau an excellent test bed for models of formation and evolution of hierarchical systems.

Key words. stars: binaries: close – stars: binaries: spectroscopic – stars: binaries: eclipsing – stars: kinematics and dynamics stars: fundamental parameters – stars: individual: ξ Tau

1. Introduction

Binaries and multiple systems play a crucial role in our understanding of the formation, stability, and evolution of stars and their hierarchies, starting from simple binaries up to galaxies.

Of all known binaries, those that eclipse have represented the most useful group because until recently, an accurate determination of component masses and radii was possible primarily for them. For binaries with components of different masses, a common origin of the system also provided a stringent test of the models of stellar evolution. At the same time, however, this fact represented an unpleasant selection effect, especially for binaries with hot components and rapid rotation: we have only observed them roughly equator-on so far.

The recent rapid advances in optical interferometry allowing the usage of longer baselines, co-phasing of more telescopes, and longer integration times provide the opportunity of obtaining accurate basic physical properties for non-eclipsing binaries as well. It is possible to obtain the spatial orbit of these binaries and derive their accurate orbital inclination. In combination with radial-velocity (RV) curves, this allows determining component masses and the absolute value of the semi-major axis. Since the interferometric orbit provides the angular value of the semi-major axis, we also obtain an estimate of the distance of the binary that is completely independent of the photometric distance modulus. In the most favourable cases, long-baseline interferometry can also provide independent estimates of the component radii.

Many binaries are members of multiple systems (Eggleton & Tokovinin 2008). When it is possible to derive masses of more than two components, not only the nuclear but also the dynamical evolution of such systems can be studied. It has been suggested that the formation of triple systems, containing a compact binary accompanied by a distant component, was dynamically

Send offprint requests to: J.A. Nemravová,
e-mail: jana.nemravova@gmail.com
⋆ Tables D.1 – D.7 are available at the CDS via anonymous ftp to cdarc.u-strasbg.fr (130.79.128.5) or at the web page http://cdsweb.u-strasbg.fr/cgi-bin/qcat?J/A+A/.
⋆⋆ Based on data from the MOST satellite, a former Canadian Space Agency mission, jointly operated by Microsatellite Systems Canada Inc. (MSCI; formerly Dynacon Inc.), the University of Toronto Institute for Aerospace Studies and the University of British Columbia, with the assistance of the University of Vienna.

very exciting. During the evolution, gravitational interactions of the three stars are expected to excite the eccentricity of the binary through the Kozai mechanism, which brings them close to each other. Later, tides stabilise the system by preventing the Kozai-pumped eccentricity from further increasing and revert the trend to circularisation (e.g. Eggleton & Kiseleva-Eggleton 2001; Fabrycky & Tremaine 2007). Even though we cannot observe the systems at their dynamically violent youth, we can still appreciate some degree of dynamical evolution produced by continued gravitational interactions of the three stars. To compare predictions of the theory with observations, the mutual orientation of orbits with respect to each other is required, that is, their inclinations and the longitudes of ascending nodes. These are available only for objects for which an astrometric orbit is known. This in turn can only be obtained with interferometry.

We here investigate one such system, the unique and rare close quadruple system ξ Tau, whose favourable orbital geometry as well as the luminosity ratios between its components allow determining physical properties of the system and its components with high precision. Possible dynamical effects in the system can be studied as well. ξ Tau (2 Tau, HD 21364, HIP 16083, and HR 1038) is a hierarchical quadruple system consisting of two sharp-lined A stars that undergo binary eclipses, a more distant broad-lined B star, and a much more distant F star. The visual magnitude $V = 3.72$ mag, the declination of $9^\circ44'$, and the quite accurate Hipparcos parallax 15.6 ± 1.04 mas (van Leeuwen 2007) make ξ Tau an easy and interesting target for a wide range of instruments and observational techniques.

The binary nature of the system was discovered by Campbell (1909). The wide orbit was first resolved by Mason et al. (1999) through speckle interferometry. All later available speckle-interferometric observations were analysed by Rica Romero (2010), who derived an astrometric orbit. The inner triple system was first mentioned by Fekel (1981), who quoted orbital periods of 7.15 d and 145.0 d based on a private communication from C.T. Bolton. The orbital elements of the triple subsystem were published in a catalogue by Tokovinin (1997). More accurate elements were given in a preliminary report by Bolton & Grunhut (2007), who obtained periods of 7.1466440(49) d and 145.1317(40) d. They were also the first to note that the inner binary is an eclipsing system, based on Hipparcos photometry. Hummel et al. (2013) reported a solution of the 145.2 d orbit based on interferometric observations. The first detailed, but still preliminary study of ξ Tau was published by Nemravová et al. (2013). These authors analysed numerous spectral, photometric and interferometric observations and discovered the apsidal motion of the 145.2 d orbit with a period 224 ± 147 yr. They were able to separate the spectra of the two A stars and the broad-lined B star.

The system is quite complex, hence we briefly summarise its orbital elements and the properties of its components based on our analysis as presented in following sections in Table 1. It serves only to introduce the system and is not to be confused with our results.

This paper represents a comprehensive study of the system, based on analyses of a huge and unique body of spectral, photometric, and spectro-interferometric and astrometric data. Each type of observation is first analysed separately by standard means (Sects. 3, 4, 5, and 6), and the results are then critically compared in Sect. 7. Using them as the initial starting point, we then present the N-body model of the whole quadruple system, in which the mutual interactions of the orbits are also modelled. This is a new approach that tries to embrace almost all available pieces of information and provides the best description of the geometry and dynamics of the system to date (see Sect. 8). Finally, we recall some results of a simple perturbation theory in Sect. 9, which allows us to understand the principal dynamical effects revealed by the numerical model in Sect. 8.

We denote the individual components and orbits of the system as follows: Components Aa and Ab are the primary and secondary of the close eclipsing subsystem revolving in a 7.15 d orbit, labelled 1. Component B is the broad-lined star of spectral type B, revolving with the close pair in the 145 d orbit, labelled 2. Finally, we denote the faint and very distant F-type star as component C and its 51 yr orbit with the triple subsystem as orbit 3.

Table 1. Brief summary of orbital elements and properties of components of ξ Tau. It serves only for introductory purposes and does not present our final results. P denotes the orbital period, e the eccentricity, i the inclination, Cpts. are the components of an orbit, Sp.T. the spectral type, m the mass, and V the apparent magnitude in the Johnson V filter.

		Orbit		
Quantity		1	2	3
P	(d)	7.14664	145.12	18 630
e		$\lesssim 0.01$	0.21	0.564
i	(deg)	86.8	86.6	-24.4
a	($R_\odot$)	25.3	233	6 097
Cpts.		Aa+Ab	A[1]+B	AB[2]+C
Sp.T.		B9V+B9V	+B5V	+F5V[3]
m	($M_\odot$)	2.25+2.13	+3.73	+0.92[4]
V	(mag)	5.46+5.53	+4.25	+7.55[3]

Notes. [1]A denotes the inner eclipsing system Aa+Ab. [2]AB denotes the intermediate system A+B. [3]Based on the magnitude difference listed in the Hipparcos and Tycho catalogue (ESA 1997). [4]The evident mismatch between the spectral type and its mass is due to the high uncertainty of both parameters.

2. Observations and reductions

Here we provide only basic information about the observational material at our disposal. More details on the datasets and their reductions are provided in Appendices A, B, and C.

Throughout this paper we use a shortened form of heliocentric Julian dates, reduced Julian dates given as RJD = HJD$-2\,400\,000.0$.

2.1. Spectral observations

The series of spectroscopic observations that has previously been used by Nemravová et al. (2013) was complemented with more recent ones secured at Ondřejov and La Silla: they were made with the echelle spectrograph FEROS (Kaufer et al. 1999), and at Cerro Armazones with the BESO spectrograph (Steiner et al. 2008; Fuhrmann et al. 2011). Four archival ELODIE echelle spectra were also used (Moultaka et al. 2004). With this rich collection of electronic spectra, we no longer needed the early radial velocities (RVs) from the David Dunlap Observatory (DDO) photographic spectra that were used by Nemravová et al. (2013). The spectra were primarily used to obtain RV measurements of all three components of the close triple subsystem. The journal of all available spectra with the number of measured RVs for the components of the inner triple subsystem is listed in Table 2. More details on the spectra and their reductions can be found in Appendix A.

Table 2. Journal of spectroscopic observations. For each instrument, ΔT refers to the time span between the first and the last measurement, N gives the number of RVs measured for components Aa, Ab, and B, $\Delta\lambda$ is the wavelength interval covered by the spectra in question, and R is the spectral resolution.

ΔT (RJD)	N Aa/Ab/B	$\Delta\lambda$ (Å)	R	Ins.
49 300.7–52 670.5	37/37/37	4357–4568	10 800	DDO
51 960.3–53 637.6	04/04/04	4270–4523	42 000	ELO
	04/04/04	4759–4991		
	04/04/04	6260–6735		
55 041.9–55 867.6	13/13/13	4270–4523	48 000	BES
	13/13/13	4759–4991		
	13/13/13	6260–6735		
55 579.4–56 357.3	34/34/34	4270–4523	19 200	OND
56 579.4–56 889.6	05/04/05	4274–4508	19 200	OND
55 579.3–55 645.3	02/02/02	4378–4632	17 700	OND
55 579.3–56 357.3	20/20/20	4753–5005	19 300	OND
56 527.6–56 592.5	05/05/05	4759–4991	21 500	OND
56 527.6–56 889.6	14/14/14	6260–6735	14 000	OND
55 561.3–56 357.3	58/58/59	6255–6767	12 700	OND
55 597.4–55 980.3	19/19/22	6497–6688	14 000	LIS
56 555.7–56 564.7	12/12/12	4270–4523	48 000	FER
	12/12/12	4759–4991		
	12/12/12	6260–6735		

Notes. In column 'Ins.': DDO - David Dunlap Observatory 1.9 m reflector, Cassegrain CCD spectrograph; ELO - Haute Provence Observatory 1.2 m reflector, echelle ELODIE CCD spectrograph; BES - Cerro Amazones Hexapod Telescope, BESO echelle CCD spectrograph; OND - Ondřejov Observatory 2 m reflector, coudé CCD spectrograph; LIS - Lisbon Observatory of the Instituto Geográfico do Exército, reflector, CCD spectrograph; FER - La Silla 2.2 m reflector, Feros echelle CCD spectrograph.

Radial velocities measured on the available spectra (see Sect. 3.2) are listed in Table D.1.

2.2. Photometric observations

The photometry that has previously been used by Nemravová et al. (2013) was complemented by very accurate observations acquired almost continuously over two weeks with the MOST satellite (Walker et al. 2003) and by another series of Johnson UBV observations from Hvar. Additionally, we analysed the photometric minima published by Zasche et al. (2014).

The MOST satellite monitored ξ Tau over 16 days almost continuously. It acquired 21 525 observations that after the initial reduction by the MOST team were still affected by two systematic effects: The stray light from the Earth atmosphere, which introduced narrow peaks with separation ≈ 101 minutes; this is the MOST orbital period. The other effect was the relaxation time after the change of the observed field, during which the CCD had to reach thermal equilibrium. This manifests itself by a slowly decreasing offset that typically lasts several tens of minutes. The first effect was, with the exception of few observations during eclipses, removed with a low-passband Butterworth filter (Butterworth 1930). The second effect forced us to neglect all observations secured before RJD = 56 522. The remaining 18 510 observations were then analysed.

Table 4. Journal of the spectro-interferometric observations. ΔT is the time span RJD of the first and the last observation, ΔB the range of the projected baselines, $\Delta\lambda$ the wavelength range, N_{V^2} the total number of visibility observations, and N_{T3_ϕ} the total number of closure phase observations.

Instr.	ΔT (RJD)	ΔB (m)	$\Delta\lambda$ (nm)	$N_{\mathrm{V}^2}/N_{\mathrm{T3}_\phi}$
1	48 275–48 563	14–30	500–800	108/0
2	51 093–56 298	0–79	550–850	13 461/4 137
3	55 825–56 228	31–279	532–760	6 132/0
4	56 264–56 264	41–139	1 200–2 600	2 160/720

Notes. In column 'Instr.': 1 - Mark III, 2 - NPOI, 3 - CHARA/VEGA, 4 - VLTI/AMBER.

A journal of available photometric observations is listed in Table 3, and more details on the observations and data reductions can be found in Appendix B.

The reduced UBV photometric observations acquired at the Hvar Observatory, at the South African Astronomical Observatory, the Four College APT, and photometric observations acquired with the MOST satellite are listed in Tables D.2, D.3, D.4, and D.5.

2.3. Interferometric observations

The system was observed by four different spectro-interferometers: The Mark III Stellar Interferometer[1] (Mark III) (Shao et al. 1988), the Navy Precision Optical Interferometer (NPOI) (Armstrong et al. 1998), the Visible spEctroGraph and polArimeter (VEGA) (Mourard et al. 2009) mounted at the Centre for High Angular Resolution Astronomy (CHARA) (ten Brummelaar et al. 2005), and the Astronomical Multi-BEam combineR (AMBER) (Petrov et al. 2007) attached to the Very Large Telescope Interferometer (VLTI) (Glindemann et al. 2004). A journal of the spectro-interferometric observations is listed in Table 4. The phase coverage of orbits 1 and 2 with all spectro-interferometric observations is shown in Fig. 1. Details on the spectro-interferometric observations and their reduction are provided in Appendix C.

Reduced spectro-interferometric observations from all four instruments are listed in the form of calibrated squared visibility moduli in Table D.6 and closure phases are provided in Table D.7.

3. Spectroscopy

The spectral lines of all three components of the triple subsystem (i.e. orbits 1 and 2) of ξ Tau are clearly seen in all available spectra. Component C was not detected in any of the spectra at our disposal because its relative luminosity is lower than 1%, which is beyond the detection limit of the available spectra. Attempts to detect its spectral lines were carried out through spectral disentangling and a comparison of the near-infrared spectra with synthetic profiles, both with null results.

Two different approaches to derive the orbital elements of the triple subsystem of ξ Tau were used. The first was a direct analysis of RVs measured with the method described in Sect. 3.2, and the second was the spectral disentangling (Simon & Sturm 1994; Hadrava 1995) in Sect. 3.3.

[1] Decommissioned in 1992.

Table 3. Journal of photometric observations. For each row, N is the number of observations in each of the filters used, ΔT is the time span covered by each dataset, column 'Passbands' shows the photometric filters used, column 'Comp/Check' lists the names of comparison and check star used. UBV denote the Johnson filters, and MO denotes the broad-band filter of the MOST satellite.

N	ΔT (RJD)	Passbands	Comp / Check	Instrument
441/451/452	46 324.6–56 882.6[1]	UBV	4 Tau / 6 Tau	HVAR
69	47 909.6–48 695.0	$V(H_{\rm p})$[2]	all-sky	HIPP
26/26/26	55 569.3–55 579.4	UBV	6 Tau / 4 Tau	SAAO
131/133/135	55 883.9–55 956.8	UBV	4 Tau / 6 Tau	VILL
18 510	56 222.0–56 238.0	MO	all-sky	MOST

Notes. [1]Only three observations were taken before RJD $= 54\,116$, all at RJD $= 46\,324$. [2]The original Hipparcos $H_{\rm p}$ broad-band observations were transformed into the Johnson V filter following Harmanec (1998). However, for the light-curve solutions the limb-darkening coefficients corresponding to the original Hipparcos passband were used. Instruments: HVAR - Hvar Observatory 0.65 m Cassegrain reflector, photoelectric photometer; HIPP - The ESA Hipparcos Astrometric Mission; SAAO - South African Astronomical Observatory 0.5 m Cassegrain reflector, Lucy photoelectric photometer; VILL - the Four College 0.8 m reflector, photoelectric photometer; MOST - the Canadian MOST satellite.

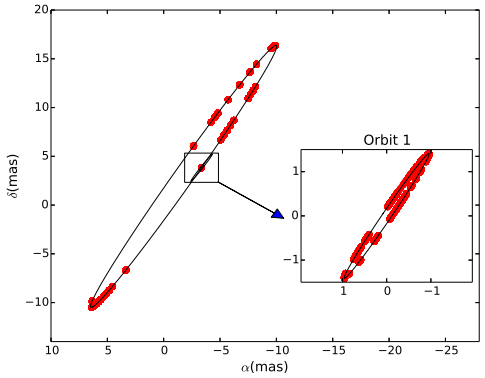

Fig. 1. Coverage of orbits 1 and 2 with the spectro-interferometric observations. *The outer plot:* the black line denotes the orbit of the centre of mass of the eclipsing binary relative to component B (which resides at the beginning of the coordinate system of the outer plot), and red dots denote the relative position of the centre of mass of the eclipsing binary relative to component B at the epochs of spectro-interferometric observations. *The inset plot:* the black line denotes the orbit of component Ab relative to component Aa (which resides at the beginning of the coordinate system of the inset plot), and red dots denote the relative position of component Ab relative to component Aa at epochs of spectro-interferometric observations. In both plots the orbital elements are invariable, i.e. they do not show the true orbits 1 and 2 as they would appear on the sky, but only demonstrate that the spectro-interferometric observations sample the orbits well enough to constrain elements of both orbits.

Additionally, we derived the basic radiative properties of ξ Tau using the comparison of the synthetic to observed and separated spectra (i.e. obtained through the spectral disentangling).

3.1. RVs measured by comparing the observed and synthetic line profiles

The RVs were derived using an automatic method based on the comparison of synthetic and observed spectra that searches for the best match with the optimisation of χ^2 given by

$$\chi^2 = \sum_{i=1}^{N_{\rm I}} \left(\frac{I_{\rm OBS}\left(\lambda_i\right) - \sum_{j=1}^{N_{\rm C}} I_{{\rm SYN},j}\left(\lambda_i, RV_j\right)}{\sigma_i} \right)^2 , \qquad (1)$$

where $I_{\rm OBS}$ is the observed spectrum, $I_{{\rm SYN},j}$ the synthetic spectrum of the j-th component, $N_{\rm I}$ is the number of discrete elements of the digitised spectrum, $N_{\rm C}$ is the number of the components of the system, RV_j is the radial velocity of the j-th component, and σ_i the standard deviation of the i-th point of the observed spectrum, which was estimated from the continuum and adopted for the whole spectrum.

The majority of the spectra at our disposal was acquired in three wavelength regions $\Delta\lambda \in \{4200-4500; 4750-5000; 6200-6700\}$ Å. Each region contains a Balmer line, which turned out to be the best for measuring the RVs of component B and several metallic lines, which gave accurate RVs of components Aa and Ab. These regions were also extracted from echelle spectra, and RVs were measured on each region independently. The last region (Hα) contains a number of telluric lines, including the Hα line itself. Our model is unable to account for a telluric spectrum, and consequently it was not possible to measure accurate RVs of Hα with this technique.

Initial RVs for the searching program were computed from the orbital solution presented in Nemravová et al. (2013), and we searched for the RV for each component in the interval $[-70; 70]$ km s^{-1} that surrounds the initial estimate. The components of the eclipsing binary Aa and Ab are very similar, therefore we had to verify that the two components had not been interchanged by the program, especially near the conjunctions. If they were, the search was repeated using a narrower search interval.

The RVs and their uncertainty were estimated in the following way:

1. The parameters of synthetic spectra were chosen randomly from the Gaussian distributions centred at values listed in Table 7, and the standard deviations were set to their uncertainties.
2. The synthetic spectra were fitted to the observed ones. The procedure was repeated five hundred times for each spectrum, and the RV including its uncertainty was estimated from the resulting distribution.

This approach allowed us to estimate only the statistical part of the total uncertainty. The statistical uncertainty $\Delta RV_{\rm stat}$ was typically $\leq 1\,{\rm km\,s^{-1}}$ for components Aa and Ab and $\leq 10\,{\rm km\,s^{-1}}$ for component B. Measuring the RVs of component B was more difficult because the majority of metallic lines in its spectrum is very shallow and smeared out by the high rotational velocity of component B. The measurements are also very sensitive to the choice of the model and its discrepancies.

The telluric lines in the red and IR parts of the spectra were used to correct for the variations of the zero-point of the RV scale. These corrections were typically $\leq 2\,{\rm km\,s^{-1}}$ for the Ondřejov spectra, hence all measurements for which the RV zero-point could not be checked in this way were assigned an uncertainty $\max(\Delta RV_{\rm stat}, 2)\,{\rm km\,s^{-1}}$, and the remaining ones were assigned an uncertainty $\max(\Delta RV_{\rm stat}, 1)\,{\rm km\,s^{-1}}$, where $1\,{\rm km\,s^{-1}}$ is the upper bound of the precision of the zero-point correction for the Ondřejov spectra.

3.2. Direct analysis of RVs

Since we were not aware of any publicly available program for orbital solutions of hierarchical systems with apsidal advance of the outer orbit(s), JN developed such a program. The measured RVs were fitted with a model, which takes into account the two dynamical interactions between the three or four components. The effects considered are the apsidal motion of orbit 2 and the light-time (LITE) effect produced by orbits 2 ($t_{\rm LITE} \approx 0.006\,{\rm d}$) and 3 ($t_{\rm LITE} \approx 0.013\,{\rm d}$). The RVs of the j-th component RV_j were fitted with the standard Keplerian model:

$$RV_j(t) = \sum_i K_i \left[\cos\left(\omega_i(t) + v_i(t)\right) + e_i \cos\omega_i(t)\right], \qquad (2)$$

where the index i goes over those orbits of ξ Tau that are relevant for the motion of the j-th component of the ξ Tau system, K_i is the semiamplitude of the RV curve, ω_i the argument of periastron, v_i the true anomaly, e_i the eccentricity, and t is time. The LITE $\Delta t_{\rm LITE}$ was computed using the following formula:

$$\Delta t_{\rm LITE,j}(t) = \sum_i \frac{P_i K_i \left(1-e_i^2\right)^{\frac{3}{2}}}{2\pi c} \frac{\sin\left[\omega_i(t) + v_i(t)\right]}{1 + e_i \cos v_i(t)}, \qquad (3)$$

where the index i goes over those orbits that are hierarchically above the orbit in which the j-th component lies (i.e. over those that produce LITE), P is the orbital period, and c is the speed of light. Otherwise the notation is the same as for Eq. (2). The argument of periastron is a linear function of time $\omega_i(t) = \omega_i(t_0) + \dot\omega_i\,(t - t_{0,i})$, where $t_{0,i}$ is the reference epoch and $\dot\omega_i$ is the mean apsidal motion of the i-th orbit.

The model elements were optimised by searching the minimum of the following χ^2:

$$\chi^2 = \sum_{k=1}^{N_{\rm S}} \sum_{j=1}^{N_{\rm C}} \sum_{l=1}^{N_{\rm O}} \frac{1}{\sigma_{j,l}^2} \left[RV_j^{\rm OBS}(\tilde t_{j,l}) - RV_j^{\rm SYN}\left(\tilde t_{j,l}\right) - \gamma_k\right]^2, \qquad (4)$$

where the index k goes over $N_{\rm S}$ subsets of the measured RVs, which are defined in Table 2, the index j over $N_{\rm C}$ components of the ξ Tau system for which RVs were measured, and the index l goes over $N_{\rm O}$ individual measurements of the RV and $\tilde t$ is time corrected for the LITE. σ denotes individual rms of the RVs estimated with the procedure described in Sect. 2, $RV^{\rm OBS}$ the measured RV, $RV^{\rm SYN}$ the model RV computed with Eq. (2), and corrected for the LITE via Eq. (3), and γ denotes the systemic velocity. The minimum of the χ^2 given by Eq. (4) was searched for with the sequential least-squares routine (Kraft 1988).

As discussed above, RVs of component B are less accurate than those of components Aa and Ab. Hence only RVs of the members of the eclipsing binary were fitted to obtain the majority of orbital elements. The individual subsets for individual types of the spectra gave very similar values of the systemic velocity (within 3σ), hence all available measurements were grouped together and a joint systemic velocity was derived for them. When a final solution was obtained, the measurements were complemented with RV measurements of component B and the mass ratio q_2 was optimised (keeping the remaining parameters fixed). The parameters corresponding to the best-fit solution are listed in Table 5. RVs and the best-fitting model are plotted against time (to show the secular evolution of the periastron argument) for orbit 2 in Fig. 2, and against phase for orbit 1 in Fig. 3.

The uncertainties and correlations of individual parameters were estimated with the bootstrap method. One thousand samples were randomly chosen from all available RVs. Each sample consisted of the same number (748) of measurements as the original (meaning that some measurements repeat within a sample). Each sample was fitted with an orbital model and the uncertainties were estimated from the distribution of the results.

The reduced χ^2 (denoted $\chi^2_{\rm R}$ throughout the article) $\chi^2_{\rm R} \approx 2$, which is greater than ideal case of 1, is probably caused by variations of the RV zero-point larger than we accounted for (we note that the estimate is based on the variations of the zero-point measured on the Ondřejov red spectra), and by the fact that the synthetic spectra need not correspond to the observed ones in all details, for which we cannot account properly. Moreover, the model does not account properly for the dynamical interaction (see Sects. 8 and 9) between all orbits.

We also fitted a model including orbit C fixed at the orbital elements given in Table 10. The reduced χ^2 was only marginally ($\leq 1\%$) lower than that in Table 5. This is expected because the semi-amplitude of the RV caused by the revolution of the triple subsystem around the common centre of gravity with component C is $\approx 1\,{\rm km\,s^{-1}}$ and the LITE produced by that motion is $\approx 0.013\,{\rm d}$, which means that both are beyond the detection limit of our measurements.

3.3. Spectral disentangling

We were only able to separate the spectra in the vicinity of five major spectral lines Hα, Hβ, He I 4471 Å, Mg II 4481 Å, and Hγ because only these regions were available for both the slit and echelle spectra. An attempt was made to separate the spectra of individual components using only the spectra from the three available echelle spectrographs. However, these separated spectra had strongly warped continua and were unsuitable for further investigation.

We used the program KOREL (Hadrava 1995, 1997, 2009) (release 04-2004), which not only separates the spectra, but also fits the spectroscopic orbital elements. This gave us the opportunity to compare the orbital solution obtained directly from the measured RVs with the result of KOREL. Only components B, Aa, and Ab were fitted because component C is not detectable. Relative luminosities of all three components were kept constant during the orbital motion. This assumption, although not exactly satisfied because of the shallow eclipses of components Aa and Ab, was necessary for the stability of the disentangling.

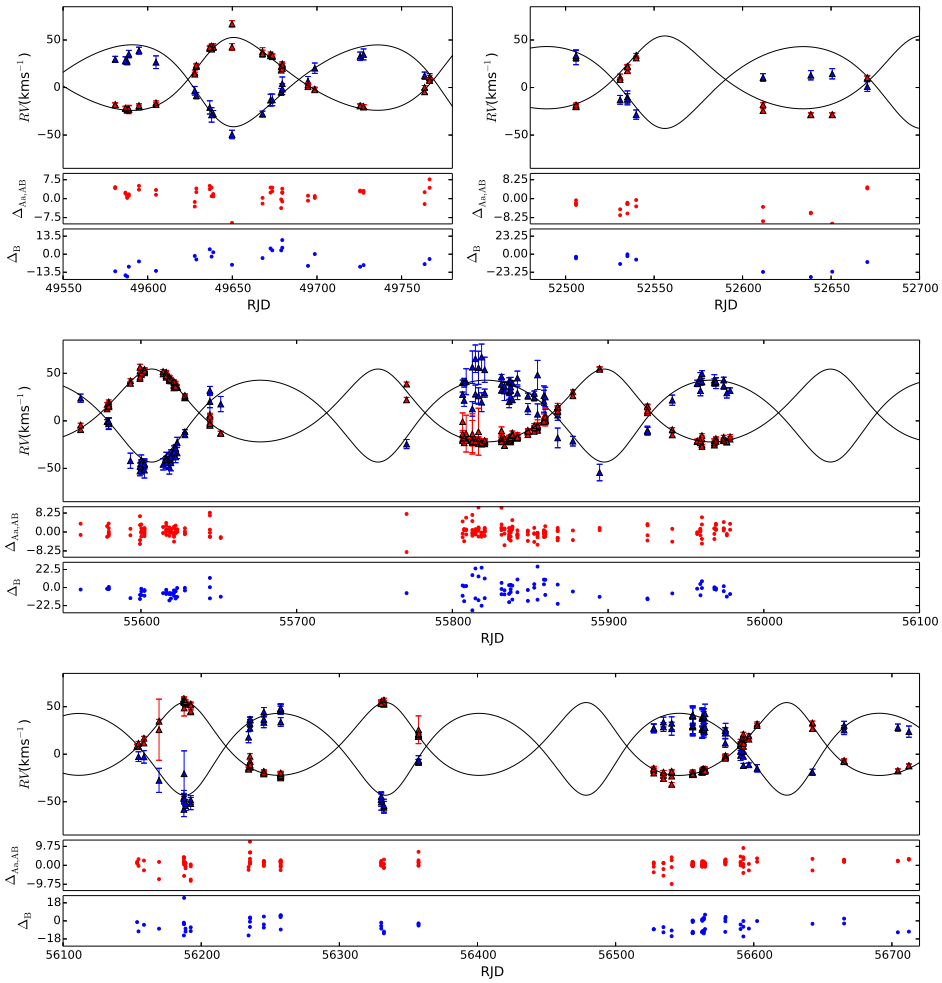

Fig. 2. RVs of the centre of gravity of the eclipsing binary (red triangles) and component B (blue triangles) against the best-fitting model (black) corresponding to parameters listed in Table 5. $\Delta_{\rm Aa,Ab}$ (in km s^{-1}) denote residuals of the fit for RVs of the centre of gravity of the eclipsing binary, and $\Delta_{\rm B}$ (in km s^{-1}) residuals of the fit for RVs of component B.

The orbital elements presented in Table 5 served as the starting estimates for the minimisation. The spectroscopic orbital elements obtained with KOREL are listed in Table 6. The separated profiles from the considered spectral regions are shown in Fig. A.1. KOREL does not provide the uncertainties of the fitted elements. Therefore a map of the χ^2 around the minimum found with the minimisation engine was drawn for every combination of two fitted parameters. The uncertainties, which are listed in Table 6, correspond to 68% confidence intervals (roughly one σ) estimated from these maps.

An attempt was carried out to separate the lines of component C within two spectral bands in the near infrared, $\Delta\lambda_{\rm IR} = \{7750-7800, 8570-8800\}$ Å. The spectrum of component C was not detected in either of these bands. It was probably caused by the relatively low signal-to-noise ratio (S/N) of the echelle spectra in the infrared region and their limited number.

Table 5. Parameters of the two-orbit (1 and 2) fit given by Eqs. (2) and (3) to measured RVs. $P_{\rm AN}$ denotes the anomalistic period, $P_{\rm S}$ the sidereal period, $T_{\rm min}$ the epoch of the primary minimum of the light curve, and $T_{\rm p}$ the epoch of the periastron passage.

El. Orb.	Units	Values 1	2
$P_{\rm AN}$	(d)	–	145.579±0.048
$P_{\rm S}$	(d)	7.14664±0.00002	145.113±0.071
$T_{\rm min}$	(RJD-56 220)	4.7067±0.0025	–
$T_{\rm p}$	(RJD-55 600)	–	9.46±0.52
K	(km s^{-1})	87.79±0.25	38.37±0.19
e		0.0[1]	0.2101±0.0053
q		0.9438±0.0036	0.889±0.056
ω	(deg)	90[1]	9.25±1.42
$\dot{\omega}$	(deg yr^{-1})	0.0[1]	2.90±0.33
N		748	
$\chi^2_{\rm R}$		2.128	
		Systemic velocity	
γ	(km s^{-1})	8.05 ± 0.18	

Notes. [1]The parameter was fixed. K_1 refers to the primary of the eclipsing binary $K^{\rm Aa}$, and K_2 to the centre of gravity of the eclipsing binary $K^{\rm Aa+Ab}$.

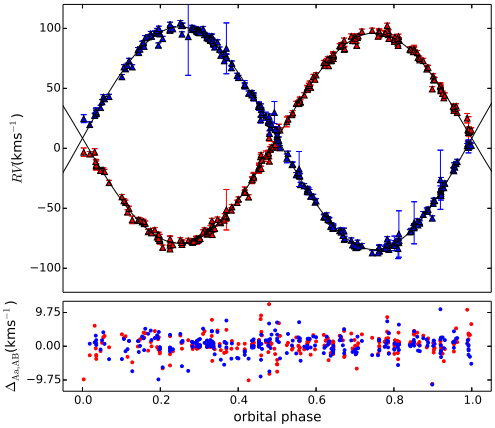

Fig. 3. RVs of components Aa (red) and Ab (blue) relative to the centre of gravity of the eclipsing binary against the best-fitting model (black) listed in Table 5. $\Delta_{\rm Aa,Ab}$ are residuals of the fit for components Aa and Ab.

We also note that we tried to use the separated profiles instead of synthetic ones to measure RVs with the PYTERPOL program written by JN. This worked well for components Aa and Ab, but failed for component B. The reason is that the shape of the separated spectral lines depends on the orbital elements, for which the spectra were separated, and vice versa. Hence the separated spectra partially "remember" the orbital elements for which they were obtained, and if they are used for the RV measurements, they would give a fine RV curve described by a solution close to these elements. This becomes a problem when one or more orbital elements suffer from a large uncertainty, which was the case for ξ Tau in the mass ratio of orbit 2.

Table 6. Orbital elements obtained by KOREL (spectral disentangling) for all available spectra containing at least one of the studied regions. The orbital model consists of orbits 1 and 2.

Elem. Orbit	Unit	1	2
$P_{\rm AN}$	(d)	–	145.612±0.056
$P_{\rm S}$	(d)	7.14664±0.00002	145.123±0.072
$T_{\rm min}$	(RJD-56220)	4.6963±0.0040	–
$T_{\rm p}$	(RJD-56000)	–	9.29±1.44
K	(km s^{-1})	87.52±0.59	37.55±0.57
e		0[1]	0.180±0.024
q		0.943±0.008	1.02±0.27
ω	(deg)	90[1]	8.52±4.1
$\dot{\omega}$	(deg yr^{-1})	0[1]	3.032±0.38
$\chi^2_{\rm R}$		1.19	

Notes. [1]The parameter was fixed. K_1 refers to the primary of the eclipsing binary $K^{\rm Aa}$ and K_2 to the centre of gravity of the eclipsing binary $K^{\rm Aa+Ab}$.

3.4. Comparison of observed and synthetic spectra

JN has developed a Python program PYTERPOL[2], which interpolates in a pre-calculated grid of synthetic spectra to obtain estimates of the radiative properties of the components of multiple systems. For ξ Tau these parameters were the effective temperature $T_{\rm eff}$, gravitational acceleration $\log g$, the projected rotational velocity $v \sin i$, RV, and the relative luminosity $L_{\rm R}$. The parameters of components Aa, Ab, and B were covered by the POLLUX grid (Palacios et al. 2010), and component C was searched for using the AMBRE grid (de Laverny et al. 2012). Solar metallicity was assumed.

The fit was carried out in four spectral regions, but only three relative luminosities were derived, since two of the regions are very close to each other and the luminosities $L_{\rm R}$ are most likely almost the same.

The spectral regions were $\Delta\lambda_1 = [4280, 4495]$ Å, $\Delta\lambda_2 = [4815, 4940]$ Å, and $\Delta\lambda_3 = \{[6330, 6390]\,; [6660, 6695]\}$ Å.

The relative luminosities were assumed to be constant over each spectral region $\Delta\lambda_i$.

Two of the regions contain a Balmer line, which constrains the gravitational acceleration of all three components, and also a large number of metallic lines, which constrain the temperature, RVs, and the projected rotational velocities. We fitted 137 spectra from the Ondřejov Observatory together because their normalisation is straightforward (a first-order polynomial often suffices to fit the continuum), so that the Balmer lines are not affected by systematics often introduced by the normalisation. The uncertainty of the relative flux was estimated from the continuum for each spectrum and set constant for each spectrum.

The bootstrap method was used to obtain a best-fit set of parameters. We randomly drew 137 spectra from the pool of 137 Ondřejov spectra (meaning that one or more spectra can be present multiple times within the random sample) and fitted them. The initial set of parameters was randomly chosen from intervals[3] which were established from the first trial fits. The ini-

[2] A detailed description with a simple tutorial how to use it is provided at https://github.com/chrysante87/pyterpol/wiki

[3] The intervals are the following: $T_{\rm eff}^{\rm B} \in [13\,000, 14\,500]$ K, $T_{\rm eff}^{\rm Aa} \in [9\,000, 11\,500]$ K, $T_{\rm eff}^{\rm Ab} \in [9\,000, 11\,500]$ K, $\log g^{\rm B} \in [4.0, 5.0]$, $\log g^{\rm Aa} \in [3.5, 4.5]$, $\log g^{\rm Ab} \in [3.5, 4.5]$, $v \sin i^{\rm B} \in [200, 250]$ km s^{-1}, $v \sin i^{\rm Aa} \in [0, 40]$ km s^{-1},

Table 7. Parameters of the fit of the synthetic spectra to 137 observed Ondřejov spectra. The modelled spectral intervals are $\Delta\lambda_1 = [4280, 4495]$Å, $\Delta\lambda_2 = [4815, 4940]$Å and $\Delta\lambda_3 = \{[6330, 6390]\,; [6660, 6695]\}$Å.

Parameter	Unit	Value		
Component		B	Aa	Ab
$T_{\rm eff}$	(K)	14 190±150	10 700±160	10 480±130
$\log g$	(cgs)	4.527±0.041	4.08±0.12	4.01±0.10
$v \sin i$	(km s^{-1})	229.2±1.7	12.6±2.6	14.3±3.1
$L_{\rm R}^{\Delta\lambda_1}$		0.660±0.024	0.179±0.018	0.165±0.022
$L_{\rm R}^{\Delta\lambda_2}$		0.688±0.026	0.162±0.024	0.155±0.027
$L_{\rm R}^{\Delta\lambda_3}$		0.665±0.036	0.173±0.028	0.161±0.031
$\chi^2_{\rm R}$			0.87	

Table 8. Parameters of synthetic spectra best-fitting the separated spectra. γ denotes the systemic velocity of ξ Tau. The fit is plotted in Fig. A.1.

Element	Unit	Value		
		Component		
		B	Aa	Ab
$T_{\rm eff}$	(kK)	14.07(14)	10.26(14)	10.050(80)
$\log g_{\rm [cgs]}$		3.99(4)	4.06(9)	4.02(4)
$v \sin i$	(km s^{-1})	253.6(16)	18.6(12)	10.2(10)
$L_{\rm R}^{\Delta\lambda_1}$		0.758(8)	0.168(3)	0.150(7)
$L_{\rm R}^{\Delta\lambda_2}$		0.711(6)	0.191(5)	0.149(3)
$L_{\rm R}^{\Delta\lambda_3}$		0.686(7)	0.188(4)	0.161(7)
γ	(km s^{-1})		8.1(27)	
$\chi^2_{\rm R}$			31.58	

tial RVs were estimated from the orbital solution presented in Nemravová et al. (2013) and randomly put slightly off (within 30 km s^{-1} vicinity of the estimate) to secure robustness of the final solution. The procedure was repeated five hundred times and the final set of parameters was estimated from the distribution of the results. The shape of the distribution was Gaussian-like, that is, describable with a mean value and its standard deviation. The results are presented in Table 7.

A comparison of four spectral regions with the model is shown in Fig. 4. The reduced $\chi^2_{\rm R}$ is lower than one, indicating that we have slightly overestimated the uncertainty of the relative flux of the observed spectra.

3.5. Comparison of synthetic and separated spectra

We fitted the separated spectra corresponding to the solution of Table 6 with the interpolated synthetic spectra to check the results of Sect. 3.4. The program `PYTERPOL` was used again. The following spectral regions were fitted:
$\Delta\lambda_1 = \{[4280, 4400]\,; [4455, 4495]\}$ Å,
$\Delta\lambda_2 = [4765, 4970]$ Å, and
$\Delta\lambda_3 = \{[6325, 6395]\,; [6510, 6620]\,; [6655, 6695]\}$Å.

The parameters corresponding to the best-fitting synthetic spectra are listed in Table 8. The best-fit parameters were estimated with a MCMC simulation and the uncertainties reflect only the statistical part of the uncertainty. The systematic uncertainty — the warp in the continua and the need for its normalisation — cannot be easily quantified and is responsible for the extremely high reduced $\chi^2_{\rm R}$ along with the very high S/N ratio of the separated spectra. Therefore the uncertainties of the parameters listed in Table 8 are very likely underestimated.

This systematic effect corrupts the estimate of $\log g$ of all components, especially component B, where the warping was the most pronounced; therefore it also applies to the rotational velocity of component B. The rotational velocity of components Aa and Ab is strongly affected by the choice of the instrumental broadening, which is very difficult to estimate for separated spectra and was set to 0.2 Å. The total light is also very likely affected by the re-normalisation, which (necessarily) changes the depths of spectral lines ($L = \sum_{i=1}^{3} L_{\rm R}^{\Delta\lambda,i} \neq 1$ for all studied bands).

Bearing all this in mind, we state that this result does not contradict, but rather supports that obtained by fitting of synthetic to observed spectra. A comparison of the synthetic spectra corresponding to the parameters listed in Table 8, of separated spectra, and of re-normalised separated spectra is in Fig. A.1.

4. Photometry

The preliminary analysis published in Nemravová et al. (2013) has shown that the light variations can be attributed to the eclipses of components Aa and Ab of orbit 1. They partially eclipse each other and produce two very narrow and nearly identical minima, which are only ≈ 0.1 mag deep in the Johnson V passband.

In addition to the binary eclipses, our new very precise MOST satellite observations unveiled persistent low-amplitude rapid cyclic light changes that are probably associated with component B, since they remain during both binary eclipses. The MOST light curve also allows determining very accurate radii of components Aa and Ab as well as detecting variations of the mean motion of the eclipsing pair. The zoomed parts of both minima of the MOST light curve are shown in Fig. 5.

4.1. Period analysis of the light curve

Our first goal in the analysis of the MOST light curve was to unveil the nature of the rapid cyclic low-amplitude changes. Two different methods were used to construct and investigate the periodogram of the light curve. The first is based on the Fourier transform (FT hereafter) and is implemented in the program `PERIOD04` (Lenz & Breger 2004). The second uses the phase dispersion minimisation technique (PDM) (Stellingwerf 1978) and is implemented in the program `HEC27`[4]. The periodogram of the whole light curve is dominated by the orbital period of the

$v \sin i^{\rm Ab} \in [0, 40]$ km s^{-1}, $L_{\rm R}^{\rm B} \in [0.55, 0.8]$, $L_{\rm R}^{\rm Aa} \in [0.10, 0.25]$, $L_{\rm R}^{\rm Ab} \in [0.10, 0.25]$.

[4] The program and a short user guide are available at `http://astro.troja.mff.cuni.cz/ftp/hec/HEC27`.

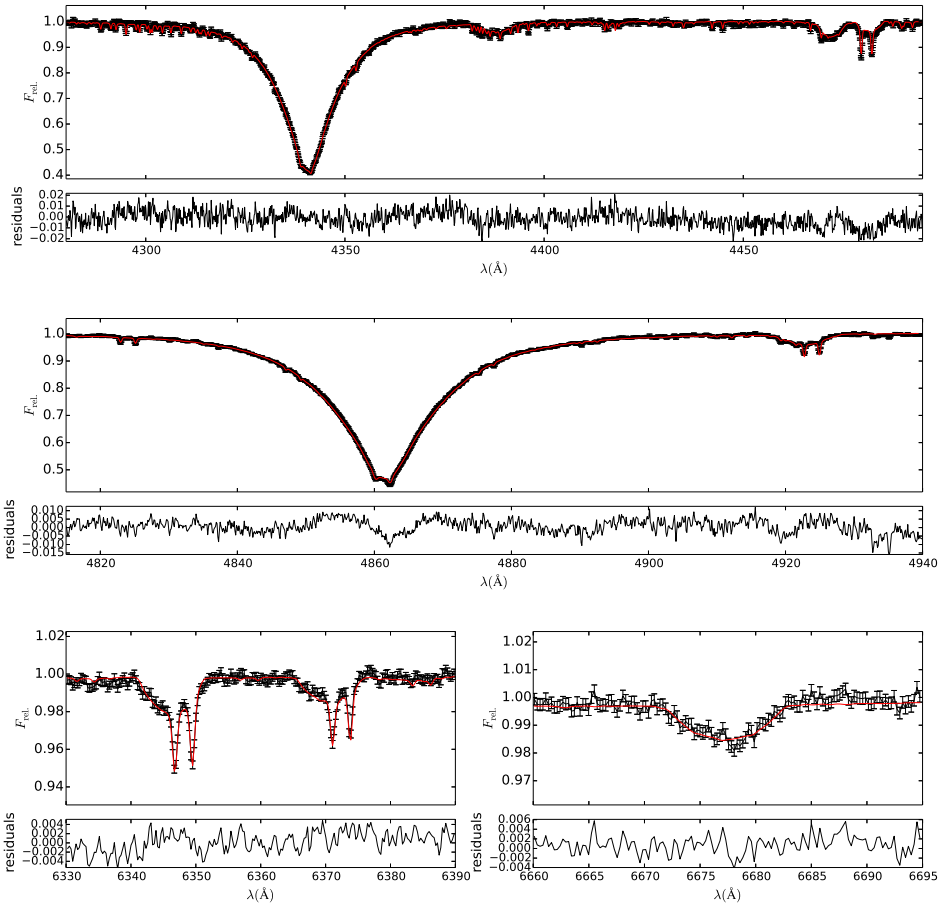

Fig. 4. Example of the fit of the synthetic spectra (red) to three observed spectra (black) in spectral regions: 1) $\Delta\lambda_1 = [4280, 4495]$ Å (top), 2) $\Delta\lambda_2 = [4815, 4940]$ Å (middle), 3) $\Delta\lambda_3 = [6330, 6390]$ Å (bottom, left), 4) $\Delta\lambda_3 = [6660, 6695]$ Å (bottom, right). The synthetic spectra are given by parameters listed in Table 7.

eclipsing binary $P_1 \approx 7.147$ d. To study the rapid low-amplitude oscillation, we removed the eclipses (see Fig. 7, top).

The periodogram of the rapid oscillations (see Fig. 6) shows a basic frequency of $f_0 = 2.38\,\mathrm{d}^{-1}$, most likely due to rotation of component B, the first harmonics of the eclipsing binary orbital frequency $f_1 = 2/P_1 = 0.279\,\mathrm{d}^{-1}$; the frequencies of $f_\mathrm{d} = 1.002738\,\mathrm{d}^{-1}$ and $f_\mathrm{MOSTorbit} = 14.2\,\mathrm{d}^{-1}$ are instrumental (i.e. the orbital frequency of the satellite). The remaining prominent frequencies $f_\mathrm{alias} = \{15.1734, 17.5385, 28.3896, 42.5825, 56.7745, 70.9720\}\,\mathrm{d}^{-1}$. seem to be either integer multiples of f_orb or its splittings with f_0 or f_d. Remaining peaks (e.g. $f = 87.1609\,\mathrm{d}^{-1}$) have relatively low S/N ratios. We are not aware of any instrumental effect that would induce oscillations at $f_0 = 2.38\,\mathrm{d}^{-1}$, hence the low-amplitude variations arise from a physical process in ξ Tau.

A closer look at Fig. 7 shows that the amplitude of the curve varies. To quantify these changes, a harmonic function $f(t) = 1 + C_0 + A_0 \sin[2\pi(t - T_0)f_0 + \phi_0]$ was sequentially fitted to segments of the light curve $\Delta t_1 = P_1/2$ d wide, and shifted with a step $\Delta t_2 = P_1/20$, where P_1 is the period of the eclipsing binary. The scan revealed that both the basic frequency f_0 and its amplitude A_0 vary on the time span of two orbital periods of the eclipsing binary (see Fig. 7, middle and bottom panels).

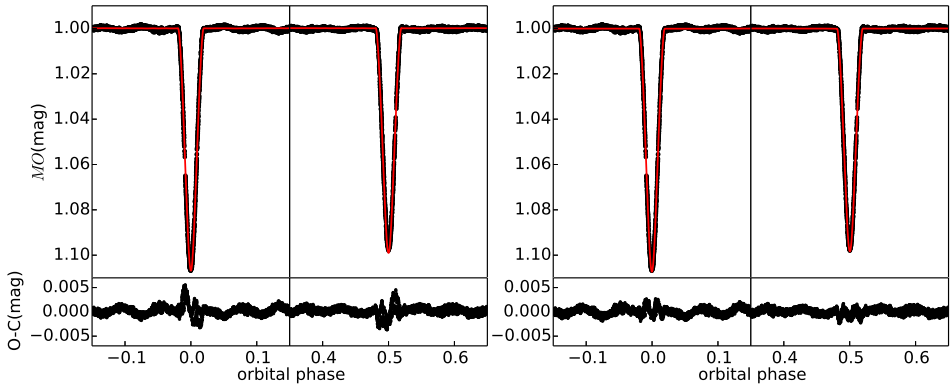

Fig. 5. Fit of the light curve from the satellite MOST. Only the light curve minima and their surroundings are shown. The primary (secondary) minimum is on the left (right) on each panel. The left panel corresponds to the global circular solution $e_1 = 0.0$ and to orbital period $P_1 = 7.14664\,\mathrm{d}$. The right panel corresponds to a local solution, where small adjustment of the eccentricity and the orbital period was allowed. MO denotes the satellite broad-band filter.

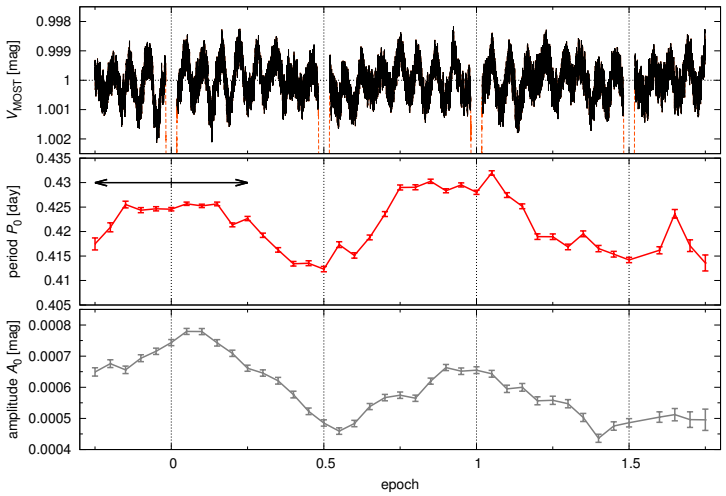

Fig. 7. Normalised light curve as reduced from MOST photometry, but without intervals of primary and secondary eclipses (top panel), together with the corresponding period P_0 (middle) and amplitude A_0 (bottom) of the harmonic function $f(t) = 1 + C_0 + A_0 \sin[2\pi(t - T_0)/P_0 + \phi_0]$, which was sequentially fitted to the light curve, always in limited intervals $\Delta E_1 = 0.5$ of the epoch (indicated by the black double arrow), shifted with a step $\Delta E_2 = 0.05$. The oscillations exhibit both frequency and amplitude modulations, with periods spanning $P_0 = (0.42 \pm 0.01)\,\mathrm{d}$ and amplitudes $A_0 = (0.00060 \pm 0.00015)\,\mathrm{mag}$. It seems that the longest P_0 and the largest A_0 are observed at around primary eclipses and vice versa.

4.2. Nature of quasiperiodic oscillations

The quasiperiodic oscillations clearly visible in the MOST light curve with an approximate period $P_0 \simeq (0.42 \pm 0.01)\,\mathrm{d}$ and an amplitude $A_0 = (0.00060 \pm 0.00015)\,\mathrm{mag}$ exhibit both a frequency (FM) and an amplitude modulation (AM) on the time span of about the two shortest orbital periods P_1 (see Fig. 7). We can think of several possibilities regarding their origin: an instrumental effect, a fifth component and ellipsoidal variations, rotation with spots, or rotation and pulsations.

The first option does not seem very likely, however, because we do not know about any instrumental period of $0.42\,\mathrm{d}$ (like one day, or a satellite orbital period 0.07042 d in this case).

A hypothetical fifth component (second option) orbiting either component B, Aa, or Ab with a period $2P_0$ can induce ellipsoidal variations of the order of A_0, but they would be expected to be very regular (without large AM, FM) and to manifest themselves in one of the RV curves as well, which is not the case. We do not see any peak in the Fourier spectrum at $f_0 = 1/P_0 = 2.38\,\mathrm{d}^{-1}$, even though the Nyquist frequency for our spectroscopic dataset is $f_{\mathrm{Ny}} = 7.1\,\mathrm{d}^{-1}$. Nevertheless,

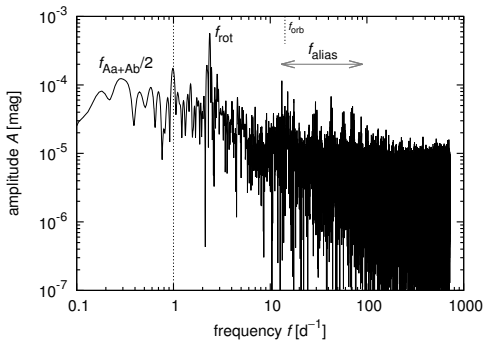

Fig. 6. Fourier spectrum of the MOST light curve from Fig. 7 (i.e. outside eclipses). Prominent frequency peaks are marked (see their description in Sect. 4.1).

the coverage and cadence are not uniform at all and the expected amplitude is small ($5\,\mathrm{km\,s^{-1}}$), which makes this particular argument weak. We would also expect to see some frequency modulation due to the (classical) Doppler effect, $P'_{\rm obs} = (1-\frac{v}{c})\gamma P_{\rm src}$, with $v \simeq 2v_{\rm kepl}$. However, for $0.423\,\mathrm{d}$ we would only obtain a change by $0.001\,\mathrm{d}$, which is one order of magnitude smaller than the observed total variation.

The lower limit for the rotation period is the critical rotation, $P_{\rm min} = 2\pi(GM/R^3)^{-1/2}$, and the upper limit is determined by rotational broadening, $P_{\rm max} = 2\pi R/(v \sin i)$ (cf. Table 8). For component Aa or Ab, the admissible range is from about $P_{\rm rot} = 0.180\,\mathrm{d}$ to $3.85\,\mathrm{d}$, for component B it is 0.325 to $0.634\,\mathrm{d}$. The observed oscillations are within both ranges, so that we cannot distinguish the source component at this point. One can argue that small axial inclination for components Aa, Ab is unlikely when their orbital inclination is large, so that their true $P_{\rm rot} > P_0$. We thus prefer to attribute these oscillations to component B. Additionally, this star is relatively brighter so that it is easier to induce the oscillations of given amplitude A_0.

It seems difficult to distinguish between spots and pulsations (options three and four above; as in Degroote et al. 2011). Especially for early-type stars, spots are infrequent, unless a star is chemically peculiar or magnetically active (Bp), but we have no observations and analyses at our disposal that could prove or disprove this for ξ Tau.

Pulsating B stars (like β Cep, SPB) always exhibit a low-frequency signal corresponding to the rotation and then a series of pulsation modes, either pressure (high-frequency) or gravity (low-frequency). The cadence of MOST photometric observations allows us to compute the Fourier spectrum up to $f_{\rm Ny} = 719\,\mathrm{d^{-1}}$, corresponding to $0.00139\,\mathrm{d} = 2\,\mathrm{min}$ (Fig. 6). Except for the basic rotational period, its aliases with the orbital period P_1 of the eclipsing binary, one-day and $P_{\rm orb}$ instrumental periods, we can unfortunately not unambiguously detect any pulsation modes with S/N ≥ 5, to say nothing about rotational splittings, which would be conclusive.

4.3. Eclipse timing variations

The orbital period of the eclipsing binary $P_1 = 7.14664\,\mathrm{d}$ introduces a small but clearly detectable shift $\Delta_{\rm PHASE} \approx 0.0003$ between the two minima recorded with the MOST satellite. The shift disappears if the orbital period and the eccentricity are optimised. The local period and eccentricity, which do not cause the phase shift, are $P_1 = 7.14466\,\mathrm{d}$ and $e_1 \simeq 0.002$. The problem is illustrated in Fig. 5, where the comparison of an eccentric model with the local value of the orbital period and a global circular model is shown. An even larger phase shift $\Delta p \sim 0.004$ was detected when a similar analysis was carried out for all photometric observations.

This led us to investigate the eclipse timing variations (ETVs) in all available photometry, divided into subsets covering time intervals shorter than $P_2/4$ (individual minima are shown in Figs B.1 and B.2). The ETVs are very noisy, and the delays themselves have an amplitude $\Delta t_{\rm OBS} \approx 0.025 \pm 0.01\,\mathrm{d}$ that cannot be explained by LITE ($\Delta t_{\rm LITE} \approx 0.006\,\mathrm{d}$). Moreover, they seem to vary on a timescale comparable to the orbital period P_2. Hence we assume that the dynamical interaction between orbits 1 and 2 is the reason for these delays. The first-order model of the physical delay (Eq. 8 from Rappaport et al. 2013), which is only a part of the total ETV, arising from dynamical interaction of two orbits in hierarchical triple systems, gives an estimate of the amplitude of the effect $\Delta t_{\rm MODEL} \approx 0.02\,\mathrm{d}$, (i.e. in rough agreement with the detected value). This is another proof of the dynamical interaction in ξ Tau (the first is the apsidal motion reported by Nemravová et al. 2013) and led us to develop an N-body model (see Sect. 8) and a perturbation theory (see Sect. 9).

4.4. Global orbital model for all light curves

The program PHOEBE 1.0 (Prša & Zwitter 2005, 2006) was used to derive the light-curve solution. The mass ratio q_1 was taken from the analysis of the RVs (see Table 5) because only light curves were modelled and they do not constrain the mass ratio for a detached system. The eccentricity was assumed to be $e_1 = 0.0$ (although Sect. 8 shows that orbit 1 is slightly eccentric). The value of the semi-major axis a was adjusted after each iteration based on $a_1 \sin i$ given by the fit of the directly measured RVs (see Table 5). The linear limb-darkening law was adopted and the coefficients were interpolated in a pre-calculated grid distributed along with PHOEBE. The bolometric albedos were taken from Claret (2001) and the gravity brightening coefficients from Claret (1998) for the corresponding temperatures of components of the eclipsing binary. The spin-orbit synchronisation, that is, the synchronicity ratios $F^{\rm Aa} = F^{\rm Ab} = 1$, was assumed, because radii $R^{\rm Aa}$ and $R^{\rm Ab}$ from Nemravová et al. (2013) and rotational velocities from Table 7 give synchronicity ratios $F^{\rm Aa} = 1.12 \pm 0.26$, and $F^{\rm Ab} = 0.74 \pm 0.20$; the deviations from the corotation are small and probably arise from an incorrect determination of the radii. The primary effective temperature $T_{\rm eff}^{\rm Aa}$ was set to the value found through a comparison of synthetic and observed spectra.

The orbital inclination i_1, Kopal surface potentials $\Omega_{\rm K}^{\rm Aa}, \Omega_{\rm K}^{\rm Ab}$ of both components and the epoch of the primary minimum $T_{\rm min,1}$, the secondary temperature $T_{\rm eff}^{\rm Aa}$, and the relative luminosity of component B $L^{\rm B}$ in each spectral band were optimised. Initial estimates of these parameters were taken from Nemravová et al. (2013), initial relative luminosities $L^{\rm B}$ of component B were estimated from the comparison of synthetic and observed profiles (Table 7). The primary luminosities $L^{\rm Ab}$ were adjusted after each iteration.

The fitting was carried out in the Python environment of PHOEBE, and the minimum was determined with the differential evolution algorithm (Storn & Price 1997). The following parametric space was searched: $T_{\rm min,1} \in [56\,224.68, 56\,224.78]$ RJD, $i_1 \in [84, 90]$ deg, $\Omega_{\rm K}^{\rm Aa} \in [11, 20]$, $\Omega_{\rm K}^{\rm Ab} \in [11, 20]$, $T_{\rm eff}^{Ab} \in [10\,000, 10\,700]$ K, $L^{\rm B} \in [0.55, 0.78]$.

Table 9. Parameters of the best-fitting circular orbital model obtained with the program `PHOEBE 1.0`. All available photometric observations were fitted. $\Omega_{\rm K}$ denotes the Kopal surface potential here, and L the relative luminosity in the filter given by the subscript. U, B, and V denote Johnson filters, MO denotes the broad-band filter in the MOST satellite, and Hp denotes the broad-band filter of the satellite Hipparcos.

Element	Unit	Value	
		Orbital properties	
P	(d)	7.14664±0.00010	
$T_{\rm min}$	(RJD)	56 224.72482±0.00022	
a	($R_\odot$)	25.552±0.097	
q		0.9439[1]	
e		0.0[1]	
i	(deg)	86.85±0.22	
ω	(deg)	90	
		Component properties	
Comp.		Aa	Ab
$T_{\rm eff}$	(K)	10 700[1]	10 450±150
$\Omega_{\rm K}$		15.97±0.25	15.93±0.32
$L_{\rm V}$		0.204±0.020	0.174±0.017
$L_{\rm B}$		0.196±0.021	0.165±0.018
$L_{\rm U}$		0.157±0.012	0.130±0.010
$L_{\rm MO}$		0.203±0.008	0.162±0.006
$L_{\rm Hp}$		0.212±0.023	0.180±0.020
		Passband luminosity of component B	
$L^B_{\rm V}$		0.622±0.060	
$L^B_{\rm B}$		0.639±0.069	
$L^B_{\rm U}$		0.713±0.071	
$L^B_{\rm MO}$		0.634±0.024	
$L^B_{\rm Hp}$		0.608±0.067	
$\chi^2_{\rm R}$		1.134	

Notes. [1] The parameter was kept fixed.

The last interval applies to each studied spectral filter (U, B, V, MOST). The parametric space was densely sampled with models during the fitting ($\approx 300\,000$ light curve models were computed). This showed that the relative luminosity of component B $L^{\rm B}$ is poorly constrained.

After a global minimum was found, we split our data and optimised the ephemeris, relative luminosity of component B, and surface potentials using only observations from the MOST satellite, after which we optimised the effective temperature of component Ab and the relative luminosity of component B using the Johnson UBV photometry. The epoch of the primary minimum was also fitted for the UBV dataset to slightly adapt it for the ETVs discussed in Sect. 4.3.

The parameters corresponding to the best-fitting model are listed in Table 9. Our model is unable to account for either the rapid light oscillations or the ETVs; therefore we raised the uncertainty of observations from the MOST satellite to deal with the former ($\Delta m_{\rm MOST} = 0.006$ given by the sinusoidal fit). The uncertainties of parameters are estimated as 68 % confidence intervals computed from a scaled χ^2 (scaled to an ideal situation, where the $\chi^2_{\rm R} = 1$), although in this case the scaling was almost unnecessary, since the best solution has $\chi^2_{\rm R} = 1.134$.

5. Astrometry of orbit 3

We used the existing astrometric positions listed in the WDS catalogue (see Mason et al. 1999, and references therein) to improve the orbital elements of orbit 3 published by Rica Romero (2010).

Table 10. Orbital elements of orbit 3 based on a fit to astrometric measurements published in WDS. The listed parameters are the orbital period P, the periastron epoch $T_{\rm p}$, the eccentricity e, the semi-major axis a, the inclination i, the argument of the periastron ω, and the position angle of the nodal line Ω.

Element	Unit	Value
P	(yr)	51.01±0.78
$T_{\rm p}$	(RJD)	54 615±251
e		0.5728±0.0028
a	(mas)	441.5±2.4
i	(deg)	25.4[1]±7.7
ω	(deg)	10.6±8.9
Ω	(deg)	106.4±2.2

Notes. [1] The inclination is determined ambiguously. A solution with $i = -25.4$ deg has exactly the same χ^2.

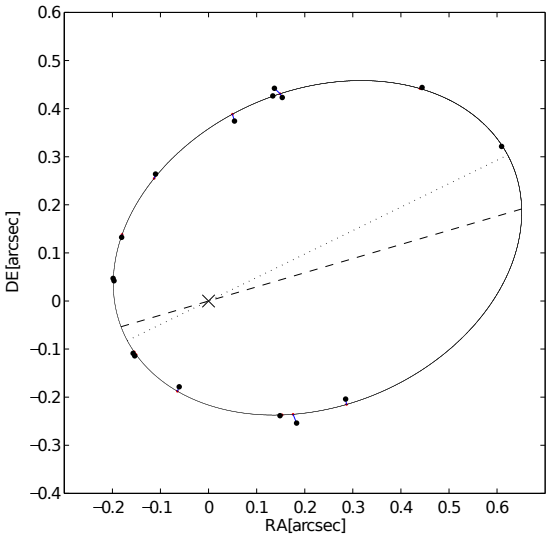

Fig. 8. Speckle-interferometric outer orbit 3 corresponding to the solution of Table 10. The dotted line stands for the line of apsides, the dashed line for the line of nodes.

The solution was carried out with the help of the program written by PZ (see Zasche & Wolf 2007, and references therein). The solution is listed in Table 10 and the orbit is shown in Fig. 8.

6. Spectro-interferometry

In this section we present an orbital analytic model of the ξ Tau system, which we fit to spectro-interferometric observations to estimate orbital elements, radii, and fractional luminosities of ξ Tau.

6.1. Global model for all available spectro-interferometric observations

The calibrated visibilities from VEGA/CHARA were fitted night by night with a model consisting of three uniform disks using the tool LitPro[5] (Tallon-Bosc et al. 2008). The observations obtained

[5] LITpro software available at `http://www.jmmc.fr/litpro`

during each single night were not numerous enough to safely estimate the positions and radii of components Aa, Ab, and B on the celestial sphere. In contrast to this, the NPOI observations are numerous enough to provide good estimates of the relative position of component B and the photocentre of the eclipsing binary for each night. They are presented in Table C.1 along with details on their acquisition (see Appendix C).

To circumvent the problem, we created a global orbital model that computes instantaneous positions of components B, Aa, and Ab with the following formulæ:

$$\alpha_i(t) = \arctan\left(\tan\left(v_i(t)+\omega_i(t)\right)\cos i_i\right)+\Omega_i, \quad (5)$$

$$\rho_i(t) = a_i\frac{1-e_i^2}{1+e_i\cos v_i(t)}\frac{\cos\left(\omega_i(t)+v_i(t)\right)}{\cos\left(\alpha_i(t)-\Omega_i\right)}, \quad (6)$$

$$x_i = \rho_i\sin\alpha_i, \quad (7)$$

$$y_i = \rho_i\cos\alpha_i, \quad (8)$$

where index i denotes the component of a binary, v is the true anomaly, ω the argument of periastron, i the orbital inclination with respect to the celestial sphere, Ω is the position angle of the nodal line, a the angular semimajor axis, and e the eccentricity. The position angle α_i is measured counter-clockwise from the north, ρ_i is the angular separation of a component, and the centre of mass, (x_i, y_i) is the same in Cartesian coordinates. The instantaneous value of the argument of periastron is given as follows: $\omega(t) = \omega_0 + \dot{\omega}\,(t - T_\mathrm{p})$, where T_p is the reference periastron epoch and ω_0 is the value of the periastron argument at the reference epoch. Instead of computing the semi-major axis for each component of a binary, the semi-major axis a and the mass ratio $q = M_1/M_2$ were used; the semi-major axes of primary and secondary can be computed with the following formulæ: $a_1 = aq/\,(1+q)$, $a_2 = a/\,(1+q)$. The periastron argument of the secondary is $\omega_2 = \omega_1 + \pi$.

In our application of Eqs. (5) – (8) component B is fixed at the beginning of the coordinate system because the observations are only sensitive to relative positions of the stars, not to the system as whole.

When the positions of all three components are known, objects representing each component can be placed at these positions. The uniform disk was chosen because all three components are detached and therefore only minor departures from spherical symmetry can be expected. The squared visibility V^2 and closure phase $T_3\phi$ for such a model can be computed analytically with the following formulæ:

$$|V_{\mathrm{S},k}(\mathbf{f})|^2 = \left|\frac{\sum_{j=1}^{N} L_{j,k}\frac{2J_1(\pi\theta_j B/\lambda_k)}{\pi\theta_j B/\lambda_k}e^{-2\pi i(\mathbf{f}\cdot\mathbf{r})}}{\sum_{j=1}^{N} L_{j,k}}\right|^2, \quad (9)$$

$$T_3\phi_{\mathrm{S},k}(\mathbf{f}_1,\mathbf{f}_2) = \arg\left[V_{\mathrm{S},k}(\mathbf{f}_1)V_{\mathrm{S},k}(\mathbf{f}_2)V_{\mathrm{S},k}(-\mathbf{f}_1-\mathbf{f}_2)\right], \quad (10)$$

where index j denotes a component of the triple system, k the spectral band, V the visibility, $\mathbf{f} = (u, v)$ the spatial frequency, L the luminosity fraction, B the length of the baseline, θ the diameter of the uniform disk, λ the effective wavelength (the central wavelength of the spectral band), J_1 the first-order Bessel function, $\mathbf{r} = (x_j, y_j)$ the Cartesian coordinates of a component computed with Eqs. (5)–(8), and N the total number of components in the system. The uniform disk diameter θ is also a wavelength-dependent quantity, therefore a different radius should be derived for each spectral band. Nonetheless, the dependency is very weak (order of 10^{-3} for the whole wavelength span of our data).

6.2. Orbital solution for all available spectro-interferometric observations

The model given by Eqs. (5) – (10) was fitted to calibrated squared visibilities from all four instruments, that is, CHARA/VEGA, NPOI, MARK III, and VLTI/AMBER. The best-fit set of parameters was determined using the least-squares method, that is, by minimising the following χ^2:

$$\chi^2 = \sum_{k=1}^{N_\mathrm{F}}\sum_{j=1}^{N_\mathrm{V}}\left|\frac{|V_k|^2(\mathbf{f}_j)-|V_{\mathrm{S},k}|^2(\mathbf{f}_j)}{\sigma_k(\mathbf{f}_j)}\right|^2 + \sum_{k=1}^{N_\mathrm{F}}\sum_{j=1}^{N_\mathrm{T}}\left|\frac{T_3\phi_k(\mathbf{f}_{1,j},\mathbf{f}_{2,j})-T_3\phi_{\mathrm{S},k}(\mathbf{f}_{1,j},\mathbf{f}_{2,j})}{\sigma_k(\mathbf{f}_{1,j},\mathbf{f}_{2,j})}\right|^2 \quad (11)$$

where V^2 ($T_3\phi$) is the observed squared visibility (the observed closure phase), V_S^2 ($T_3\phi_\mathrm{S}$) the synthetic squared visibility computed with Eq. (9) (the synthetic closure phase, Eq. 10), $\mathbf{f} = (u, v)$ the spatial frequency, σ the standard deviation of an observation, N_V the total number of squared visibility observations, N_T the total number of closure phase observations, and N_F the total number of spectral bands.

The phase coverage of the inner and the outer orbits is good enough (see Fig. 1) to allow fitting of all orbital elements. Our strategy was to keep as many parameters free as possible, since this model is independent of those presented in Sects. 3 and 4. However, the angular size of the inner orbit is small and its ephemeris is obtained with greater precision by the photometry and spectroscopy. The eccentricity of orbit 1 was set to zero (see Table 5) because there were no signs of a significant eccentricity in previous analyses. A number of trial runs have shown that the inclination i_1 and the mass ratio q_1 are poorly constrained by the interferometric observations. If optimised, both converged to values not consistent with previous analyses ($i \approx 78 \pm 5$ deg, $q_1 = 0.8 \pm 0.10$). Investigation of χ^2 maps surrounding these values has shown large shallow valleys that spread up to regions with values consistent with photometric and spectroscopic models. To stay on the safe side, we fixed both parameters at values obtained from the spectroscopy and photometry because they were estimated with much higher precision.

The global minimum of Eq. (11) was determined with the differential evolution algorithm (Storn & Price 1997) and was locally optimised with the sequential least-squares routine (Kraft 1988). The parameters of the best-fitting model are listed in Table 11. A large portion of the parametric space was searched.[6] The initial parametric space was equally sampled with a population which consisted of 1 500 members. The population evolved until the mean energy of the population (i.e. the mean χ^2 divided by its standard deviation and multiplied by the tolerance) was greater than one. The tolerance was set to 10^{-3} and the procedure took from 50 to 100 iterations to finish.

The final reduced $\chi^2_\mathrm{R} \approx 5.806$ is much larger than 1 because the true uncertainty of the V^2 derived with the reduction pipeline is underestimated. The reason is that the high χ^2_R is given mainly by data that were acquired at low spatial resolution and are expected to be easiest to reduce. Another reason is that the angular slit width of all interferometric instruments is comparable to the angular separation of component C and the triple, meaning

[6] The investigated parametric space is given by the following ranges: $\theta_\mathrm{B} \in [0.0, 1.0]$ mas; $L_\mathrm{B} \in [0.4, 0.8]$; $L_\mathrm{Aa} \in [0.1, 0.3]$; $T_{\mathrm{p},2} \in [55\,600.0, 55\,620.0]$ RJD; $a_2 \in [13, 18]$ mas; $e_2 \in [0.1, 0.3]$; $i_2 \in [50, 130]$ deg; $\omega_2 \in [0, 180]$ deg; $\Omega_2 \in [0, 360]$ deg; $\dot{\omega}_2 \in [1.5, 4.0]$ deg yr^{-1}; $a_1 \in [1.0, 3.0]$ mas; $\Omega_1 \in [0, 360]$ deg.

that it cannot be guaranteed that it was recorded. The full amplitude of squared visibility variations caused by component C ranges from 0.035 in the V band to 0.050 in the K band. It introduces systematic errors that we cannot correct for. The last reason are imperfections of the model. We had to accept several simplifications to stabilise the fit. Uncertainties of the best-fit parameters were estimated at 68 % confidence intervals from the $\chi^2_{\rm R}$ scaled to one.

Several attempts have shown that we are insensitive to the diameters of components Aa and Ab, because we lack enough observations at very long baselines (reaching up to 300 m). If they were set free, the solution would converge to unrealistic values ($\gtrsim 1.0$ mas), therefore they had to be fixed at values given by the parallax of the system and the light-curve solution (see Table 9). Convergence of the orbital parameters of orbit 1 was in general slow because the bulk of observations (NPOI, AMBER) was taken at low spatial resolution, at which this orbit is almost mainly on observations from VEGA/CHARA.

Our model allows fitting separate sets of relative luminosities $L_{\rm R}$ for each passband because the visibilities were estimated in narrow passbands: four for CHARA/VEGA, sixteen for NPOI, and ≈ 40 for VLTI/AMBER. It was not possible to divide the data into a larger number of small groups and to densely sample the relative luminosity of components Aa, Ab, and B as a function of the wavelength. After a set of trial attempts, we split the data into two subsets: visible (MARKIII, NPOI, CHARA/VEGA) and infrared (AMBER). This sampling is justified by the very low variability of the luminosity ratios with wavelength of all stars within the visible and infrared regions, which we checked using synthetic spectra from the PHOENIX grid (Husser et al. 2013). The relative luminosities of components Aa and Ab did not converge to plausible values for the infrared subset (it generally predicted a too low luminosity ratio between the two components of orbit 1), therefore we decided to use the estimate based on the PHOENIX grid and radii obtained from the light-curve analysis for components Aa and Ab, and the radius of component B was taken from Harmanec (1988).

The best-fit set of parameters is listed in Table 11 and a plot of the model vs. the observations is shown in Figs. C.1 – C.10. The model qualitatively fits the variations of the V^2 (i.e. the curvature of the model data agrees with the curvature of the observed V^2) for all spectro-interferometric data very well.

7. Summary of analyses based on simple analytic models

Here we critically compare the results of individual observational methods and derive the properties of the system.

7.1. Performance of different observational methods

Despite the subtitle, the individual models we used to evaluate different observational methods were not completely independent because the results from one method often served as a starting point for another. In some cases it was mandatory to take a parameter value from another model to stabilise the convergence to a steady solution. In the following paragraphs we discuss the outcome of different methods and their accuracy. An overview of all fitted parameters is given in Table 12 obtained through different methods (i.e. more values are given for some parameters). Corresponding properties of the orbits and stars are also listed. Orbital elements of orbit 3 are not listed because their properties were constrained only by astrometry, and they are presented separately in Table 10. The mass of component C is briefly discussed here.

- **The spectroscopic elements:** Elements (K, e, $T_{\rm p}$, P, ω, $\dot{\omega}$) of both orbits are estimated better from the fit of directly measured RVs with an analytic model (see Table 5, Eqs. 2 and 3). The spectral disentangling works with a much more complex model, and the resulting orbital elements depend on the shape of the separated profiles (and vice versa), which come out warped (the degree of the warp is shown by grey line in Fig A.1). The warp is most pronounced for component B, meaning that especially the mass ratio q_2 coming from the method cannot be trusted. On the other hand, the thin lines of components Aa and Ab constrain the RVs very well even if the separated spectrum is not perfect, and for the remaining orbital parameters the disentangling therefore provides values that agree with the fit of directly measured RVs.
- **The ephemeris of orbit 1:** The photometric solution presented in Table 9 yields the best ephemeris ($T_{\rm min,1}$, P_1) of orbit 1 especially thanks to high-precision observations from the satellite MOST. The ephemeris for orbit 1 estimated from the RVs does not agree within uncertainties with the photometric one. It can be caused by the lower precision of RV measurements around eclipses.
- **The eccentricity of orbit 1:** It was set to zero throughout the analyses because the precision of data does not allow a reliable determination. The analysis of the light curve from the satellite MOST shows a hint of a small eccentricity, but the relative position of minima is also affected by ETVs, and we are unable to discern one from the other with the analytic models. The dynamics of the system (see Sects. 8 and 9) shows that the eccentricity should oscillate with an amplitude $\Delta e \approx 0.01$. This introduces a jitter of the relative position of the primary and secondary minimum and increases uncertainty of the radii when a circular model is applied.
- **The inclination of orbit 1:** It is determined accurately using the light-curve analysis presented in Table 9. The value obtained from the interferometric model suffers from large uncertainty and is about 10 deg off the photometric solution. This is probably caused by the low number of observations at high spatial frequencies and the calibration systematic errors, which are likely more pronounced for high-frequency data.
- **The longitude of the ascending node:** The longitude of the ascending node of orbit 1 has a mirror solution $\Omega_1 = \Omega_1 + 180$ deg with (almost) the same value of the $\chi^2_{\rm R}$, while the Ω_2 is determined uniquely because the NPOI instrument acquired a large number of closure phase measurements. This means that it is not possible to say whether the motion of orbit 1 relative to orbit 2 is prograde or retrograde based solely on the spectro-interferometric data.
- **The relative luminosities:** They were determined from the light-curve solution, the comparison of synthetic and observed spectra, and from the interferometric solution.
  - The light-curve solution best describes their variations with the wavelength, but the values suffer from large uncertainties because of correlations between the fitted parameters.
  - The fit of synthetic spectra to observed ones is quite insensitive to relative luminosities, but this is the case only because small parts of red spectra were fitted that contain only three weak spectral lines. The relative luminosities obtained in the regions around $H\gamma$ and $H\beta$ roughly agree

Table 11. Parameters corresponding to the best fit of all available interferometric observations with the model defined by Eqs. (5) – (10). θ denotes the angular (uniform-disk) diameter.

Elements	Units	Values		
		Component properties		
Component		B	Aa	Ab
θ	(mas)	0.407±0.031	0.252[1,2]	0.231[1,2]
$L_{\rm R}^{\Delta\lambda_1}$		0.6373±0.0085	0.197±0.014	0.166±0.016
$L_{\rm R}^{\Delta\lambda_2}$		0.60[1]	0.22[1]	0.18[1]
		Orbital properties		
Orbit		2		1
$P_{\rm AN}$	(d)	145.471±0.045		–
$P_{\rm S}$	(d)	145.150±0.061		7.14664[1]
$T_{\rm p}$	(RJD)	55 609.36±0.64		–
$T_{\rm min}$		–		56 224.7248[1]
a	(mas)	15.93±0.070		1.89±0.11
e		0.212±0.0040		0.0[1]
q		–		0.945[1]
i	(deg)	86.67±0.12		86.85[1]
ω	(deg)	8.4±1.6		90.0[1]
Ω	(deg)	148.453±0.066		148.435[3]±1.9
$\dot{\omega}$	(deg yr^{-1})	2.02±0.31		0.0[1]
$\chi^2_{\rm R}$		5.806		

Notes. [1]The parameter was kept fixed. [2]Estimated from the solution from Table 9 and the Hipparcos parallax. [3]A solution shifted by 180 deg is also possible and has an identical reduced $\chi^2_{\rm R}$. $\Delta\lambda_1 = [500, 800]$ nm, and $\Delta\lambda_2 = [1200, 2410]$ nm.

with the values obtained for the B band from the light-curve solution.

- The bulk of the interferometric observations falls somewhere between the V and R bands. Therefore the relative luminosities detected with the spectro-interferometry are close to the V -band value obtained from the light-curve solution. We were not able to obtain plausible estimates of relative luminosities for the infrared subset (AMBER) because the observations have low spatial resolution and do not resolve the eclipsing binary well.

– **The effective temperatures:** They are given better by the fits of observed spectra to synthetic ones because the fitted regions contain many spectral lines (especially the region $\Delta\lambda = [4280, 4495]$ Å) where the photometry relies on four broad-band filters alone. In addition, Prša & Zwitter (2006) stated that it is not possible to obtain accurate effective temperatures of the two components of an eclipsing binary from the light-curve solution unless the colour-constraining method (described by them) is employed. According to the authors, the problem is even more pronounced when the two components are alike. Therefore we fixed the primary temperature and only optimised the secondary temperature. The result agrees with that obtained from the comparison of observed and synthetic profiles within the respective errors. The spectral types corresponding to these temperatures are B9 for components Aa and Ab and B5-6 for component B.

– **The semi-major axes and masses:** The physical size of the semi-major axes derived from the spectro-interferometry and the Hipparcos parallax (orbits 1 and 2) and those derived from the spectroscopy and photometry (orbit 1) and spectroscopy and spectro-interferometry (orbit 2) agree with each other within their uncertainties. The same applies to masses, which seem to fall within the limits of normal main-sequence (MS hereafter) masses corresponding to the respective spectral types (Harmanec 1988) – $m^{\rm Aa} = 2.25 \pm 0.03 \in [1.71, 2.41]\,{\rm M}_\odot$, $m^{\rm Ab} = 2.13 \pm 0.03 \in [1.71, 2.41]\,{\rm M}_\odot$, $m^{\rm B} = 3.89 \pm 0.25 \in [3.63, 4.6]\,{\rm M}_\odot$.

– **The total mass of the system and mass of component C:** Using the parallax $\pi_{\rm a_2} = 14.96 \pm 0.51$ and the solution presented in Table 10, we can estimate the total mass of the system $m^{\rm Aa+Ab+B+C} = 9.88 \pm 1.06\,{\rm M}_\odot$. A comparison with the masses of the inner triple subsystem gives an estimate of the mass of component C $m^{\rm C} = 1.61 \pm 1.18\,{\rm M}_\odot$that agrees with early F-type or late A-type star.

– **The component radii:** All components seem to have normal radii for their respective spectral type (again checked against Harmanec 1988) — $R^{\rm Aa} = 1.70 \pm 0.04 \in [1.40, 2.06]\,{\rm R}_\odot$, $R^{\rm Ab} = 1.62 \pm 0.04 \in [1.40, 2.06]\,{\rm R}_\odot$, $R^{\rm B} = 2.8 \pm 0.3 \in [2.13, 2.85]\,{\rm R}_\odot$.

– **The dereddened colour index B-V:** These are derived with a high level of uncertainty because of the high uncertainty in the luminosity ratios in different bands and the uncertainty of bolometric magnitudes. We compared the dereddened colour indices against tables computed by Flower (1996),
$T^{\rm B}_{\rm teff,FLOWER}(-0.120) = 12\,370$ K,
$T^{\rm Aa}_{\rm teff,FLOWER}(-0.018) = 9\,810$ K, and
$T^{\rm Aa}_{\rm teff,FLOWER}(-0.015) = 9\,760$ K.
They very roughly agree with the values found by the comparison of the observed and synthetic spectra. The uncertainty bars of the colour indices are very generous and match a wide range of temperatures.

– **The distance:** The number of applied observational methods allows us to estimate the distance of ξ Tau from the ratio of the physical and angular size of the semimajor axes and from the distance modulus. The former seems to prefer parallax, which is slightly lower than the Hipparcos parallax (but still within error bars), the latter also places ξ Tau farther than the Hipparcos observations, but their uncertainties are large, meaning that they do not contradict the Hipparcos parallax. The parallax estimated from the ratio of the physical and an-

gular size of the semi-major axis of the outer orbit yields the most precise parallax, $\pi_{\rm a_2} = 14.96 \pm 0.51$ mas.

7.2. Conclusion of the analytic models

The spectroscopy, the photometry, and the interferometry were studied with traditional (semi-) analytic models. We found that results obtained from different methods are consistent with each other, although some of them give better estimates of a particular set of parameters than others. We took advantage of this differential sensitivity and compiled a resulting set of fundamental properties of the system.

During the analyses described in previous sections, we noted two effects that indicate the dynamical interaction in ξ Tau: the advance of the apsidal line of orbit 2, and the eclipse timing variations (ETVs) in system 1. The first effect was explicitly taken into account because omitting it would cause significant inconsistency between observations and model. The latter effect was almost overlooked if it had not been for the indication in the very accurate photometric data from the MOST satellite. However, the analytic models above give only limited insights into dynamical effects in a four-body system such as ξ Tau. Nonetheless, they provide very good results that are also needed as a starting point for a more sophisticated solution based on an approach that includes dynamical evolution in a more complete way. We proceed in two steps.

In Sect. 8 we develop a numerical model that consistently takes into account the gravitational interaction of all stars in the ξ Tau . We use a fully numerical implementation, basically a standard N-body integrator, which we extend by subroutines that allow us to model several types of observables relevant for the ξ Tau dataset.

Next, in Sect. 9 we summarise relevant analytic formulæ obtained by methods of perturbation theory, which provide insights into results from the fully numerical approach in Sect. 8. Despite their limitations, we find the analytic formulation of the most important orbital perturbations useful. It does not only allow us to understand basic features in the numerical integrations, but also readily provides the parametric dependencies.

8. N-body model of ξ Tauri with mutual interactions

The quadruple nature of ξ Tauri and its relatively compact packing require us to proceed with an advanced N-body model that can account for mutual gravitational interactions of all four components. To this point, we now describe our numerical integrator, a definition of a suitable χ^2 metric, and the overall results of our fitting procedure.

8.1. Numerical integrator and χ^2 metric

We use a standard Bulirsch–Stoer N-body numerical integrator from the SWIFT package (Levison & Duncan 2013). Our method is quite general. We can model classical Keplerian orbits, of course, but also non-Keplerian orbits (involving N-body interactions). We treat all stars as point masses only, however. We have no higher-order gravitational terms and no tides in our model.

As explained below, this is a significant improvement of our previous application in Brož et al. (2010) because we can now account not only for the light-time effect, but for complete eclipse timing variations (ETVs) of the inner binary that arise from both direct and indirect gravitational perturbations. At the same time, we do not use the simplification of Brož et al. (2010) and consider all the components separately because the equivalent gravitational moment

$$J_2 \simeq \frac{1}{2}\left(\frac{a_1}{r}\right)^2 \frac{m^{\rm Aa} m^{\rm Ab}}{(m^{\rm Aa}+m^{\rm Ab})^2} \simeq 2\times 10^{-3} \tag{12}$$

of the inner eclipsing binary Aa+Ab is large at the distance of the component B.

We used five different coordinate systems: (i) Aa-centric (to generally specify initial conditions and eclipse detection), (ii) barycentric (for the numerical integration itself), (iii) Aa+Ab photocentric (to compare with interferometric observations of component B), (iv) Aa+Ab+B photocentric (ditto for component C), and (v) Jacobian (to compute hierarchical orbital elements).

Initial conditions at a given epoch T_0 can be specified either in Cartesian coordinates with x, y in the sky plane and z in the radial direction, or in osculating orbital elements. This very choice has a substantial role because the outcome of the fitting procedure will be generally (slightly) different. The orbital elements can be considered less strongly correlated quantities than Aa-centric Cartesian coordinates.

We accounted for as many observational data as possible using the following joint metric:[7]

$$\chi^2 = \chi^2_{\rm rv} + \chi^2_{\rm etv} + \chi^2_{\rm edv} + \chi^2_{\rm sky}\,, \tag{13}$$

$$\chi^2_{\rm rv} = \sum_{j=1}^{4}\sum_{i=1}^{N_{{\rm rv}\,j}} \frac{\left(v'_{{\rm zb}\,ji} + \gamma - v_{{\rm rad}\,ji}\right)^2}{\sigma^2_{{\rm rv}\,ji}}\,, \tag{14}$$

$$\chi^2_{\rm etv} = \sum_{i=1}^{N_{\rm etv}} \frac{\left(t'_{{\rm A}i} - t_{{\rm A}i}\right)^2}{\sigma^2_{{\rm etv}\,i}}\,, \tag{15}$$

$$\chi^2_{\rm edv} = \sum_{i=1}^{N_{\rm edv}} \frac{\left(\epsilon'_{{\rm A}i} - \epsilon_{{\rm A}i}\right)^2}{\sigma^2_{{\rm edv}\,i}}\,, \tag{16}$$

$$(\Delta x_{ji}, \Delta y_{ji}) = \mathbf{R}\left(-\phi_{\rm ellipse} - \frac{\pi}{2}\right) \times \begin{pmatrix} x'_{{\rm p}\,ji} - x_{{\rm p}\,ji} \\ y'_{{\rm p}\,ji} - y_{{\rm p}\,ji} \end{pmatrix}\,, \tag{17}$$

$$\chi^2_{\rm sky} = \sum_{j=3}^{4}\sum_{i=1}^{N_{{\rm sky}\,j}} \left\{ \frac{(\Delta x_{ji})^2}{\sigma^2_{{\rm sky\,major}ji}} + \frac{(\Delta y_{ji})^2}{\sigma^2_{{\rm sky\,minor}ji}} \right\}\,, \tag{18}$$

where the notation is briefly described in Table 13. The dashed quantities are the model values linearly interpolated to the exact times t_i of observations. The index j goes over the list of components Aa, Ab, B, C (i.e. $j = 1 =$ Aa, ...), while the index i corresponds to the observational data.

In our N-body model we do not fit the observed spectra using synthetic ones, individual light curve points, or interferometric fringes. We use higher-level observational data instead that were reduced and derived in previous sections. Hence we fit RV measurements for the three components Aa, Ab, and B, altogether $N_{\rm rv} = 843$, minima timings for the eclipses in the inner binary (Aa+Ab), $N_{\rm etv} = 35$, and astrometric observations for components B and C, $N_{\rm sky} = 49$. The latter is a subset of measurements from NPOI and WDS, for which it was possible to convert fringe visibilities (averaged over one night) into distance–angle

[7] The program used for these computations, including sources and all input data, is available at `http://sirrah.troja.mff.cuni.cz/~mira/xitau/`.

Table 13. Notation used for various coordinates, velocities, and uncertainties that we used in our N-body model.

x, y, z	Aa-centric coordinates
v_x, v_y, v_z	Aa-centric velocities
$x_{\rm pB}, y_{\rm pB}$	Aa+Ab photocentric sky-plane coordinates (of component B)
$x_{\rm pC}, y_{\rm pC}$	Aa+Ab+B photocentric coordinates (of component C)
$v_{z\rm b}$	barycentric radial velocity
γ	systemic velocity
$v_{\rm rad}$	observed radial velocity
$t_{\rm A}$	mid-epoch of an eclipse of the Aa+Ab pair
$\epsilon_{\rm A}$	eclipse duration
$\sigma_{\rm rv}$	uncertainty of the radial velocity
$\sigma_{\rm etv}$	uncertainty of the eclipse mid-epoch timing
$\sigma_{\rm edv}$	uncertainty of the eclipse duration
$\sigma_{\rm sky\,major,\,minor}$	uncertainty of the astrometric position, angular sizes of the uncertainty ellipse
$\phi_{\rm ellipse}$	position angle of the ellipse
$\mathbf{R}(\dots)$	the corresponding 2×2 rotation matrix

values. The individual uncertainties of the observations used in this section were modified as follows: $\sigma_{\rm rv} \geq 2\,{\rm km\,s^{-1}}$ due to calibration uncertainties, $\sigma_{\rm etv} \geq 0.001\,{\rm d} = 1.5\,{\rm min}$ because the quasi-periodic oscillations visible in the MOST light curve shift minima timings in a random fashion, and $\sigma_{\rm sky} = 3\,{\rm mas}$ (as in Tokovinin et al. 2015) or $5\,{\rm mas}$ if not reported in WDS.

We assumed the nominal distance $d = 64.1\,{\rm pc}$ for ξ Tau. The stellar radii for an eclipse detection were $R^{\rm Aa} = 1.700\,R_\odot$ and $R^{\rm Ab} = 1.612\,R_\odot$, in agreement with the photometric inversion. The expected correlation among $R^{\rm Aa}$, $R^{\rm Ab}$, eclipse depth, eclipse duration and third light contribution is removed to some extent through spectroscopic observations (cf. Table 9).

The synthetic minimum distance Δ' between components Aa and Ab in the sky plane was determined analytically as the distance of the piece-wise straight line $(x_{\rm Ab}, y_{\rm Ab})$ from the origin in the Aa-centric coordinates, as provided by the numerical integration. The condition for an eclipse is then $\Delta' \leq R^{\rm Aa} + R^{\rm Ab}$ and the corresponding time $t'_{\rm A}$ is linearly interpolated from neighbouring points. The eclipse duration is then given by a simple geometry, $\epsilon'_{\rm A} = 2\sqrt{(R^{\rm Aa} + R^{\rm Ab})^2 - \Delta'^2}/\bar{v}$, where $\bar{v}$ denotes the average velocity between the points. We thus straightforwardly account for disappearing eclipses and their durations, but we do not model (possible) eclipse depth variations at this stage.

To remove minor systematics in minima timings and eclipse duration, we attempted to suppress quasi-periodic oscillations visible in the MOST light curve by subtracting a function of the following form:

$$f(t) = C_0 + C_1(t - T_1) - [A_0 + A_1(t - T_1)] \sin\left[\frac{2\pi(t - T_1)}{P_0 + P_1(t - T_1)}\right]. \quad (19)$$

Its coefficients $(C_0, C_1, T_1, A_0, A_1, P_0, P_1)$ were always determined by a local fit in the surroundings of the given minimum. The resulting data are reported in Table 14.

The relative luminosities for photocentre computations were set to $L^{\rm Aa} = 0.204$, $L^{\rm Ab} = 0.174$, and $L^{\rm B} = 0.622$, again in agreement with photometric observations.

Mass constraints also arise from the spectroscopic classification of the ξ Tau components (A9 V, A9 V, B5 V, and F V). We

Table 14. Subset of minima timings $t_{\rm A}$ and eclipse durations $\epsilon_{\rm A}$ determined from MOST light curves, which were corrected for quasi-periodic oscillations by means of Eq. (19), and corresponding uncertainties $\sigma_{\rm etv}$ and $\sigma_{\rm edv}$.

$t_{\rm A}$ RJD	$\sigma_{\rm etv}$ day	$\epsilon_{\rm A}$ day	$\sigma_{\rm edv}$ day
56 224.7242	0.0010	0.2656	0.0069
56 228.3017	0.0012	0.2611	0.0035
56 231.8686	0.0010	0.2678	0.0069
56 235.4452	0.0010	0.2573	0.0035

can easily enforce reasonable limits for the component masses with the following artificial term:

$$\chi^2_{\rm mass} = \sum_{j=1}^{4} \left[\left(m_j - \frac{m_{j\,\rm min} + m_{j\,\rm max}}{2}\right) \frac{2}{m_{j\,\rm max} - m_{j\,\rm min}}\right]^{100}, \quad (20)$$

where we used $m^{\rm Aa}$ and $m^{\rm Ab} \in (0.9, 3.0)\,M_\odot$, $m^{\rm B} \in (3.5, 3.9)\,M_\odot$, $m^{\rm C} \in (0.9, 2.0)\,M_\odot$ as the limits; the exponent is rather arbitrary.

The integrator and its internal time step were controlled by the parameter $\epsilon_{\rm BS} = 10^{-8}$ (unitless), which ensures a sufficient accuracy. The integration time span was 1 000 d forward and 11 000 d backward, and the output timestep $\Delta t = 0.5\,{\rm d}$ for initial runs. We verified that this sampling is sufficient even for the trajectory with the strongest curvature and all necessary interpolations to the times of observations. For the final optimisation we decreased the value further to $\Delta t = 0.1\,{\rm d}$ to suppress interpolation errors.

We used a standard simplex algorithm (Press et al. 1993) to search for local minima of χ^2. We have 23 potentially free parameters, masses m_j, coordinates x_j, y_j, z_j, velocities v_{xj}, v_{yj}, v_{zj} in the Aa-centric frame, or, alternatively, masses m_j and three sets of orbital elements $a_j, e_j, I_j, \Omega_j, \omega_j, M_j$ in Jacobian coordinates, and the systemic velocity γ. The convergence tolerance for χ^2 was set to $\epsilon_{\rm tol} = 10^{-6}$, and the maximum number of iterations to 10 000 or to as low as 300 for extended surveys of the parameter space. We verified that this low number is sufficient to quickly detect local minima or to exclude their existence.

The initial epoch $T_0 = 2\,456\,224.724705$ is very close to the first precise minimum of the MOST light curve. We can thus (almost) fix $x_{\rm Ab} \simeq y_{\rm Ab} = 0$. At the same time, it is possible to (approximately) fix positions $x_{\rm pB}, y_{\rm pB}$ and $x_{\rm pC}, y_{\rm pC}$, derived by interferometry for an epoch close to T_0.

8.2. Resulting best fits

As expected, the 23-dimensional parameter space is vast and full of local minima, even at high χ^2. We proceeded sequentially to avoid complications and used a set with 2012 data only, a set with data from 2011–2013, and one set with all observational data. Next we performed a survey of the parameter space (to ensure we did not miss an obvious global minimum), an optimisation of individual orbits (2 and 3), the mutual inclination of orbits 1 and 2, and then we switched from Cartesian coordinates to orbital elements. Finally, we let all parameters be free. The optimisation means that we started the simplex from scratch many times (with different initialisation) and let it converge (for a limited number of iterations). Our largest survey consisted of

10^5 simplex runs, 300 steps each, that is, 3×10^7 models in total, so that we are confident that there is no other hidden minimum, at least within the ranges searched so far.[8]

We are aware of three mirror solutions (and 2^3 combinations), namely the inner binary can orbit in a retrograde or prograde sense with respect to orbit 2, so that $i'_1 = 180^\circ - i_1$. Moreover, its node can be shifted by 180°, $\Omega'_1 = \Omega_1 + 180^\circ$. Last but not least, orbit 3 can have the opposite inclination, $i'_3 = -i_3$ (we have no direct RV measurements). These ambiguities are discussed and partly resolved in the following paragraphs.

Our best fit is presented in Fig. 9 and Table 15. We note that this is not the only fit that seems reasonable; there are many more available in the surroundings. This can be partially seen in Fig. 10 where one-dimensional χ^2 maps exhibit relatively broad minima for the plotted parameters. Consequently, if we were to use simplex within these ranges, we would surely find a different minimum with slightly larger χ^2 (or even slightly smaller).

We clearly see that the value of $\chi^2 = 2\,578$ is still about three times higher than the number of degrees of freedom, $\nu = N_{\rm data} - M_{\rm free} = 931 - 23 = 908$, and formally speaking, we should be ready to admit that our model is plainly wrong. Nevertheless, the residua seem to be distributed normally, and realistic uncertainties (including some systematics) may be larger than expected. To obtain $\chi^2 \simeq \nu$ we would need measurement uncertainties as large as $\sigma_{\rm rv} \simeq 3.5\,{\rm km\,s^{-1}}$, $\sigma_{\rm etv} \simeq 10\,{\rm min}$, $\sigma_{\rm sky} \simeq 1\,{\rm mas}$ (for component B) or $10\,{\rm mas}$ (for component C). We consider these numbers to be quite realistic given the heterogeneous data set we have. Additional problems may contribute to the error budget, such as nightly and night-to-night variations of dispersion relations, unaccounted blending of spectral lines, systematics due to the normalisation procedure, or photocentre motions of the inner binary affecting astrometric positions.

8.3. Differences between traditional and N-body models

Most importantly, orbital elements do change in the course of time; especially $i_1, \Omega_1, \omega_1, \Omega_2, \omega_2$ seem to be critical in the case of ξ Tau (see Fig. 11). While the precession of ω_2 was accounted for, the remaining terms were not. The precession of nodes Ω_1, Ω_2 about the total angular momentum axis occurs with a ≈ 19 year period. In the Laplace plane, which is perpendicular to the total angular momentum, this would cause a circulation of Ω's from 0° to 360°, but we can only see an oscillation of at most 3.5° that is due to the purely geometrical projection to the plane of the sky. There are also inevitable coupled oscillations of inclinations, with i_1 ranging from 84.5° to 88.2°. All these rather expected secular effects are discussed in much more detail in Sect. 9.1.

Additionally, there are short-period oscillations not described by the secular theory. While $a_1$and a_2 only oscillate about constant mean values, there seems to be a mid-term evolution of both $e_1$and e_2, with amplitudes reaching 0.008, which is larger than the uncertainty of their initial values, that is, $e_2 = 0.1974^{+0.0009}_{-0.0010}$. In this particular case, this is related to the periastron passage of component C.

[8] The ranges expressed in Cartesian coordinates were $z_{\rm Ab} \in (-0.148, -0.088)\,{\rm au}$, $z_{\rm B} \in (-1.47, -0.87)\,{\rm au}$, $z_{\rm C} \in (-8.72, -2.72)\,{\rm au}$, $v_{x{\rm Ab}} \in (-0.092, -0.032)\,{\rm au\,d^{-1}}$, $v_{y{\rm Ab}} \in (0.050, 0.110)\,{\rm au\,d^{-1}}$, $v_{x{\rm B}} \in (-0.078, -0.018)\,{\rm au\,d^{-1}}$, $v_{y{\rm B}} \in (0.042, 0.102)\,{\rm au\,d^{-1}}$, $v_{z{\rm B}} \in (-0.022, 0.038)\,{\rm au\,d^{-1}}$, $v_{x{\rm C}} \in (-0.082, -0.022)\,{\rm au\,d^{-1}}$, $v_{y{\rm C}} \in (0.025, 0.085)\,{\rm au\,d^{-1}}$, and $v_{z{\rm C}} \in (-0.030, 0.030)\,{\rm au\,d^{-1}}$.

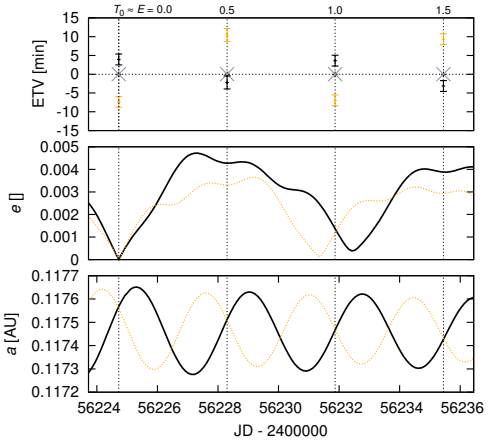

Fig. 12. Comparison of the osculating semi-major axis a_1 (bottom) and eccentricity e_1 evolution (middle) as computed by our N-body model for two mirror solutions with $\Omega_1 \simeq 331^\circ$ (bold solid) and $\Omega'_1 \simeq 151^\circ$ (red dashed). Only a short time span of 12 days is shown, close to the epoch T_0. The corresponding ETVs of minima observed by MOST are also shown at the top. The former solution $\Omega_1 \simeq 331^\circ$ has the corresponding $\chi^2_{\rm etv}$ (for all $N_{\rm etv} = 35$ measurements) significantly lower than the latter, 150 vs 390, so that we consider it as the preferred value.

We emphasise that it is absolutely necessary to use an N-body model (like ours), otherwise traditional methods assuming constant orbital elements (or precessing ωs only) may result in systematic discrepancies or artefacts. When the parameters reported in Table 15 are compared to those derived by classical models (Table 12), the general agreement between the elements is evident, but their uncertainty intervals do not always overlap. This is probably to be expected because we compare osculating (apples) and fixed orbital elements (oranges).

An outstanding example of how classical methods may fail is a detailed analysis of MOST light curves and the corresponding minima timings from 2012. At first, we thought that the uneven spacing of minima indicates a non-zero eccentricity of the inner orbit, $e_1 \simeq 0.002$. However, this is in stark contrast with past RV measurements, which constrain forcing of $e_1(t)$ due to perturbations by component B and require $e_1(t = T_0) \to 0$. Figure 12 shows upon close scrutiny that the oscillation of the semi-major axis a_1 has a period 3.76 days, which is half of the synodic period $P_{\rm syn1}$ of orbit 1, in a system that corotates with orbit 2. Moreover, its amplitude slightly decreases as component B moves farther away. These tiny perturbations are the real cause of the observed eclipse timing variations. They also allow us to discard mirror models with $\Omega'_1 \neq \Omega_2$ and prefer those with $\Omega_1 \simeq \Omega_2$ because the resulting $\chi^2_{\rm etv} = 390$ vs 150 is significantly different. Again, the eclipse variations are explained in more detail in Sect. 9.2.

8.4. Model with closure phases to resolve mirror solutions

The admissible solutions presented in Table 15 are degenerate in the sense that we cannot distinguish among several mirror models (in particular i'_1, i'_3). To resolve this degeneracy, we constructed an N-body model that accounts for interferometric visibilities and closure phases. The latter are especially suitable to

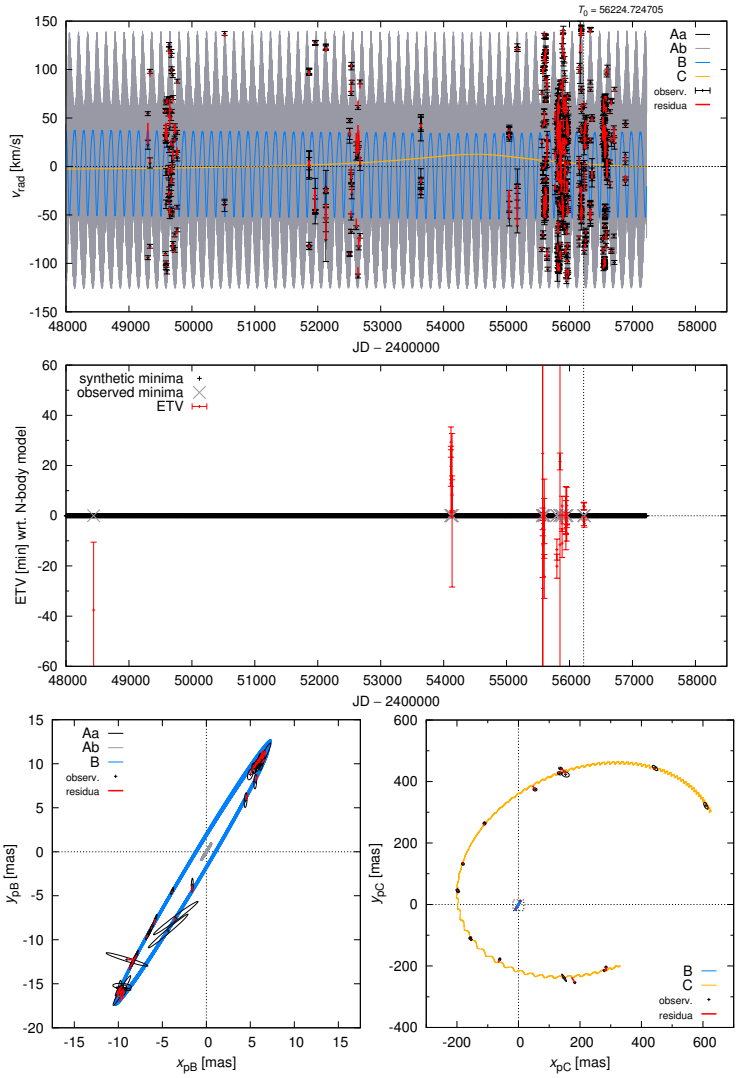

Fig. 9. One of the best-fit solutions for the ξ Tau system with our N-body model and using all available observational data. In this case, the resulting total χ^2 is 2 578, while the number of degrees of freedom $\nu = 908$. Top: Radial velocities v_{zbAa}, v_{zbAb}, v_{zbB}, v_{zbC} of the individual components; model values are denoted by lines (component Aa is black, not clearly visible, Ab grey, B blue, and C orange), observations by black error bars and residuals by thick red lines. Middle: $O - C$ values for both primary and secondary minima timings; model timings are denoted by black points (very densely packed), observations by grey crosses, and $O - C$ with its uncertainty by red error bars. Bottom left: Astrometric positions of component B based on NPOI interferometric observations; model orbit x_{pB}, y_{pB} with respect to photocentre Aa+Ab (i.e. not w.r.t. B, as usually) is again denoted by a blue line, observations by black error bars and residuals by thick red lines. The orbit is not a single ellipse, but rather a complex trajectory that quickly precesses and is moreover affected by (slight) photocentre motions. Bottom right: Similarly, astrometric positions of the distant component C x_{pC}, y_{pC} with respect to the Aa+Ab+B photocentre is denoted by an orange line. Component B is relatively luminous, which makes the orbit in these photocentric coordinates slightly jagged.

detect any asymmetries, while the former are necessary to correctly obtain (symmetric) angular positions and separations. (21)

In addition to Eqs. (14) to (18), we have a few more relations:

$$V'(u,v) = \frac{1}{L_{\mathrm{tot}}} \sum_{j=1}^{4} L_{ij}\, 2\frac{J_1\left(\pi\theta_j\sqrt{u^2+v^2}\right)}{\pi\theta_j\sqrt{u^2+v^2}}\, \mathrm{e}^{-2\pi\mathrm{i}(ux'_{\mathrm{a}j}+vy'_{\mathrm{a}j})}\,, \qquad L_{ij}(T_{\mathrm{eff}\,j}, R_j) \simeq \int_{\lambda_i-\Delta\lambda_i/2}^{\lambda_i+\Delta\lambda_i/2} 4\pi R_j^2\, \pi B_\lambda(T_{\mathrm{eff}\,j})\,\mathrm{d}\lambda\,, \tag{22}$$

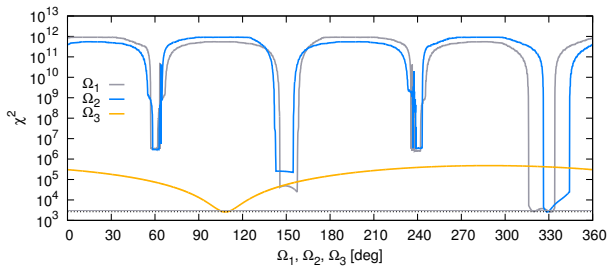

Fig. 10. Example of the one-dimensional χ^2 mapping used to derive uncertainties of orbital elements for the ξ Tau system. The dependencies of the χ^2 values on the three nodes Ω_1, Ω_2, Ω_3 are shown, while the remaining elements correspond to the best-fit values from Table 15. The preferred solution for $\Omega_1 \simeq 331°$, with $\chi^2 = 2\,578$, and a hint of a mirror solution at $\Omega_1 \simeq 151°$ are clearly visible. If the latter is optimised separately, we would obtain χ^2 as low as 2 749. The sudden increase of $\chi^2_{\rm etv}$ corresponds to the disappearance of the eclipses of the inner binary, which naturally results in extreme $O-C$'s.

Table 16. Notation used for additional coordinates and quantities needed in our extended N-body model.

$x_{\rm a}, y_{\rm a}$	Aa-centric angular coordinates
V	complex visibility; squared visibility is $\lvert V\rvert^2$
T_3	complex triple product; closure phase is $\arg T_3$
u, v	projected baselines (expressed in cycles, B/λ)
$\theta = \frac{2R}{d}$	angular diameter
d	distance to the system
$L, L_{\rm tot}$	component luminosity and the total luminosity
$T_{\rm eff}$	effective temperature
R	stellar radius (uniform disk)
λ, $\Delta\lambda$	effective wavelength and bandwidth
$B_\lambda(T)$	the Planck function
$\sigma_{\rm vis}$	uncertainty of the squared visibility
$\sigma_{\rm clo}$	uncertainty of the closure phase

$$\chi^2_{\rm vis} = \sum_{i=1}^{N_{\rm vis}} \frac{\left(|V'(u_i,v_i)|^2 - |V|^2_i\right)^2}{\sigma^2_{{\rm vis}\,i}}\,, \tag{23}$$

$$T'_3 = V'(u_1,v_1)V'(u_2,v_2)V'(-(u_1+u_2),-(v_1+v_2))\,, \tag{24}$$

$$\chi^2_{\rm clo} = \sum_{i=1}^{N_{\rm clo}} \frac{(\arg T'_3 - \arg T_{3i})^2}{\sigma^2_{{\rm clo}\,i}}\,, \tag{25}$$

with the notation described in Table 16. The complex visibilities V' and their triple products T'_3 were computed assuming uniform disks for individual components. Relative luminosities L_{ij} at a given effective wavelength λ were computed by a blackbody approximation.

This extended model minimises $\chi^2 = \chi^2_{\rm rv} + \chi^2_{\rm etv} + \chi^2_{\rm edv} + \chi^2_{\rm sky} + \chi^2_{\rm vis} + \chi^2_{\rm clo}$ and has nine additional free parameters: distance d to ξ Tau , uniform-disk radii R_j, and effective temperatures $T_{{\rm eff}\,j}$ of all the components, even though the contribution of component C is only minor (clearly lower than 10 % at the longest wavelength, $\lambda = 2.6\,\mu$m).

We used all observational data from the MARKIII, NPOI, CHARA/VEGA, and VLTI/AMBER spectro-interferometers, with $N_{\rm vis} = 17\,391$ measurements of the squared visibility $|V|^2$ and $N_{\rm clo} = 4\,856$ measurements of the closure phase $\arg T_3$ (from NPOI and VLTI/AMBER). The total number of degrees of freedom is thus $\nu = N_{\rm data} - M_{\rm free} = 28\,019 - 32 = 27\,987$. At the same time, we did not use astrometric positions ($\chi^2_{\rm sky}$) of component B because they are not independent; all the information should be contained in $|V|^2$ and $\arg T_3$ measurements.

Initially, we used nominal uncertainties and weights $w_{\rm vis} = 1$, $w_{\rm clo} = 1$, but the resulting $\chi^2_{\rm vis} + \chi^2_{\rm clo}$ value was too high ($\approx 10^5$), even for our best-fit models (cf. Fig. 13). The most likely reason is that we did not account properly for all calibration uncertainties. To resolve this problem, an internal re-calibration would be necessary. A possible explanation for the too high χ^2 has been given in Sect. 6. For example, CHARA/VEGA interferometry from Sep 29 2012 exhibits unrealistically quick changes of $|V|^2$ at an almost constant baseline $B/\lambda \simeq 1.3$ to 1.4×10^8 cycles (see Fig. C.8). In our case, we decreased the weight $w_{\rm vis} = 0.1$ to avoid it dominating other χ^2 contributions (e.g. eclipse timing variations).

We focused on a limited set of seven mirror models, always with one or two modified orbital elements (see Table 17). For each of them, we performed one simplex run, verified by simulated annealing with the initial temperature 100 000 kelvin, schedule $T^{i+1} = 0.99T^i$ and 100 iterations at given T^i, so that other free parameters were able to adapt themselves to a new situation, and we computed χ^2s that are reported in the same table. If the final value remains relatively high, it means the model is not compatible with the respective interferometric data.

Clearly, we are sufficiently sensitive to resolve Ω_2 and i_2, that is, the longitude of the ascending node and the inclination of component B (see Fig. 14), but not directly to resolve Ω_1, i_1, or i_3 elements. Consequently, we can discard Ω'_2, i'_2 and prefer $\Omega_2 \simeq 331°$, $i_2 \simeq 86°$ solution on the basis of the closure phase measurements alone.

Moreover, because our N-body model is constantly constrained by RV, ETV, ETD, and astrometric data, which prevent a convergence to unrealistic values of all the parameters, we can spot (in Table 17) that the squared visibility measurements are not compatible with Ω'_1 and i'_1, therefore they were discarded as well and the $\Omega_1 \simeq 329°$, $i_1 \simeq 86°$ solution was preferred.

Finally, as demonstrated in Sect. 8.3, the N-body dynamics and ETV measurements allow us to safely discard any $\Omega_1 \neq \Omega_2$, therefore we clearly prefer $\Omega_1 = 329°$. The only remaining ambiguity is thus the inclination i_3 vs i'_3. To conclude this section, a combination of approximately orthogonal measurements (RV, ETV, ETD, $|V|^2$, $\arg T_3$) leads to interesting and solid results, which is as expected.

We also comment on the fact that even this type of model may be insufficient. Other physical effects exist that we did not account for, such as tidal interactions of non-spherical stars, spin–orbital coupling, various magneto-hydrodynamic phenom-

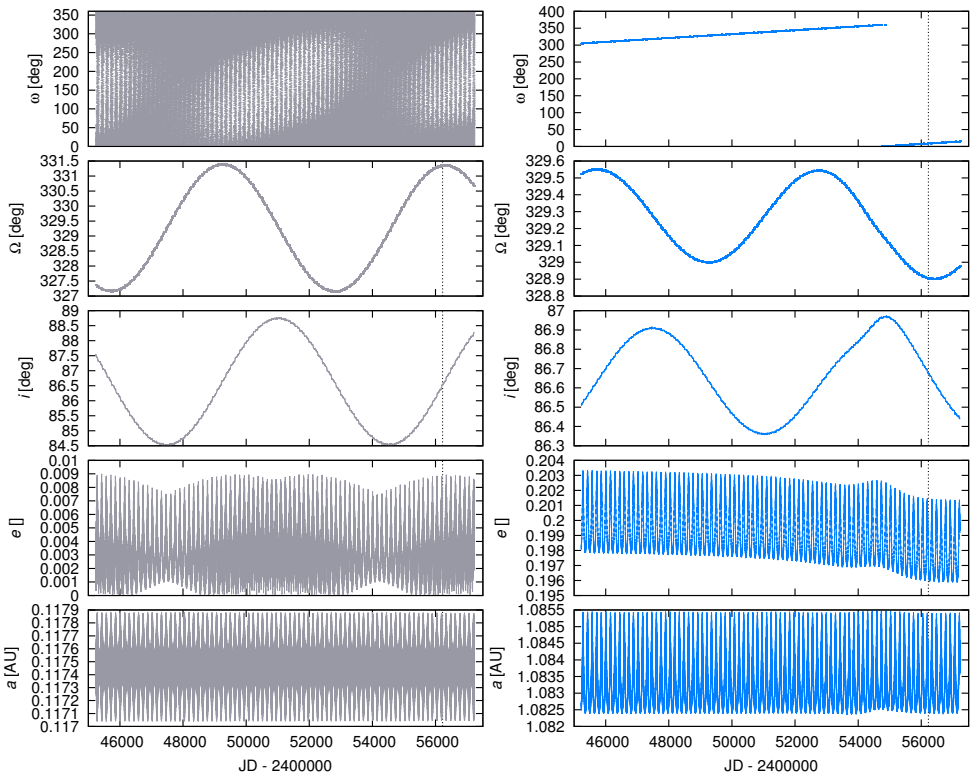

Fig. 11. Time evolution of the osculating orbital elements over a time span $-11\,000$ to $+1\,000$ days from the epoch $T_0 = 2\,456\,224.724705$, covered by observations of ξ Tau. Left: The semi-major axis a_1, eccentricity e_1, inclination i_1, longitude of ascending node Ω_1, and the argument of pericentre ω_1 (poorly defined because $e_1 \to 0$) of the inner, eclipsing binary orbit (components Aa and Ab). Right: The same parameters $a_2, e_2, i_2, \Omega_2, \omega_2$ for orbit 2 (i.e. components (Aa+Ab) and B). All these plots correspond to the simulation with $\chi^2 = 2\,578$, presented in Fig. 9. Variations in the inclination i_1 and argument of pericentre ω_2 are of major interest, since they result in observable effects. On the other hand, the distant orbit 3 (not shown here) exhibits only minor variations of its elements. The bump in the osculation elements of orbit 2 at JD $\approx 2\,455\,500$ is related to the passage of component C through its pericentre.

ena, or pulsations of (all) components. Their importance for the dynamics of ξ Tau is yet to be assessed.

9. Dynamical evolution of the Aa+Ab+B subsystem

The osculating orbital elements shown in Fig. 11 exhibit many variations over different timescales, from the short period of the inner eclipsing binary, to the intermediate period of the orbital motion of component B with respect to the eclipsing binary, up to long periods of tens to hundreds of years. Are we able to understand some of these terms, including their amplitude, and determine parametric dependencies on stellar masses and periods of orbits 1 and 2? To do so, we need to turn to perturbation theory. In this section we neglect dynamical effects of the distant component C and focus on the triple subsystem Aa+Ab+B.

The hierarchy of the ξ Tau system implies a preferential choice of Jacobi coordinates to describe its dynamics, in which on the one hand, $\mathbf{r}$ is the relative position of Ab with respect to Aa, and on the other, $\mathbf{R}$ is the relative position of component B with respect to the barycentre of orbit 1. The conjugate momenta involve reduced masses $m'_1 = m^{\mathrm{Aa}} m^{\mathrm{Ab}}/M^1$ and $m'_2 = m^{\mathrm{B}} M_1/M_2$ of orbits 1 and 2, with $M_1 = m^{\mathrm{Aa}} + m^{\mathrm{Ab}}$

Table 17. Summary of χ^2_{vis} and χ^2_{clo} values for squared visibility $|V|^2$ and closure phase $\arg T_3$ measurements. Only a limited set of mirror models is shown with respect to the nominal model ($\Omega_1 \simeq 331°$, $\Omega_2 \simeq 329°$, $\Omega_3 \simeq 110°$, $i_1 \simeq 86°$, $i_2 \simeq 86°$, $i_3 \simeq -24°$). The closure phase measurements allow us to discard four of them, namely those with Ω'_2 and i'_2, because the 3-σ level corresponds to a relative increase by 1.051, i.e. $\chi^2_{\mathrm{clo}} \simeq 24\,331$. Moreover, the $|V|^2$ measurements do not favour Ω'_1 and i'_1 (3σ is at 1.028, $\chi^2_{\mathrm{vis}} \simeq 137\,229$). The symbol × in the last column indicates we discard this possibility.

Orbital elements	χ^2_{vis}	χ^2_{clo}	Note
nominal	133 492	23 151	
$\Omega'_1 = \Omega_1 + 180° \simeq 151°$	**162 632**	23 053	×
$\Omega'_2 = \Omega_2 + 180° \simeq 149°$	355 456	**105 975**	×
(Ω'_1, Ω'_2)	322 079	**100 480**	×
$i'_1 = 180° - i_1 \simeq 94°$	**149 901**	24 683	×
$i'_2 = 180° - i_2 \simeq 94°$	734 267	**69 102**	×
$i'_3 = -i_3 \simeq 24°$	138 316	23 393	
(i'_1, i'_2)	755 013	**69 463**	×

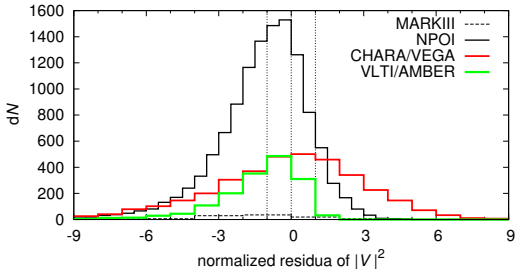

Fig. 13. Distributions of normalised residuals $(|V'|^2 - |V|_i^2)/\sigma_{\mathrm{vis}\,i}$ of the squared visibility for our best-fit model with $\chi^2_{\mathrm{vis}} = 133\,492$, while the total number of measurements is $N_{\mathrm{vis}} = 17\,391$. Four separate datasets are shown, corresponding to the MARKIII, NPOI, CHARA/VEGA, and VLTI/AMBER interferometers. The distributions are not perfectly symmetric about zero and for CHARA/VEGA data are significantly wider, probably due to unaccounted calibration uncertainties.

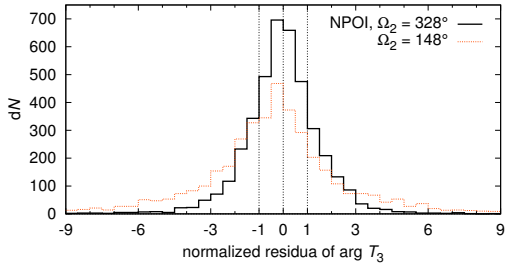

Fig. 14. Distributions of normalised residuals $(\arg T_3' - \arg T_{3i})/\sigma_{\mathrm{clo}\,i}$ of the closure phase measured with the NPOI instrument for two best-fit models with different values of the longitude of the ascending node $\Omega_2 = 329°$ and $\Omega_2' = 149°$. Both distributions seem symmetric about the origin, indicating there are no serious systematics in $\arg T_3$ measurements. However, the former distribution is substantially narrower than the latter, so that the mirror solution Ω_2' can be discarded.

and $M_2 = M_1 + m^{\mathrm{B}}$. To zero-order approximation, both systems evolve on Keplerian orbits, but their interaction introduces a perturbation that causes $\mathbf{r}$ and $\mathbf{R}$ to follow trajectories described by numerical integrations in Sect. 8 that are more complicated than Keplerian orbits. The elliptical approximation may be only applicable to a certain interval of time. The latter becomes short especially for compact systems. ξ Tau is a good representative of this class.

In the world of perturbation theory, both orbits 1 and 2 are represented by a set of osculating orbital elements that evolve in time as a result of their mutual interaction. From a plethora of perturbations described in this way, we recall two results relevant for the observed features of the ξ Tau system. We first describe the secular effects, whose duration is conveniently short for this compact system to be detected, and then some of the long- and short-period eclipse time variations in the eclipsing binary.

9.1. Secular effects

We define Delaunay momenta $L_1 = m_1'\sqrt{GM_1 a_1} = m_1' n_1 a_1^2$ and $L_1 = m_2'\sqrt{GM_2 a_2} = m_2' n_2 a_2^2$ of orbits 1 and 2 (e.g. Harrington 1968, 1969; Soderhjelm 1975; Breiter & Vokrouhlický 2015). Here n_1 and n_2 are the mean motion values of the orbits 1 and 2, both related to the semi-major axes a_1 and a_2 through the third Kepler law: $n_1^2 a_1^3 = GM_1$ and $n_2^2 a_2^3 = GM_2$ (G is the gravitational constant). In a secular approximation, when the orbital longitude for both orbits 1 and 2 is removed from the interaction (e.g. Harrington 1969; Breiter & Vokrouhlický 2015), the semi-major axes a_1 and a_2 are constant.

The dynamics of the Aa+Ab+B system may in principle be studied in an arbitrary reference frame. However, its description becomes very simple in a preferred frame that is often called Laplacian. The z-axis of this frame is aligned with the total orbital angular momentum of the system. To distinguish osculating orbital elements in the observer-oriented frame we used above, we denote the elements in the Laplacian frame with a tilde. For instance, the orbital inclinations for orbits 1 and 2 are denoted $\tilde{\imath}_1$ and $\tilde{\imath}_2$, and the corresponding longitudes of nodes $\tilde{\Omega}_1$ and $\tilde{\Omega}_2$.

The secular evolution of the triple system is particularly simple when three conditions are met: the eccentricity e_1 of the inner orbit is negligible, the mutual angle $\tilde{J} = \tilde{\imath}_1 + \tilde{\imath}_2$, of orbital planes 1 and 2 is small, and the system is wide enough, such that on the timescale of interest only the quadrupole interaction of the inner and outer orbits is relevant. The mutual angle $\tilde{J}$ can be determined by the orbital elements in the observer reference frame using

$$\cos\tilde{J} = \cos i_2 \cos i_1 + \sin i_2 \sin i_1 \cos(\Omega_1 - \Omega_2)\ . \tag{26}$$

These conditions fortunately currently apply to the ξ Tau system.We also note for the third condition that the octupole interaction is very small because of nearly equal masses in orbit 1, i.e., $m^{\mathrm{Aa}} \simeq m^{\mathrm{Ab}}$. The next secular contribution would arise from the non-linear quadrupole effect (e.g. Breiter & Vokrouhlický 2015), which is small on a timescale of some decades. Then, $e_1 = 0$ is a stable solution, and e_2 and $\tilde{J}$ are constant in time. When the orbital elements are referred to the invariable plane that is normal to the total angular momentum, the orbital inclinations $\tilde{\imath}_1$ and $\tilde{\imath}_2$ of orbits 1 and 2 are constant as well, and both orbital planes uniformly precess in the inertial space about the total angular momentum direction. Their nodes $\tilde{\Omega}_1 = \tilde{\Omega}$ and $\tilde{\Omega}_2 = \tilde{\Omega} + \pi$ linearly advance with a rate (e.g. Soderhjelm 1975; Breiter & Vokrouhlický 2015)

$$\frac{\dot{\tilde{\Omega}}}{n_2} \simeq \frac{3}{4\eta_2^3}\frac{m^{\mathrm{B}}}{M_2}\frac{n_2}{n_1}\cos\tilde{J}\sqrt{1+\gamma^2+2\gamma\cos\tilde{J}}, \tag{27}$$

where $\gamma = L_1/(L_2\eta_2)$ is the ratio of the angular momenta of the two orbits, and $\eta_2 = \sqrt{1-e_2^2}$. In triple systems the outer orbit typically has a dominant share of the total angular momentum of the system, thus $\gamma < 1$. For ξ Tau we have approximately $\gamma \simeq 0.132$. Unless precisely coplanar, the main effect of the orbital-plane precession is in periodic changes of inclinations i_1 and i_2 in the observer system. These variations directly affect magnitude depths of the eclipses, or might eventually cause the system to become non-eclipsing for a certain period of time.

In addition to the steady precession of the orbital planes, the second secular effect in the given setup consists of precession of the pericentre of the outer orbit. Denoting its longitude $\tilde{\varpi}_2$, we have

$$\frac{\dot{\tilde{\varpi}}_2}{n_2} \simeq \frac{3}{8\eta_2^3}\frac{m^{\mathrm{B}}}{M_2}\frac{n_2}{n_1}\gamma\left(3\cos^2\tilde{J} - 1 - \frac{\gamma\sin\tilde{J}\sin 2\tilde{J}}{1+\gamma\cos\tilde{J}+\sqrt{1+\gamma^2+2\gamma\cos\tilde{J}}}\right). \tag{28}$$

Comparing Eqs. (27) and (28), we note that the pericentre precession frequency of the outer orbit is slower by a factor $\simeq \gamma$ than the nodal frequency (assuming $\tilde{J}$ sufficiently small). Thus nodes and inclinations vary on shorter timescales than the argument of pericentre of orbit 2.

9.2. Long- and short-period eclipse variations

The mutual interaction of the orbits also results in a palette of periodic perturbations. So far, the long-period effects, namely those with a period P_2 of orbit 2, have been extensively studied (e.g. Soderhjelm 1975, 1982; Borkovits et al. 2003, 2011, 2015). We here focus on the ETVs, that is, on advances and delays $\delta t_{\rm LP}$ in epochs of eclipse of orbit 1 that are due to the variations in its mean motion n_1 caused by component B. Assuming for simplicity coplanar orbits $\tilde{J} = 0\,$deg, we obtain (e.g. Soderhjelm 1975; Borkovits et al. 2011, 2015; Rappaport et al. 2013, which also contain terms proportional to $\propto \tilde{J}^2$)

$$n_1 \delta t_{\rm LP} \simeq \frac{m^{\rm B}}{M_2} \frac{n_2}{n_1} W\left(e_2, \ell_2\right), \tag{29}$$

with

$$W\left(e_2, \ell_2\right) = f_2 - \ell_2 + e_2 \sin f_2, \tag{30}$$

where f_2 and ℓ_2 are the true and mean anomalies of orbit 2. For a low eccentricity e_2 we have $W \simeq 3 e_2 \sin \ell_2$. Obviously, the principal component of ETV in (29) becomes zero for a circular orbit 2 because it is related to variations of n_1 triggered by variations in the distance R to component B.

In the course of this work, we noted that dominant short-period effects may also be of interest (those with the period of the inner orbit 1), provided high-quality eclipse data are collected. Using methods of first-order perturbation theory, we found that the leading short-period term reads

$$n_1 \delta t_{\rm SP} \simeq \frac{21}{8} \frac{m^{\rm B}}{M_2} \left(\frac{n_2}{n_1}\right)^2 \left(\frac{a_2}{R}\right)^3 \sin 2\left(\lambda_1 - \tilde{F}_2\right), \tag{31}$$

where R is the distance of component B to the barycentre of the inner binary system, and $\tilde{F}_2 = \tilde{\varpi}_2 + f_2$ is its true orbital longitude. The term has a period equal to half the synodic period of the Aa+Ab system in a reference frame corotating with the motion of component B.

This effect is not primarily dependent of the eccentricity e_2 because it is triggered by variations in the mutual positions of components Aa and Ab with respect to component B. Its magnitude is smaller by a factor 0.4 at periastron and by 0.1 at apoastron of orbit 2. Nevertheless, the effect is not entirely negligible, and we found that it contributes to the observed eclipse shift in the MOST data (see Fig. 12).

9.3. Comparison of the secular theory with the results of the analytic and numerical models

Here we compare the apsidal motion detected with both analytic and numerical methods and additional secular and periodical variations of orbital elements predicted by the numerical model presented in Sect. 8

- **The apsidal motion of orbit 2:** First, we use results of the analytic theory above. Using nominal orbital parameters from Table 12, we obtain $\tilde{J} = 0.19 \pm 1.89\,$deg, and consequently $\dot{\omega}_2 = 2.185 \pm 0.045\,\mathrm{deg\,yr^{-1}}$. We note that $\dot{\omega}_2$ may be directly obtained from Eq. (28) because the nodal longitude Ω_2 in the observer frame oscillates without any secular drift. This is about a third lower than the value detected with the analytic RV curve model (see Table 5), but in excellent agreement with the N-body model, whose prediction is $\dot{\omega}_2 = 2.11\,\mathrm{deg\,yr^{-1}}$, and with fit of the interferometric observations (see Table 11).
- **The nodal motion of orbits 1 and 2:** Inserting nominal parameters from Table 12 provides the mean nodal drift $\dot{\tilde{\Omega}} = 18.98 \pm 0.53\,\mathrm{deg\,yr^{-1}}$ (Eq. 27), which is again in excellent agreement with results of the N-body model; we note that the periods of the nodal oscillations are effectively $\simeq 19.43\,\mathrm{deg\,yr^{-1}}$ for orbit of component A (Ω_1) and $\simeq 19.81\,\mathrm{deg\,yr^{-1}}$ for orbit B (Ω_2). Values are not exactly the same, probably because of interaction with component C, which was not included in the perturbation theory. There is a hint of a shallower depth of the Hvar photometric observations from early 2007 when our model predicts a higher value of the inclination i_1. However, to determine the inclination variations, we need more accurate photometric observations in the future.
- **Eclipse-timing variations – orbit 1:** Eqs. (29, 30, and 31) provide amplitudes of the ETVs (assuming that component B is at periastron) of orbit 1 $\delta t_{\rm ETV,long} = 0.0162 \pm 0.0007\,$d, $\delta t_{\rm ETV,short} = 0.0068 \pm 0.0003\,$d. Their sum agrees with the detected amplitude of ETVs ($\delta t_{\rm ETV,OBS} = 0.025 \pm 0.010\,$d). We also note that the two primary eclipse minima in the MOST data were found to be phase-shifted by $\simeq 0.0003$ in Sect. 4.3. This is about 0.1° in orbital longitude of inner orbit 1. Combining results in Eqs. (29, 30, and 31) and taking into account $\ell_2 \simeq 86^\circ$ and $\lambda_1 \simeq F_2$ from Table 15, we obtain very good agreement with the observed shift.

10. Motivations for future observations of ξ Tauri

First, it seems desirable to continue the observations of the times of minima and, more importantly, eclipse duration and depth. At an epoch after approximately RJD 59 405.0, that is, in the second half of 2021, we would expect either persisting or disappearing eclipses of the inner pair Aa+Ab for different mirror solutions. Consequently, this is a direct and independent test of our analysis of closure phase measurements in Sect. 8.4. We note that the nominal solution shown in Fig. 11 exhibits too small variations of i_1, such that the eclipsing binary would be eclipsing constantly.

Nevertheless, even the nominal solution predicts nearly 4° full amplitude of variation in i_1 and we expect fairly well observable effects. We suggest, for instance, a space-born observation of a similar quality to that of MOST, obtained at the turn of 2016 and 2017, when the predicted i_1 value would be highest (about 88.2°). The change in eclipse depth, as compared to the MOST data, should be about 0.05 magnitude, which is very easily detectable. Such a single observation would further constrain parameters of ξ Tau with an exceptional accuracy.

It would be of great help if the line spectra of the faint component C, separated by 200 to 600 mas from the triple Aa+Ab+B, were obtained and the corresponding radial velocity measured. This would also allow us to distinguish between the remaining two mirror orbital solutions for the motion of this component.

Precise and uninterrupted space-based photometry on a longer time-span would be useful to unambiguously resolve oscillation modes and splittings. Given the high rotation frequency $f_{\rm rot} = 2.38\,\mathrm{d^{-1}} \simeq 27.5\,\mu$Hz, it should not be that difficult (the

minimum time-span $\Delta t \simeq 1/f_{\rm rot}$), but currently aliases with instrumental frequencies seem to limit the S/N in the Fourier spectrum.

As an alternative, series of high-resolution high S/N spectra would be needed to detect the oscillation modes independently, as the travelling sub-features in the line profiles of component B are broadened by a relatively high rotation. Precise RV measurements of components Aa and Ab may also reveal the Rossiter-McLaughlin effect, which gives the rotational sense of the two components.

A new series of long-baseline optical spectro-interferometric observations including measurements of closure phase are highly desirable, because they would provide a fully independent estimate of the orbital elements of orbit 1, would independently determine the sense of revolution of the components of orbit 1 with respect to orbit 2, and would finally provide an independent estimate of the radii of components Aa and Ab.

11. Conclusion

We have conducted an in-depth study of the quadruple stellar system ξ Tau, starting from simple analytic models for different types of observations (see Sects. 3-7), and concluding with a complex N-body model that combines astrometric, photometric, spectroscopic, and spectro-interferometric observations to a certain degree (see Sect. 8). We were able to set tight constraints on three components of ξ Tau, and they will provide an excellent test case for models of stellar evolution, while the full description of the geometry of the hierarchy will provide a test of the binary formation.

The analytic models allowed us to estimate properties of components Aa, Ab, and B that are highly consistent (see the critical summary of the analytic models in Sect. 7) and mean orbital elements of orbits 1, 2, and 3 using different methods that are again consistent with each other, but provided limited-to-no insight into the dynamic evolution of orbits of the ξ Tau.

This discrepancy was fixed with the N-body model, which properly accounts for the dynamic interaction within the system and is able to fit RVs, ETVs, and astrometric positions simultaneously. It provided a set of osculating elements and component masses whose evolution fits the observables (see Table 13). It also provided insight into the long- and short-term evolution of the osculating elements (see Fig. 11) and also resolved the prograde and retrograde solution (between orbits 1 and 2) solely from ETVs. The result also supports previous analyses because it did not vary much from their outcome.

Perturbation theory shows that the most pronounced secular evolution of elements, that is, the advance of the apsidal line of orbit 2, the harmonic variation of the inclination $i_{1,2}$, and the longitude of the ascending node $\Omega_{1,2}$, are explained by a quadrupole interaction between orbits 1 and 2. The same applies to the predicted size of ETVs, which agree well with observations.

Acknowledgements. The research of JN, PH, MW, and PZ was supported by grants P209/10/0715 and GA15-02112S of the Czech Science Foundation. The research of JN and PH was also supported by grant no. 678212 of the Grant Agency of the Charles University. The Navy Prototype Optical Interferometer is a joint project of the Naval Research Laboratory and the US Naval Observatory, in cooperation with Lowell Observatory and is funded by the Office of Naval Research and the Oceanographer of the Navy. The authors thank Jim Benson and the NPOI observational support staff, whose efforts made this project possible. This research has made use of the SIMBAD astronomical literature database, operated at CDS, Strasbourg, France. The CHARA Array is operated with support from the National Science Foundation through grant AST-0908253, the W. M. Keck Foundation, the NASA Exoplanet Science Institute, and from Georgia State University. This publication is supported as a project of the Nordrhein-Westfälische Akademie der Wissenschaften und der Künste in the framework of the academy programme by the Federal Republic of Germany and the state Nordrhein-Westfalen. HB acknowledges financial support by Croatian Science Foundation under the project 6212 "Solar and Stellar Variability". The project is based on data obtained from the ESO Science Archive Facility under request number jnemravova217453, on spectral data retrieved from the ELODIE archive at Observatoire de Haute-Provence (OHP), and on observations made at the South African Astronomical Observatory (SAAO). PZ wish to thank the staff at SAAO for their warm hospitality and help with the equipment. AFJM is grateful for financial assistance to NSERC (Canada) and FQRNT (Quebec). The observations with the MPG 2.2 m telescope were supported by the Czech Ministry of Education, Youth and Sports project LG14013 ("Tycho Brahe: Supporting Ground-based Astronomical Observations") during run P2 in May 2015. We acknowledge the use of the electronic database from the CDS, Strasbourg and electronic bibliography maintained by the NASA/ADS system. We acknowledge the constructive criticism by the referee Peter P. Eggleton, which helped us to improve the paper.

References

Aller, L. H., Appenzeller, I., Baschek, B., et al., eds. 1982, Landolt-Börnstein: Numerical Data and Functional Relationships in Science and Technology - New Series " Gruppe/Group 6 Astronomy and Astrophysics " Volume 2 Schaifers/Voigt: Astronomy and Astrophysics / Astronomie und Astrophysik " Stars and Star Clusters / Sterne und Sternhaufen
Armstrong, J. T., Mozurkewich, D., Rickard, L. J., et al. 1998, ApJ, 496, 550
Baranne, A., Queloz, D., Mayor, M., et al. 1996, A&AS, 119, 373
Benisty, M., Malbet, F., Millour, F., Absil, O., & Duvert, G. 2015
Bolton, C. T. & Grunhut, J. H. 2007, in IAU Symposium, Vol. 240, IAU Symposium, ed. W. I. Hartkopf, P. Harmanec, & E. F. Guinan, 66
Bonneau, D., Clausse, J.-M., Delfosse, X., et al. 2006, A&A, 456, 789
Borkovits, T., Csizmadia, S., Forgács-Dajka, E., & Hegedüs, T. 2011, A&A, 528, A53
Borkovits, T., Érdi, B., Forgács-Dajka, E., & Kovács, T. 2003, A&A, 398, 1091
Borkovits, T., Rappaport, S., Hajdu, T., & Sztakovics, J. 2015, MNRAS, 448, 946
Breiter, S. & Vokrouhlický, D. 2015, MNRAS, 449, 1691
Brož, M., Mayer, P., Pribulla, T., et al. 2010, AJ, 139, 2258
Butterworth, S. 1930, Wireless Engineer, 7
Campbell, W. W. 1909, Astrophysical Journal, 29, 224
Claret, A. 1998, A&AS, 131, 395
Claret, A. 2001, MNRAS, 327, 989
de Laverny, P., Recio-Blanco, A., Worley, C. C., & Plez, B. 2012, A&A, 544, A126
Degroote, P., Acke, B., Samadi, R., et al. 2011, A&A, 536, A82
Drimmel, R., Cabrera-Lavers, A., & López-Corredoira, M. 2003, A&A, 409, 205
Eggleton, P. P. & Kiseleva-Eggleton, L. 2001, ApJ, 562, 1012
Eggleton, P. P. & Tokovinin, A. A. 2008, MNRAS, 389, 869
ESA. 1997, VizieR Online Data Catalog, 1239
Fabrycky, D. & Tremaine, S. 2007, ApJ, 669, 1298
Fekel, J. F. C. 1981, ApJ, 246, 879
Flower, P. J. 1996, ApJ, 469, 355
Fuhrmann, K., Chini, R., Hoffmeister, V. H., et al. 2011, MNRAS, 411, 2311
Glindemann, A., Albertsen, M., Andolfato, L., et al. 2004, in Proc. SPIE, Vol. 5491, New Frontiers in Stellar Interferometry, ed. W. A. Traub, 447
Hadrava, P. 1995, A&AS, 114, 393
Hadrava, P. 1997, A&AS, 122, 581
Hadrava, P. 2009, ArXiv e-prints [arXiv:0909.0172]
Harmanec, P. 1988, Bulletin of the Astronomical Institutes of Czechoslovakia, 39, 329
Harmanec, P. 1998, A&A, 335, 173
Harmanec, P. & Horn, J. 1998, Journal of Astronomical Data, 4, 5
Harmanec, P., Horn, J., & Juza, K. 1994, A&AS, 104, 121
Harrington, R. S. 1968, AJ, 73, 190
Harrington, R. S. 1969, Celestial Mechanics, 1, 200
Hummel, C. A., Benson, J. A., Hutter, D. J., et al. 2003, AJ, 125, 2630
Hummel, C. A., Mozurkewich, D., Armstrong, J. T., et al. 1998, AJ, 116, 2536
Hummel, C. A., Zavala, R. T., & Sanborn, J. 2013, Central European Astrophysical Bulletin, 37, 127
Husser, T.-O., Wende-von Berg, S., Dreizler, S., et al. 2013, A&A, 553, A6
Kaufer, A., Stahl, O., Tubbesing, S., et al. 1999, The Messenger, 95, 8
Kraft, D. 1988, A software package for sequential quadratic programming, Deutsche Forschungs- und Versuchsanstalt für Luft- und Raumfahrt Köln: Forschungsbericht (Wiss. Berichtswesen d. DFVLR)
Lafrasse, S., Mella, G., Bonneau, D., et al. 2010, VizieR Online Data Catalog, 2300, 0

Lenz, P. & Breger, M. 2004, in IAU Symposium, Vol. 224, The A-Star Puzzle, ed. J. Zverko, J. Ziznovsky, S. J. Adelman, & W. W. Weiss, 786–790
Levison, H. F. & Duncan, M. J. 2013, SWIFT: A solar system integration software package, Astrophysics Source Code Library
Mason, B. D., Martin, C., Hartkopf, W. I., et al. 1999, AJ, 117, 1890
Moultaka, J., Ilovaisky, S. A., Prugniel, P., & Soubiran, C. 2004, PASP, 116, 693
Mourard, D., Clausse, J. M., Marcotto, A., et al. 2009, Astronomy and Astrophysics, 508, 1073
Mozurkewich, D., Armstrong, J. T., Hindsley, R. B., et al. 2003, AJ, 126, 2502
Nemravová, J. A., Harmanec, P., Bencheikh, J., et al. 2013, Central European Astrophysical Bulletin, 37, 207
Palacios, A., Gebran, M., Josselin, E., et al. 2010, A&A, 516, A13
Petrov, R. G., Malbet, F., Weigelt, G., et al. 2007, A&A, 464, 1
Press, W. H., Teukolsky, S. A., Vetterling, W. T., & Flannery, B. P. 1993, Numerical Recipes in FORTRAN; The Art of Scientific Computing, 2nd edn. (New York, NY, USA: Cambridge University Press)
Prša, A. & Zwitter, T. 2005, ApJ, 628, 426
Prša, A. & Zwitter, T. 2006, Ap&SS, 304, 347
Rappaport, S., Deck, K., Levine, A., et al. 2013, ApJ, 768, 33
Rica Romero, F. M. 2010, Rev. Mexicana Astron. Astrofis., 46, 263
Shao, M., Colavita, M. M., Hines, B. E., et al. 1988, A&A, 193, 357
Simon, K. P. & Sturm, E. 1994, A&A, 281, 286
Soderhjelm, S. 1975, A&A, 42, 229
Soderhjelm, S. 1982, A&A, 107, 54
Steiner, I., Stahl, O., Seifert, W., Chini, R., & Quirrenbach, A. 2008, in Society of Photo-Optical Instrumentation Engineers (SPIE) Conference Series, Vol. 7014, Society of Photo-Optical Instrumentation Engineers (SPIE) Conference Series, 4
Stellingwerf, R. F. 1978, ApJ, 224, 953
Storn, R. & Price, K. 1997, Journal of Global Optimization, 11, 341
Tallon-Bosc, I., Tallon, M., Thiébaut, E., et al. 2008, in Society of Photo-Optical Instrumentation Engineers (SPIE) Conference Series, Vol. 7013, Society of Photo-Optical Instrumentation Engineers (SPIE) Conference Series
ten Brummelaar, T. A., McAlister, H. A., Ridgway, S. T., et al. 2005, ApJ, 628, 453
Tody, D. 1986, in Society of Photo-Optical Instrumentation Engineers (SPIE) Conference Series, Vol. 627, Instrumentation in astronomy VI, ed. D. L. Crawford, 733
Tody, D. 1993, in Astronomical Society of the Pacific Conference Series, Vol. 52, Astronomical Data Analysis Software and Systems II, ed. R. J. Hanisch, R. J. V. Brissenden, & J. Barnes, 173
Tokovinin, A., Mason, B. D., Hartkopf, W. I., Mendez, R. A., & Horch, E. P. 2015, AJ, 150, 50
Tokovinin, A. A. 1997, A&AS, 124, 75
van Belle, G. T., Creech-Eakman, M. J., & Hart, A. 2009, MNRAS, 394, 1925
van Leeuwen, F. 2007, A&A, 474, 653
Walker, G., Matthews, J., Kuschnig, R., et al. 2003, PASP, 115, 1023
Zasche, P., Uhlář, R., Kučáková, H., Svoboda, P., & Mašek, M. 2014, Information Bulletin on Variable Stars, 6114, 1
Zasche, P. & Wolf, M. 2007, Astronomische Nachrichten, 328, 928

[1] Astronomical Institute of the Charles University, Faculty of Mathematics and Physics, V Holešovičkách 2, CZ-180 00 Praha 8 - Troja, Czech Republic
[2] Laboratoire Lagrange, OCA/UNS/CNRS UMR7293, BP4229, 06304 Nice Cedex, France
[3] European Southern Observatory, Karl–Schwarzschild–Str. 2, 85748 Garching bei München, Germany
[4] Department of Mathematics, Physics & Geology, Cape Breton University, 1250 Grand Lake Road, Sydney, NS B1P 6L2, Canada
[5] Department of Physics & Astronomy, University of British Columbia, 6224 Agricultural Road, Vancouver, BC V6T 1Z1, Canada
[6] Department of Astronomy and Astrophysics University of Toronto 50 St. George Street, Toronto, Ontario Canada M5S 3H4
[7] Hvar Observatory, Faculty of Geodesy, Zagreb University, Kačićeva 26, 10000 Zagreb, Croatia
[8] Astronomisches Institut, Ruhr-Universität Bochum, Universitätsstraße 150, D-44780 Bochum, Germany
[9] Instituto de Astronomía, Universidad Católica del Norte, Avenida Angamos 0610, Casilla 1280 Antofagasta, Chile
[10] Department of Astronomy and Astrophysics, Villanova University, Villanova, PA 19085, USA
[11] CHARA Array, Mount Wilson Observatory, Mount Wilson, CA 91023, USA
[12] Department of Astronomy and Physics, Saint Mary's University, Halifax, N.S., B3H 3C3, Canada
[13] Astronomical Institute, Academy of Sciences of the Czech Republic, 251 65 Ondřejov, Czech Republic
[14] Institute of Astronomy, University Vienna, Türkenschanzstrasse 17, A-1180 Vienna, Austria
[15] Department de Physique, Université de Montréal, C.P. 6128, Succursale Centre-Ville, Montréal, QC H3C 3J7, Canada
[16] Observatório do Instituto Geográfico do Exército, R. Venezuela 29 3 Esq., 1500-618, Lisbon, Portugal
[17] NASA Ames Research Center, Moffett Field, CA 94035, USA; SETI Institute, Mountain View, CA 94043, USA
[18] Université de Lyon, Université Lyon 1, Ecole Normale Supérieure de Lyon, CNRS, Centre de Recherche Astrophysique de Lyon UMR5574, F-69230, Saint-Genis-Laval, France
[19] U.S. Naval Observatory, Flagstaff Station, 10391 West Naval Observatory Road, Flagstaff, AZ 86005-8521

Table 12. Summary of parameters derived from the spectroscopic, photometric, and spectro-interferometric analyses. In some cases more values are listed for a parameter, to show that the methods do not contradict each other. Because they were safely resolved only with the astrometry, elements of orbit 3 are not listed here, but in Table 10 and the mass of component C is estimated and briefly discussed in Sect. 7. The listed parameters are the anomalistic period $P_{\rm AN}$, the sidereal period $P_{\rm S}$, the periastron epoch $T_{\rm p}$, the epoch of the primary minimum $T_{\rm min}$, the semi-major axis a, the mass ratio q, the eccentricity e, the inclination i, the periastron argument ω, the position angle of the nodal line Ω, the effective temperature $T_{\rm eff}$, the surface gravitational acceleration $\log g$, the projected rotational velocity $v \sin i$, the mass m, the radius R, the angular diameter θ, the bolometric magnitude $M_{\rm BOL}$, the Johnson V magnitude and colour indices V, $B-V$, $U-B$, the dereddened Johnson V magnitude and colour index V_0, B_0-V_0, and the parallax π.

Parameter	Unit	Source	Value		
			Orbital properties		
Orbit			2	1	
$P_{\rm AN}$	(d)	RV/LC	145.579±0.048	7.14664±0.00002	
$P_{\rm S}$	(d)	RV/LC	145.113±0.071	7.14664±0.00002	
$T_{\rm p}$	(RJD)	RV/–	55 609.46±0.52	–	
$T_{\rm min}$	(RJD)	–/LC	–	56 224.72482±0.00022	
a	($R_\odot$)	IF+HP/IF+HP	219±15	26.1±2.3	
	($R_\odot$)	IF+RV/IF+RV	*229.0±7.7	–	
	($R_\odot$)	–/RV+LC	–	*25.550±0.090	
$a_{\rm angular}$	(mas)	IF/IF	15.93±0.10	1.89±0.11	
e		RV/–	*0.2101±0.0053	0.0[1]	
		IF/–	0.2120±0.0040	0.0[1]	
q		RV/RV	0.889±0.056	0.9438±0.0036	
i	(deg)	IF/IF	86.67±0.12	86.85[1]	
	(deg)	–/LC	–	*86.85±0.22	
ω	(deg)	RV/–	*9.25±1.42	90.0[1]	
	(deg)	IF/–	8.4±1.6	90.0[1]	
$\dot{\omega}$	(deg yr^{-1})	RV/–	2.90±0.33	0.0[1]	
$\dot{\omega}$	(deg yr^{-1})	IF/–	2.02±0.31	0.0[1]	
Ω	(deg)	IF/IF	148.453±0.066	148.4[2]±1.9	
			Component properties		
Component			B	Aa	Ab
$T_{\rm eff}$	(K)	SP	14 190±150	10 700±160	*10 480±130
	(K)	LC	–	10700[1]	10450±150
$\log g_{\rm [cgs]}$		SP	4.527±0.041	4.08±0.12	4.01±0.10
		RV+LC	4.09±0.11	4.330±0.019	4.348±0.022
$v \sin i$	(km s^{-1})	SP	229.2±1.7	12.6±2.6	14.3±3.1
m	($M_\odot$)	RV+LC	*3.89±0.25	*2.252±0.027	*2.125±0.027
	($M_\odot$)	RV+IF	3.60±0.52	2.08±0.48	1.96±0.45
R	($R_\odot$)	RV+LC	–	1.700±0.035	1.618±0.039
	($R_\odot$)	IF+HP	2.81±0.28	–	–
θ	(mas)	IF	0.407±0.031	–	–
	(mas)	LC+HP	–	0.247±0.017	0.235±0.017
$M_{\rm BOL}$	(mag)	LC+RV+IF	-1.14±0.22	0.923±0.079	1.120±0.075
V	(mag)	LC	4.250±0.10	5.46±0.11	5.63±0.11
$B-V$	(mag)	LC	-0.12±0.16	-0.05±0.16	-0.03±0.14
$U-B$	(mag)	LC	-0.446±0.16	-0.09±0.14	-0.07±0.14
V_0	(mag)	LC	4.24±0.65	5.54±0.65	5.68±0.65
B_0-V_0	(mag)	LC	-0.120±0.085	-0.018±0.167	-0.015±0.162
				Parallax	
$\pi_{\rm a_1}$	(mas)			15.91 ± 0.93	
$\pi_{\rm a_2}$	(mas)			$*14.96 \pm 0.51$	
$\pi_{\rm DM,Aa}$	(mas)			14.3 ± 4.3	
$\pi_{\rm DM,Ab}$	(mas)			14.4 ± 4.4	
$\pi_{\rm DM,B}$	(mas)			13.3 ± 2.2	

Notes. [1]Assumed. [2]A solution where $\Omega_1 = 328.4 \pm 1.9$, is also plausible and has identical χ^2. *Parameters that are likely the closest to the true nature of ξ Tau. Sources: RV.. solution of the RV curve presented in Table 5, SP.. comparison of the observed and synthetic spectra presented in Table 7, LC.. solution of the light curve presented in Table 9, IF.. solution of the V^2 and $T_3\phi$ presented in Table 11, HP.. the Hipparcos parallax $\pi = 15.60 \pm 1.04$ mas. The parallaxes: $\pi_{\rm a_1}$ estimated from the size of the semi-major axis of orbit 1 (physical and angular), $\pi_{\rm a_2}$ estimated from the size of the semi-major axis of orbit 2 (physical and angular), $\pi_{\rm DM,Aa}$ estimated from the distance modulus of component Aa, $\pi_{\rm DM,Ab}$ estimated from the distance modulus of component Ab, $\pi_{\rm DM,Ab}$ estimated from the distance modulus of component B.

Table 15. Initial osculating orbital elements $a_j, e_j, i_j, \Omega_j, \omega_j, M_j$ of the ξ Tau system as derived by our N-body model. The epoch is $T_0 = 2\,456\,224.724705$. The values below correspond to that of best-fit solutions with $\chi^2 = 2\,578$, with individual contributions: $\chi^2_{\rm rv} = 2\,237$, $\chi^2_{\rm etv} = 151$, $\chi^2_{\rm edv} = 3.3$ and $\chi^2_{\rm sky} = 185$. The masses of components in $M_\odot$ units were $m^{\rm Aa} = 2.232911^{+0.000091}_{-0.000093}$, $m^{\rm Ab} = 2.009948^{+0.000092}_{-0.000093}$, $m^{\rm B} = 3.7343^{+0.0070}_{-0.0073}$ and $m^{\rm C} = 0.90^{+0.73}_{-0.04}$. Component B is on its lower limit $m^{\rm B}_{\rm min}$. The mass of component C is very poorly constrained, it is more of a distant test mass compared to the others. The 3-σ uncertainties of the elements were determined by a simplified one-dimensional χ^2 mapping, assuming a relative increase of χ^2 by a factor of 1.13, i.e. suitable for the number of degrees of freedom we have ($\nu = 908$). The uncertainty values were verified using the bootstrap method with 100 random selections of datasets and corresponding simplex optimisation, but realistic uncertainties are likely to be larger than that because there are a number of local minima with statistically equivalent χ^2 values. We do not report a full correlation matrix of our solution here. Its non-diagonal terms indicate higher values of uncertainties for those elements that are strongly correlated or anti-correlated with others (e.g. $r_{m^{\rm Aa},\omega_2} = 0.74$, $r_{a_1,\Omega_2} = -0.77$, $r_{a_1,\omega_2} = -0.80$, $r_{a_3,i_3} = -0.79$).

Parameter	Value					Unit	Note
a_1	$0.1175673^{+0.0000007}_{-0.0000007}$	a_2	$1.08296^{+0.00033}_{-0.00031}$	a_3	$28.35^{+0.81}_{-0.78}$	au	
e_1	$0.0000^{+0.0020}_{-0.0000}$	e_2	$0.1974^{+0.0009}_{-0.0009}$	e_3	$0.569^{+0.022}_{-0.023}$		
i_1	$86.5^{+3.8}_{-1.5}$	i_2	$86.7^{+2.1}_{-1.9}$	i_3	$-26.3^{+11.6}_{-\ 8.0}$	deg	
Ω_1	$331.4^{+1.4}_{-2.0}$	$\Omega_2^\dagger$	$328.9^{+1.4}_{-1.2}$	Ω_3	$108.3^{+3.3}_{-3.3}$	deg	
ω_1	$274.11^{+0.15}_{-0.15}$	ω_2	$9.62^{+0.14}_{-0.14}$	ω_3	$9.0^{+3.2}_{-3.2}$	deg	
M_1	$176.02^{+0.15}_{-0.15}$	M_2	$85.68^{+0.13}_{-0.12}$	M_3	$31.3^{+1.4}_{-1.4}$	deg	
γ	$8.5^{+1.6}_{-1.6}$					$\mathrm{km\,s^{-1}}$	
i_1'	$93.5^{+1.5}_{-2.8}$					deg	mirror solution with $\chi^2 = 2\,545$, Aa+Ab eclipses partially disappear
Ω_1'	$148.5^{+5.8}_{-2.9}$					deg	mirror solution with $\chi^2 = 2\,749$, Aa+Ab eclipses partially disappear, orbit 1 is retrograde w.r.t. orbit 2
				i_3'	$25.6^{+\ 9.3}_{-15.2}$	deg	mirror solution with $\chi^2 = 2\,678$

Notes. † The value is expressed in hierarchical Jacobian elements, with respect to Aa+Ab barycentre because this pair is the most compact and massive. If the reference point were the photocentre of the brightest component B instead, then the longitude of the ascending node would be shifted by $-180°$.

Appendix A: Supplementary material to the spectroscopic observations and their analyses

Details of the reduction procedure of the spectroscopic observations used in this study along with supplementary material to its analysis are given in this section.

Appendix A.1: Acquisition and reduction of the spectroscopic observations

The reduction procedure applied to spectra from different observatories (the labelling of observatories corresponds to that introduced in Table 2) were the following:

i) *OND*: All slit spectra were secured at the coudé focus of the 2 m reflector in Ondřejov, Czech Republic, and were recorded with the CCD detector PyLoN 2048x512BX. The bias subtraction, flat-fielding, and wavelength calibration were carried out using IRAF[9] (Tody 1986, 1993). The spectra were normalised with Hermite polynomials (order $k \leq 10$).
ii) *FER*: The echelle spectra were acquired with the 2.2 m ESO/MPG reflector at La Silla, Chile, and were reduced (bias subtraction, flat-fielding, and wavelength calibration) with a MIDAS pipeline developed specifically for the instrument (Kaufer et al. 1999). The studied regions of the reduced spectra were normalised with Hermite polynomials (order $k \leq 10$).
iii) *BES*: The spectra were acquired with an echelle spectrograph mounted at the 1.5 m Hexapod Telescope at Cerro Amazones, Chile, which is the same as the FEROS spectrograph, and the same MIDAS pipeline was used to carry out the reduction (bias subtraction, flat-fielding, wavelength calibration). The studied regions were normalised with Hermite polynomials (order $k \leq 10$).
iv) *ELO*: The echelle spectra were obtained with the 1.93 m reflector at Observatory Haute Provence. The initial reductions (bias subtraction, flat-fielding, wavelength calibration) were carried out with a pipeline described in Baranne et al. (1996). The studied regions were normalised with Hermite polynomials (order $k \leq 10$).
v) *DDO*: The slit spectra were acquired with the 1.88 m reflector at the David Dunlap Observatory. The initial reductions (bias subtraction, flat-fielding, wavelength calibration) were carried out using IRAF. The spectra were normalised with Hermite polynomials (order $k \leq 10$).
vi) *LIS*: The slit spectra were acquired with the 0.356 m reflector at the Astronomical Observatory of the Instituto Geográfico do Exército, Lisbon. The dark-frame subtraction and flat-fielding were carried out in Maxim DL[10]. The wavelength calibration was carried out using neon comparison spectra and telluric lines in the program Visual Spec[11]. The instrumental response was also removed in this program, using Castor as a reference star. The spectra were normalised with Hermite polynomials (order $k \leq 10$).

[9] IRAF is distributed by the National Optical Astronomy Observatories, which are operated by the Association of Universities for Research in Astronomy, Inc., under cooperative agreement with the National Science Foundation.
[10] Maxim DL is a commercial software designed for astronomical imaging `http://www.cyanogen.com/maxim/main.php`.
[11] Visual Spec is a freeware designed for the wavelength calibration and the instrumental response removal `http://www.astrosurf.com/vdesnoux/index.html`.

Appendix A.2: Supplementary materials to the analysis of spectroscopic observations

The spectroscopic supplementary material consists of Fig. A.1 that shows a comparison of the separated and synthetic profiles. The related analyses are described in Sects. 3.5 and 3.3.

Appendix B: Supplementary material to the photometric observations and their analysis

Details on the reduction procedure of the photometric observations used in this study along with supplementary material to their analysis are given in this section.

Appendix B.1: Acquisition and reduction of the photometric observations

The reduction procedure applied to photometric observations from different observatories (the labelling of observatories corresponds to the labelling introduced in Table 3) were the following:

i) *HVAR*: The differential observations were obtained with the 0.65 m reflector at the Hvar Observatory, Croatia, which is equipped with a photoelectric photometer with an EMI 6256 tube. The observations were acquired relative to the comparison star 4 Tau with the check star 6 Tau observed as frequently as ξ Tau and transformed to the standard UBV system ($UBVR$ for observations acquired after RJD = 56 000) using the non-linear transformations implemented in the reduction package HEC22[12] (see Harmanec et al. 1994; Harmanec & Horn 1998). All observations were reduced with the latest release 18, which allows for time variation in the linear extinction coefficients in the course of the observing night.
ii) *HIPP*: The all-sky observations were acquired with the 0.29 m reflector of the Hipparcos satellite and transformed to V magnitude using the formulæ derived by Harmanec (1998).
iii) *SAAO*: The differential observations were acquired at the South African Astronomical Observatory, South Africa with 0.5 m reflector equipped with a photoelectric photometer. The observations were acquired relative to the comparison star 4 Tau and 6 Tau served as a check star and were transformed to the standard Johnson system using HEC22.
iv) *VILL*: The differential observations were acquired with the Automatic Photometric Telescope at Villanova, USA. The observations were taken relative to the comparison star 4 Tau and 6 Tau served as a check star.
v) *MOST*: The all-sky observations were obtained with the 0.15 m reflector in the MOST satellite. The initial reduction was carried out according to Walker et al. (2003) and references therein. Removal of the remaining instrumental artefacts and the stray light from Earth's atmosphere is described in Sect. 4.

Appendix B.2: Supplementary materials to the analysis of the photometric observations

The photometric supplementary material consists of Figs. B.1 and B.2 that show the available primary and secondary light-

[12] The whole package along with a detailed manual, auxiliary data files, and results is available at `http://astro.troja.mff.cuni.cz/ftp/PHOT`

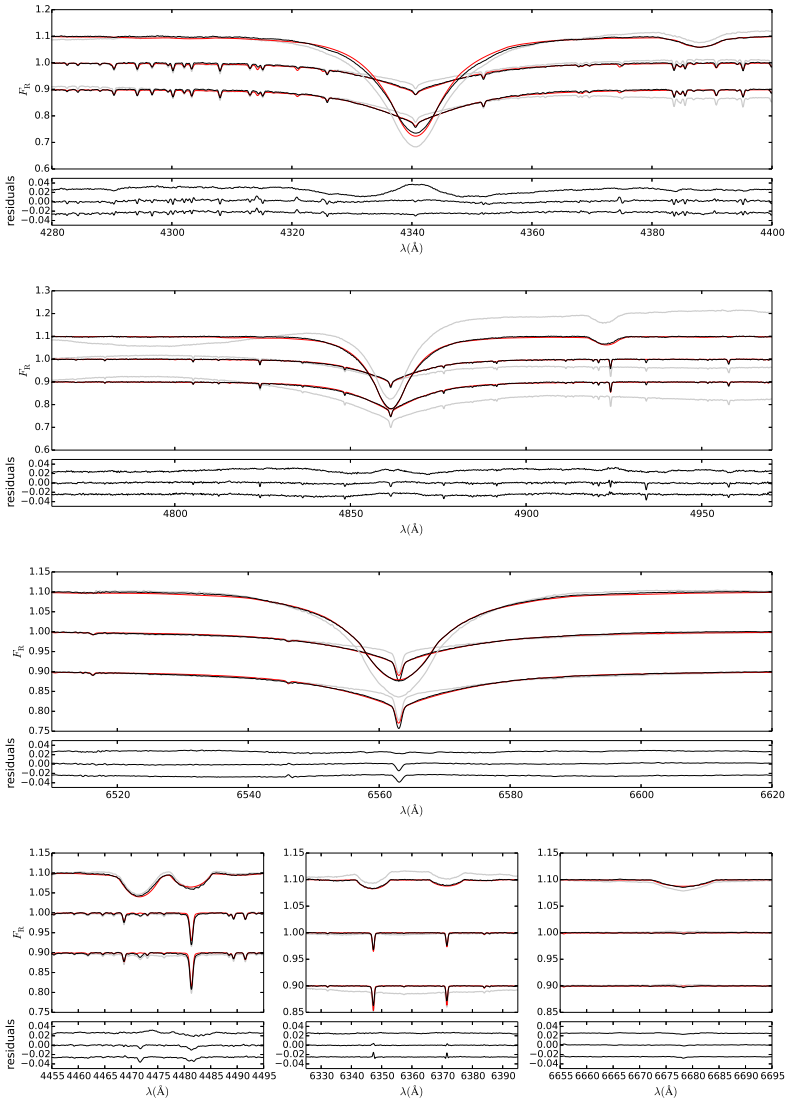

Fig. A.1. Comparison of the separated and synthetic spectra. The parameters defining the synthetic spectra are listed in Sect. 3.5. In each panel we show in the top spectrum component B, in the middle spectrum component Aa, and in the bottom spectrum component Ab. The thick grey line plots spectra, the thin black line separated and re-normalised spectra, and the thin red line synthetic spectra. The residuals are computed for synthetic and re-normalised separated spectra.

curve minima. All minima cover a time interval no longer than 30 d. See Sect. 4 for related analyses.

Appendix C: Supplementary material to the spectro-interferometric observations and their analyses

Details on the acquisition and reduction of the spectro-interferometric observations, along with tables and figures illustrating the analysis are presented in Sect. 6.

Appendix C.1: Mark III observations

The observations were carried out using a single north-south baseline three times on January 19, October 19, and November 2, 1991. The baseline length was 32 m on the first night and 15 m on the two other nights. Visibilities were recorded in three narrow-band channels at 5000 Å, 5500 Å, and 8000 Å. μ and η Tau (limb-darkened diameters of 0.41 mas and 0.98 mas, respectively, with 10% uncertainties) served as the calibrators. The calibrated visibilities were obtained from the Mark III data archive,

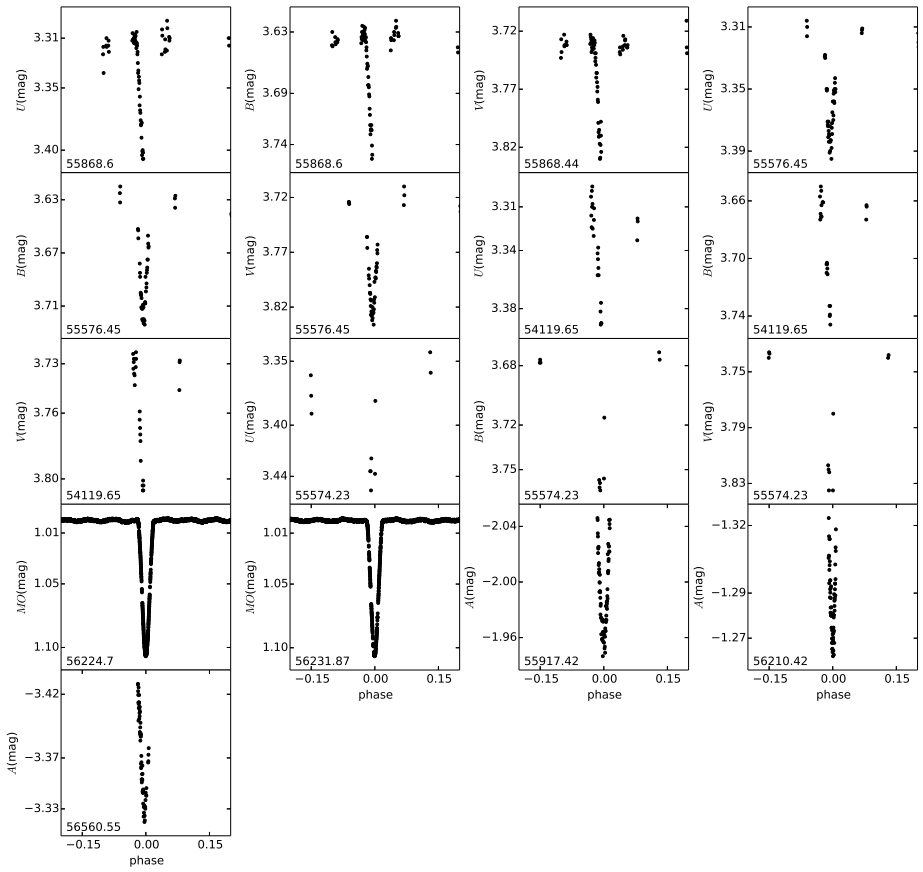

Fig. B.1. All available primary minima of orbit 1. The filters are denoted as follows: UBV - Johnson UBV filters, MO the MOST filter, and A differential measurements taken in the visible without any filter. Mean RJD is given in the bottom left corner of each panel.

which was created using the reduction and calibration methods described by Mozurkewich et al. (2003).

Appendix C.2: NPOI observations

The observations were carried out with the three-beam combiner in 1998 and 2000, and from 2003 to 2013 with the six-beam combiner. Visibilities, complex triple amplitudes, and closure phases were recorded in 16 narrow-band channels between 5500 Å and 8500 Å. The journal of the NPOI observations including the calibrator stars is given in Table C.2, and the calibrator information is given in Table C.4.

The calibrators were taken from a list of single stars maintained at NPOI with diameters estimated from V and $(V-K)$ using the surface brightness relation by Mozurkewich et al. (2003) and van Belle et al. (2009). Values of $E(B-V)$ were derived from comparison of the observed and theoretical colours as a function of spectral type by Schmidt-Kaler in Aller et al. (1982). Values for the extinction derived from $E(B-V)$ were compared to estimates based on the maps by Drimmel et al. (2003), and used to correct V if they agreed within $0^{\rm m}.5$. Even though the surface brightness relation based on $(V-K)$ colours is to first order independent of the reddening, we included this small correction. The minimum (squared) visibility amplitudes corresponding to the diameter estimates are given in Table C.4 for all NPOI observations and show that the calibrators are either unresolved or only weakly resolved.

NPOI data and their reductions were described by Hummel et al. (1998) and Hummel et al. (2003). For the first time,

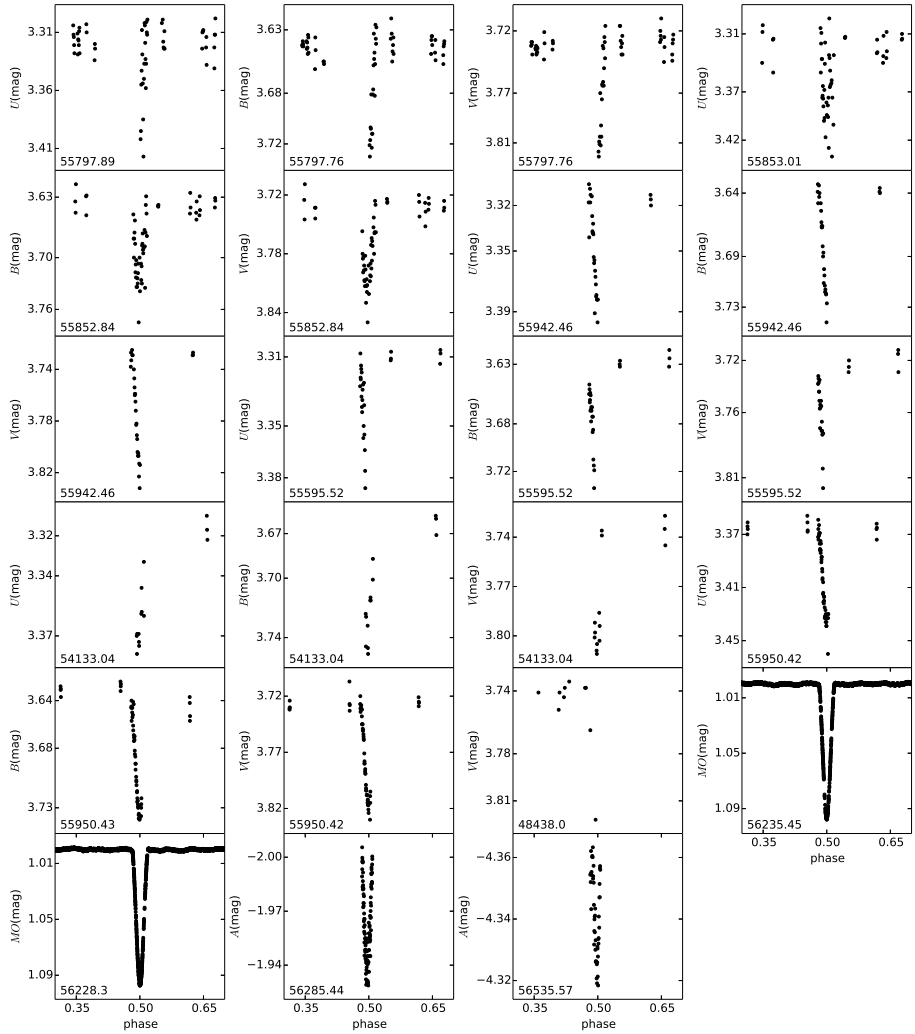

Fig. B.2. All available secondary minima of orbit 1. The filters are denoted as follows: UBV - Johnson UBV filters, MO the MOST filter, A differential measurements taken in the visible without any filter. Mean RJD is given in the bottom left corner of each panel.

we used a pipeline written in GDL[13] for the OYSTER[14] NPOI data reduction package. The pipeline automatically edits the one-second averages produced by another pipeline directly from the raw frames, based on expected performance such as the variance of fringe tracker delay, photon count rates, and narrow-angle tracker offsets. Visibility bias corrections are derived as usual from the data recorded away from the stellar fringe packet. After averaging the data over the full length of an observation, the closure phases of the calibrators were automatically unwrapped

[13] http://gnudatalanguage.sourceforge.net
[14] http://www.eso.org/~chummel/oyster

so that their variation with time, as well as that of the visibility amplitude, could be interpolated for the observations of ξ Tau. For the calibration of the visibilities, the pipeline used all calibrator stars observed during a night to obtain smooth averages of the amplitude and phase-transfer functions using a Gaussian kernel of 80 minutes in length. The residual scatter of the calibrator visibilities and phases around the average set the level of the calibration uncertainty and was added in quadrature to the intrinsic data errors. The amplitude calibration error of typically a few percent in the red channels up to 15% in the blue channels was added in quadrature to the intrinsic error of the visibilities. The phase calibration was good to about a couple of degrees.

Appendix C.3: VEGA/CHARA observations

The observations were carried out during two runs in 2011 and in 2012. Preliminary results, based on the observations obtained during the first run, were published by Nemravová et al. (2013). The reduction procedure was the same for both runs.

Five observations were acquired in 2011. All observations were obtained in the three-telescope (3T) mode and included the CHARA baselines E1E2W2, W1W2S2, and W2E2S2, ranging from 63 m to 245 m (E1, E2, S1, S2, W1, and W2 denote the telescopes in the CHARA telescope array). Ten new observations were secured in 2012. Four of them were taken in the 3T mode and the remaining six were taken in the two-telescope (2T) mode. The 2T observations included the CHARA baselines S2S1 and E2E1, their projected lengths ranging from 34 m to 66 m. The 3T observations contained the E2E1W2 and W2W1S1 baselines, their projected lengths were from 65 m to 279 m. A detailed journal of all interferometric observations with the instrument CHARA/VEGA is in Table C.3.

The observations were obtained with two cameras centred on 5350 Å (denoted BLUE) and 7300 Å (denoted RED) at spectral resolution $R \simeq 5\,000$. Individual frames were recorded with a frequency of 100 Hz and grouped into blocks containing 2500 frames. Each block was coherently summed and each observation had from 20 to 90 blocks. Two 20 nm wide bands were chosen in the BLUE region and two 30 nm wide bands in the RED region. The four bands used are $\Delta\lambda_{\rm IF} = \{5320-5520, 5400-5600, 7000-7300, 7300-7600\}$[15] Å. The frames were summed within these bands and the raw squared visibility $V_{\rm RAW}$ was derived from the sum. The spectral bands have to be narrow because of the limited coherence of the waves due to the atmospheric turbulence. There are no strong stellar lines in any of the four spectral bands used; the spectral band $7300-7600$ Å is affected by the telluric water vapour lines, but even those are smeared out by the low resolution of the spectra.

A calibrator was observed before and after each observation of ξ Tau. Calibrators were selected with the tool SearchCal (Bonneau et al. 2006), and their list along with their basic properties is given in Table C.5. The instrumental visibility was estimated according to the formula

$$V^2_{\rm SCI}(u,v) = V^2_{\rm SCI-RAW}\frac{V^2_{\rm CAL-UD}}{V^2_{\rm CAL-RAW}}(u,v), \quad \text{(C.1)}$$

where $V^2_{\rm SCI}$ is the calibrated visibility of ξ Tau, $V^2_{\rm SCI-RAW}$ the raw visibility of ξ Tau, $V^2_{\rm CAL-UD}$ the visibility of a uniform disk with a diameter listed in Table C.5, and $V^2_{\rm CAL-RAW}$ the raw visibility of a calibrator. To avoid inaccurate observations, we removed all blocks with a S/N<2 and whose optical path delay (OPD) differed from the mean OPD by more than 2σ. Such blocks usually represent only random noise rather than a physical signal. In rare cases, when the raw visibility of ξ Tau was close to zero, but safely detected, and there was no suitable observation of a calibrator, the raw visibilities of ξ Tau were used in the analysis as if they were calibrated, but they were assigned an error $\Delta V^2 = 0.05$. This allowed us to save more usable observations for very long baselines giving strong constraints by low-visibility measurements.

Appendix C.4: VLTI/AMBER observations

ξ Tau was observed by VLTI/AMBER in 2012 Dec 03. The observations were acquired in three-telescope mode in J, H, and K bands and the low-resolution regime ($R = 35$). The baselines ranged from 41 m to 139 m.

The unprocessed observations were downloaded from the ESO archive and the reduction was made with the AMBER data reduction software `amdlib` (Benisty et al. 2015). Following the manual step by step, we applied the bad pixel and flat-field maps, computed pixel-to-visibility matrix, subtracted the dark frame, and performed frame selection based on the fringe S/N ratio (the best 20 % were kept).

Four stars were used as calibrators; they are listed along with their basic properties is in Table C.5. The uniform-disk diameters were taken from the JMMC Stellar Diameters Catalogue (Lafrasse et al. 2010). The calibration was made using the library `amdlib`.

Additionally, we had to filter the data. Observations with an effective wavelength at the edges of the J, H, and K bands were not removed, although they had large uncertainties and displayed an abrupt drop in visibility inconsistent with the remaining data. Only observations whose effective wavelength lay in any of following bands $\Delta\lambda \in \{1.155-1.34; 1.49-1.77; 2.02-2.05; 2.075-2.41\}$ μm were used. Furthermore, several observations suddenly had very low visibility compared to neighbouring data, which was very likely caused by an instrumental and/or atmospheric effect. These are data taken at RJD = 56 264.767145, all data with $B/\lambda < 1.76\times10^7$, and data taken from RJD = 56 264.776653 to RJD = 56 264.778568 with $B/\lambda > 9.25\times10^7$.

Appendix C.5: Night-by-night analysis of NPOI observations

The calibrated visibility and phase estimates are rich enough to permit night-by-night estimation of positions of individual components. Owing to the lower resolution, the NPOI interferometer is almost insensitive to orbit 1 and diameters of the three components (Aa, Ab and B) of ξ Tau. Therefore the system was represented by two point sources, and the relative position of component B and the eclipsing binary was estimated. The results of the night-by-night analysis are given in Table C.1.

The uncertainty ellipses of position of the photocentre of orbit 1 (which is almost identical with its centre of mass because the two components of the eclipsing binary are similar) relative to component B were computed from fits to contours of the χ^2 surfaces at the minima instead of deriving them from the interfer-

[15] The only difference between the reduction procedure of the observations acquired in 2011 and 2012 is in the choice of the spectral bands. The following bands were used in 2011 $\Delta\lambda_{\rm IF(OLD)} = \{5350-5450, 5450-5600\}$ Å, and $\Delta\lambda_{\rm IF(OLD)} = \{7000-7200, 7100-7300, 7200-7400\}$ Å.

Table C.1. Astrometric positions of the photocentre of orbit 1 relative to component B derived from night-by-night analysis of MARK III and NPOI observations. ρ is the separation, θ the position angle measured counter-clockwise from the north, a, b and α are the semi-major axis, semi-minor axis, and the position angle (again measured counter-clockwise from the north) of the uncertainty ellipse.

RJD	ρ (mas)	θ (deg)	a (mas)	b (mas)	α (deg)
NPOI					
51 093.906	9.71	145.08	0.831	0.157	177.1
51 097.971	11.87	148.00	0.838	0.169	169.1
51 171.722	18.31	327.53	0.844	0.153	173.7
51 815.933	7.36	142.65	0.842	0.156	176.2
51 835.927	11.98	149.63	0.853	0.163	171.7
52 913.988	18.72	327.60	0.628	0.111	151.8
52 927.944	18.46	328.68	1.962	0.223	149.7
52 930.924	18.30	329.24	0.608	0.263	167.0
55 463.974	12.48	148.89	1.874	0.256	152.7
55 464.970	12.23	148.82	0.675	0.256	162.2
55 465.970	12.22	149.96	0.666	0.252	162.2
55 466.962	11.74	149.30	0.653	0.254	162.7
55 467.963	11.41	150.01	0.651	0.256	162.8
55 468.959	11.12	150.03	0.650	0.257	162.7
55 469.886	10.93	150.16	0.624	0.274	180.0
55 470.955	10.11	150.39	0.643	0.272	163.5
55 999.608	10.00	334.30	2.952	0.229	130.3
56 001.610	8.30	335.23	3.155	0.250	126.8
56 221.917	5.90	318.92	0.424	0.091	158.9
56 227.894	9.59	322.81	0.544	0.081	160.8
56 228.900	10.52	324.06	0.609	0.098	154.1
56 229.901	11.28	324.86	0.620	0.095	154.8
56 230.899	11.53	324.83	0.631	0.088	156.9
56 235.880	14.12	325.89	0.527	0.081	160.3
56 236.878	14.59	325.94	0.497	0.088	158.4
56 237.869	15.02	326.35	0.552	0.080	161.1
56 238.864	15.45	326.38	0.550	0.080	161.2
56 297.679	4.12	337.15	0.787	0.107	178.3
MARK III					
48 275.689	18.18	328.84	0.852	0.146	80.6
48 548.925	15.20	323.62	2.490	0.219	72.8
48 562.870	18.02	327.93	1.066	0.314	85.6

ometric PSF to take the limitations of fitting a component position very far from the phase centre into account. For the contour we chose 25% above minimum to obtain a reduced $\chi^2_{\rm R}$.

An astrometric fit to positions listed in Table C.1 confirms that NPOI is insensitive to the eclipsing binary because the derived orbital properties do not differ significantly from those obtained from a global fit to V^2 presented in Table 11.

Appendix C.6: Supplementary materials to the analysis of the spectro-interferometric observations

The spectro-interferometric supplementary material consists of the following tables and figures:

i) Table C.2 lists all available spectro-interferometric observations acquired with the NPOI and MARK III instruments. For each observation the observing stations, its baselines $[B_{\rm min}; B_{\rm max}]$, phase coverage of orbits 1, and 2 ϕ_1, and, ϕ_2, and associated calibrators are given. The numbering of calibrators is given in Table C.4.

ii) Table C.3 lists all available spectro-interferometric observations acquired with the CHARA/VEGA instrument. For each observation the lengths of the projected baselines B and their orientation θ, the phase coverage of orbits 1, and 2 ϕ_1, and, ϕ_2, and associated calibrators are given.

iii) Table C.4 lists all calibrators which were used to calibrate the NPOI observations of ξ Tau. For each calibrator its Johnson V magnitude, spectral type, colour index $V-K$, interstellar reddening $E(B-V)$, the minimum amplitude squared visibility V^2 , and the uniform disk diameter $\theta_{\rm V-K}$ for wavelength range from V to K band are given.

iv) Table C.5 lists all calibrators which were used for calibration of the CHARA/VEGA and VLTI/AMBER observations. For each calibrator the spectral type, effective temperature $T_{\rm eff}$, gravitational acceleration $\log g$, Johnson V (K) magnitude V (K), and the uniform disk diameter in these bands $\theta_{\rm V}$, $\theta_{\rm K}$ are given.

v) Figures C.1 – C.10 show fits of the global model given by Eq. (9), and corresponding parameters are listed in Table 11.

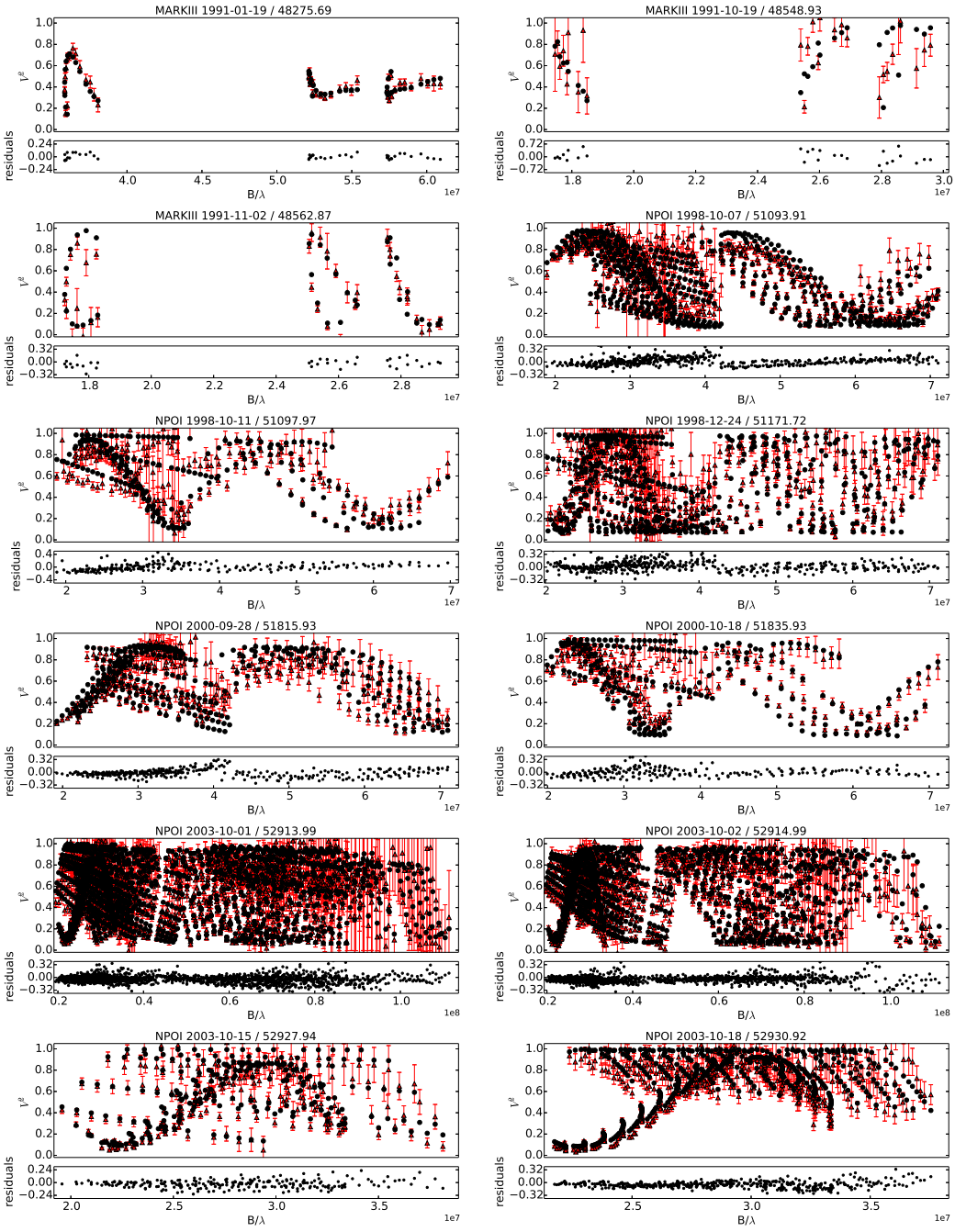

Fig. C.1. Best-fitting model (part one) plotted against the observations from the MARKIII and NPOI spectro-interferometers. In each panel, the observed squared visibility V^2 is plotted with red triangles; the model corresponding to parameters listed in Table 11 is denoted with black points. Residuals of the fit are shown below each panel. The mean acquisition date, the corresponding mean heliocentric Julian date, and the instrument are indicated above each panel.

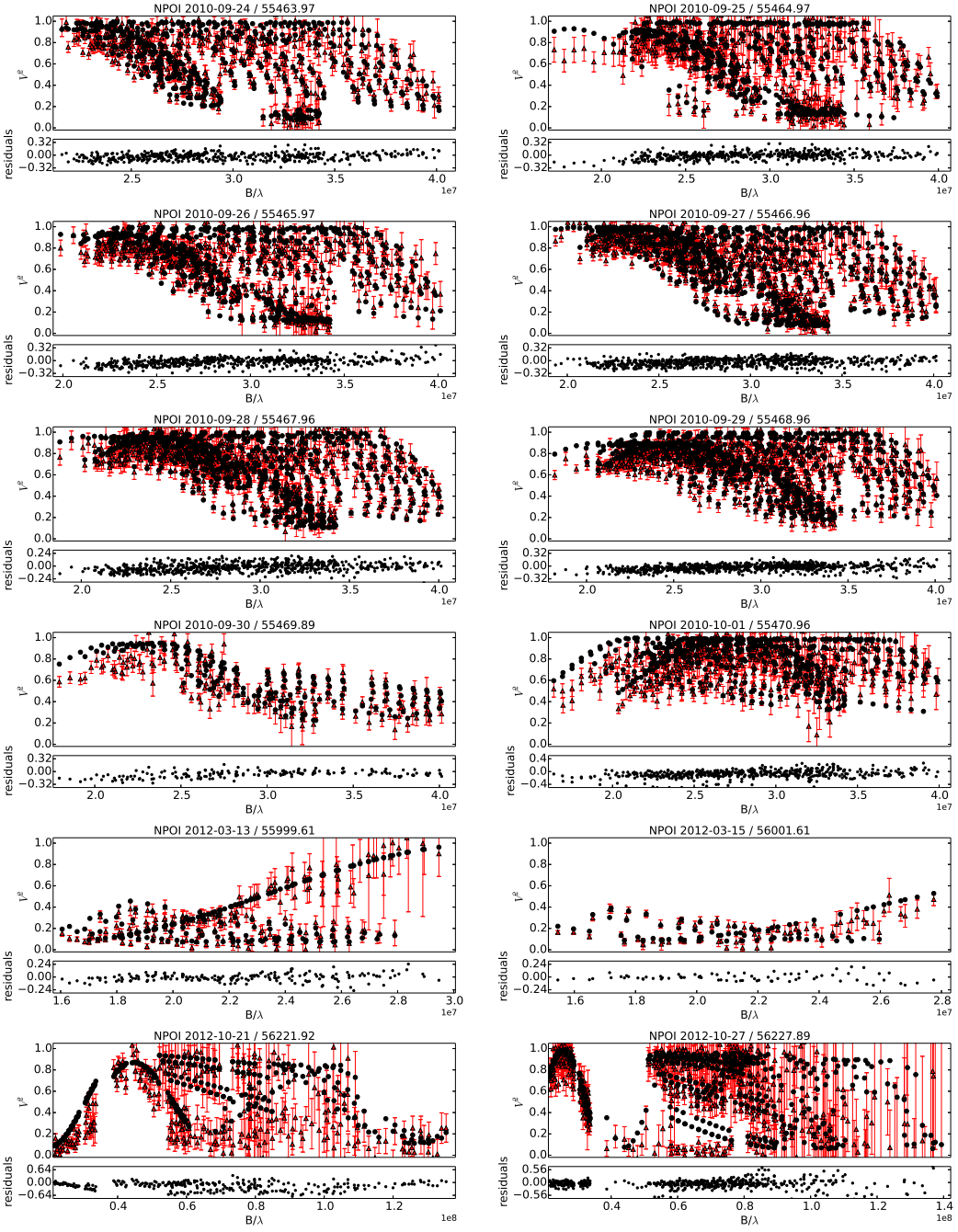

Fig. C.2. Best-fitting model (part two) plotted against the observations from the NPOI spectro-interferometer. In each panel, the observed squared visibility V^2 is plotted with red triangles; the model corresponding to parameters listed in Table 11 is denoted with black points. Residuals of the fit are shown below each panel. The mean acquisition date, the corresponding mean reduced heliocentric Julian date, and the instrument are indicated above each panel.

Table C.2. NPOI and MARK III observations of ξ Tau. Column 2 lists the configuration used as a triple of stations (e.g. "AC-AE-W7", using astrometric stations centre and east, as well as imaging station W7) if data from all three involved baselines were recorded, including the corresponding closure phase. When a single baseline is listed, only squared visibility data were recorded but no closure phases on that baseline. ϕ_1 (ϕ_2) refers to mean orbital phase of orbit 1 (2) at the given RJD. Calibrator numbers correspond to the numbering in Table C.4.

RJD[1]	Triangles/baselines	$B_{\min}$ (m)	$B_{\max}$ (m)	ϕ_1	ϕ_2	Calibrators
		NPOI				
51 093.906054	AC-AE-AW	15	37	0.066	0.897	09 11 14 18
51 097.971703	AC-AE-AW	16	37	0.635	0.925	09 11 14 18
51 171.722612	AC-AE-AW	17	37	0.954	0.433	09 11
51 815.933549	AC-AE-AW	16	37	0.096	0.871	01 03 09 08
51 835.927180	AC-AE-AW	17	37	0.894	0.008	20 09 12 14 15 08
52 913.988131	AC-AE-W7, AC-AW-W7	17	63	0.742	0.435	19
52 927.944213	AE-AC, AW-AC	17	49	0.695	0.531	05 19
52 930.924441	AE-AC, AW-AC	19	56	0.112	0.551	05 19
55 463.974404	AC-AE, AC-AW	18	22	0.551	0.000	06 15 16 17 21
55 464.970628	AC-AE, AC-AW	14	22	0.690	0.007	06 15 16 17 21
55 465.970834	AC-AE, AC-AW	17	22	0.830	0.014	06 15 16 17 21
55 466.962039	AC-AE, AC-AW	16	22	0.969	0.021	06 15 16 17 21
55 467.963919	AC-AE, AC-AW	16	22	0.109	0.028	06 15 16 17 21
55 468.959529	AC-AE, AC-AW	15	22	0.248	0.034	06 15 16 17 21
55 469.886574	AC-AE, AC-AW	15	22	0.378	0.041	06 15 16 17 21
55 470.955776	AC-AE, AC-AW	14	22	0.528	0.048	06 15 16 17 21
55 999.608038	AE-AC, AW-AC	13	16	0.500	0.690	10 11 13
56 001.610251	AE-AC, AW-AC	13	15	0.780	0.704	10 11 13
56 221.917782	AC-E6-W7, AC-AE	19	73	0.607	0.221	01 07 11
56 227.894044	AC-AE-W7, AC-E6-W7	19	79	0.443	0.262	07 11 16 02 21
56 228.900174	AC-AE-W7	18	64	0.584	0.269	07 11 16 02 21
56 229.901258	AC-AE-W7	19	67	0.724	0.276	07 11 16 02 21
56 230.899631	AC-AE-W7, W7-E6	18	73	0.863	0.283	07 11 16 02 21
56 235.880496	AC-AE-W7, AC-E6-W7	18	77	0.560	0.317	07 11 16 02 21
56 236.878894	AC-AE-W7, AC-E6-W7	19	75	0.700	0.324	07 11 16 02 21
56 237.869383	AC-AE-W7, AC-E6-W7	19	77	0.839	0.331	07 11 16 02 21
56 238.864654	AC-AE-W7, AC-E6-W7	18	78	0.978	0.338	07 11 16 04 21
56 297.679445	AC-AW-E6	0	53	0.208	0.743	10 11
		Mark III				
48 275.689	NF-SF	29	30	0.725	0.484	μ Tau, η Tau
48 548.925	ND-SC	14	15	0.958	0.366	μ Tau, η Tau
48 562.870	ND-SC	14	15	0.909	0.462	μ Tau, η Tau

Notes. [1]Mean RJD. Ephemeris used to compute the orbital phases: 1 - $T_{\min,1}(\mathrm{RJD}) = 7.1467 \times E + 56\,224.7246$, 2 - $T_{\mathrm{p},2}(\mathrm{RJD}) = 145.17 \times E + 55\,609.05$, where E is the epoch, $T_{\min,1}$ the epoch of the primary minimum of orbit 1, $T_{\mathrm{p},2}$ the epoch of the periastron passage of orbit 2.

Table C.4. List of NPOI calibrators used for ξ Tau, where V (K) is the apparent magnitude in the Johnson V (K) filter, $E(B-V)$ the interstellar reddening, V^2 the squared visibility, and θ the uniform disk diameter.

No	HD	Type	V	$V-K$	$E(B-V)$	V^2	$\theta_{\mathrm{V-K}}$ (mas)
01	886	B2IV	2.83	-0.940	0.010	0.85	0.498
02	7804	A3V	5.16	0.239	-0.010	0.91	0.366
03	7964	A3V	4.76	0.224	-0.050	0.97	0.434
04	11171	F3III	4.65	0.778	-0.035	0.73	0.653
05	12216	A2V	3.98	0.059	-0.060	0.98	0.562
06	16582	B2IV	4.07	-0.632	0.020	0.99	0.343
07	17081	B7V	4.25	-0.255	-0.010	0.89	0.403
08	20630	G5Vvar	4.83	1.873	0.000	0.86	0.956
09	23630	B7III	2.90	0.264	0.010	0.85	0.981
10	24760	B0.5V	2.88	-0.833	0.110	0.91	0.519
11	25490	A1V	3.91	0.127	0.020	0.77	0.600
12	37128	B0Ia	1.70	-0.573	0.040	0.84	1.012
13	76756	A5m	4.20	0.256	0.190	0.98	0.582
14	184006	A5Vn	3.79	0.192	-0.010	0.93	0.668
15	192696	A3IV-Vn	4.30	0.222	0.030	0.96	0.536
16	195810	B6III	4.03	-0.351	0.020	0.88	0.421
17	196724	A0V	4.82	-0.034	0.000	0.99	0.360
18	213558	A1V	3.77	-0.081	0.000	0.95	0.568
19	214923	B8.5V	3.40	-0.166	0.003	0.85	0.635
20	216735	A1V	4.90	0.060	-0.010	0.99	0.366
21	217891	B6Ve	4.53	-0.220	0.030	0.92	0.360

Table C.5. List of stars used for calibration of CHARA/VEGA and VLTI/AMBER observations. All data were taken from the JMMC Stellar Diameters Catalogue (Lafrasse et al. 2010). T_{eff} denotes the effective temperature, g the gravitational acceleration, θ_{X} the uniform-disk diameter in the passband X, X the magnitude in the passband X.

Calibrator	Parameter								
	T_{eff} (K)	$\log g_{[\mathrm{cgs}]}$	V (mag)	K (mag)	θ_{V} (mas)	θ_{R} (mas)	θ_{J} (mas)	θ_{H} (mas)	θ_{K} (mas)
CHARA/VEGA									
HD 21686	9790	4.1	5.125	5.167	0.245(18)	0.247(18)	0.251(18)	0.252(18)	0.252(18)
HD 18604	13000	3.4	4.703	4.910	0.257(18)	0.257(18)	0.262(18)	0.262(18)	0.263(18)
HD 26793	10500	4.0	5.210	5.357	0.207(15)	0.209(15)	0.212(15)	0.213(15)	0.214(15)
VLTI/AMBER									
HD 25490	9500	4.1	3.891	3.783	0.513(37)	0.518(37)	0.526(37)	0.529(37)	0.530(37)
HD 34909	4660	2.1	7.987	5.775	0.310(23)	0.315(23)	0.323(23)	0.326(23)	0.328(23)
HD 38277	5700	4.4	7.119	5.597	0.318(23)	0.322(23)	0.329(23)	0.331(23)	0.333(23)
HD 38406	5790	4.4	8.197	6.735	0.186(14)	0.188(14)	0.192(14)	0.193(14)	0.194(14)

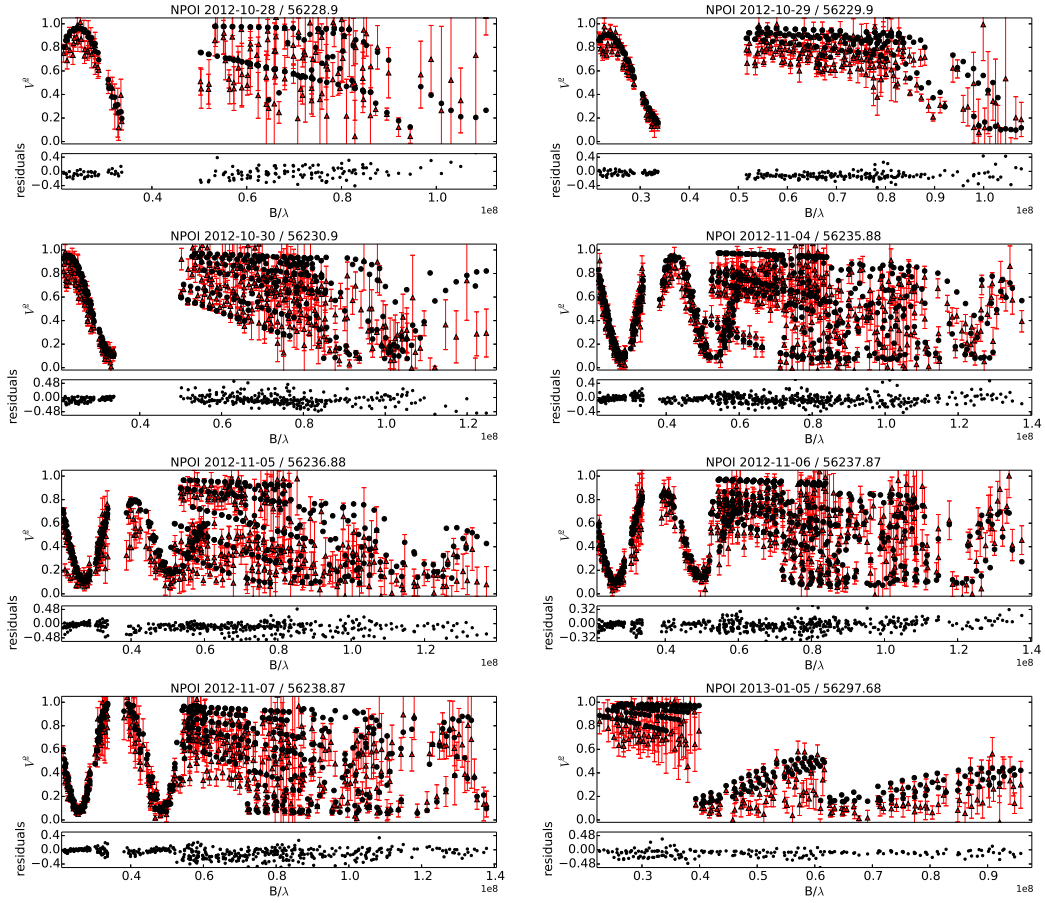

Fig. C.3. Best-fitting model (part three) plotted against the observations from the NPOI spectro-interferometer. In each panel, the observed squared visibility V^2 is plotted with red triangles; the model corresponding to parameters listed in Table 11 is denoted with black points. Residuals of the fit are shown below each panel. The mean acquisition date, the corresponding mean reduced heliocentric Julian date, and the instrument are indicated above each panel.

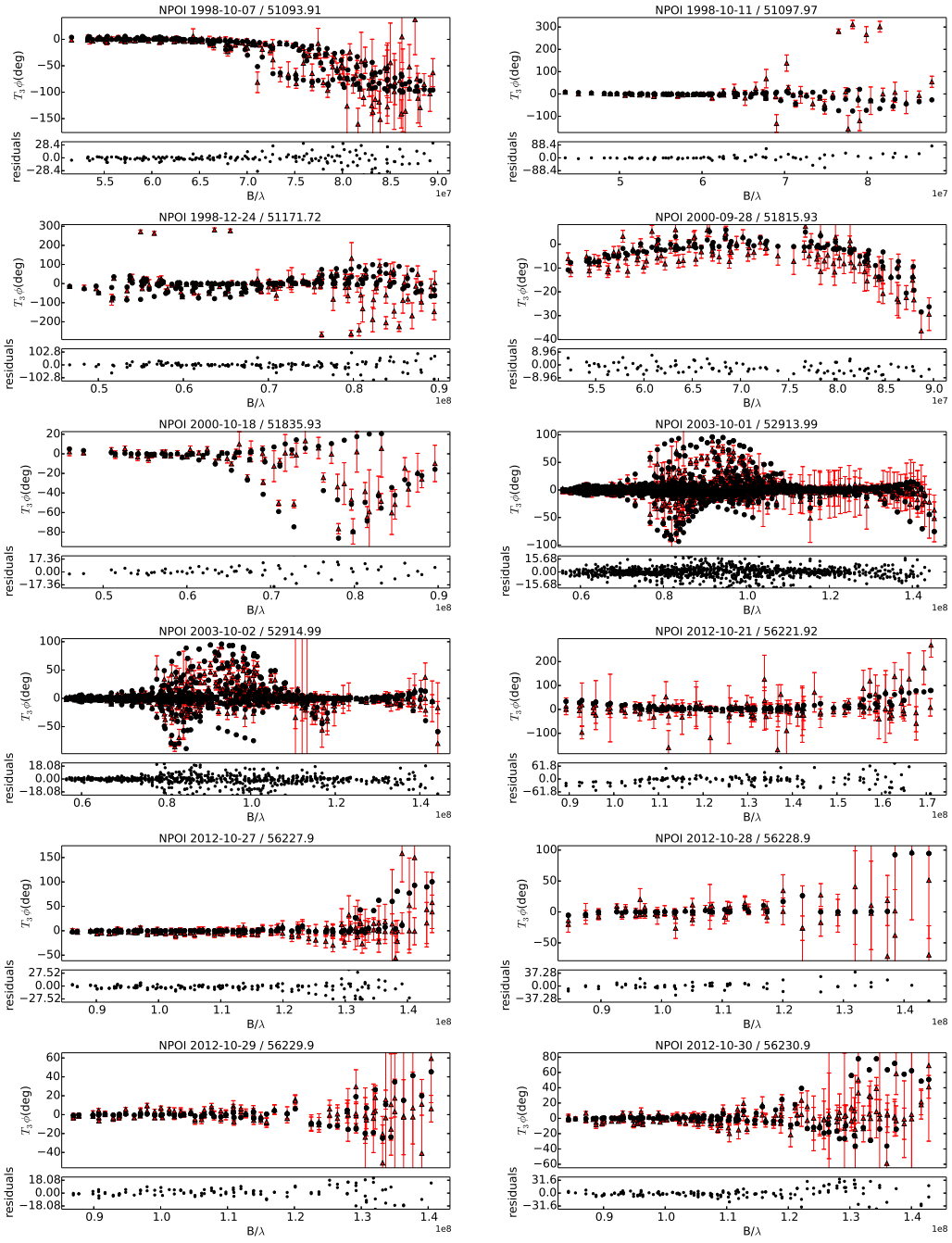

Fig. C.4. Best-fitting model (part four) plotted against the observations from the NPOI spectro-interferometer. In each panel, the observed closure phase $T_3\phi$ is plotted with red triangles; the model corresponding to parameters listed in Table 11 is denoted with black points. Residuals of the fit are shown bellow each panel. The mean acquisition date, the corresponding mean reduced heliocentric Julian date, and the instrument are indicated above each panel.

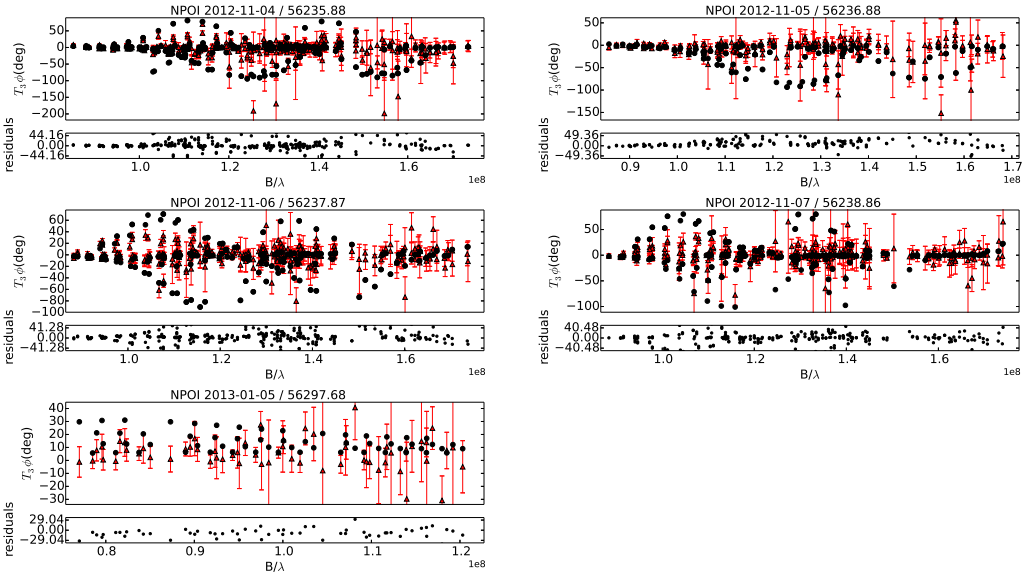

Fig. C.5. Best-fitting model (part five) plotted against the observations from the NPOI spectro-interferometer. In each panel, the observed closure phase $T_3\phi$ is plotted with red triangles; the model corresponding to parameters listed in Table 11 is denoted with black points. Residuals of the fit are shown bellow each panel. The mean acquisition date, the corresponding mean reduced heliocentric Julian date, and the instrument are indicated above each panel.

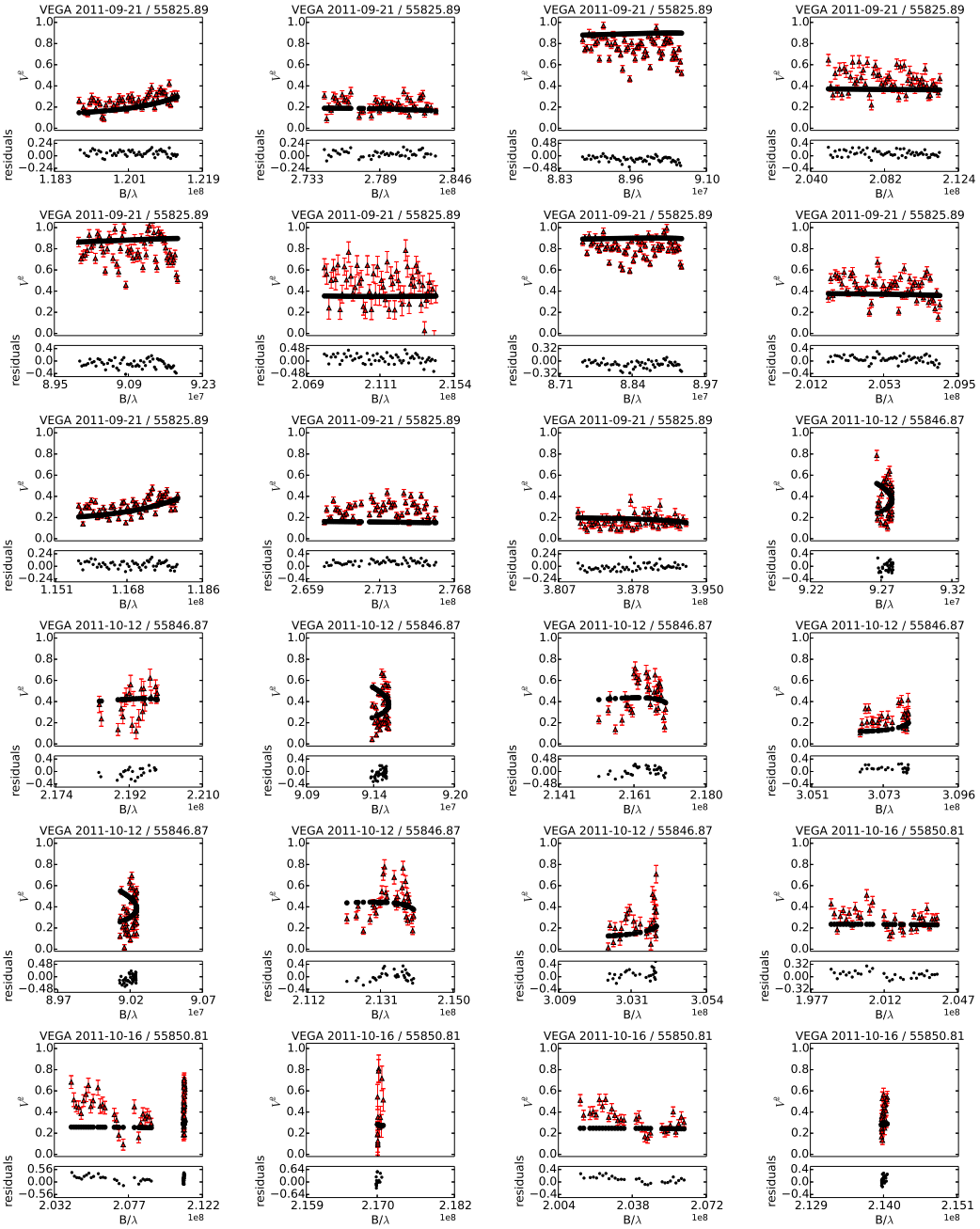

Fig. C.6. Best-fitting model (part six) plotted against the observations from the CHARA/VEGA spectro-interferometer. In each panel, the observed squared visibility V^2 is plotted with red triangles; the model corresponding to parameters listed in Table 11 is denoted with black points. Residuals of the fit are shown below each panel. The mean acquisition date, the corresponding mean reduced heliocentric Julian date, and the instrument are indicated above each panel.

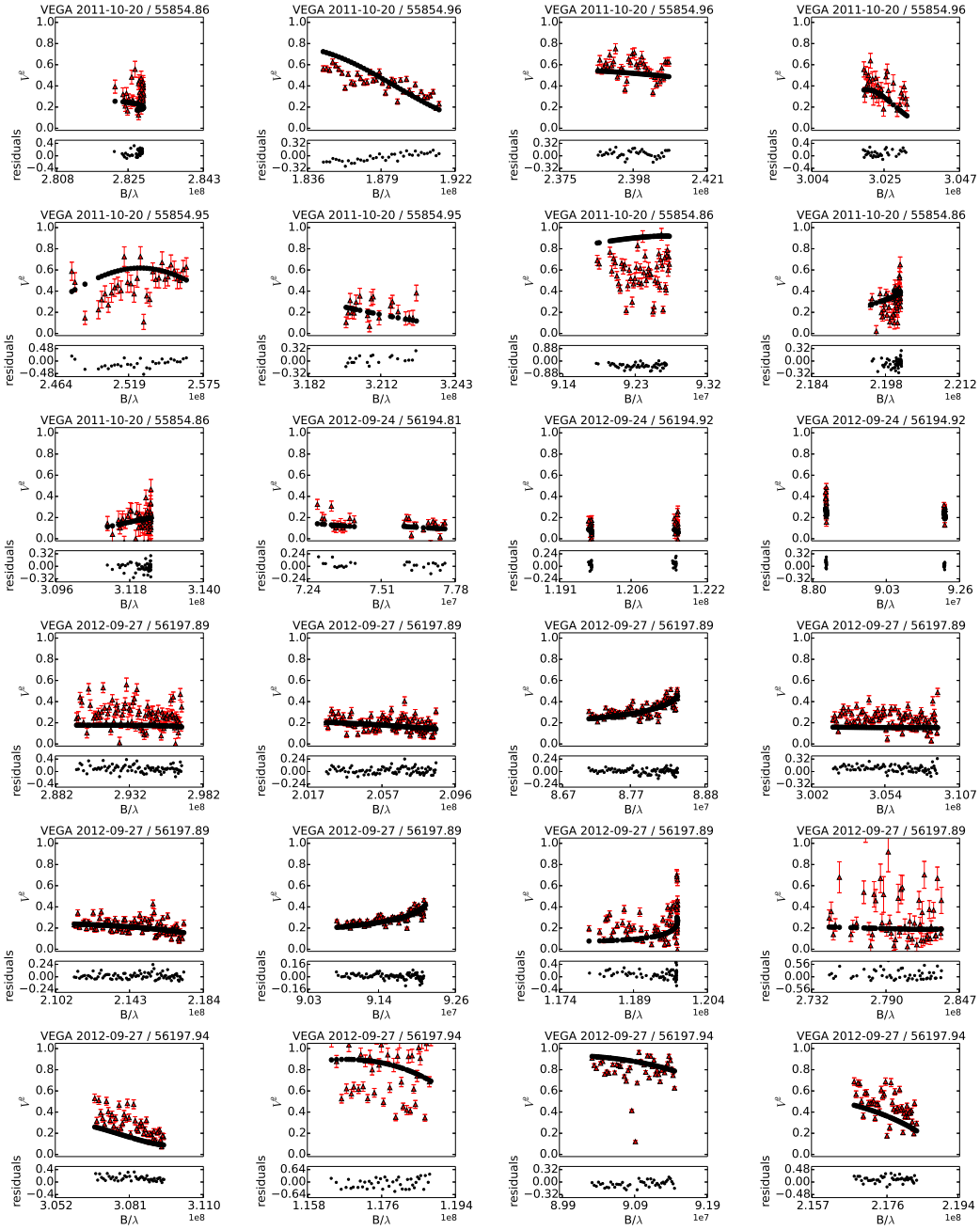

Fig. C.7. Best-fitting model (part seven) plotted against the observations from the CHARA/VEGA spectro-interferometer. In each panel, the observed squared visibility V^2 is plotted with red triangles; the model corresponding to parameters listed in Table 11 is denoted with black points. Residuals of the fit are shown below each panel. The mean acquisition date, the corresponding mean reduced heliocentric Julian date, and the instrument are indicated above each panel.

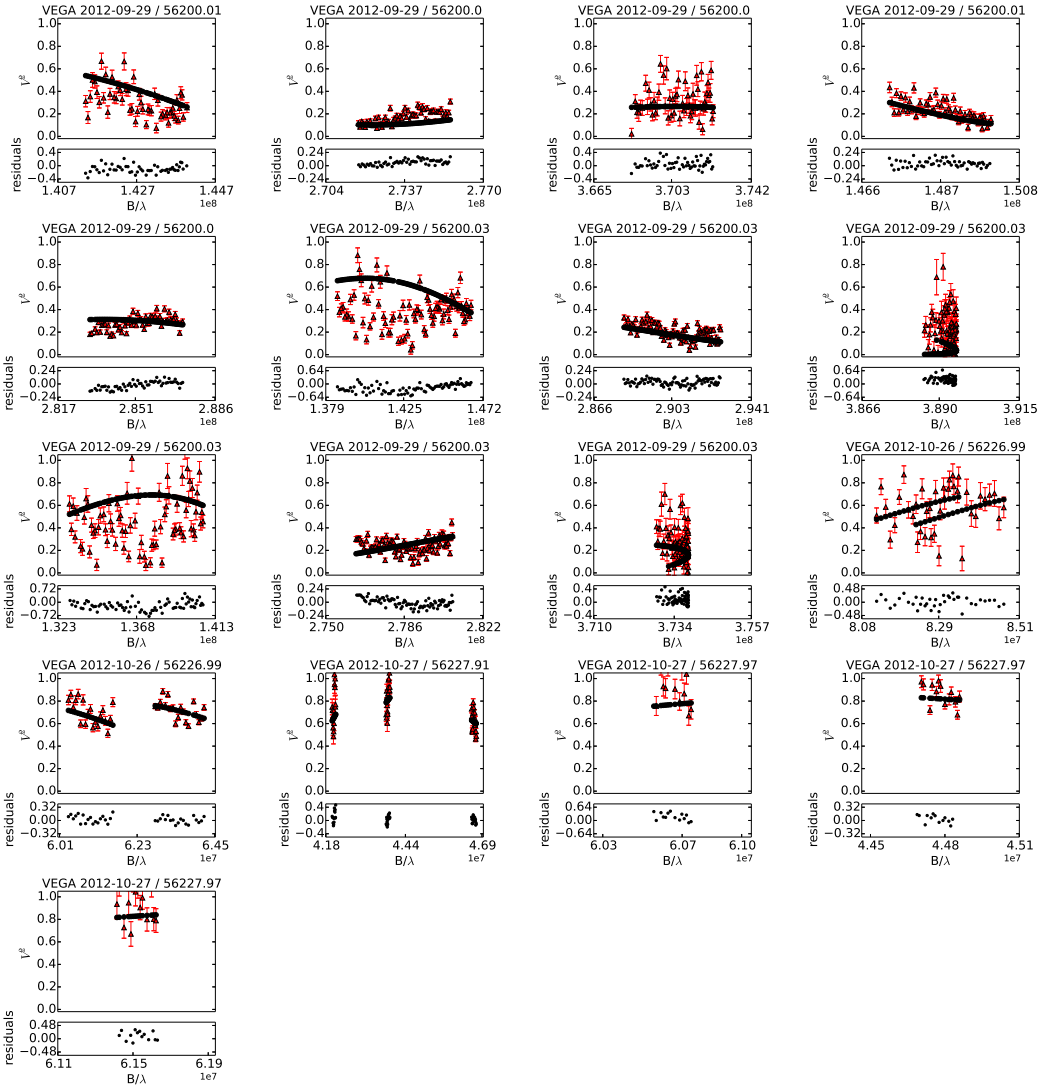

Fig. C.8. Best-fitting model (part eight) plotted against the observations from the CHARA/VEGA spectro-interferometer. In each panel, the observed squared visibility V^2 is plotted with red triangles; the model corresponding to parameters listed in Table 11 is denoted with black points. Residuals of the fit are shown below each panel. The mean acquisition date, the corresponding mean reduced heliocentric Julian date, and the instrument are indicated above each panel.

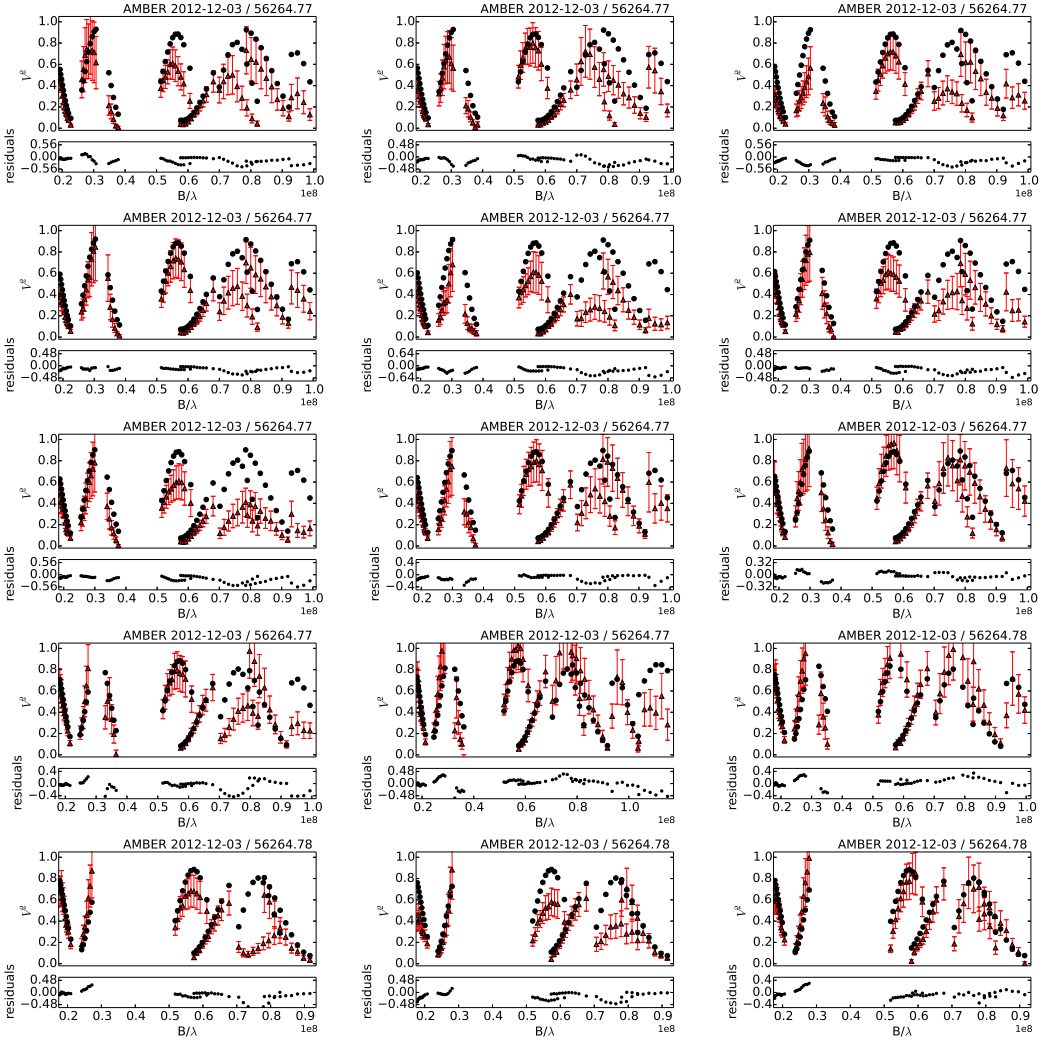

Fig. C.9. Best-fitting model (part nine) plotted against the observations from the VLTI/AMBER spectro-interferometer. In each panel, the observed squared visibility V^2 is plotted with red triangles; the model corresponding to parameters listed in Table 11 is denoted with black points. Residuals of the fit are shown below each panel. The mean acquisition date, the corresponding mean reduced heliocentric Julian date, and the instrument are indicated above each panel.

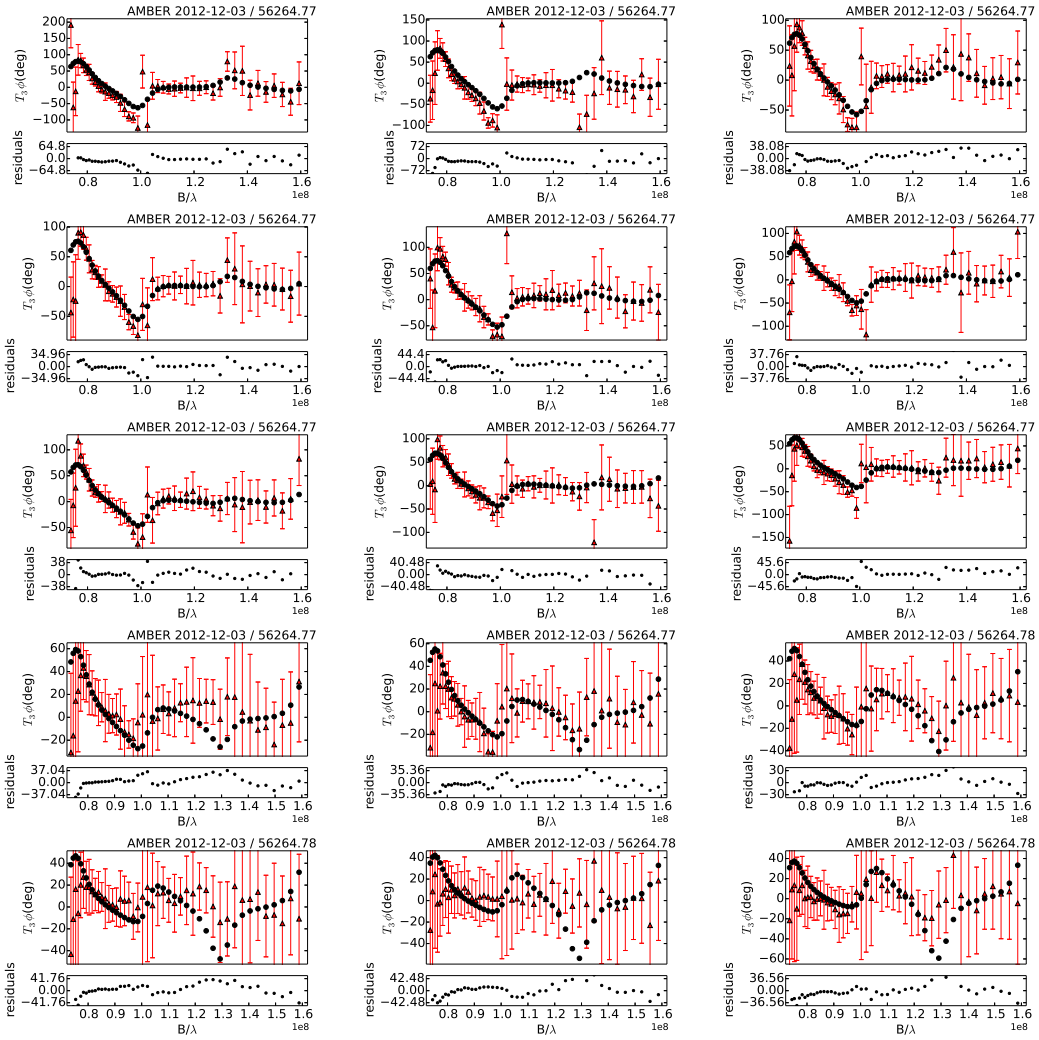

Fig. C.10. Best-fitting model (part ten) plotted against the observations from the VLTI/AMBER spectro-interferometer. In each panel, the observed closure phase $T_3\phi$ is plotted with red triangles; the model corresponding to parameters listed in Table 11 is denoted with black points. Residuals of the fit are shown bellow each panel. The mean acquisition date, the corresponding mean reduced heliocentric Julian date, and the instrument are indicated above each panel.

Appendix D: Description of the observational material

This section contains templates of tables with observational material.

- Radial velocity measurements are published in Table D.1.
- Photometric observations are published separately for each photometric filter (MO, U, B, V) in Tables D.2, D.3, D.4, D.5.
- The spectro-interferometric observations are published in form of calibrated squared visibility moduli in Table D.6, and closure phases in Table D.7.

Table C.3. Journal of the spectro-interferometric observations of ξ Tau. ϕ_1 (ϕ_2) denotes the orbital phase of orbit 1 (2), B the mean length of the projected baseline, θ the position angle of the projected baseline. The calibrator stars are identified as follows: 1 - HD 21686, 2 - HD 18604, and 3 - HD 26793.

RJD	NB	ϕ_1	ϕ_2	B (m)	θ (deg)	Cal.
The 2011 run						
55 825.8907	3-1	0.193	0.488	064.6	-155.9	1,2
	3-2			150.0	-160.6	1,2
	3-3			217.2	-158.9	1,2
55 846.8703	3-1	0.129	0.633	065.8	-154.2	2
	3-2			155.8	-159.3	2
	3-3			221.4	-157.8	2
55 850.8130	3-1	0.680	0.660	147.0	-160.9	1,2
	3-2			154.1	-090.1	1,2
	3-3			244.8	+056.0	1,2
55 854.8645	3-1	0.247	0.688	065.6	-153.1	1,2
	3-2			156.2	-158.3	1,2
	3-3			221.6	-156.8	1,2
55 854.9548	3-1	0.260	0.688	135.3	-148.5	1,2
	3-2			172.7	-057.7	1,2
	3-3			217.7	+084.1	1,2
55 856.8928	3-1	0.531	0.702	063.3	-149.9	2,3
	3-2			152.5	-155.6	2,3
	3-3			216.3	-154.2	2,3
The 2012 run						
56 194.8118	2-1	0.814	0.029	054.8	-156.0	1
56 194.9180	2-1	0.829	0.030	065.9	-154.1	1
56 197.8894	3-1	0.245	0.050	065.6	-155.2	1
	3-2			153.5	-160.1	1
	3-3			218.7	-158.6	1
56 197.9362	3-1	0.252	0.051	065.0	-152.1	1
	3-2			155.6	-157.5	1
	3-3			220.4	-155.9	1
56 200.0052	3-1	0.541	0.065	106.3	-002.5	1
	3-2			203.9	-060.1	1
	3-3			276.1	-041.1	1
56 200.0306	3-1	0.545	0.065	099.2	-000.3	1
	3-2			207.7	-056.8	1
	3-3			278.3	-039.2	1
56 226.9927	2-1	0.317	0.251	045.4	-125.8	1
56 227.0299	2-1	0.323	0.251	040.0	-109.9	1
56 227.8758	2-1	0.441	0.257	031.3	+100.3	1
56 227.9720	2-1	0.454	0.258	033.4	+117.0	1

Notes. Ephemeris used to compute the orbital phases: 1 - $T_{\rm min,1}({\rm RJD}) = 7.1467 \times E + 56\,224.7246$, 2 - $T_{\rm p,2}({\rm RJD}) = 145.17 \times E + 55\,609.05$, where E is the epoch, $T^1_{\rm min}$ the epoch of the primary minimum of orbit 1, $T_{\rm p,2}$ the epoch of the periastron passage of orbit 2.

Table D.1. RV measurements obtained with the cross-correlation technique described in Sect. 3.2. t denotes time, RV the heliocentric radial velocity, $\sigma_{\rm RV}$ the uncertainty of the heliocentric radial velocity, and *component* denotes members of ξ Tau (Aa, Ab, or B).

t (RJD)	RV (km s^{-1})	$\sigma_{\rm RV}$ (km s^{-1})	component

Notes. RJD = HJD − 2 400 000, components: Aa.. primary of orbit 1, Ab.. secondary of orbit 1, and B.. primary of orbit 2.

Table D.2. Reduced photometric observations acquired with the MOST satellite. t denotes time, MO the magnitude in the MOST filter, and $\sigma_{\rm MO}$ the uncertainty of the magnitude in the MOST filter.

t	MO	$\sigma_{\rm MO}$
(RJD)	(mag)	(mag)

Notes. RJD = HJD − 2 400 000

Table D.3. Reduced photometric observations acquired in the Johnson U filter. t denotes time, U the magnitude in the Johnson U filter, $\sigma_{\rm U}$ the uncertainty of the magnitude in the Johnson U filter, and *source* the origin of an observation.

t	U	$\sigma_{\rm U}$	source
(RJD)	(mag)	(mag)	

Notes. RJD = HJD − 2 400 000, sources: 1.. Hvar Observatory, 2.. South African Astronomical Observatory, 3.. Four College Automatic Photometric Telescope.

Table D.4. Reduced photometric observations acquired in the Johnson B filter. t denotes time, B the magnitude in the Johnson B filter, $\sigma_{\rm B}$ the uncertainty of the magnitude in the Johnson B filter, and *source* the origin of an observation.

t	B	$\sigma_{\rm B}$	source
(RJD)	(mag)	(mag)	

Notes. RJD = HJD − 2 400 000, sources: 1.. Hvar Observatory, 2.. South African Astronomical Observatory, 3.. Four College Automatic Photometric Telescope.

Table D.5. Reduced photometric observations acquired in the Johnson V filter. t denotes time, V the magnitude in the Johnson V filter, $\sigma_{\rm V}$ the uncertainty of the magnitude in the Johnson V filter, and *source* the origin of an observation.

t	V	$\sigma_{\rm V}$	source
(RJD)	(mag)	(mag)	

Notes. RJD = HJD − 2 400 000, sources: 1.. Hvar Observatory, 2.. South African Astronomical Observatory, 3.. Four College Automatic Photometric Telescope.

Table D.6. Calibrated squared visibility moduli estimated from studied spectro-interferometric observations. t denotes time, u the baseline projected in the east-west direction, v the baseline projected in the north-south direction, $\lambda_{\rm eff}$ the effective wavelength, V^2 the calibrated squared visibility modulus, $\sigma_{\rm V^2}$ the uncertainty of the calibrated visibility, and *src* the origin of an observation.

t	u	v	$\lambda_{\rm eff}$	V^2	$\sigma_{\rm V^2}$	src
(RJD)	(m)	(m)	(m)			

Notes. RJD = HJD − 2 400 000, sources: 1.. CHARA/VEGA, 2.. MARK III, 3.. NPOI, 4.. VLTI/AMBER.

Table D.7. Closure phases estimated from studied spectro-interferometric observations. t denotes time, u_1 the first baseline in a closing triangle projected in the east-west direction, v_1 the first baseline in a closing triangle projected in the north-south direction, u_2 the second baseline in a closing triangle projected in the east-west direction, v_2 the second baseline in a closing triangle projected in the north-south direction, $\lambda_{\rm eff}$ the effective wavelength, $T_3\phi$ the closure phase, $\sigma_{\rm T_3\phi}$ the uncertainty of the closure phase, and *src* the origin of an observation.

t	u_1	v_1	u_2	v_2	$\lambda_{\rm eff}$	$T_3\phi$	$\sigma_{\rm T_3\phi}$	src
(RJD)	(m)	(m)	(m)	(m)	(m)	(deg)	(deg)	

Notes. RJD = HJD − 2 400 000, sources: 1.. CHARA/VEGA, 2.. MARK III, 3.. NPOI, 4.. VLTI/AMBER.